2014-12-01

Kinetic Experimental and Modeling Studies on Iron-Based Catalysts Promoted with Lanthana for the High-Temperature Water-Gas Shift Reaction Characterized with Operando UV-Visible Spectroscopy and for the Fischer-Tropsch Synthesis

Basseem Bishara Hallac
Brigham Young University - Provo

Kinetic Experimental and Modeling Studies on Iron-Based Catalysts Promoted with Lanthana for the High-Temperature Water-Gas Shift Reaction Characterized with *Operando* UV-Visible Spectroscopy and for the Fischer-Tropsch Synthesis

Basseem Bishara Hallac

A dissertation submitted to the faculty of
Brigham Young University
in partial fulfillment of the requirements for the degree of

Doctor of Philosophy

Morris D. Argyle, Chair
William C. Hecker
Bradley C. Bundy
Thomas H. Fletcher
W. Vincent Wilding

Department of Chemical Engineering

Brigham Young University

December 2014

ABSTRACT

Kinetic Experimental and Modeling Studies on Iron-Based Catalysts Promoted with Lanthana for the High-Temperature Water-Gas Shift Reaction Characterized with *Operando* UV-Visible Spectroscopy and for the Fischer-Tropsch Synthesis

Basseem Bishara Hallac
Department of Chemical Engineering, BYU
Doctor of Philosophy

The structural and functional roles of lanthana in unsupported iron-based catalysts for the high-temperature water-gas shift reaction and Fischer-Tropsch synthesis were investigated. The performance of the catalysts with varying lanthana contents was based on their activity, selectivity, and stability. With regard to the former reaction, extent of reduction of the iron in $Fe_2O_3/Cr_2O_3/CuO/La_2O_3$ water-gas shift catalysts is a key parameter that was characterized using UV-visible spectroscopy. Minor addition of lanthana (<0.5 wt%) produces more active and stable catalysts apparently because it stabilizes the iron-chromium spinel, increases the surface area of the reduced catalysts, enhances the reduction of hematite to the magnetite active phase, and facilitates the adsorption of CO on the surface of the catalyst modeled by an adsorptive Langmuir-Hinshelwood mechanism. Statistical 95% confidence contour plots of the adsorption equilibrium constants show that water adsorbs more strongly than CO, which inhibits the reaction rate. A calibration curve that correlates the oxidation state of surface iron domains to normalized absorbance of visible light was successfully generated and applied to the water-gas shift catalysts. UV-visible studies indicated higher extent of reduction for surface Fe domains for the catalysts promoted with 1 wt% of lanthana and showed potential to be a more convenient technique for surface chemistry studies than X-ray absorption near edge spectroscopy (XANES).

Lanthana addition to iron-based Fischer-Tropsch catalysts enhances the olefin-to-paraffin ratio, but decreases their activity, stability, and selectivity to liquid hydrocarbons. Adding lanthana at the expense of potassium reduces the water-gas shift selectivity and enhances the activity and stability of the catalysts.

Finally, a model that simulates heat and mass transfer limitations on the particle scale for the Fischer-Tropsch reaction applicable at lab-scale suggests optimal operating and design conditions of 256°C, 30 bar, and 80 μm particle size for maximum observed reaction rate. Low H_2:CO ratios are recommended for higher selectivity to liquid hydrocarbons. The model considers pressure drop, deactivation, pore diffusion, film heat transfer, and internal heat transfer when solving for the optimal conditions, and maps them as functions of design variables. This model can be up-scaled to provide guidance for optimal design of commercial-size reactors.

Keywords: iron catalysts, lanthana, UV-visible spectroscopy, water-gas shift, Fischer-Tropsch

ACKNOWLEDGEMENTS

I owe my deepest gratitude to Dr. Morris Argyle who has always been a supportive, encouraging, and helpful mentor. I sincerely thank you for your wisdom and keen guidance.

Further, I would like to thank the committee for their help. Special thanks to Dr.'s William Hecker, Calvin Bartholomew, Larry Baxter, and John Hedengren who spent a tremendous amount of time helping me with statistical analysis, optimization and modeling. Dr. Bartholomew provided invaluable expertise and consultations.

I would also like to thank Eli Stavitski from Brookhaven National Lab for collaborating with our lab and testing our samples.

To my colleagues who worked hard and struggled with me on projects, including Jared Brown, Rabindra Sharma, Rupak Bajagain, Trevor Slade, Aslan Omar Mahmoud, Brandon Clark and Sora Lee, thank you for your productive and responsible work!

Friends, thank you for making life more interesting during monotonous times. You will always be remembered!

Finally, I would like to especially acknowledge Dr. Erlend Peterson and Kate Anderson of the international vice president office at Brigham Young University. You are my spiritual parents who made me feel at home with your endless love and constant care. I owe you my greatest debt. Thank you!

DEDICATION

I dedicate this dissertation work to my family who has always been standing firmly by my side throughout this process. Much gratitude to my wonderful parents, Bishara and Mary Hallac, whose supportive stance, encouraging words, and persistence on education are the seeds that cultivated the person I am today. Considerable appreciation and respect to my brothers Boutros and Bassem who are great examples of highly-motivated, inspired, and enlightened individuals and who were always there for me to keep me on track.

Also, I dedicate this work to Uncle Robert, Aunt Rima, Aunt Mary, and my cousins for their constant support.

Another dedication goes to the memory of my deceased grandparents whom I wish were still among us to observe the accomplishment of this work. However, I am confident that they are in a better place now and that their investment in me has nurtured.

I finally dedicate this work to my beloved country Palestine and its strong, proud, and enduring nation. I truly hope that peace will prevail in the land of peace. I believe that our tenacity on education and self-development are key factors for achieving our endeavors. Cheers to everyone who believes in the richness of learning!

TABLE OF CONTENTS

LIST OF TABLES

LIST OF FIGURES

NOMENCLATURE

a	Catalyst activity
A	Arrhenius constant
A_d	Arrhenius constant of deactivation
A_{reac}	Cross sectional area of the reactor
ASP	Aspect ratio for sphericity calculations
c_p	Specific heat capacity
C_i	Concentration of species i
$\boldsymbol{d_c}$	Crystallite size
d_p	Particle diameter
d_{pore}	Pore diameter
D_{AB}	Bulk diffusivity
D_e	Effective diffusivity
D_K	Knudsen diffusivity
E_a	Activation energy
E_d	Activation energy of deactivation
f	Friction factor
$F(R)$	Kubelka-Munk function
F	F-statistic
$F^0{}_i$	Feed molar flow rate of species i
g	Gravitational constant
h	Convective heat transfer constant
j_H	Chilton-Colburn factor
k	Rate constant
k_d	Deactivation rate constant
K	Water-gas shift equilibrium constant/absorbance term in Kubelka-Munk function
K_i	Adsorption equilibrium constant of species i
L_p	Characteristic particle length
L_{bed}	Catalyst bed length
m	Power on CO concentration
M_A	Molecular weight of solute
M_B	Molecular weight of solvent
M_w	Weisz-Wheeler modulus
n	Overall order of reaction/power on H_2O concentration
n_r	Number of data points
$NRSS$	Squared sum of the normalized residuals
$NTSS$	Total sum of squared errors
p	Power on CO_2 concentration
p_r	Number of fitting parameters
P	Reaction pressure
P_i	Partial pressure of species i
PA_i	GC peak area for species i
Pr	Prandtl number
q	Power on H_2 concentration
q_r	Number of linear regressors
r^2	Coefficient of determination
r_d	Deactivation rate
$-r_{CO}$	Rate of CO depletion
R_g	Universal gas constant
R_p	Particle radius
R_{WGS}	Ratio of the feed molar flow rates of CO and H_2 to the feed molar flow rate of H_2O

RF_i	GC response factor for species i
Re	Reynolds number
S	Scattering term in Kubelka-Munk function
S_i	Selectivity to species i
$S(\boldsymbol{\theta})$	Sum of squared errors for a vector $\boldsymbol{\theta}$
$S(\widehat{\boldsymbol{\theta}})$	Sum of squared errors for a vector of optimal values $\widehat{\boldsymbol{\theta}}$
SA	Surface area of catalyst
t	Reaction time
T	Temperature
TOS	Time on stream
u	Velocity
$\bar{V}$	Specific molar volume
$\dot{V}_i$	Feed volumetric flow rate of species i
V_{pore}	Pore volume
W_{cat}	Mass of catalyst
X_{CO}	CO conversion
x_i	Kubelka-Munk number for catalyst i
y_i	Oxidation state of iron for catalyst i

Greek Letters

β_{eq}	Fractional approach to equilibrium for the water-gas shift reaction
β_{th}	Ratio of particle temperature gradient to the surface temperature
β_c	Full width at half maximum of XRD diffraction lines
δ_{GW}	Pressure drop per unit length for gas flowing in a packed bed
ΔH_r	Heat of reaction
ΔP	Pressure drop
ΔT_{film}	Film temperature gradient
ΔT_p	Particle temperature gradient
ε_b	Bulk porosity
$\varepsilon_{l,dyn}$	Dynamic liquid void fraction
$\varepsilon_{l,stat}$	Static liquid void fraction
ε_p	Particle porosity
ε_w	Void fraction adjusted for static liquid holdup
θ	Half of the XRD diffraction angle
λ_c	Wavelength of XRD radiation
λ_e	Effective thermal conductivity
ρ_b	Bulk density
σ_i	Hard-sphere diameter of species i
ϕ	Thiele modulus
η	Effectiveness factor
ρ_b	Bulk density
ρ_p	Particle density
μ	Viscosity
τ	Tortuosity

Subscripts

g	Gas property
l	Liquid property
s	Surface property

CHAPTER 1. INTRODUCTION

This chapter provides an introduction to the motivation for the work presented in this dissertation, and background information about the three major areas studied in this work which are: (1) the water-gas shift reaction, (2) Fischer-Tropsch synthesis, and (3) *operando* UV-visible spectroscopy.

1.1 Background

Most of the energy supply in the U.S. comes from petroleum, natural gas, and coal. The dwindling petroleum sources and continuous long-term demand for energy require investing research efforts in exploring, developing, and optimizing other chemical processes for the production of liquid fuel sources that satisfy this energy demand. With the advancement of upstream technology and engineering drilling tools, natural gas can be extracted from deep reservoirs with the aid of hydraulic fracturing, making it a cheap, abundant, and feasible energy source. The cheaper natural gas and coal sources have not only lowered the operating price of current well-developed chemical processes that use them as feedstock, but also increased the interest in exploring processes which convert them to liquid fuels that have higher energy value by volume. Such processes are known as natural gas to liquids (GTL) or coal to liquids (CTL). Royal Dutch Shell plc. and Sasol Ltf. have commercialized these technologies for production of fuels. The Fischer-Tropsch synthesis (FTS) serves as a critical reaction step in both processes as it produces liquid hydrocarbons from syngas, which is a mixture of carbon monoxide (CO) and

hydrogen (H_2). The water-gas shift (WGS) reaction, on the other hand, not only controls the H_2:CO ratio in FTS catalyzed over iron-based catalysts, but is also a key step in the hydrogen production industry.

1.1.1 The Water-Gas Shift Reaction

Hydrogen is an invaluable highly-reactive chemical with an energy density of 33 kWh/kg. It is used in numerous industrial processes, beginning notably in the early 20th century when the Haber process for ammonia production was developed [1]. Hydrogen is also used in the following processes [2]:

1- hydrogenation of unsaturated hydrocarbons to form saturated ones;
2- fuel industries where it is used to fuel proton exchange membrane fuel cells (PEMFC) as part of the low-carbon environmentally benign energy sources;
3- metallurgical industries to capture oxygen and reduce metals, such as iron ore;
4- petroleum industries during the hydrotreatment processes to remove sulfur from the crude oil products;
5- semiconductor industry to passivate surface layers of pure silicon; and
6- electrical generators, where it acts as a coolant.

Hydrogen can be produced as a component of synthesis gas *via*: (1) steam methane reforming (SMR) or any other autothermal reforming process of an abundant carbon or hydrocarbon source, or (2) coal or biomass gasification, or (3) electrolysis. Gasification processes typically yield low-hydrogen syngas. Renewable energy procedures to produce hydrogen are not commonly used due to high cost and inefficiency. Therefore, steam methane reforming serves as

the primary process for industrial production of hydrogen, according to the following endothermic chemical reaction at 700 – 1000 °C [3]:

$$CH_4 + H_2O_{(g)} \leftrightarrow CO + 3H_2 \qquad \Delta H°_{298K} = 206\ kJ/mol \qquad (1.1)$$

This reaction is followed downstream by the WGS reaction (Eq. 1.2) to decrease the CO composition in effluent gas stream to below 0.2%.

$$CO + H_2O_{(g)} \leftrightarrow CO_2 + H_2 \qquad \Delta H°_{298K} = -41\ kJ/mol \qquad (1.2)$$

The exothermicity and reversibility of the WGS reaction lead it to be performed in 2 steps: (1) high-temperature (HT) at ~400 °C and (2) low-temperature (LT) at ~220 °C, as shown in Figure 1.1.

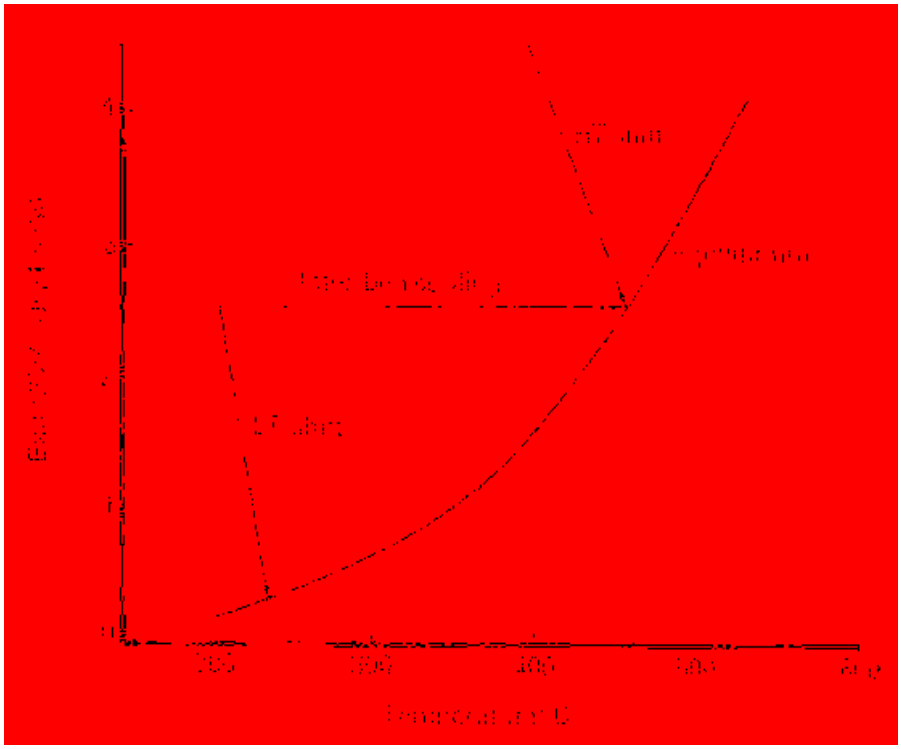

Figure 1.1: Schematic of the high and low temperature water-gas shift reaction [1].

The non-catalytic homogeneous HT WGS reaction operating with supercritical water (above 647 K and 22 MPa) has a reaction rate about 10^7 times slower compared to the reaction in the presence of catalytic iron at non-supercritical conditions [4], which emphasizes the importance of the heterogeneous catalyst. Industrial HT WGS catalysts usually contain iron oxide, chromia, and copper ($Fe_3O_4/Cr_2O_3/Cu$), whereas $Cu\text{-}ZnO\text{-}Al_2O_3$ catalysts are used for the LT WGS reaction [1, 3]. The active phase of the high-temperature shift (HTS) catalysts is magnetite, Fe_3O_4, because of its apparent ability to dissociate water molecules into atomic hydrogen and hydroxyl radicals [3].

1.1.2 The Fischer-Tropsch Synthesis

The WGS reaction plays a critical role in Fe-catalyzed FTS as it controls the H_2:CO ratio. The FTS produces a wide range of saturated and unsaturated hydrocarbons from syngas according to the following polymerization chemistries [3]:

$$CO + 3H_2 \leftrightarrow CH_4 + H_2O_{(g)} \quad \text{Methane formation} \quad (1.3)$$

$$CO + 2H_2 \rightarrow (1/n)C_nH_{2n} + H_2O_{(g)} \quad \text{Alkene Synthesis Reaction} \quad (1.4)$$

$$nCO + (2n+1)H_2 \rightarrow C_nH_{2n+2} + nH_2O_{(g)} \quad \text{Alkane Synthesis Reaction} \quad (1.5)$$

$$CO + H_2O_{(g)} \leftrightarrow CO_2 + H_2 \quad \text{Water-Gas Shift Reaction} \quad (1.6)$$

$$2CO \leftrightarrow C + CO_2 \quad \text{Boudouard Reaction} \quad (1.7)$$

The products of interest from this process are liquid hydrocarbons, such as gasoline ($C_5 - C_{11}$) and diesel ($C_{12} - C_{17}$), which serve as primary energy sources for combustion. Waxes can be separated and hydrocracked to form lighter hydrocarbons. The exothermicity of this reaction

decreases with increasing carbon number, n. The standard enthalpy of formation for methane is -247 kJ/mol. Thermodynamic calculations based on Gibbs free energies (ΔG°) show that methane production is favored over heavier hydrocarbons [5]. Lower reaction temperatures, higher reaction pressures, and lower H_2:CO ratios increase C_{2+} hydrocarbon selectivity, while decreasing selectivity to methane.

Catalysts are required for the synthesis reaction to occur at industrially relevant rates at moderate reaction temperatures, pressures, and H_2:CO ratios. Extreme operating conditions cause catalytic deactivation. Typical heterogeneous FTS processes operate at 180 – 270 °C, 15 – 40 bar, and H_2:CO ratios of 1 to 2. Current FT catalysts that are widely used are iron (Fe)– or cobalt (Co)-based, as they show high selectivity to hydrocarbons heavier than methane. Ruthenium (Ru) is ineffective due to high cost, while nickel (Ni) gives higher selectivity to methane. Fe-based FT catalysts simultaneously catalyze the WGS reaction, while Co-based catalysts do not, which leads to varying requirements for the feed syngas composition. For Fe-based catalysts, the H_2:CO ratio is usually around 1 and for Co-based catalysts the ratio is typically 2. The active phase of the Fe-based catalysts is believed to be iron carbide, $\chi - Fe_5C_2$, known as the Hägg carbide [3].

A tremendous amount of research is being invested in studying and modeling FTS reactors due to the large amounts of heat and wide range of hydrocarbons generated from the reaction. The three well-known types of industrial FT reactors are fixed-bed, slurry bubble-column, and fluidized-bed reactors. While each reactor type has its own advantages and disadvantages, fixed-bed reactors are simple to build and operate and the catalyst particles have lower attrition due to the stationary bed of catalyst [6]. The drawback of a fixed-bed reactor is

that the heat generated within the stationary catalyst particles and their pores filled with the distribution of hydrocarbons formed by the FTS reaction generally lead to transport limitation concerns [7 – 8]. Slurry-bubble column and fluidized-bed reactors provide better heat distribution and removal, but are more expensive to build, introduce complexity in separating the wax from the catalyst, and potentially cause catalyst particle attrition and physical damage [6].

1.1.3 Ultraviolet-Visible Spectroscopy

Characterization techniques are essential for understanding the chemical and physical properties of catalysts that affect their performance. *Operando* spectroscopic techniques for surface analysis are critical characterization methods in the field of heterogeneous catalysis, due to their sensitivity to changes in the surface chemistry of catalysts under operating conditions [9 – 10]. Ultraviolet-visible (UV-vis) diffuse reflectance spectroscopy is one technique that can be used to determine the extent of reduction of catalyst samples by exposing them to a broad spectrum of UV and visible wavelengths. The physical theory behind this phenomenon is that different oxidation states of the same metal have different Fermi (energy) band gaps and thus absorb light of different quantized energies [11 – 13]. X-ray absorption near edge structure (XANES) is a powerful and sensitive absorption spectroscopic technique from which extent of metal reduction of the bulk can be quantified by exposing the sample to highly energetic X-ray photons that are absorbed by core electrons, causing photoelectrons to be emitted at characteristic energies. The multiple scattering of the excited electrons specify the spatial configuration of the atoms using extended X-ray absorption fine structure (EXAFS) analysis. Any changes in the distribution of charge around an atom of a given element produce shifts to the absorption edge regions caused by variations in the binding energies of the electrons [14 – 15].

1.2 Objective

The water-gas shift is a critical reaction step in steam reforming processes for hydrogen production, while Fischer-Tropsch technology is growing as a method for the production of liquid fuels. Both reactions can be catalyzed by similar iron-based catalysts. Enhancement of catalytic performance for such reactions is important to optimize the following metrics: (1) activity (conversion rate of reactants to products), (2) selectivity (yield of the desired products), and (3) stability (catalyst life). The main goal of this research work is to study the structural and functional roles of lanthana in iron catalysts for promoting the HT WGS and FTS reactions. Furthermore, *operando* UV-visible spectroscopy was employed as a cheaper, more feasible, and more convenient tool than XANES for studying surface chemistries of catalysts. The following approach was followed to accomplish this goal:

1. Prepare industrially relevant HT WGS (5 samples) and FTS (4 samples) iron catalysts modified with varying amounts of lanthana addition.
2. Characterize the fresh and spent catalysts using different techniques to compare the physical and chemical properties of the different catalysts.
3. Acquire activity and kinetic data under differential conditions and perform microscale kinetic modeling by fitting the data to rate models derived from proposed elementary step mechanisms.
4. Characterize the catalysts using *operando* UV-visible spectroscopy with concurrent mass spectroscopy to quantify extent of reduction of the HT WGS catalysts while operating under reaction conditions.

5. Study and understand the kinetics and activity of the WGS reaction on FTS iron catalysts, separately from FTS.
6. Develop an optimized simulation model that predicts internal and external heat transfer rates and pore diffusion limitations within FTS iron catalyst particles for different operating (temperature, pressure, H_2:CO ratio) and catalyst design (agglomerate particle size) conditions.

1.3 Chemical and Physical Properties of Lanthana

Lanthanum oxide or lanthana (La_2O_3) is considered in this work as a promoter for the HT shift and FTS Fe-based catalysts based on the following chemical and physical properties that it possesses [11]:

i. Thermal stability

Lanthana is recognized as a good thermal stabilizer for catalysts because it can withstand high temperatures, therefore potentially decreasing sintering that would otherwise decrease catalytic surface area. The melting point of lanthana is 2315 °C.

ii. Large, stable, and highly charged trivalent La^{3+}.

The ionic radius of La^{3+} is 103.2 nm, compared to 64.5 nm for high-spin Fe^{3+} [11], and has a coordination number of 7. The large size of the lanthanide ion and high coordination number, along with the same ionic charge as Fe^{3+}, allow it to integrate more easily in the lattice structure and provide more sites for the reactants to adsorb on the catalyst surface.

iii. Two oxidation states: +2 and +3.

Lanthanum also exhibits multiple oxidation states, including +2 and +3, which means that it has the ability to be oxidized or reduced during a catalytic cycle.

iv. Minimized ligand-ligand repulsions.

Compared to other commonly used rare earth oxides, such as Ce^{4+}, La^{3+} is a bigger cation with a lower oxidation state that creates weaker field strengths, thus minimizing ligand-ligand repulsions because ligands are not attracted too close to the metal on the catalyst surface.

v. Soft lewis acid.

Polarizability is another characteristic which makes La^{3+} a promising candidate as a promoter. La^{3+} is considered to be the softest Lewis acid among all lanthanide cations. Since CO is a soft Lewis base and Fe^{3+} is a hard Lewis acid, there might exist a more favorable soft-soft interaction between CO and the La. Therefore, in terms of catalysis, lanthana might facilitate the adsorption of CO.

1.4 Organization of Dissertation

This dissertation contains a thorough study of three closely-related projects: (1) HT WGS reaction, (2) extent of reduction using *operando* UV-visible spectroscopy, and (3) FTS. It is divided into 7 chapters, including this introductory chapter. Chapter 1 provides background information about the chemistries of the WGS and FTS reactions and typical catalysts and reactors used for such processes in industry. Chapter 2 includes a comprehensive literature review on catalyst preparation, promoters, characterization, mechanisms, mesoscale catalyst

design modeling, and *operando* studies performed on catalysts using UV-visible spectroscopy. Chapter 3 describes the findings on the HT WGS reaction, where the results and discussion of kinetic experiments accompanied with statistical analysis, performance (activity and stability), and characterization of the catalysts with varying contents of lanthana are reported. Chapter 4 presents and discusses the calibration data obtained for extent of reduction of HT WGS iron catalysts using UV-visible spectroscopy and describes the feasibility and convenience of using this technique over XANES for analysis of surface chemistry. Chapter 5 reports and discusses the results of the mesoscale modeling and optimization of the design of FTS iron catalysts to minimize pore diffusion and internal and external heat transfer limitations for transport-limited reactions. Chapter 6 reports and discusses the results of kinetic experiments, FTS performance (activity, selectivity, and stability), kinetics and activity of WGS, CO_2 selectivity, and characterization of Fe-based FTS catalysts with varying amounts of lanthana. Chapter 7 summarizes the findings of the research work presented in the preceding chapters and proposes recommendations for future work.

The work presented in Chapters 3 and 5 have been published in peer-reviewed journals (International Journal of Hydrogen Energy and Chemical Engineering Journal, respectively). The work of Chapter 4 is currently under review by the Journal of Physical Chemistry C, which is a peer-reviewed journal. The study reported in Chapter 6 is also being considered for publication.

CHAPTER 2. LITERATURE REVIEW

This chapter presents a thorough literature review on: (1) high-temperature (HT) water-gas shift (WGS) reaction, (2) UV-visible spectroscopy, and (3) Fischer-Tropsch synthesis (FTS).

2.1 High-Temperature Water-Gas Shift Reaction

2.1.1 Catalysts, Promoters, and Preparation

The most widely used catalyst for the HT WGS reaction was invented in 1912 by Bosch and Wild. They formed Fe-based catalysts with chromia added as a structural stabilizer to prevent sintering and deactivation at high temperatures [16]. The catalyst is highly active at temperatures between 400 and 500 ºC. Industrial catalysts are typically synthesized with concentrations of 90-95 wt% of Fe_2O_3 and 5-10 wt% of Cr_2O_3. The catalysts operate industrially at temperatures between 350 – 550 °C and pressures that can be as high as 3 MPa. The use of high temperatures and pressures increase the reaction rate and therefore minimize the reactor size and cost. The drawback of running the catalysts under these extreme operating conditions is deactivation by either sintering or carbon deposition. The catalysts can have low-pressure operating lives up to 15 years [1, 17, 18].

The structural support that chromia adds to these catalysts is depicted in Figure 2.1, which compares the magnetite spinel (left) with the iron-chromium spinel (right). Addition of Cr^{3+}

replaces Fe^{3+} in the octahedral sites and rearranges the spinel structure in a way that decreases the lattice parameters. This results in the formation of tighter and more compact lattice structures that possess higher lattice energy [19 - 24].

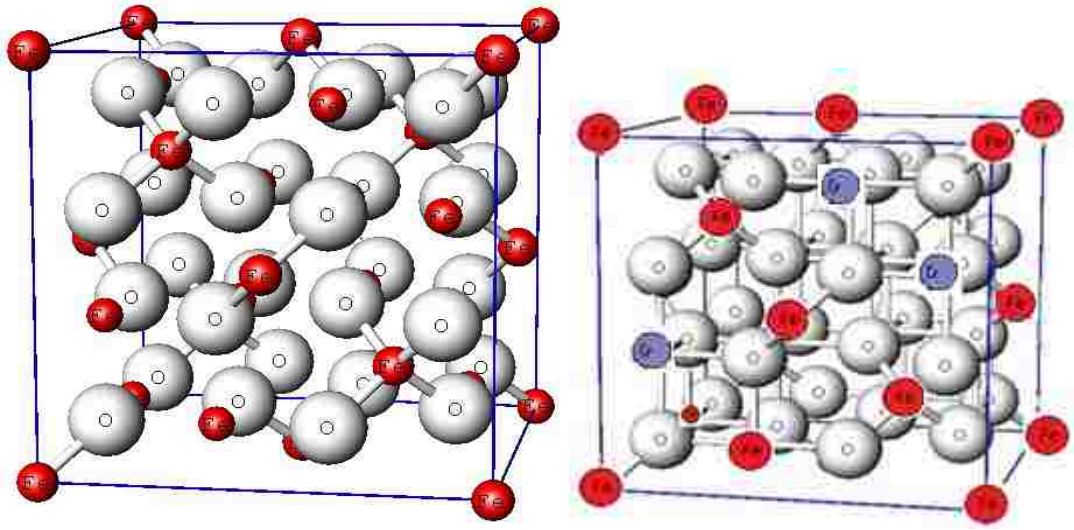

Figure 2.1: Spinel lattice structure of the form AB_2O_4 of magnetite Fe_3O_4 (left) and iron-chromium $Cr_xFe_{(2-x)}O_4$ (right). The normal spinel structure of $Cr_xFe_{(2-x)}O_4$ has tetrahedral sites occupied by Fe^{2+} and octahedral sites shared between Cr^{3+} and Fe^{3+} [24].

The effect of increased structural stability provided by chromia was studied with temperature-programmed reduction (TPR) by Reddy *et al* [25]. 20 wt% addition of chromia allowed the catalyst to reduce at 60 °C higher than the catalyst with 2 wt% chromia, as shown in Figure 2.2. Furthermore, Doppler *et al.* [26] attributed the increase in overall surface area to increased chromia content due to reduced particle agglomeration. Their study was performed on three catalysts (Fe_3O_4, $Fe_{2.75}Cr_{0.25}O_4$, and $Fe_{2.5}Cr_{0.5}O_4$) with measured reductions in surface area of 0.17, 0.15, and 0.05 $m^2/g_{cat}/h$, respectively. Although 14 wt% addition of chromia provide the most stability against sintering [21], 8 wt% is used industrially because this amount provides the optimum balance between stability and activity [1].

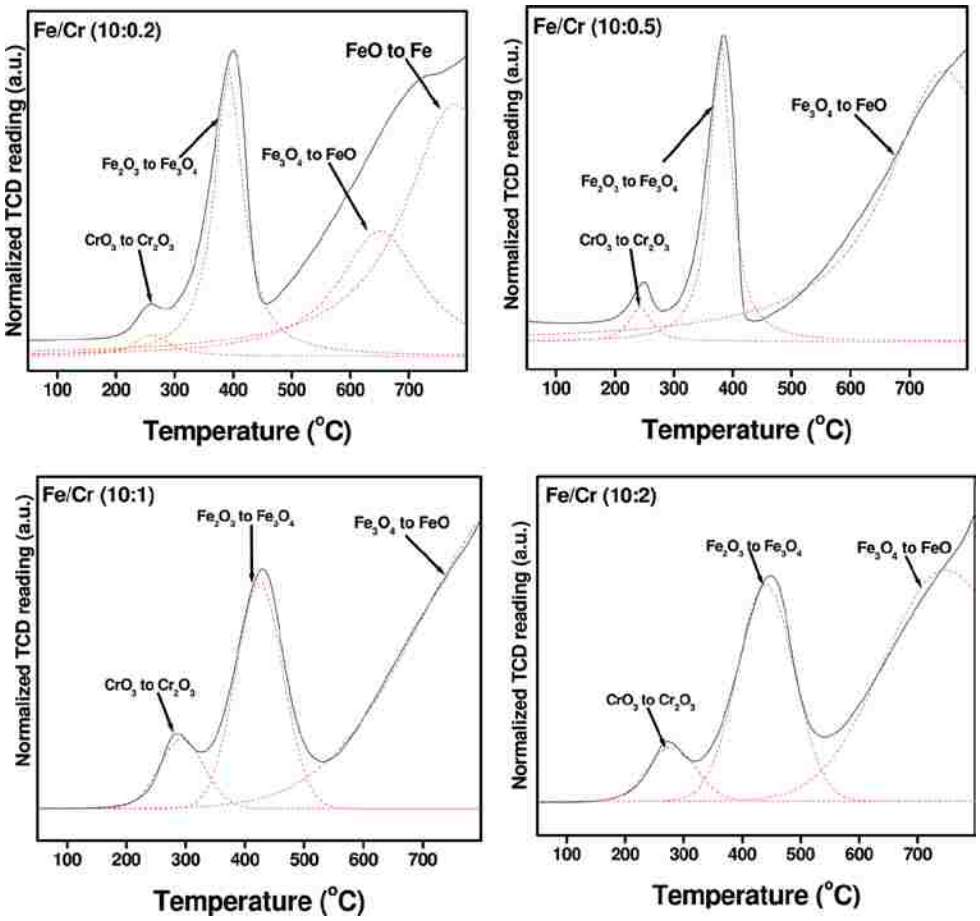

Figure 2.2: TPR profiles of Fe_2O_3 catalysts with varying amounts of chromia. Increased chromia content increases the reduction temperature [25].

The activation energy of the HT WGS reaction over Fe_3O_4/Cr_2O_3 catalysts has been measured experimentally as 129.4 ± 2.1 kJ/mol [27]. These catalysts are usually synthesized by co-precipitation of $Fe_2(SO_4)_3$ and $Cr_2(SO_4)_3$ using Na_2CO_3 (or NaOH) to yield precipitates of metal carbonates (or hydroxides). The sulfate ions must be carefully washed and dried to remove any residuals that could form H_2S (upon activation), which would poison and deactivates the copper-based LT shift catalysts employed downstream. Therefore, metal nitrate precursors are typically used instead of the sulfate precursors to avoid the poisoning effect of the sulfide ions [1, 19]. Calcination of the resulting solids within a temperature range of 300 - 450 °C converts

$Fe_2(CO_3)_3$ (or $Fe(OH)_3$) to Fe_2O_3 (hematite) [1]. Calcination is typically preferred at lower temperatures due to possible sintering and loss of surface area at higher temperatures [28]. The calcined catalysts have to be activated before operation under HT WGS conditions. The activation process involves the reduction of Fe_2O_3 to Fe_3O_4. Magnetite serves as the active phase of the catalyst because it is believed to be responsible for the dissociation of H_2O molecules [1]. The activation process is performed very carefully using the ratio, R_{WGS}, shown in Eq. 2.1 to avoid over-reduction to FeO or metallic Fe. Steam is added to the reactant syngas during the reduction process to bring this ratio close to 1 (~1.1) [7, 29, 30].

$$R_{WGS} = \frac{F^0{}_{CO} + F^0{}_{H_2}}{F^0{}_{H_2O} + F^0{}_{CO_2}} \tag{2.1}$$

where R_{WGS} is the ratio of the feed molar flow rates of the reducing agents CO and H_2 ($F^0{}_{CO}, F^0{}_{H_2}$) to the feed molar flow rate of the oxidizing agents H_2O and CO_2 ($F^0{}_{H_2O}, F^0{}_{CO_2}$). The catalysts can be reoxidized after experimental runs under reaction conditions by passing air over the catalyst. This converts Fe_3O_4, (magnetite, the reduced active form of the catalyst), back to Fe_2O_3, the oxidized form [1].

Xue *et al*. [31] studied the effect of H_2O:CO ratio on the activity of the catalyst. A stoichiometric amount of steam and CO resulted in coke deposition on the blank quartz reactor at atmospheric pressure and temperature range 375 – 450 °C and a total feed flow rate of 50 sccm. Low H_2O:CO feed ratios (< 1.3) result in coking and/or over-reducing the catalysts, which cause the production of undesired products, such as methane or carbon, *via* the side reactions shown in Table 2.1 [31 – 32]. Furthermore, Chen *et al*. also studied the effect of H_2O:CO ratio on CO conversion and found out that a ratio greater than 4 had no further positive promotion on

hydrogen generation. When the ratio was increased from 2 to 4, the CO concentration decreased in the feed gas stream and thus CO conversion increased from 70% to 90% [33].

Table 2.1: Possible Side Reactions of the WGS Reaction at Stoichiometric H2O:CO Ratios [31, 32].

$2CO \rightleftharpoons C + CO_2$	(2.2)
$CO + H_2 \rightleftharpoons C + H_2O$	(2.3)
$CO_2 + 2H_2 \rightleftharpoons C + 2H_2O$	(2.4)
$2CO + 2H_2 \rightleftharpoons CO_2 + CH_4$	(2.5)
$CO_2 + 4H_2 \rightleftharpoons CH_4 + 2H_2O$	(2.6)
$C + 2H_2 \rightleftharpoons CH_4$	(2.7)

The activity, stability, and selectivity of Fe/Cr catalysts can be enhanced by the addition of promoters. Cu is one critical promoter for these catalysts that has been widely studied. Studies showed that the promoting role of 1 – 2 wt% of Cu is embedded in its ability to: (1) stabilize the reduction of the catalyst with CO, which enhances the yield of H_2 by minimizing CH_4 formation [19, 29, 34, 35], (2) lower the activation energy for HT WGS reaction to 75 – 80 kJ/mol compared to 110 - 130 kJ/mol for the non-promoted catalyst [34], and (3) reduce to metallic Cu which can act as another catalytic active phase [36 – 37]. Rhodes *el al*. [29] also tested the addition of 2 wt% of B, Ba, Cu, Pb, Hg, and Ag to Fe/Cr catalysts in the temperature range 623 – 713 K. Results showed that B poisons the catalyst and thus decreases its activity while the rest improve the activity as the cations incorporate into the solid solution. Hg^{2+} exhibited highest promotion, followed by Ag^{+}, Ba^{2+}, Cu^{2+}, and Pb^{2+} in decreasing order of effect. Different studies showed that the addition of 0.97 wt% rhodium by incipient wetness to HT WGS Fe/Cr catalyst increases the rate activity of both the forward and reverse reactions, possibly due to increased adsorption of CO and H_2, as suggested by the kinetic data fit to a power-law model [38-39]. 4 wt% Cu was added to Fe/Cr catalysts prepared for this work to promote WGS activity because it is the most economically feasible choice and has significant effect on the activation energy of the

reaction and the reduction of the catalyst with no associated health hazards. Industrial HT WGS catalysts typically contain 88 wt% Fe, 8 wt% Cr and 4 wt% Cu [3].

Ceria was also studied as a potential promoter for Fe/Cr catalysts. The results showed enhanced activity for the $Fe_{2.4}Cr_{0.3}Ce_{0.3}O_4$ catalyst operating in the temperature range 400 – 500 °C and with a H_2O:CO ratio of 3.5. The results were attributed to the ability of ceria to easily change oxidation state from Ce^{4+} to Ce^{3+} during reaction [25]. Cerium is well known for its capability to exhibit multiple oxidation states [11, 40], and to store and release oxygen and hydrogen and to form intermetallic compounds [41]. Hu *et al*. [42] showed that the presence of ceria in HT WGS iron catalysts facilitates the oxidation of the reduced surface sites by water. H_2 temperature-programmed reduction (TPR) experiments showed that the reduction of the ceria-promoted catalyst occurs at 100 K lower temperature than the base catalyst, which means that the former could be reduced more readily under the same reaction conditions.

La and Ce are both rare-earth metals and have many chemical and physical properties in common. However, La possesses unique chemistries compared to the other elements in its lanthanide family. La^{3+} exhibits a similar oxidation state as Fe^{3+} in its most stable phase, and is also a bigger cation and a softer lewis acid; therefore, it is expected to further minimize ligand-ligand repulsions and facilitate the adsorption of CO. Lanthana is also a more inexpensive promoter than most precious metals, such as Rh, Ag, and Hg. Therefore, testing and understanding its functional and textural effects on Fe/Cr/Cu catalysts is necessary.

Other researchers are interested in exploring Cr-free Fe-based catalysts for the HT WGS reaction due to the carcinogenic health hazards of hexavalent chromium (Cr^{6+}) formed in solid solution. In contrast, trivalent chromium (Cr^{3+}) has much lower toxicity. Cr^{6+} is also water-soluble and can be released to the environment from the catalyst through steam or water [43]. In

one study performed by Lee *et al*. [30, 44], Cr was replaced with Ni and either Zn or Co. Catalysts were prepared by co-precipitation and exposed to 3:1 H_2O:CO ratio. Experimental results showed that 5 wt% Zn or Co, 20 wt% Ni, and 75 wt% Fe have the best catalytic activity among all the tested catalysts. BET surface areas were measured to be 64.8 and 51.5 m^2/g, respectively. The 20 wt% Ni catalysts showed the maximum CO conversion of around 70%. In another study done by Martos *et al*. [45], Cr was replaced with molybdenum (Mo). The catalysts were prepared by oxi-precipitation. CO conversion was 79% with Cr and 80% with Mo. BET surface area increased linearly with Mo content, which increased the catalytic activity. Junior *et al*. [46] studied the replacement of Cr with vanadium (V). X-Ray photoelectron spectroscopy (XPS) showed that V^{+3} and V^{+4} cations were present on the surface of the catalyst. V-doped catalysts had an activity of 6.9×10^{-7} mol g_{cat}^{-1} s^{-1}, which was lower than the activity of a tested Fe/Cr catalyst. However, V increased the specific surface area of the Fe-based catalyst from 19 m^2/g_{cat} for the chromia-doped catalyst to 25 m^2/g_{cat} for the V-doped catalysts. It also provided more stability because it kept the catalyst particles from touching and thus prevented sintering from taking place. In other studies [47 – 48], lanthana addition to Cr-free iron oxide HT WGS catalysts was shown to create a perovskite-like structure with a chemical formula of $La_{0.9-x}Ce_xFeO_3$, which provides the catalyst with higher activity at temperatures above 550°C, compared to the standard industrial Fe/Cr catalysts. In fact, the WGS activity of these catalysts reaches 45 mmol/(g_{cat}·min) at 600 °C. In both of these studies [47, 48], small amounts of cerium, up to 0.22 atom fraction, were included with the lanthanum. Small amounts of cerium ($0.2 < x < 0.6$) produced high WGS activity. Higher amounts of cerium ($x > 0.6$) prevented the formation of the perovskite structure.

In a review by Lee *et al*. [49], they concluded that (1) Al and Th can replace Cr for its textural role to prevent sintering; (2) Ce and Cu can replace Cr for its functional role with its redox properties during HT WGS reaction (assuming that the reaction follows a redox mechanism); and (3) rare-earth metals, such as Ce and La, can replace Cr to form a stable perovskite-like structure with Fe to support the catalyst against sintering.

By comparing chromia to the more expensive dopants discussed above, chromia is a better choice because it provides higher surface area for more active and stable iron-based HTS catalysts with lower cost and can operate under higher reaction temperatures. With regard to the carcinogenic effects of Cr^{6+}, the chromium species in fresh Fe/Cr is usually Cr^{3+} and therefore the health hazards accompanied with Cr^{6+} are not a major concern [1, 3]. Therefore, chromia was added to the WGS catalysts studied in this work.

2.1.2 Water-Gas Shift Kinetics and Mechanisms

Many studies on HT WGS reaction kinetics have been conducted over the last 40 years during which over 20 mechanisms and kinetic models have been proposed, a few of which are most accepted [1, 3, 39, 50, 51, 52]. Power-law, Langmuir-Hinshelwood (LH), and regenerative (redox) models generally fit best and represent the steady-state (non-transient) kinetics of the HT WGS reaction [50 – 51]. Details on step-by-step derivation of these models from the corresponding mechanism can be found in Appendix C. In brief, the LH model follows an adsorptive mechanism, in which the reactants adsorb on the catalyst surface to react to products that then desorb, as shown in Equations 2.8 – 2.12, where s represents a vacant adsorbing site. (The dissociation of water and reaction of its products with adsorbed CO likely proceed through more complicated steps than shown in this simplified mechanism. This is also true for the redox

model presented below. However, the rate expressions from these more complicated mechanistic steps retain similar forms to the ones presented.)

$$H_2O + s \rightleftharpoons H_2O - s \tag{2.8}$$

$$CO + s \rightleftharpoons CO - s \tag{2.9}$$

$$CO - s + H_2O - s \rightleftharpoons CO_2 - s + H_2 - s \tag{2.10}$$

$$CO_2 - s \rightleftharpoons CO_2 + s \tag{2.11}$$

$$H_2 - s \rightleftharpoons H_2 + s \tag{2.12}$$

The general expression for the LH model is depicted in Equation 2.13:

$$-r_{CO} = \frac{kK_{CO}K_{H_2O}([CO][H_2O]-[CO_2][H_2]/K)}{(1+K_{CO}[CO]+K_{H_2O}[H_2O]+K_{CO_2}[CO_2]+K_{H_2}[H_2])^2} \tag{2.13}$$

where $-r_{CO}$ is the reaction rate of CO consumption, k is the rate constant, K_i is the adsorption equilibrium constant for species i, K is the WGS reaction equilibrium constant, and $[i]$ is the concentration of species i. The proposed LH model assumes non-dissociative adsorption of water (in Equation 2.8); therefore, water dissociation occurs as part of the rate-determining step (Equation 2.10). In contrast, only one reactant adsorbs on the surface and the denominator is raised to the first power in the Eley-Rideal (ER) model, as shown in Equation 2.14:

$$-r_{CO} = \frac{kK_i([CO][H_2O]-[CO_2][H_2]/K)}{1+K_i[i]} \tag{2.14}$$

The regenerative model follows an oxidation-reduction mechanism, hence the name redox, in which H_2O oxidizes a reduced center on the catalyst surface to form H_2, and then CO reduces the oxidized center to form CO_2, completing the catalytic cycle. The mechanism can be written in two steps, where * and O*, respectively, represent a reduced and an oxidized active site on the surface of the catalyst, as follows:

$$H_2O + * \rightleftharpoons H_2 + O* \tag{2.15}$$

$$CO + O* \rightleftharpoons CO_2 + *$$ (2.16)

The rate expression for this model is shown in Equation (2.17),

$$-r_{CO} = \frac{k_1 k_2([CO][H_2O] - [CO_2][H_2]/K)}{k_1[CO] + k_2[H_2O] + k_{-1}[CO_2] + k_{-2}[H_2]}$$ (2.17)

where k_1 is the rate constant for the oxidation of CO to CO_2, k_2 is the rate constant for the reduction of H_2O to H_2, k_{-1} is the rate constant for the reduction of CO_2 to CO, and k_{-2} is the rate constant for the oxidation of H_2 to H_2O.

The total concentration of surface sites in the LH, ER, and redox models is assumed to be constant and is therefore lumped into the effective rate constant.

The power-law model is empirical and carries no direct mechanistic meaning. The power-law rate expression is given by:

$$-r_{CO} = k[CO]^m[H_2O]^n[CO_2]^p[H_2]^q(1 - \beta_{eq})$$ (2.18)

where β_{eq} is the fractional approach to equilibrium:

$$\beta_{eq} = \frac{1}{K}\frac{[CO_2][H_2]}{[CO][H_2O]}$$ (2.19)

The equilibrium constant of the WGS reaction decreases with increasing reaction temperature and drops below 1 at temperatures above 1100 K and is around 12 at 673 K (typical operating temperature for the HT WGS reaction), as described by Equation 2.20 and Figure 2.3 [53].

$$\log(K) = -2.4198 + 0.0003855\,T/K + \frac{2180.6}{T/K} \quad (2.20)$$

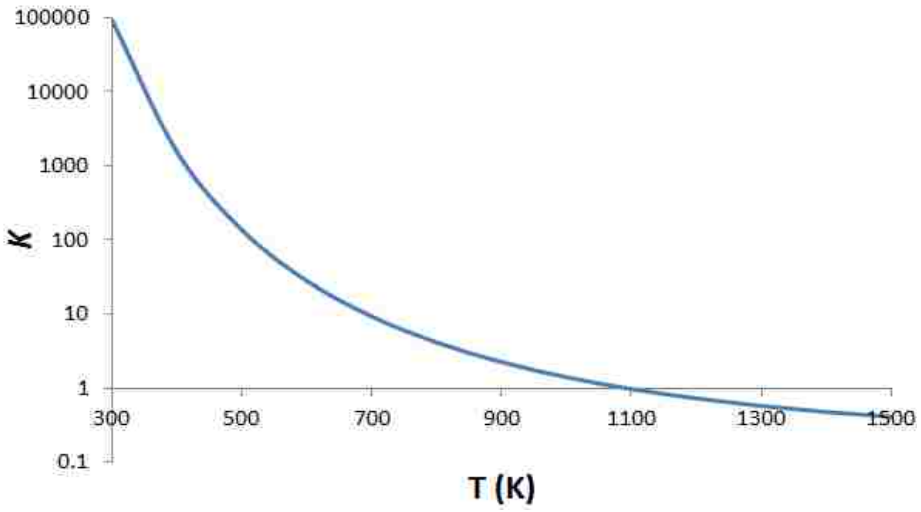

Figure 2.3: Temperature dependence of the equilibrium constant of the WGS reaction [53].

More specific microkinetic studies have been conducted previously [50 – 55], in which models were derived from detailed mechanisms with elementary steps that involve the dissociative adsorption of H_2O molecules, but study of these details were not the purpose of this work. The results presented in this dissertation provide parameters and comparative fits and mechanistic interpretations for these four models. Simple mechanisms use less number of fitting variables, which provide higher statistical certainty with the same number of experimental data points.

2.2 *Operando* UV-Visible Spectroscopy

2.2.1 UV-Visible Spectra Features and Extent of Reduction

Part of this work discusses how UV-visible spectra, along with concurrent on-line mass spectrometer, can be used to determine and quantify extent of reduction of Fe-based catalysts. Weckhuysen and co-workers [9] studied the dehydrogenation of isobutane over supported

chromium oxide catalysts and were able to quantify surface reduced centers (Cr^{3+}/Cr^{2+}) using *in situ* UV-visible spectroscopy and relate them to the dehydrogenation activity. Absorption bands over the UV region were observed due to ligand-to-metal charge transfer (LMCT) in which the metal cations were reduced by electron transfer from oxygen (O^{2-}) species. Previous work [15, 56 – 58] also examined the edge and pre-edge absorption regions in UV-visible spectra, with the pre-edge region being extremely sensitive to changes in oxidation state, while the edge region is not. Argyle *et al.* performed similar UV-visible studies [56 – 57] on vanadium-oxide catalysts for oxidative dehydrogenation of propane and formulated a calibration curve for extent of reduction as a function of Kubelka-Munk function, which will be discussed in details in Section 2.2.2. A relationship between the pre-edge region and the number of reduced centers was determined by the number of oxygen molecules needed to obtain the initial UV-visible spectra after the catalyst has been reduced by hydrogen flow. Determining extent of reduction from near-edge features of the XANES spectra of these same catalysts was rendered unsuccessful due to overlapping features of the cationic spectra. Figure 2.4 shows the edge (~2.4 eV) and pre-edge (< 2.4 eV) features of UV-visible spectra that was obtained during these studies [56].

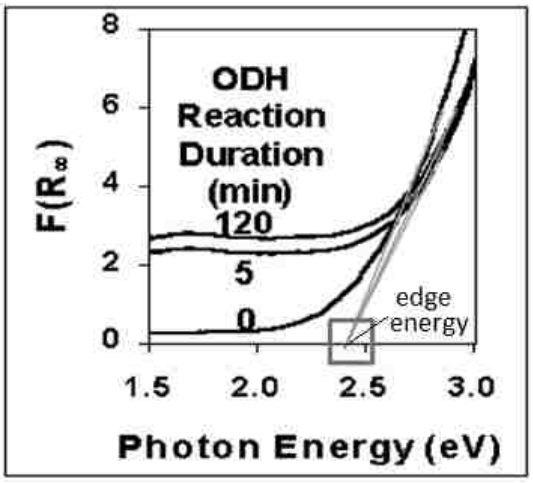

Figure 2.4: Sensitivity of pre-edge and edge features of UV-visible spectra to extent of reduction of vanadium-based catalysts for oxidative dehydrogenation of propane using Kubelka-Munk function $F(R_\infty)$ [56].

Therefore, despite iron-based shift catalysts appearing dark and unchanging in color to the unaided eye, absorbance of light over a range of visible (380-750 nm) and UV (<380 nm) wavelengths are still responsive to electronic changes in oxidation states, or electronic occupation of d-orbitals, of surface Fe domains. *Operando* (defined as analysis of an operating catalyst under realistic reaction conditions) UV-visible spectroscopy, has the potential to provide new insights on surface electronic configurations at an atomic level to determine the extent of reduction of a fully oxidized catalyst as measured by the absorbance of light by the catalyst surface [9, 10, 56, 57, 59]. The physical theory behind this phenomenon is that different oxidation states of the same metal have different Fermi (energy) band gaps and thus absorb light of different quantized energies [11, 12, 60]. For clarification, Figure 2.5 shows the molecular orbital (MO) diagram for Fe_2O_3 [13]. From the perspective of solid state physics, a solid mixture of hematite (Fe_2O_3) consists of countless of these orbitals combining and overlapping to form bands, as shown in Figure 2.6 [61]. The band gap for some iron oxide minerals falls in the range 2.0-2.5 eV (2.2 eV for hematite and 2.3 eV for wüstite), while that for magnetite is only 0.1 eV. (Metals, including Fe, have no band bap because the Fermi level lies within the conduction band [51 – 63]). Sherman [64] has shown that O(2p) → Fe^{3+}(3d) charge transfer requires 4.2 - 4.7 eV of energy.

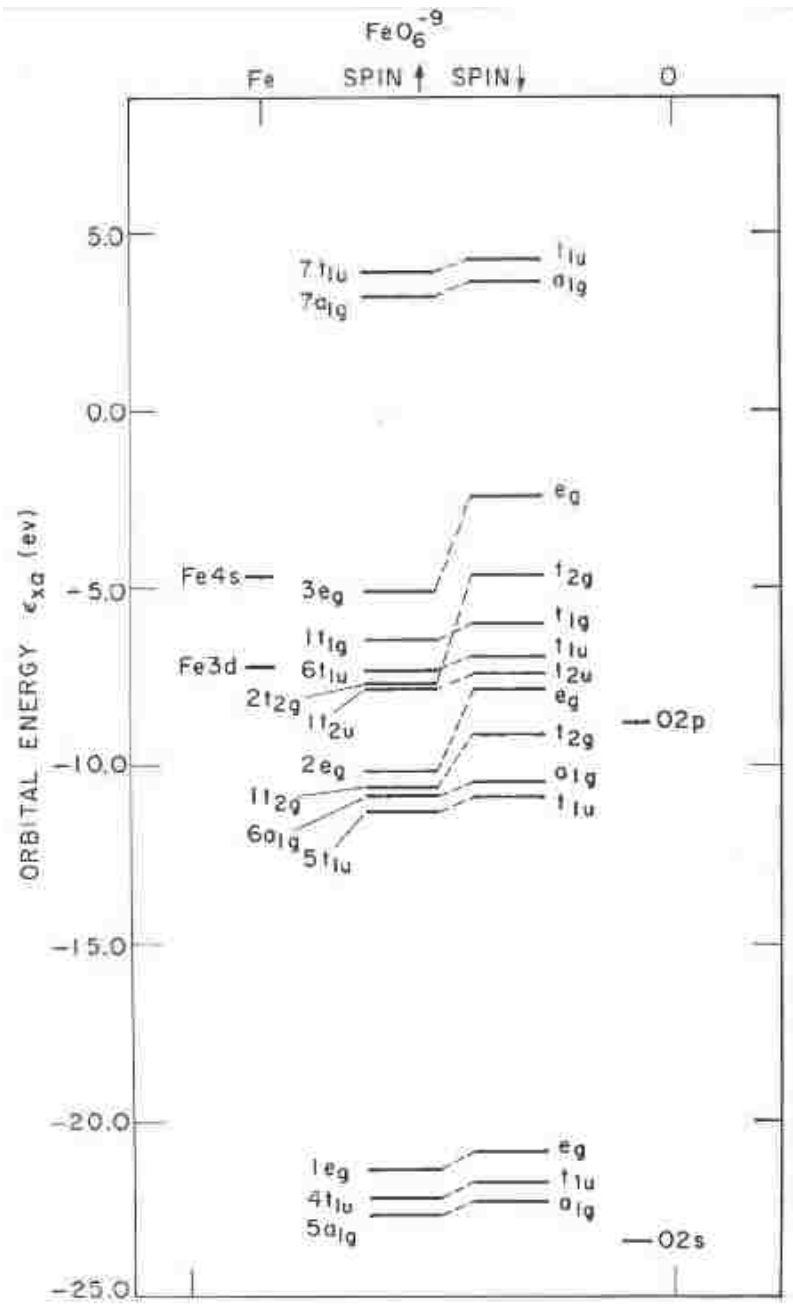

Figure 2.5 Molecular orbital diagram for (FeO6)-9 showing the orbitals in the valence and conduction bands [13]. Reproduced with permission of The Mineralogical Society of America.

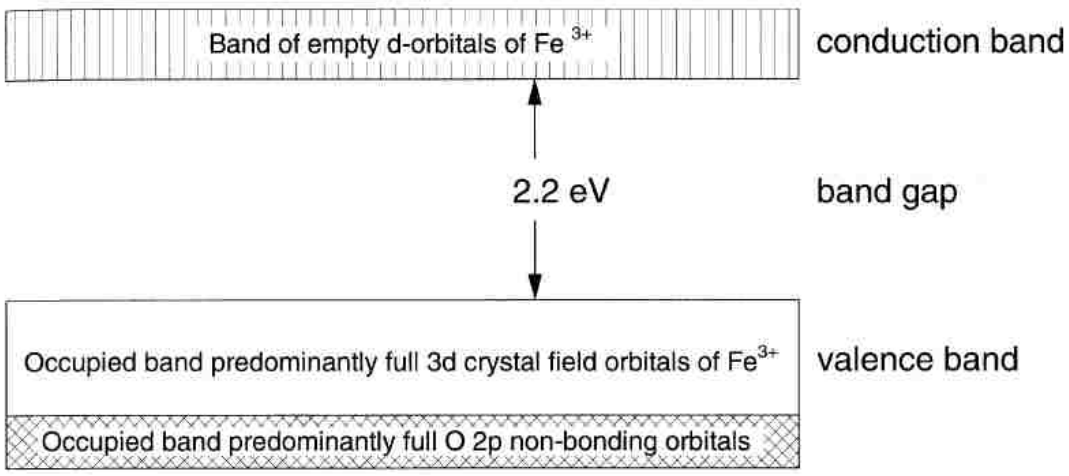

Figure 2.6: Band structure for hematite showing the valence and conduction bands separated by the band gap [61]. Reprinted with permission of the Royal Society of Chemistry.

2.2.2 The Kubelka-Munk Theory: Derivation and Limitations

Diffuse reflectance UV-visible data are frequently analyzed using a normalized absorbance, which is referred to as the Kubelka-Munk (K-M) function [65 – 66], $F(R_\infty)$, shown in Equation (2.21),

$$F(R_\infty) = \frac{(1-R_\infty)^2}{2R_\infty} = \frac{K}{S} \qquad (2.21)$$

where R_∞ is the infinite reflectance (assuming the sample is infinitely thick) relative to a reference perfect reflector (powdered magnesium oxide or Teflon® are commonly used in practice), K is proportional to the K-M absorbance coefficient (k) and is greater than zero, and S is proportional to the K-M scattering coefficient (s) and is greater than zero. Both coefficients have units of inverse length. The scattering theory to model diffuse reflectance was first introduced by Schuster [67] and Kubelka and Munk [68] and is analogous to Beer's law for absorption. They proposed that scattering is a first order phenomenon that decreases the flux as the light is absorbed and scattered as it passes through the material. The K-M equation can be

obtained by performing a shell balance on the flux of light moving in the downward direction (I) and in the upward direction (J) through a differential distance dz (see Figure 2.7), and solving the resulting coupled differential equations (Equations 2.22 and 2.23) [67 – 69]:

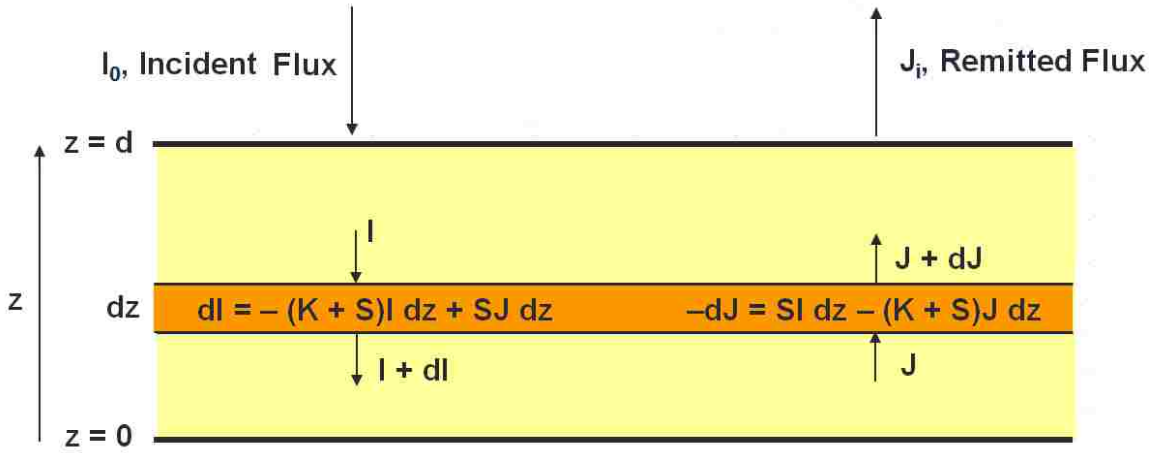

Figure 2.7 Shell balance on the flux of light moving in the upward and downward directions. The flux is dependent on both absorbance and scattering.

$$\frac{dI}{dz} = -(k+s)I + sJ \tag{2.22}$$

$$\frac{dJ}{dz} = (k+s)J - sI \tag{2.23}$$

Equation 2.21 assumes a continuous infinite medium and does not account for changes in particle size. Typical challenges with the K-M theory are: (1) morphological changes (due to changes in particle size distribution or variation in pressure), and (2) repeatable preparation of the samples. For powdery catalysts, changes in the particle size distribution can significantly alter the UV-visible spectra. A study by Christy *et al.*[65] has modified the K-M equation to account for the inverse relationship with particle size. Particle size distribution affects both the scattering and absorbance terms [70 – 71]. With regards to compositions and catalyst preparation procedures, Herranz *et al*. [72] showed that samples prepared differently can result in significant

differences in the UV-vis signal. Therefore, sample preparation must be repeatable and calibration curves for each sample must be obtained in case the constituent chemical compositions of the catalysts do vary.

Qualitatively, K-M values increase with increasing absorbance, which will typically correspond to a higher extent of reduction [56 – 57]. The proportionality of $F(R_\infty)$ with the number of reduced centers can be quantified by measuring the amount of oxygen required to return the catalyst to its fully oxidized state after it has been reduced. Demonstrating that extent of reduction can be evaluated using UV-visible spectroscopy that is more accessible than other characterization methods that require synchrotron X-ray sources will be very beneficial. For this study, the reference was chosen as the fully oxidized catalyst to permit sensitive detection of changes in the oxidation state of the catalyst relative to this fully oxidized reference. This allows the quantification of extent of reduction using light spectroscopy from the UV-visible spectrophotometer.

2.3 The Fischer-Tropsch Synthesis

2.3.1 Catalysts, Promoters, and Preparation

Current FT catalysts that are widely studied or used in industry are generally Fe or Co-based, as they show high selectivity to hydrocarbons heavier than methane. Ru-based catalysts are ineffective due to high cost and Ni-based catalysts have high selectivity to methane because they preferentially catalyze the methanation reaction. Co-based catalysts are typically used for FTS at ~220°C, while Fe-based catalysts are used for FTS at ~250 - 280°C [3]. The performance of both types of catalysts can be compared in terms of activity, selectivity, and stability.

However, from an industrial and business perspective, selectivity is most important because higher selectivity can provide the same yield of desired products with lower reaction rates and therefore less heat generation. Co-based catalysts are typically operated in the low temperature regime to avoid high methane selectivity and therefore tend to produce heavier hydrocarbons than gasoline. Fe-based catalysts have more flexibility with the temperature effect on methane and therefore can be operated at higher temperatures to increase the selectivity of liquid hydrocarbons. Table 2.2 compares the selectivity of Co-based and Fe-based catalysts and shows that Fe-based catalysts have better selectivity to $C_5 - C_{16}$ liquid hydrocarbons, despite the higher selectivity to methane at the 120°C higher temperature [73]. Due to this selectivity advantage, plus the 230 times cheaper cost of iron relative to cobalt and the WGS activity of Fe catalysts, researchers continue to invest significant effort to enhance Fe-based catalysts for FTS technology.

Table 2.2: Comparison of product distribution from FTS for Fe-based and Co-based catalysts. Fe-based catalysts have higher selectivity to liquid hydrocarbons [73].

Product	HT FT (Fe-based catalyst at 340°C)	LT FT (Co-based catalyst at 220°C)
Methane	8	5
Ethane	3	1
Ethylene	4	0
Propane	2	1
Propylene	11	2
Butane	1	1
Butylenes	9	2
$C_5 - C_{16}$	36	19
Distillates	16	22
Heavy Oil/Was	5	46
Oxygenates	5	1
Total	100	100

Potassium and copper are two common promoters added to Fe-based FT catalysts [3, 73 – 86]. A study by Yang *et al*. [74] showed that an optimum content of K (0.7 wt%) in unsupported Fe/Mn catalysts provides maximum FTS rates because it increases the extent of carbiding (or iron carbide content) with reaction time and higher reaction temperatures and crystallite sizes. Higher contents of potassium (> 0.7 wt%) impose the opposite effects. Potassium addition also appears to enhance selectivity to olefins as potassium subdues the hydrogenation activity of the catalyst [74]. Raje *et al.* [75] also showed that a maximum FTS activity on unsupported 100 Fe/4.6 SiO_2 catalysts occurs with an optimum potassium content of 100 Fe/1.4 K. A study by Bukur *et al.* [76] depicted that promoting unsupported 100 Fe/3 Cu FTS catalysts with 100 Fe/0.5 K potassium increase the FTS activity and selectivity to C_{5+} of these catalysts with an increase in olefin to paraffin ratio and water-gas shift activity. In an experimental study conducted by Graf *et al*. [77], the heat of dissociative CO adsorption on the catalyst surface is 225 kJ/mol for a K-promoted catalyst, compared to a value of 165 kJ/mol for the non-promoted one, as shown in Figure 2.8. As suggested by Dry *et al*. [78] K_2O helps forming stronger Fe-C bonds. Graf *et al*.'s results agree with this. In further agreement with these conclusions, temperature-programmed desorption (TPD) showed that CO desorption occurs at a higher temperature for the K-promoted Fe-FTS catalysts due to the stronger Fe-C bond, as depicted in Figure 2.9 [77].

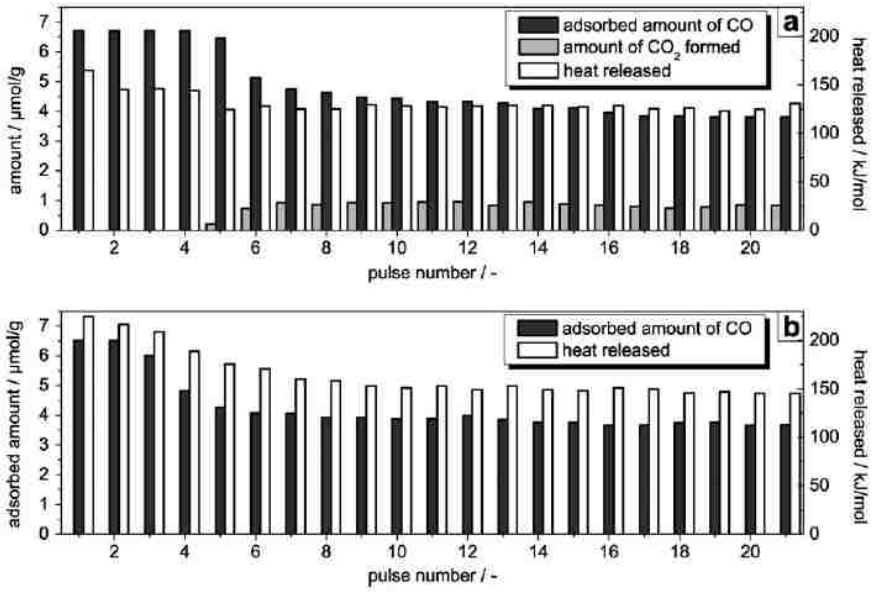

Figure 2.8: Calorimetric CO pulse adsorption at 613 K for a) Fe-FTS and b) K-Fe-FTS [77].

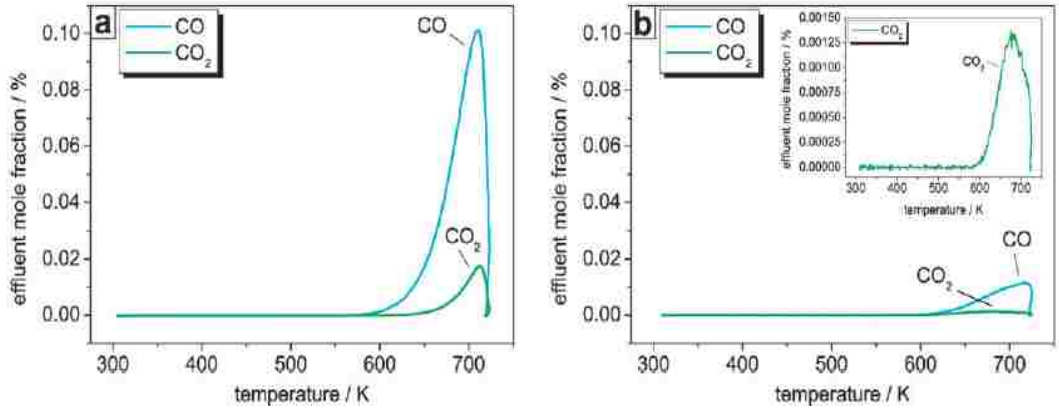

Figure 2.9: TPD results for a) Fe-FTS and b) K-Fe-FTS [77].

On the other hand, copper addition to Fe-FTS catalysts has quite different effects. In one study, Ma *et al*. [79] concluded that copper in activated-carbon-supported Fe/K-FTS catalysts facilitates reduction. Figure 2.10 shows that 2 wt% of Cu allowed the reduction to occur at lower temperatures compared to 0 and 1 wt% Cu. As shown in Figure 2.11, the FTS activity of Cu-promoted catalysts, however, is lower than the catalyst with no Cu, possibly due to the formation of Fe/Cu clusters and deposition of carbon on the catalyst surface. The selectivity is not affected by Cu promotion. Quite different results were obtained by Zhang *et al*. [80], whose studies

revealed that that Cu promotion not only facilitates the reduction of Fe/Mn/K/SiO_2 FTS catalysts, but also expedites catalyst activity and the rates of carbiding. However, the steady-state activity and hydrocarbon selectivity are not affected by Cu promotion according to this study [80].

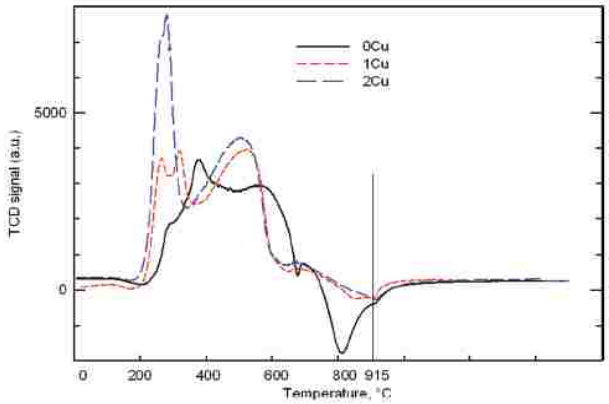

Figure 2.10: TPR profiles for Fe-FTS catalysts with a) no Cu b) 1 wt % Cu and c) 2 wt% Cu [79].

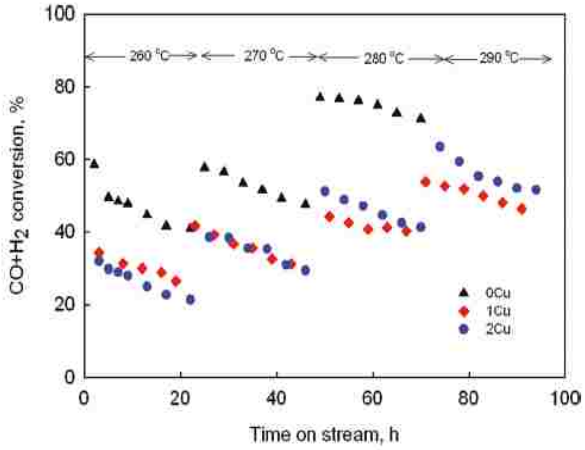

Figure 2.11: Syngas conversions at different temperatures with different Cu loadings [79].

Lohitarn *et al*. [81] studied the promoting effects of several transition metals (Cr, Mn, Mo, Ta, V, W, and Zr) on 100 Fe/5 Cu/17 Si FT catalysts that were prepared using the same precipitation preparation method with the transition metal (M) added at the expense of Fe to end up with 95 Fe/5 Cu/ 5 M/17 Si catalysts. These metals are well known for their ability to form

metal carbides [5]. All of these metals, except W, showed an increase in CO conversion for the FTS and WGS reaction, with Cr, Mn, and Zr being the best promoters. This increased activity was due to increased Fe dispersion on the catalyst surface, as shown by CO chemisorption experiments. However, hydrocarbon selectivity was not affected by the addition of any of the transition metal promoters [81].

Wang *et al*. [82] studied the effect of lanthana addition on Zr-Co/activated carbon catalysts for FT synthesis. Different La loadings were tested and compared in terms of catalyst activity and selectivity to long-chain hydrocarbons (C_{5+}). Experimental results showed that La loading of 0.2 wt% increased the catalyst activity from 86.4% to 92.3% and the selectivity to C_{5+} increased from 71.0% to 74.7%. As the selectivity to C_{5+} increased, the selectivity to methane decreased from 14.2% to 11.5%. Higher loadings of La (0.3-1 wt %) resulted in effects opposite to those observed with the 0.2 wt% loading. Activity and selectivity tend to depend on the reducibility of the catalyst. Temperature-programmed reduction (TPR), CO-temperature-programmed desorption (CO-TPD), and temperature programmed CO hydrogenation showed that the reducibility of the catalyst increased with 0.2 wt% lanthana loading, but decreased with lanthana content higher than 0.3 wt%. Increased reducibility decreased the yield of methane and thus increased the selectivity to C_{5+} [82].

In summary, potassium promotion of Fe-based FTS catalysts increases (1) selectivity to high molecular weight hydrocarbons; (2) olefin to paraffin ratio; (3) FTS activity with optimum potassium content (roughly 4 parts of potassium for every 100 parts of Fe; while higher contents lead to lower activity); (4) WGS activity with optimum potassium content; (5) strength of Fe-C bonds, while C-O bonds are weakened; and (6) carbon deposition and catalyst deactivation rate.

Copper promotion (1) enhances the reducibility of the catalyst; (2) increases FTS and WGS activities (with maximum copper content of 5 parts of copper for 100 parts of Fe, as higher loadings do not affect the FTS and WGS activities); and (3) does not affect hydrocarbon selectivity. Both promoters were studied in this work.

Fe/Cu/K/SiO_2 catalysts developed at Texas A&M University (TAMU) are among the most active, stable, and selective unsupported Fe-based FT catalysts reported in literature [76, 83 – 85]. They achieved catalytic activity of 73 mmol (H_2 + CO)/g_{cat}/h with 94% hydrocarbon selectivity to C_{2+} and 48.5 % selectivity to CO_2 on a precipitated 100 Fe/3 Cu/4 K/16 SiO_2 catalyst operating at 320 psi and 260 °C in a stirred tank slurry reactor using H_2:CO = 0.68 [84]. Bukur *et al.* [84] showed that potassium and copper promotion increases the FTS and WGS activities and enhances selectivity to higher molecular weight hydrocarbons. Unsupported Fe/Cu/K/SiO_2 catalysts developed at Brigham Young University (BYU) are very competitive in terms of activity, selectivity, and stability to those developed by TAMU. The most active unsupported Fe-based catalyst synthesized at BYU is 100 Fe/5 Cu/4 K/16 SiO_2 with a catalytic activity reaching 58 mmol (CO)/g_{cat}/h, 91 % hydrocarbon selectivity to C_{2+}, and 34% selectivity to CO_2 at 260 °C and 320 psi in a fixed-bed reactor with H_2:CO = 1 [86]. The value of these catalysts was enhanced by their simple synthesis process. The catalysts at BYU are synthesized using a solvent-deficient precipitation method, rather than conventional aqueous co-precipitation. The solvent-deficient precipitation method to make nanoparticles was developed by the BYU Chemistry Department and Cosmas [87 – 90] and was applied to the synthesis of unsupported FTS catalysts by Brunner and coworkers [86]. This method provides increased control over pore size and structure and better distribution of nanoparticles by mixing hydrated precursors (metal

nitrates) without the addition of a solvent [86, 90]. The solvent-deficient method was used to synthesize the catalysts studied in this work.

2.3.2 Pretreatment of Iron FTS Catalysts

Fe-based FTS catalysts have to be activated to form the iron carbide phase that is active for the FTS reaction. Activation parameters, i.e. temperature, pressure, and composition of the reducing gas, affect the catalyst activity, selectivity, and stability. Bukur *et al*. [85] have studied different activation procedures for Fe-based FT catalysts and concluded that the activation of the catalysts consists of two steps at 280°C with either H_2, CO, or syngas (H_2:CO = 0.68) as the reducing gas: (1) phase transformation from Fe_2O_3 to a mixture of Fe_3O_4 and/or α-Fe, which was completed in 15-30 minutes and (2) phase transformation from Fe_3O_4 or α-Fe to χ-Fe_5C_2 (Hägg carbide) with CO or syngas activation for 24 h. α-Fe phase is an intermediate phase formed when the catalyst is reduced in H_2. They found that the catalyst that is pretreated with CO at 280 °C and atmospheric pressure is initially the most active and selective, but its activity decreases with reaction time. The activity of the catalyst that is reduced in H_2 is initially lower but increases with time as the catalyst carbides under reaction conditions [85]. Similar phase transformations were observed by Li and Iglesia [91] for the reduction in syngas where Fe_2O_3 transforms to Fe_3O_4 then to FeC_x in the temperature range of 180 – 400 °C. A different study by Xu [92] showed that pretreatment with CO causes the activity of silica-supported Fe/Pt/K catalyst to increase very slowly with time even after 200 h, while that treated with H_2 reaches its highest activity after 2 h under reaction conditions and then starts to decrease. Pretreatment with syngas (H_2:CO = 1) causes a moderately rapid rise in activity, which then starts to decrease after 30 h

under reaction conditions. All pretreatments were performed at 280 °C and atmospheric pressure for 16 h. By comparing all three pretreatment procedures, reduction with syngas (H_2:CO = 1) produces the most active catalyst after 200 h onstream at 250 °C and 315 psi, but is the least stable [92]. Analysis of phase compositions by Bartholomew *et al.* [93] using Mossbauer spectroscopy showed that the largest fraction of Hägg carbide is formed at activation pressures higher than 11 atm, while no carbide phases were formed at atmospheric pressure. Increasing Hägg carbide content positively correlates to FTS catalyst activity [91 – 93]. Brunner [86] reduced his unsupported iron catalysts that have been prepared *via* the solvent-deficient method with H_2 at atmospheric pressure and 300°C prior to activation with 1:1 H_2:CO at 20 atm and 250°C. Brunner's pre-treatment procedures were followed since the catalysts studied in this work were prepared by the same method.

2.3.3 Water-Gas Shift Kinetics during Fischer-Tropsch Synthesis

Part of the reason using iron based catalysts for FTS is their water-gas shift activity, which allows use of coal or biomass-derived, low-hydrogen syngas [3]. The drawback of the WGS activity is the increased conversion of CO to CO_2, which decreases the overall carbon selectivity of catalysts to desired hydrocarbons by about 1/3. However, CO_2 is a weaker oxidizing agent than H_2O; therefore, with higher water-gas shift activity, the H_2/H_2O ratio is higher, which reduces the likelihood of oxidizing and deactivating the catalyst. One study [94] showed that addition of potassium reduces the oxidation of the catalyst by introducing a more reducing environment through the water-gas shift reaction. Oxidation of the carbide phase is considered as a main cause of deactivation for Fe FTS catalysts [3]. Therefore, the kinetics of the

WGS reaction on FTS catalysts must be understood in order to properly control the H_2:CO ratio and to study catalytic deactivation routes.

Studies on WGS kinetics of FTS catalysts have been performed by few research groups due to the complexity of WGS reaction mechanism under typical FTS reaction conditions [95 – 101]. Some of these studies used power-law models with simultaneous fitting for simplicity to describe the kinetics of FTS and WGS kinetics [95 – 99]. The complexity and coupling of the FTS reaction adds difficulty and uncertainty to fitting WGS kinetics and therefore, the WGS and FTS parameters should be determined separately [100]. Some research groups [100 – 101] have attempted to overcome this issue by using a continuous spinning basket reactor instead of a fixed-bed reactor because the reaction conditions are more uniform and do not vary axially in the former type of reactor. They found that the WGS reaction follows the formate mechanism, outlined in Table 2.3, which provided the best fit for WGS kinetics on FTS Fe/Mn catalysts when step 4 (Equation 2.27) was identified as the rate-determining step (rds) [100]:

Table 2.3: Formate mechanism of the WGS reaction on iron FTS catalysts [100].

1	$\boldsymbol{CO + s \leftrightarrow CO - s}$	(2.24)
2	$\boldsymbol{H_2O + 2s \rightleftharpoons OH - s + H - s}$	(2.25)
3	$\boldsymbol{CO - s + OH - s \rightleftharpoons HCOO - s + s}$	(2.26)
4	$\boldsymbol{HCOO - s \rightleftharpoons CO_2 + H - s}$	(2.27)
5	$\boldsymbol{2H - s \rightleftharpoons H_2 + 2s}$	(2.28)

The rate expression for the formate mechanism is:

$$r_{CO_2} = \frac{\left(k_4 K_1 K_2 K_3 P_{CO} P_{H_2O} - \frac{k_{-4} P_{H_2} P_{CO_2}}{K_5}\right)}{\left(1 + \sqrt{\frac{P_{H_2}}{K_5}} + K_1 P_{CO} + \frac{K_2 P_{H_2O}}{\sqrt{\frac{P_{H_2}}{K_5}}} + \frac{K_1 K_2 K_3 P_{CO} P_{H_2O}}{\sqrt{\frac{P_{H_2}}{K_5}}}\right)\sqrt{P_{H_2}/K_5}} \qquad (2.29)$$

where K_j is the adsorption equilibrium constant for elementary step j, P_i is the partial pressure of species i, $k_{\pm 4}$ is the reaction rate constant of rds (reaction 4), and $[S]$ is the concentration of surface sites. The mean absolute relative residual (MARR) was 7.85% when the kinetic data were modeled using the rate expression in Equation 2.29. A simplified mechanism, proposed in Table 2.4, was developed to reduce the complexity of the rate expression and compared with the mechanism in Table 2.3. Teng *et al.*[100] showed that the MARR value of the rate expression derived from the simplified mechanism is 8.48%, which is still the lowest among all other mechanisms considered, and is also close to the value of the original rate expression.

Table 2.4: Simplified formate mechanism of the WGS reaction on iron FTS catalysts [100].

1	$\boldsymbol{CO + H_2O + 2s \rightleftharpoons HCOO - s + H - s}$	(2.30)
2	$\boldsymbol{HCOO - s \rightleftharpoons CO_2 + H - s}$	(2.31)
3	$\boldsymbol{2H - s \rightleftharpoons H_2 + 2s}$	(2.32)

$$r_{CO_2} = \frac{(k_2 K_1 K_3 P_{CO} P_{H_2O} - k_{-2} P_{H_2} P_{CO_2})}{\left(1 + \sqrt{\frac{P_{H_2}}{K_3}} + \frac{K_1 P_{CO} P_{H_2O}}{\sqrt{\frac{P_{H_2}}{K_3}}}\right)\sqrt{K_3 P_{H_2}}} \qquad (2.33)$$

The mechanism and rate expression described in Equations 2.30 – 2.33 were planned to describe the WGS kinetics of iron FTS catalysts studied in this work.

CHAPTER 3. Kinetic Study of Unsupported Iron-Based High-Temperature Water-Gas Shift Catalysts Promoted with Lanthana

This chapter presents the experimental work, results and discussion of the kinetic and characterization studies performed on unsupported iron-based WGS catalysts promoted with lanthana. The structural and textural effects of lanthana on the activity and stability of these catalysts is explained. This work has been published in a peer-reviewed journal [102].

3.1 Experimental Methods and Apparatus

The same experimental procedure was followed to test the high-temperature shift iron-based catalysts. The chart in Figure 3.1 summarizes the flow and process of the experimental work.

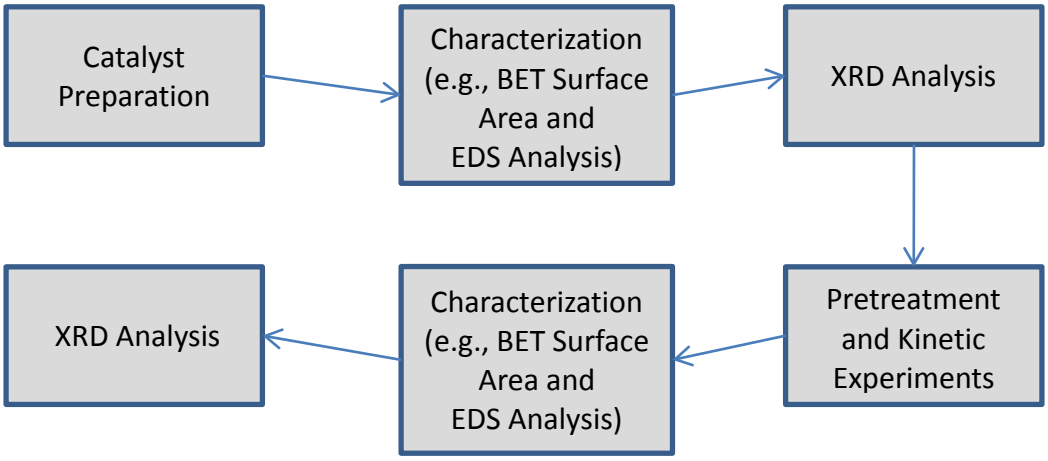

Figure 3.1: Flow of experimental work procedures for HT WGS catalysts.

3.1.1 Catalyst Preparation, Calcination, and Screening

Different batches of catalysts were prepared *via* co-precipitation with nominal compositions of 8 wt% Cr_2O_3, 4 wt% CuO, and varying wt% (0, 0.5, 1, 2, and 5, hereafter identified as 0La, 0.5La, 1La, 2La, and 5La, respectively) of lanthana added at the expense of the balance iron oxide phase (assumed to be Fe_2O_3 for calculation purposes). The preparation of these oxides occurs according to the following chemical reactions:

$$M(NO_3)_{x(aq)} + x\,NaOH_{(aq)} \rightarrow M(OH)_{x(s)} + Na(NO_3)_{x(aq)} \quad (3.1)$$

$$M(OH)_{x_s} + heat + \frac{x}{4}O_2 \rightarrow MO_{x(s)} + \frac{x}{2}H_2O_{(l)} \quad \text{(calcination)} \quad (3.2)$$

Appropriate amounts (shown in Table 3.1) of $Fe(NO_3)_3{\cdot}9H_2O$ (99.99%, Sigma-Aldrich), $Cr(NO_3)_3{\cdot}9H_2O$ (99.99%, Fischer Scientific), $Cu(NO_3)_2{\cdot}2.5H_2O$ (98%, Sigma-Aldrich) and $La(NO_3)_3{\cdot}6H_2O$ (99.999%, Sigma-Aldrich) were dissolved in distilled water. The hot, stirred solution was titrated with a pre-calculated amount of an aqueous solution of NaOH (Fischer Scientific, 97% reagent grade flakes) added all at once, to bring the metered pH (Hannah Instruments, pH 211) to a value of ~8. The amount of NaOH was calculated based on the solubilities of the metal hydroxides. Additional amounts of aqueous NaOH solution (1-2 mL) were added drop-wise to raise the final pH to ~11. Table 3.2 shows the solubility product constants (K_{sp}) and pH values for the precipitation of each metal hydroxide and indicates that a pH of 11 is sufficient to keep the solids precipitated at room temperature. The resulting mixture was aged for an hour to ensure maximum precipitation of the metal hydroxides. The solids were filtered, washed five times with deionized water to remove soluble sodium ions, and dried in an oven at 70°C overnight. The dried catalysts were calcined at 300°C for 3 h with a temperature ramp rate of 3°C/min from room temperature and with a dry air flow of 100 mL/min in a

Thermolyne 1400 furnace. The calcined catalysts were ground in a mortar and pestle and sieved to retain 106-250 μm particle sizes.

Table 3.1: Weights of metal nitrates and sodium hydroxide for the preparation of 20-gram batches of unsupported HT WGS catalysts with different wt% of lanthana.

Catlyst ID	$Fe(NO_3)_3$ (g)	$Cr(NO_3)_3$ (g)	$Cu(NO_3)_2$ (g)	$La(NO_3)_3$ (g)	NaOH (g)
0La	89.050	8.426	2.339	0.000	30.185
0.5La	88.544	8.426	2.339	0.266	30.034
1La	88.038	8.426	2.339	0.532	29.884
2La	87.026	8.426	2.339	1.063	29.583
5La	83.991	8.426	2.339	2.658	28.682

Table 3.2: Solubility product constants at 25°C and pH values for the precipitation of metal hydroxides.

Compound	K_{sp} [103]	pH
$Fe(OH)_3$	$1.0 \cdot 10^{-38}$	4.6
$Cr(OH)_3$	$6.3 \cdot 10^{-31}$	6.6
$Cu(OH)_2$	$2.2 \cdot 10^{-20}$	7.6
$La(OH)_3$	$2.0 \cdot 10^{-21}$	8.9

3.1.2 Characterization Procedures

Different techniques were used to characterize the physical and chemical properties of the fresh calcined and used catalysts. Details about each technique are described below.

3.1.2.1 Nitrogen Physisorption

The specific surface area, pore size, and pore volume of the fresh and used samples were determined by the Brunauer-Emmet-Teller (BET) [104] and Barrett-Joyner-Halenda (BJH) [105] methods using nitrogen physisorption at -196°C (Tristar 2030 BET, Micrometrics). The samples were vacuum degassed at 120°C for 12-24 h prior to analysis.

3.1.2.2 Energy Dispersive X-ray Spectroscopy (EDS) and Scanning Electron Microscopy (SEM)

An environmental scanning electron microscope (Philips, XL30) equipped with an energy dispersive X-ray spectrometer was used to measure the elemental compositions in the catalysts and to evaluate the distribution of the components across the catalyst surface. The scans were taken at 20 keV voltage in low-vacuum mode, which did not require coating the non-conductive catalysts with sputtered gold and palladium. Each scan took 50 seconds. Scanning electron micrographs (SEM) of the fresh and used catalysts were also taken using the same microscope at 50x and 400x magnifications with a 20 keV beam voltage.

3.1.2.3 Powder X-ray Diffraction (XRD)

Powder XRD analysis was performed on all fresh and used catalysts (X'Pert Pro PANalaytical with X-Celerator detector) to determine structural changes with different lanthana content in the iron catalysts. The instrument was operated at 45 kV and 40 mA, using Cu Kα1 radiation and a graphite monochromator. The results were obtained over the 2θ range of 10°-90° with 1° divergence and receiving slits, and 400 seconds per step. The sizes of the crystallites were calculated using the Debye-Scherrer equation [106];

$$d_c = \frac{0.9\lambda_c}{\beta_c cos\theta} \tag{3.3}$$

where $\boldsymbol{d_c}$ is the crystallite size, $\boldsymbol{\lambda_c}$ is the wavelength of the Cu Kα1 radiation, $\boldsymbol{\beta_c}$ is the full width at half maximum of the diffraction lines, and $\boldsymbol{\theta}$ is half of the diffraction angle $\boldsymbol{2\theta}$.

3.1.2.4 Temperature-Programmed Reduction with Hydrogen (H_2-TPR)

Temperature-programmed reductions (TPR) were performed on the catalysts to determine their reducibility. Initially, 0.04 grams of sample were fully oxidized in flowing air (Zero Air, Airgas) at 30 sccm with a temperature ramp of 10°C/min from room temperature to 450°C followed by a two-hour soak time. The sample was then cooled to room temperature. After purging the system with argon, TPR's were performed in 10 mol% H_2/Ar (5 sccm of H_2 with 45 sccm of Ar) and a temperature ramp of 10°C/min from room temperature to 450°C. Hydrogen consumption was quantified *via* mass spectrometry (MKS Cirrus 100) by integrating the areas under the peaks of H_2 consumption relative to a calibrated baseline.

3.1.3 Kinetic Analysis: Reaction Apparatus, Conditions, and Calculations

Kinetic experiments were performed in a quartz U-tube flow microreactor (0.6 cm inside diameter). The flow rates of CO (99.995%, Airgas), H_2 (99.95%, Airgas), and Ar (99.997%, Airgas) were set using calibrated mass flow controllers (Porter Instruments 201). Water was metered (ISCO pump model 260d) at a 3:1 H_2O:CO molar ratio through a boiler operating at 350°C. Within the quartz reactor, the catalyst was supported on a quartz frit with ~100 μm pores. The reactor was heated inside an electric furnace (National Element FA 120) at a ramp rate of 10°C/min from room temperature to the desired reaction temperature. A separate thermocouple in contact with the catalyst bed itself measured the reaction temperature. Water was removed from the reactor effluent in a condenser and desiccator columns (Drierite, 97% anhydrous calcium sulfate) prior to analysis in a gas chromatograph (GC, Agilent Technologies 7890A with a Supelco Carboxen 1004 packed column (2 m x 1.5 mm) and thermal conductivity detector). The reactor tubing prior to the water removal system was heat traced at 130°C and insulated to

prevent water condensation. After each experiment, the reactor was cleaned with nitric acid (70%, Sigma Aldrich) using an ultrasonic cleaner and was then washed with distilled water and acetone and dried in an oven overnight. Figure 3.2 shows a flow diagram of the reactor setup.

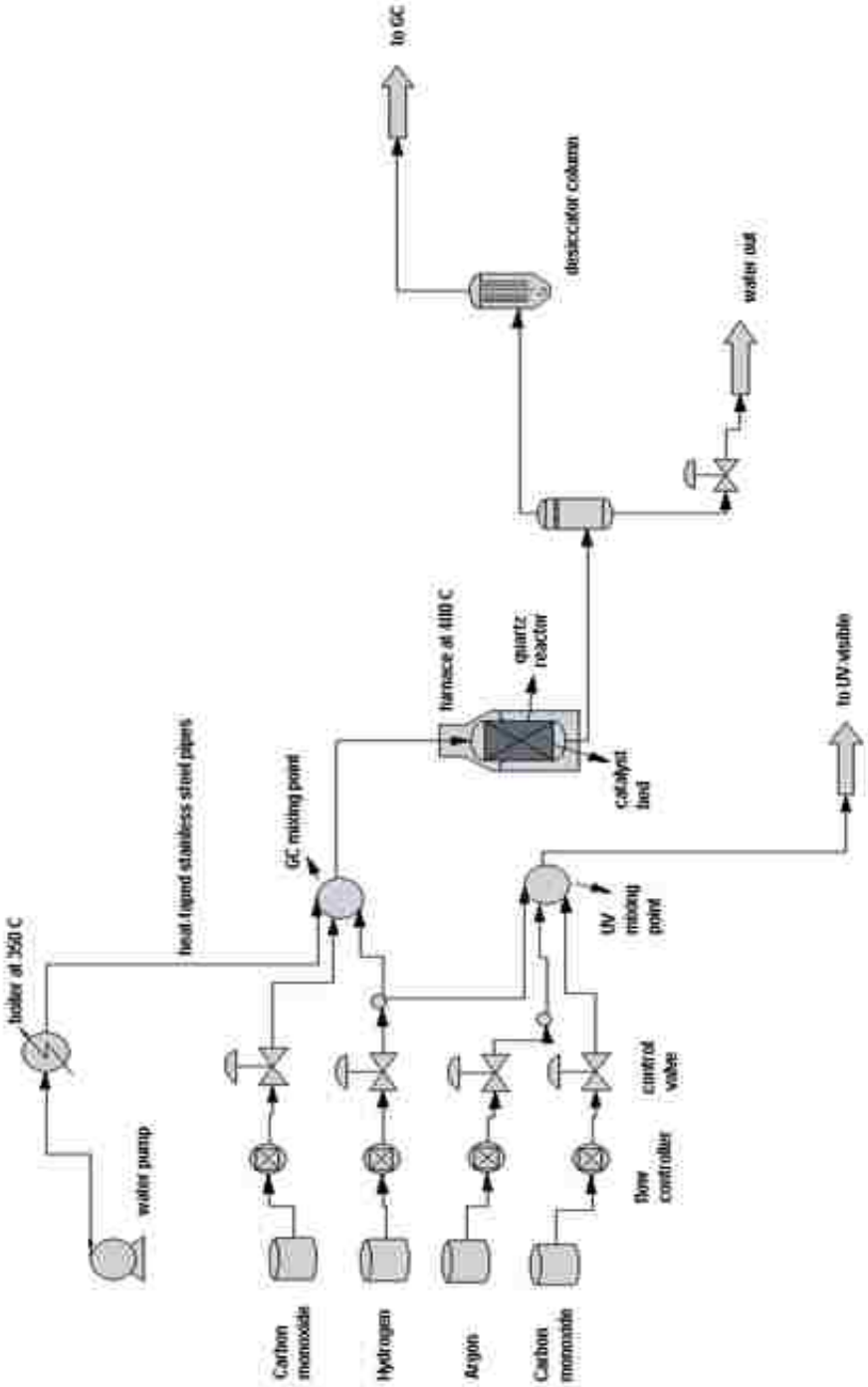

Figure 3.2: Reactor flow diagram for HT WGS reaction

Prior to reaction, the catalysts were reduced at 400°C for 2 h to convert the iron oxide to the active magnetite phase (Fe_3O_4) [1, 3]. The reduction conditions were set to avoid over-reduction to FeO or metallic iron. These conditions were quantified by setting the ratio of the reductant to oxidant molar flow rates, R_{WGS}, at 1.1

$$R_{WGS} = \frac{F^0{}_{CO} + F^0{}_{H_2}}{F^0{}_{H_2O}} = 1.1 \qquad (3.4)$$

Argon was also used as a diluent to maintain low partial pressures of the reducing gases in the reactor system. After the reduction process, HT WGS conditions were initiated with a H_2O:CO molar ratio of 3 to prevent carbon deposition or methanation side reactions from taking place [31]. Table 3.3 shows the reduction and the HT WGS conditions. 0.02 grams of catalyst were used for each experimental run. The reactant flow rates and the catalyst mass were chosen to minimize CO conversion and yet meet the detection limit of the GC. Minimum CO conversions (<20%) were intended to approximate differential reactor conditions used in the analyses.

Table 3.3: Reduction and HT WGS reaction conditions.

Gas	Reduction Flow rate (mmol/min)	HT WGS Flow rate (mmol/min)
CO	0.13	0.87
H_2	0.53	0
Ar	1.00	0
Water (Steam)	0.61	2.78

Four days elapsed before any kinetic data were collected to ensure that the catalyst performance approached steady state. Data were acquired at atmospheric pressure and 4 sequential reaction temperatures: 400, 375, 350, and 425°C, with 4 different CO flow rates at each temperature: 0.87, 1.74, 2.61, and 3.39 mmol/min. Four GC injections were made at each

flow rate to obtain statistically reliable results. Initial forward reaction rates were obtained by extrapolating to infinite CO flow rate (or zero CO conversion) from these varying space velocity data. The reaction temperature was returned to 400°C on the last day of experimentation to measure deactivation and the stability of the catalysts. The stability of the catalysts was determined by comparing their initial and final water-gas shift rates at 400°C, which were separated by five days of reaction time. Reaction rates were calculated from the following differential reactor equation:

$$-r_{CO} = \frac{X_{CO} \cdot \dot{V}_{CO} \cdot P}{W_{cat} \cdot R_g \cdot T} \tag{3.5}$$

where $-r_{CO}$ is the rate of CO consumption, X_{CO} is the CO conversion, $\dot{V}_{CO}$ is the inlet volumetric flow rate of CO, P is the atmospheric pressure, W_{cat} is the mass of the catalyst, R_g is the universal gas constant, and T is the absolute ambient temperature. CO conversion, X_{CO}, was calculated from equation (3.6):

$$X_{CO} = \frac{f \cdot PA_{CO_2}}{f \cdot PA_{CO_2} + PA_{CO}} \tag{3.6}$$

where $f = 1.7$ is the sensitivity factor for CO_2 relative to CO from calibrated runs on the GC and PA_{CO_2} and PA_{CO} are the integrated areas of CO_2 and CO, respectively, from the GC. The reaction rate as a function of reaction temperature was regressed using the Arrhenius equation to determine the activation energies for the different catalysts.

A separate series of experimental data on the 0La, 0.5La, and 5La catalysts were obtained to evaluate the mechanism and proposed Langmuir-Hinshelwood, redox, Eley-Rideal, and power-law rate laws by quantifying the kinetic parameters. The experiments involved changing

the flow rate of one reactant by a factor of 1.5 while holding the other's constant at 400°C and 1 atm, as shown in Table 3.4.

Table 3.4: Experimental runs for fitting rate-law models to kinetic data at 400°C and 1 atm.

Experimental run	Inlet CO partial pressure (atm)	Inlet H_2O partial pressure (atm)	Total inlet flow at 400°C and 1 atm (mL/min)
1	0.24	0.76	198
2	0.13	0.87	349
3	0.17	0.83	182
4	0.32	0.68	221
5	0.32	0.68	147
6	0.26	0.74	366
7	0.25	0.75	564
8	0.25	0.75	727

Non-linear, least squares regression for each of the four models assuming independent experimental errors with constant variance identified corresponding kinetic parameters. First-order differential equations solved in Mathcad (v15, Mathsoft, PTC) provided starting values that were further optimized using the generalized reduced gradient (GRG) solver algorithm in Excel (2010, Microsoft) to reach to a final set of optimal kinetic parameters. All of the actual kinetic data (which did not include the initial rates obtained by extrapolation) were analyzed for the three catalysts (0La, 0.5La, and 5La) at 400°C. The suitability of each model was analyzed by calculating the coefficients of determination (r^2) according to equation (3.7), which is appropriate for a finite number of samples [107],

$$r^2 = 1 - \frac{NRSS/(n_r - q_r)}{NTSS/(n_r - 1)} \qquad (3.7)$$

where $NTSS$ is the total squared sum of the errors (defined as the difference between the measured and the mean values) normalized by the variance, n_r is the number of data points, q_r is the number of linear regressors, and $NRSS$ is the squared sum of the normalized residuals (where

the residual is defined as the difference between the measured and predicted values). The 95% confidence regions were estimated according to the following criterion [108]:

$$\frac{S(\boldsymbol{\theta})-S(\hat{\boldsymbol{\theta}})}{S(\hat{\boldsymbol{\theta}})} \leq \frac{p_r}{n_r-p_r} F^{\alpha}{}_{p_r,n_r-p_r} \tag{3.8}$$

where $S(\theta)$ is the sum of squared errors at arbitrary values of kinetic parameters, represented by the vector θ, $S(\hat{\theta})$ is the sum of squared errors at the optimal values of the parameters $\hat{\theta}$, p_r is the number of fitting parameters in the corresponding model, and F is the F-statistic value for p_r and $n_r - p_r$ degrees of freedom at a significance level of α and a probability of 1- α.

The model parameters are highly correlated and not mutually independent, meaning they cannot be independently varied over the full range of the individual confidence intervals for each parameter. To quantify this effect, a nonlinear statistical analysis was performed considering this covariance to generate 95% interval joint confidence regions for a pair of parameters using Mathematica software (v9.0, Wolfram Research).

3.2 Results and Discussion

This section discusses in detail the results of the characterization and kinetic experiments. Characterization of the chemical and physical properties of the fresh and used catalysts explains the performance observed for each catalyst.

3.2.1 Surface Area

Table 3.4 shows the BET surface areas (SA), the average pore diameters (d_{pore}), and the pore volumes (V_{pore}) of the fresh calcined and used catalysts. 0.5 wt% addition of lanthana has no significant effect on the fresh BET surface area and average pore diameter. Further lanthana

additions reduce the fresh BET surface area and cause a slight increase in the average pore diameter. However, little change is observed in either of the measurements on the 2La and 5La catalysts, which suggests that a limit has been reached and that further lanthana additions would probably have no positive effect on the physical characteristics of the catalysts. However, lanthana has significant influence on the catalysts after reaction conditions. The used 0.5La catalyst has the highest surface area and smallest average pore diameter, which suggests that it is the most stable catalyst with the least reduction in surface area. In fact, based on the relative surface area changes, the 0.5La catalyst retains 63% more surface area compared to the 0La sample. No measurements are reported for the used 1La catalyst due to the small amount (<10 mg) of catalyst available for characterization, but its surface area and pore diameter measurements are expected to be intermediate between the 0La and the 2La results based on the kinetic results presented in Section 3.2.5 (see Figure 3.8).

Table 3.5: BET surface area and average pore diameter measurements for the calcined and used catalysts along with crystallite sizes for the used catalysts determined from XRD peak broadening.

Catalyst ID	Calcined (Fresh)			After WGS Reaction (Used)			
	SA (m^2/g_{cat})	d_{pore} (Å)	V_{pore} (cm^3/g)	SA (m^2/g_{cat})	d_{pore} (nm)	V_{pore} (cm^3/g)	d_c (nm)
0La	219	31	0.17	41	15.4	0.18	26
0.5La	220	32	0.18	67	14.3	0.23	31
1La	188	34	0.19	N/A	N/A	N/A	27
2La	149	36	0.16	43	14.5	0.15	23
5La	146	35	0.15	29	17.5	0.05	20

3.2.2 Powder X-ray Diffraction (XRD)

Figure 3.3 shows the XRD patterns of the fresh calcined and the used catalysts, respectively. Four conclusions drawn from these graphs follow:

1- In the fresh catalysts prior to calcination, the iron phase is mostly ferrihydrite [109], or hematite (Fe_2O_3) containing water, while magnetite (Fe_3O_4) is the predominant phase in the used catalysts. The diffraction angles for magnetite at 30°, 35.5°, 43°, 57°, and 63° were compared with the powder diffraction file (PDF) of the International Centre for Diffraction Data (ICDD) database for magnetite. No peaks for FeO, Fe, or Fe_2C were observed either after the reduction or reaction conditions, indicating that the catalysts have not been over-reduced. This is consistent with studies performed by Longbottom and Kolbeinsen [110].

2- The fresh catalysts are largely amorphous, while the used catalysts contain some crystallinity. This is consistent with the formation of the magnetite-chromium cubic spinel structure after the catalysts are reduced.

3- The 0.5La used catalyst is the most crystalline with the sharpest and most intense peaks. The degree of crystallinity decreases with increasing wt% of lanthana. Therefore, 0.5 wt% addition of lanthana appears to add some stability to the spinel structure, while further loadings disrupt the structure. The disruption of the spinel structure is likely caused by the larger La^{3+} cations that replace some of the Fe^{3+} cations. The ionic radius of La^{3+} is 103.2 pm, which is much larger than that of the high-spin Fe^{3+} (64.5 pm) [11]; hence, the octahedral holes in the spinel structure are apparently not flexible enough to accommodate too many of the large La^{3+} cations.

4- The diffraction angles at 35.5°, 57°, and 62.5° in the pattern for the 0.5La catalyst are slightly shifted to the right (~0.5° higher), suggesting that this minor addition of lanthana is affecting

(and possibly incorporating into) the unit cell and making it more compact and ordered. On the other hand, the peaks at 57° and 62.5° are slightly shifted to the left (~0.5° lower) for the 1La, 2La, and 5La catalysts, implying that the lattice parameters of the corresponding unit cells are larger. The disruption of the spinel, therefore, comes as a result of larger unit cells. The pattern of the 0La is slightly shifted to the left compared to that of the reference magnetite due to the incorporation of copper into the spinel once the catalyst is activated [111].

5- The crystallite sizes calculated from the Debye-Scherrer equation for each of the used catalysts, reported in the last column of Table 3.4, indicate that the 0.5La catalyst contains the largest crystallites. A more crystalline structure with a larger crystallite size implies a more ordered and extensive spinel structure. The more extensive spinel structure in the 0.5La catalyst is likely due to a small fraction of the larger La^{3+} ions integrating into the structure that appear to stabilize it during the high temperature (up to 425°C) reaction conditions. In the case of the 2La and 5La catalysts, lanthana addition clearly decreases their crystallite sizes as it apparently disrupts the spinel structure. As a result, the internal structure is not as crystalline or stable compared to the samples with no or low (0.5 wt%) lanthana.

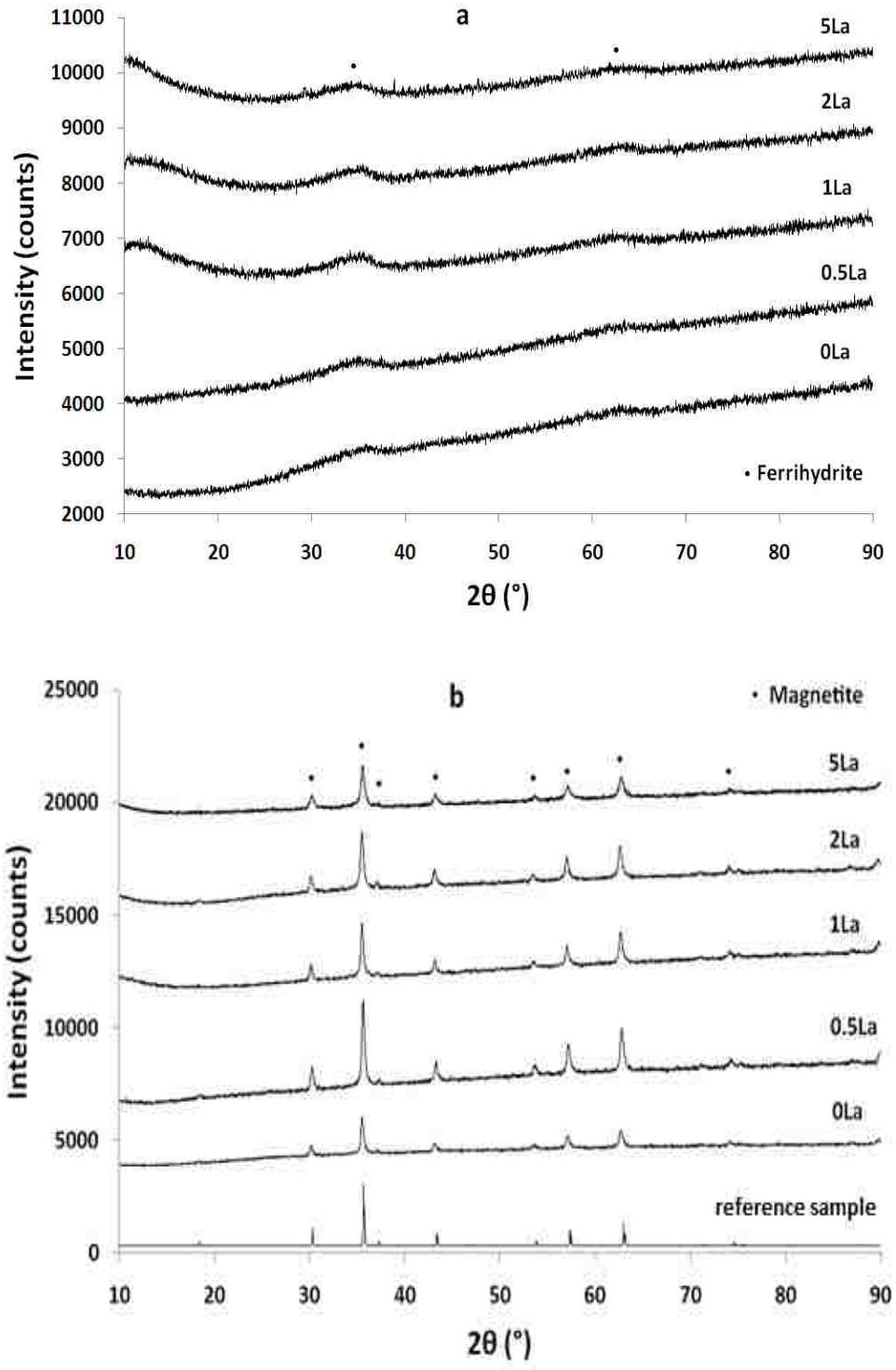

Figure 3.3: The XRD patterns of (a) the calcined fresh catalysts before HT WGS treatment and (b) the spent catalysts after 10 days of HT WGS treatment compared to magnetite reference sample from the International Centre for Diffraction Data (ICDD) database.

3.2.3 Scanning Electron Microscopy (SEM) and Energy-Dispersive Spectroscopy (EDS)

Figure 3.4 shows the scanning electron micrograph (SEM) images for the fresh and used 0La, 0.5La, and 2La catalysts. Agglomerate particle sizes of the fresh samples (in the left panels of Figure 3.4) appear to be the same. The elemental compositions of the metals analyzed by EDS are approximately the same for the scans taken at different spots on each catalyst, indicating that the bulk components are well distributed and mixed, as shown in Table 3.5. Quantitative analysis by the software is not accurate for calculating the low compositions of lanthana. However, qualitative analysis shows similar contents for the different scans. The surfaces of some agglomerates are rougher than others. Further X-ray analysis was performed at low voltage (12 keV) to determine the compositions of the accumulations on top of the larger agglomerate particles. The results showed that these accumulations contain 2-3 wt% higher copper content. This segregation of copper might be due to the different (+2) oxidation state that Cu carries, compared the other (+3) metals, but is also likely induced by the reduction of the copper oxide to metallic copper in the used catalysts [34, 37].

The SEM images of the used catalysts, shown in the right panels of Figure 3.4, are quite different. The 0La and 2La catalysts are cracked and ruptured, while the 0.5La catalyst experienced the least damage. This observation is consistent with the surface area results that show the 0.5La catalyst is the most physically stable catalyst after treatment under reaction conditions, which is explainable in terms of the structural stability that the small addition of lanthana adds to the crystal structure.

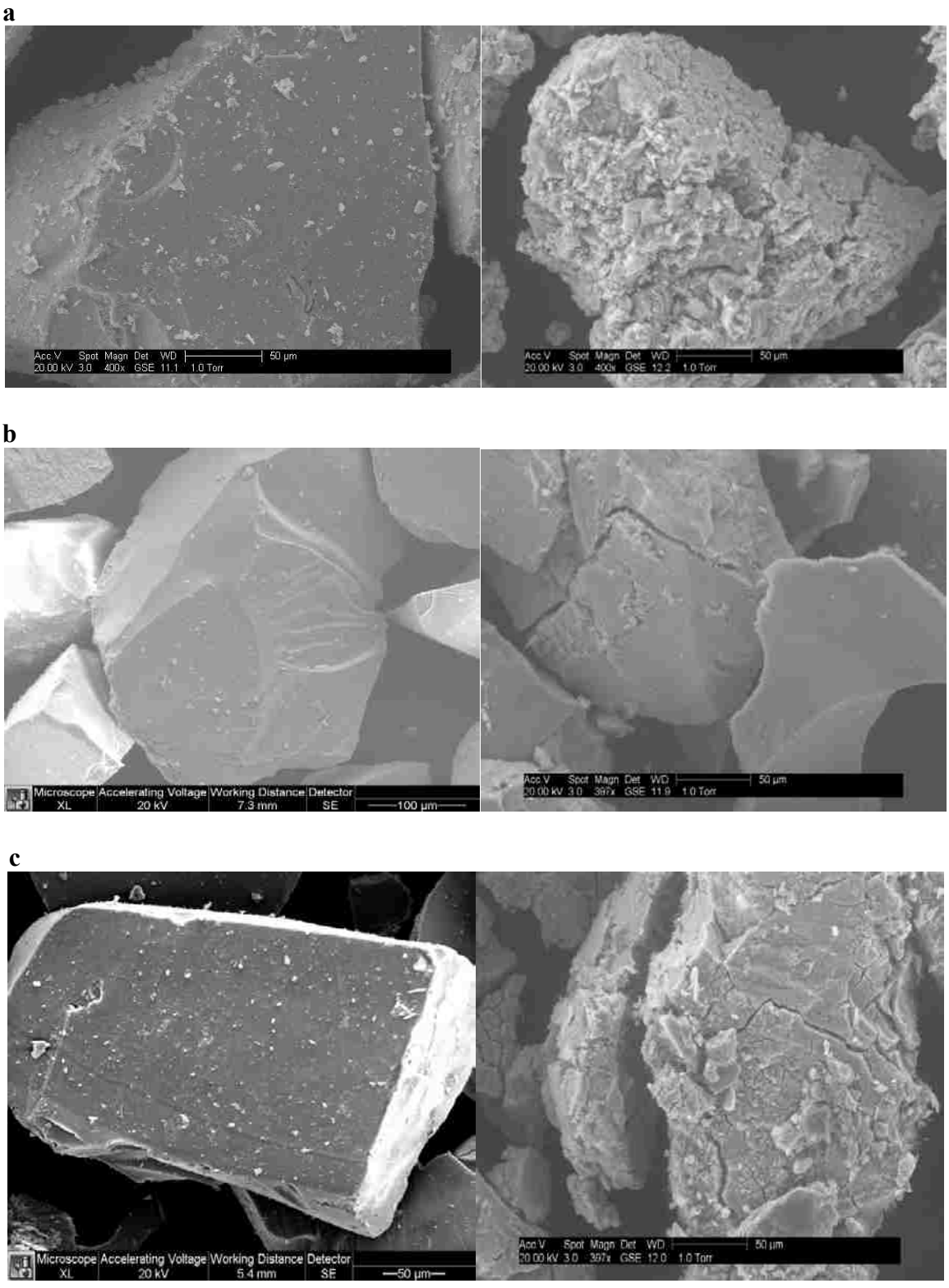

Figure 3.4: Scanning electron micrographs of (a) fresh (left) and used (right) 0La, (b) fresh (left) and used (right) 0.5La, and (c) fresh (left) and used (right) 2La catalysts.

Table 3.6: Quantitative EDS analysis on the fresh calcined catalysts. The numbers show wt% contents of each element for a scan across the surface of the sample holder and a one-point scan at a randomly chosen particle.

Catalyst ID	Scan Across Surface				One-point scan			
	La wt%	Cr wt%	Fe wt%	Cu wt%	La wt%	Cr wt%	Fe wt%	Cu wt%
0La	0.00	7.85	86.15	6.00	0.00	7.81	87.12	5.07
0.5La	1.23	8.87	86.00	3.90	1.41	8.94	85.66	3.99
1La	1.92	8.95	84.88	4.25	1.80	8.46	84.90	4.84
2La	3.17	9.13	83.40	4.30	3.16	8.52	83.83	4.49
5La	6.97	9.18	79.33	4.52	7.27	8.90	79.61	4.22

3.2.4 Temperature-Programmed Reduction with Hydrogen (H_2-TPR)

The phase of iron in the fully-oxidized 0La catalyst characterized by XRD is α-Fe_2O_3 (hematite) as shown in Figure 3.5a, ensuring that hematite is the phase that is being reduced. The O_2 and H_2O signals from the mass spectrometer, shown in Figure 3.5b, indicate that H_2O is produced while O_2 is being consumed during the oxidation of the catalyst as ferrihydrite converts to hematite.

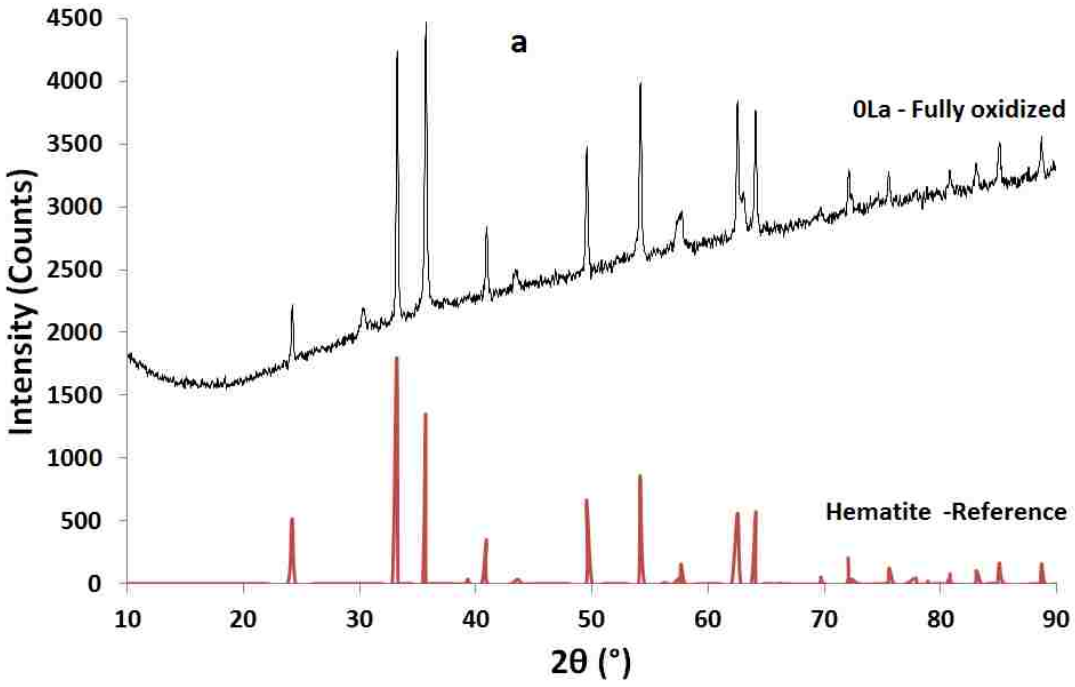

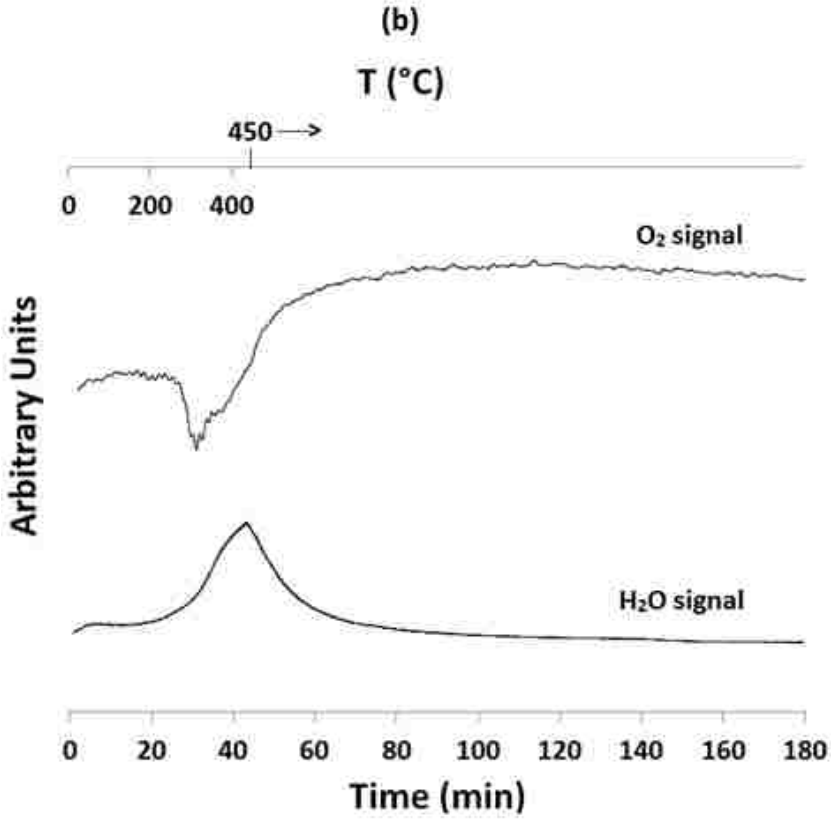

Figure 3.5: (a) XRD pattern for the fully oxidized 0La catalyst and (b) H_2O release during initial oxidation of the 0La catalyst and O_2 consumption during the temperature-programmed oxidation following TPR.

Two phases of reduction were observed for the five fully-oxidized catalysts during H_2-TPR. The first peak is attributed to the reduction of Fe_2O_3 to Fe_3O_4, CuO to Cu, and possibly Cr^{6+} to Cr^{3+}, while the second peak is ascribed to the reduction of Fe_3O_4 to FeO and metallic Fe [36,112-114]. However, the temperature was not increased beyond 450°C during the TPR experiments to fully characterize the second peak due to equipment limitations and because the catalytically relevant reduction processes occur at lower temperatures. Therefore, only the first peak is compared and discussed in Figure 3.6, which shows the TPR profiles of this first reduction phase for all of the samples. The maximum rate of reduction for the 0.5La sample occurs at a temperature 10°C lower than that for the 0La sample, while the peaks for the 1La, 2La, and 5La catalysts occur at higher temperatures, indicating that 0.5La is the most easily

reduced of the catalysts. Table 3.6 reports the extent of reduction of the catalysts from Fe_2O_3 to Fe_3O_4. The results show that the actual amounts of H_2 consumed during the TPR experiments are less than the stoichiometric amounts required for the full reduction of Fe_2O_3 to Fe_3O_4. Therefore, Fe_2O_3 does not fully reduce to Fe_3O_4 in the temperature range of 200°C - 300°C. These results are consistent with the XRD spectra that show the iron phase to be Fe_3O_4 in the used catalysts, which were treated under reduction conditions at higher temperatures and for extended periods of time prior to reaction.

Furthermore, the amount of H_2 consumed increases with the lanthana content in the catalysts, making the 5La catalyst the most reducible in terms of overall hydrogen consumption, but this increased extent of reduction is detrimental to the catalytic activity, as discussed in the next two sections. The disruption of the spinel observed in the XRD results at lanthana contents above 0.5 wt% is likely responsible for weaker interactions between Fe and the other promoters (such as Cr) in the bulk of the catalyst. The spinel structure in the 5La catalyst, once it is formed during the reduction of Fe_2O_3 to Fe_3O_4, appears to be destabilized by the presence of high concentrations of the large lanthanum ions and, therefore, Fe ions do not interact as strongly with Cr ions as they would if the spinel structure were sustained. This loss of interaction might cause the 5La catalyst, which is still mostly iron oxide, to reduce to a greater extent, but at temperatures well above those of the other samples.

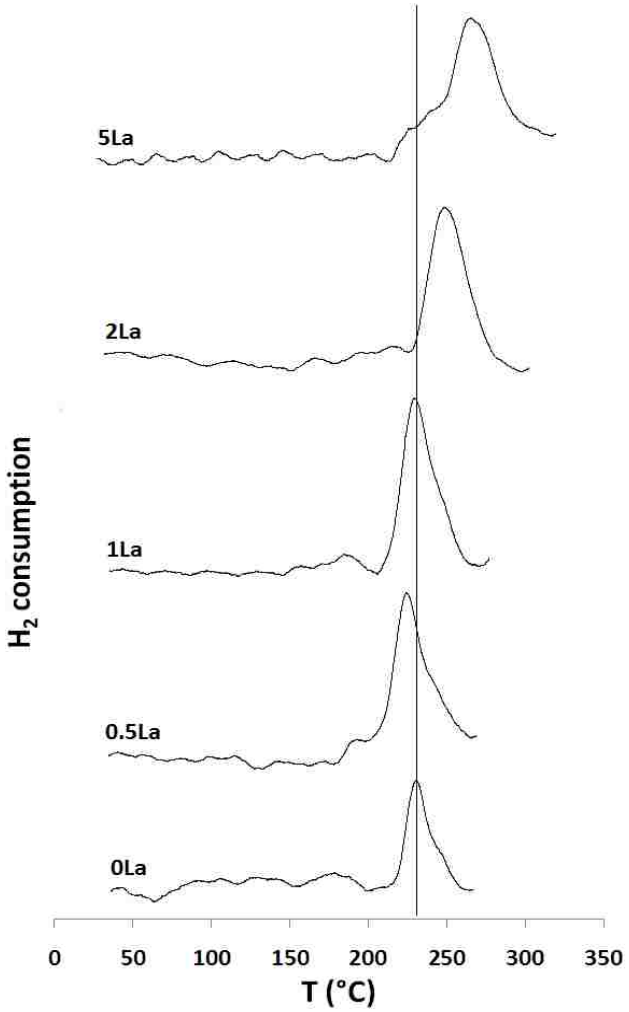

Figure 3.6: H_2-TPR profiles of the HT WGS catalysts: 10 mol% H_2/Ar, temperature ramp rate = 10°C/min, total flow = 50 sccm.

Table 3.7: Summary of H_2-TPR results. This table compares the reduction temperature of Fe_2O_3 to Fe_3O_4 as well as the extent of reduction in terms of hydrogen consumption.

Catalyst ID	Temperature at first peak maximum (°C)	Extent of reduction to Fe_3O_4 (%)[a]
0La	231	42
0.5La	219	53
1La	229	67
2La	246	79
5La	265	82

[a] Extent of reduction calculated for 0.04 grams of sample; 10 mol% H_2/Ar, temperature ramp = 10 °C/min, total flow = 50 sccm.

3.2.5 Catalyst Performance: Stability and Water-Gas Shift Activity

The initial (extrapolated to zero conversion) WGS rate results for all the catalysts plotted at the tested reaction temperatures in Figure 3.8 were obtained from the y-intercepts of the trend lines of reaction rate against the inverse of the specific molar flow rate of CO ($\dot{n}_{CO}$) shown in Figure 3.7. Plots for only the 0La and 0.5La catalysts are shown in Figure 3.7; however, similar plots were acquired for the other catalysts. The reaction rates at the lowest CO flow rate and 400°C and 425°C were not considered in this analysis because the CO conversions were too far (X_{CO}>20%) from differential conditions, which caused the rate data to lose their linearity. Figure 3.8 clearly shows that the 0.5La catalyst is the most active at all temperatures. However, addition of 1 wt% lanthana or more to the Fe-Cr-Cu catalysts inhibits their CO conversion rate, as summarized in Table 3.7, and makes them increasingly less active at higher temperatures. The deactivation percentages (measured by comparing the WGS rate at 400°C at the start of kinetic data collection and after an additional 120 h of reaction) reported in Table 4 prove that the 0.5La catalyst is also the most stable. These observations can be explained in terms of the disruption of the spinel structure discussed earlier, which makes the 1La, 2La, and 5La catalysts much less active than the 0La and 0.5La catalysts, especially at the higher reaction temperatures.

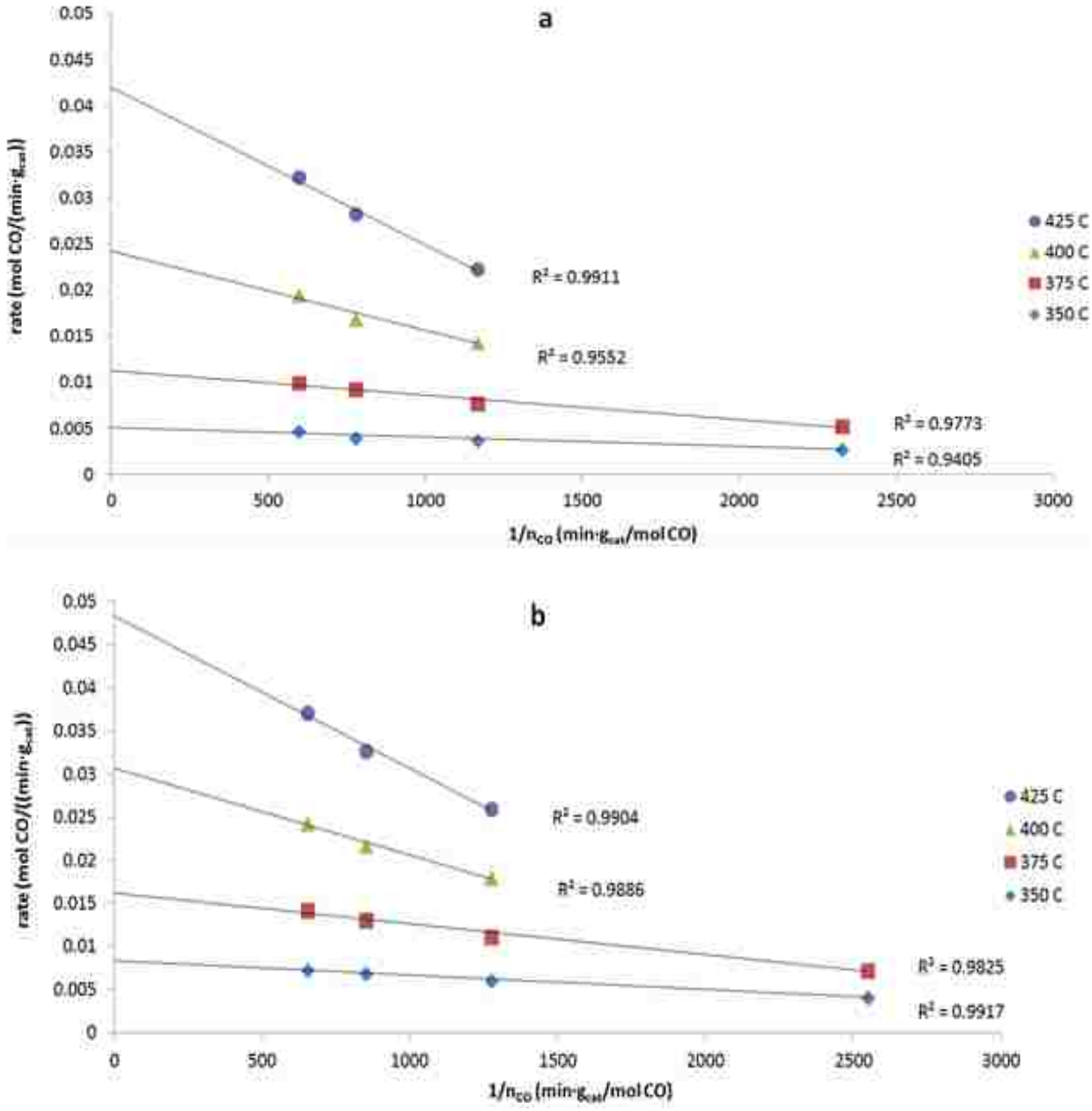

Figure 3.7: Rates of CO consumption as they vary with CO molar flow rate and reaction temperature for (a) 0La catalyst and (b) 0.5La catalyst. The rate at the lowest flow rate at 400°C and 425°C are not shown because the CO conversion under these conditions is far from differential conditions (X_{CO} > 20%).

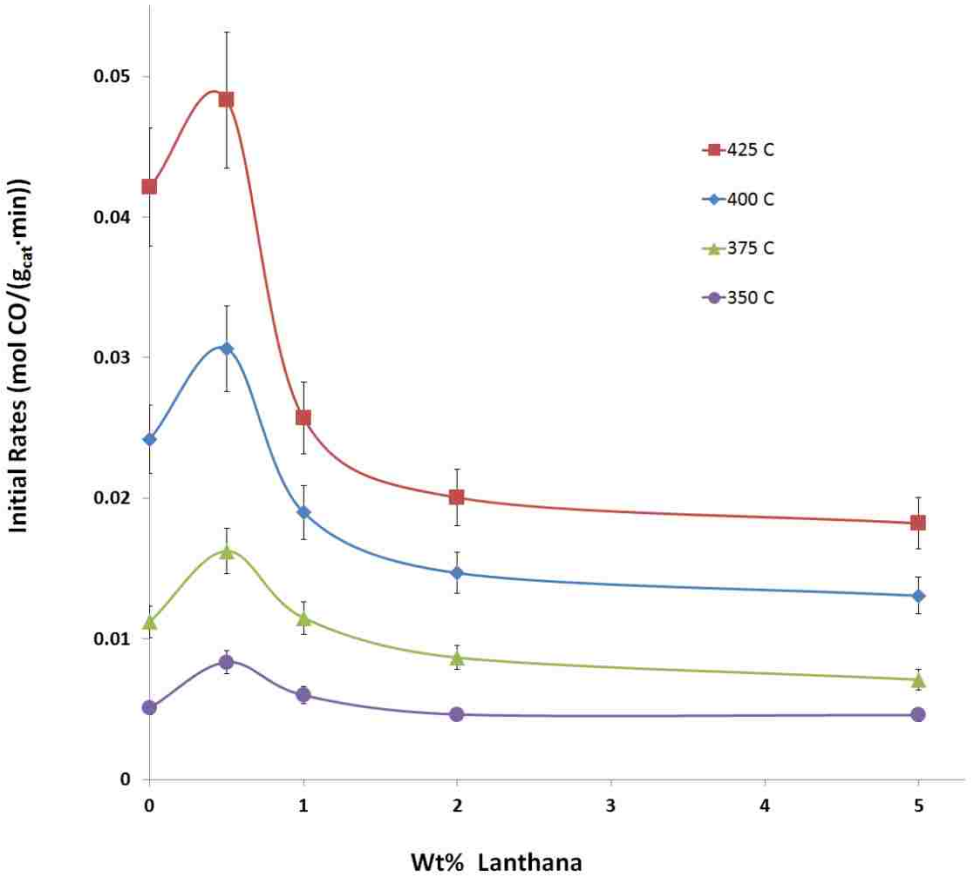

Figure 3.8: Initial rates of CO consumption as a function of lanthana loadings and four reaction temperatures with 5% error bars. 0.5La catalyst is the most active catalyst.

Table 3.8: Performance of HT WGS catalysts at 400°C under HT WGS conditions in terms of rate activity and stability. Deactivation % is compared at 120 h of operation after steady-state.

Catalyst ID	$-r_{CO}$ (mmol/(g_{cat}·min))	E_a (kJ/mol)	Deactivation (%)
0La	24	96 ± 5	23
0.5La	31	80 ± 4	11
1La	19	63 ± 7	20
2La	15	64 ± 7	22
5La	13	66 ± 6	24

During industrial hydrogen production, the products from a steam methane reformer exit at temperatures well above 400°C (around ~900°C [3]) and therefore must be cooled prior to the

WGS reactors. Based on these results, it is recommended to consider 0.5 wt% lanthana addition to industrial unsupported Fe-Cr-Cu WGS catalysts, as they may have the potential to provide more operating flexibility and activity at higher temperatures for better overall thermal efficiency, while maintaining reasonable stability.

3.2.6 Modeling: Rate Models and Kinetic Analysis

Table 3.8 compares the fit for each of the four kinetic models (Langmuir-Hinshelwood, Eley-Rideal, redox, and power-law) for the three tested catalysts (0La, 0.5La, 5La) by showing the respective r^2 values. The kinetic data (outlet concentrations) for the 0.5La catalyst are shown in Appendix C.3. The data show that the simple power-law model provides the best overall fit, but the Langmuir-Hinshelwood model, which provides greater mechanistic insight, is nearly as good and is substantially better than the Eley-Rideal or redox models. This point is emphasized in the parity plots that show the calculated *vs.* experimental rates in Figure 3.9. This suggests that the reaction follows an adsorptive, LH, mechanism. The fitting parameters for the LH (Equation 2.13) and power-law (Equations 2.18 and 2.19) models are shown in Tables 3.9 and 3.10, respectively.

Table 3.9: The coefficients of determination (r^2) for the different WGS kinetic models to determine which model best fits the rate data.

Catalyst ID	Langmuir-Hinshelwood	Redox	Eley-Rideal	Power-law
0La	0.93	0.72	0.54	0.95
0.5La	0.90	0.79	0.70	0.97
5La	0.91	0.49	0.79	0.91

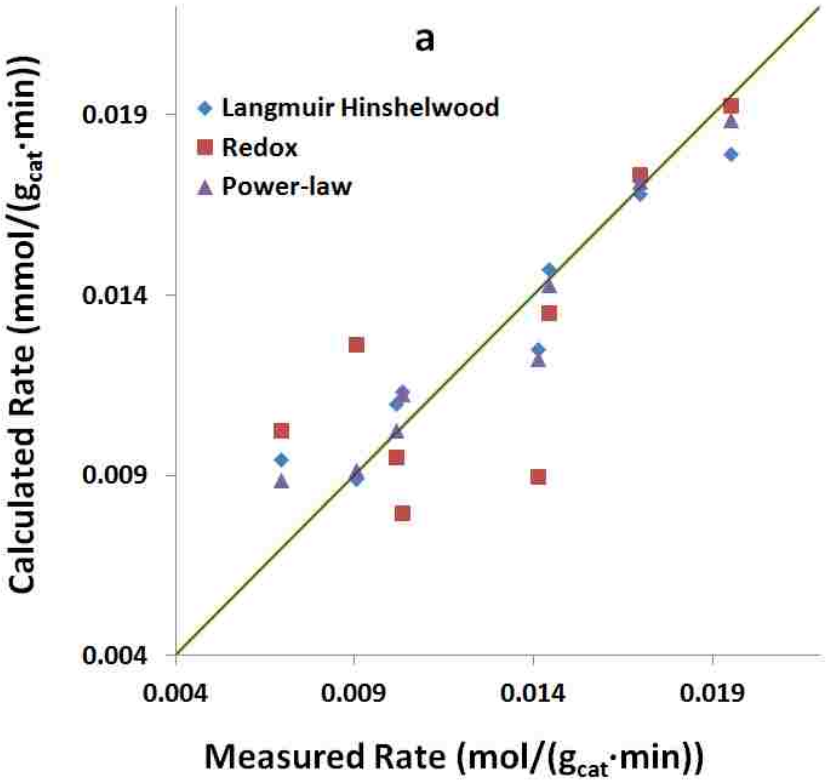
a
Langmuir Hinshelwood
Redox
Power-law
0.019
0.014
0.009
0.004
0.004
0.009
0.014
0.019
Calculated Rate (mmol/(gcat·min))
Measured Rate (mol/(gcat·min))

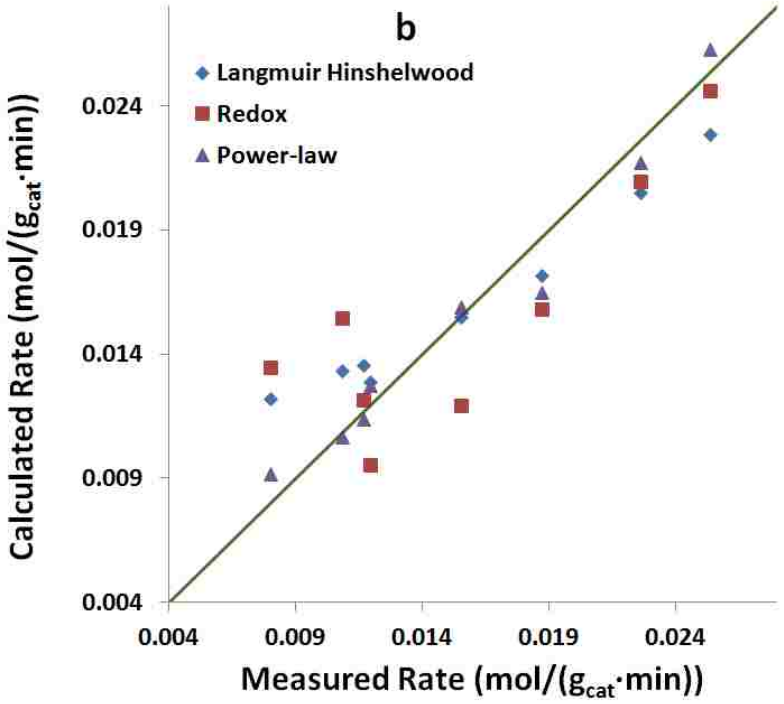
b
Langmuir Hinshelwood
Redox
Power-law
0.024
0.019
0.014
0.009
0.004
0.004
0.009
0.014
0.019
0.024
Calculated Rate (mol/(gcat·min))
Measured Rate (mol/(gcat·min))

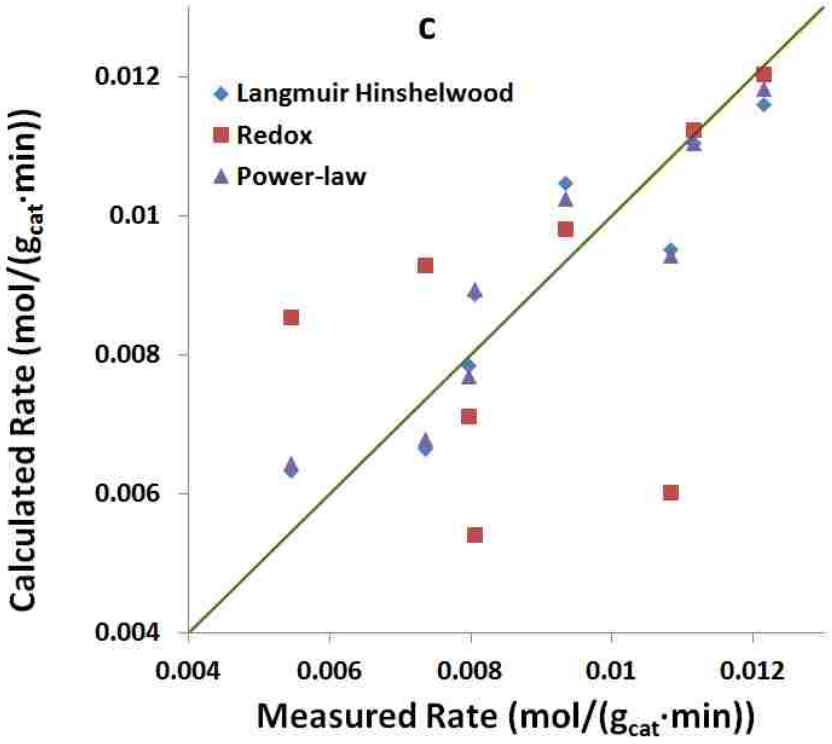

Figure 3.9: Parity plots for the WGS kinetic models for (a) 0La, (b) 0.5La, and (c) 5La catalysts at 400°C.

The reported values for the LH adsorption equilibrium constants of the reactants and products in Table 3.9 shows that CO has the smallest equilibrium constant, which indicates that water binds more strongly to the catalyst than CO due to the polarity of water molecules and their potential for hydrogen bonding with surface oxygen species. K_{CO} is largest for the 0.5La catalyst, which agrees with the pattern for higher CO conversions observed experimentally for this catalyst. 0.5 wt% addition of lanthana to the catalyst appears to facilitate the adsorption of CO, while further addition inhibits it. This can be explained in terms of the structural stability discussed earlier. The 0.5La catalyst has a larger surface area with a more stable spinel structure, which increases the accessibility of CO to the iron domains to form adsorbed Fe-CO surface species. Furthermore, in terms of polarizability, La^{3+} is a more polarizable cation than Fe^{3+} due to its larger ionic radius; hence, it is a softer Lewis acid. Keeping in mind that CO is a soft

Lewis base, it binds preferentially with the catalyst that has the softer Lewis acidity and a more polarizable electronic structure. The value of the overall reaction rate constant, k, is 43% higher for the 0.5La catalyst, but 52% lower for the 5La catalyst, when compared to the 0La catalyst. Therefore, the increase in rate activity for the 0.5La catalyst is attributed to both increased CO adsorption and a larger overall reaction rate constant. The proposed explanation for these observations is summarized in the following three points (which are likely to apply for the 1La and 2La catalysts):

1- High concentrations (5 wt%) of lanthana disrupt the spinel structure and possibly cover some of the surface, making Fe domains less accessible to the reactants. Therefore, the adsorption equilibrium constants of CO and H_2O are lower for the 5La catalyst.

2- Lanthana is added at the expense of the active Fe_3O_4 iron phase, which is responsible for the dissociation of H_2O molecules to hydrogen radicals. This step in the reaction mechanism is considered rate-determining [26-27] and accounts for the lower value of k, which is proportional to the surface reaction kinetics, observed for the 5La catalyst with the highest lanthana content. Furthermore, although not detected in the XRD results, but suggested by the TPR results, over-reduction of Fe_3O_4 to FeO might have occurred, resulting in lower content of the active magnetite phase on the catalyst surface.

3- Low lanthana (0.5 wt%) concentrations enhance the onset of reduction of the catalyst at reaction temperatures and therefore optimize the extent of reduction to the active Fe_3O_4 phase to enhance the rate-determining step.

Table 3.10: Kinetic fitting parameters of the Langmuir-Hinshelwood model shown in Equation 2.13 at 400°C. 95% confidence intervals are given in brackets next to the corresponding predicted values.

Catalyst ID	k (mmol/min)	K_{CO} (L/mol)	K_{H_2O} (L/mol)	K_{CO_2} (L/mol)	K_{H_2} (L/mol)
0La	5.6 (±1.0)	600 (±90)	1300 (±600)	4100 (±3000)	4100 (±3000)
0.5La	8.0 (±2.0)	930 (±200)	1600 (+1500/-1100)	6000 (±5000)	6000 (±5000)
5La	2.8 (±0.4)	370 (±60)	720 (+200/-160)	1500 (±1400)	1500 (±1400)

Table 3.9 shows the Langmuir-Hinshelwood parameters obtained from the nonlinear regression. Statistically, the confidence intervals on some of the parameters are relatively large due to limited range of the variables and the number of data points used in the regression analysis. The values of K_{CO} for the different catalysts have the most accurate (smallest) confidence region. The uncertainty in K_{H_2O} is larger on a percentage basis compared to that of K_{CO}, leading to the generation of the 95% joint confidence regions shown in Figure 3.10. The red dot represents the optimal set of parameters; however, it does not represent the only feasible value. There are infinite combinations for the pair of the parameters within the shaded 95% joint confidence region, which emphasizes the point discussed at the end of Section 3.1.3 that both parameters are dependent on each other and thus the confidence region is an ellipsoid instead of a rectangle. The plots in Figure 3.10 show that the values of K_{H_2O} are larger than those of K_{CO} over the whole range of possible values, assuring that the model shows that CO adsorbs less strongly than water. The contour plots also indicate that for K_{CO} and K_{H_2O}, the former is largest for the 0.5La catalyst and the latter is largest for the 0La catalyst by comparison of the lower range of each respective axis in Figures 3.10a and 3.10b. Furthermore, analysis of the shape of these 95% confidence regions indicates that both parameters in the LH model are positively

correlated, meaning that a higher value of K_{CO} is generally associated with a higher value of K_{H_2O} and vice versa. The values of the product adsorption equilibrium constants, K_{CO_2} and K_{H_2}, are included in Table 3.9 for completeness, despite their large uncertainty ranges, which are due to the low product concentrations (generally <10 mol%) that resulted from the approach to differential conversion conditions of the kinetic data used for the regression analysis. Studies on the reverse WGS reaction are required to provide more accurate and statistically reliable adsorption equilibrium constants for the products.

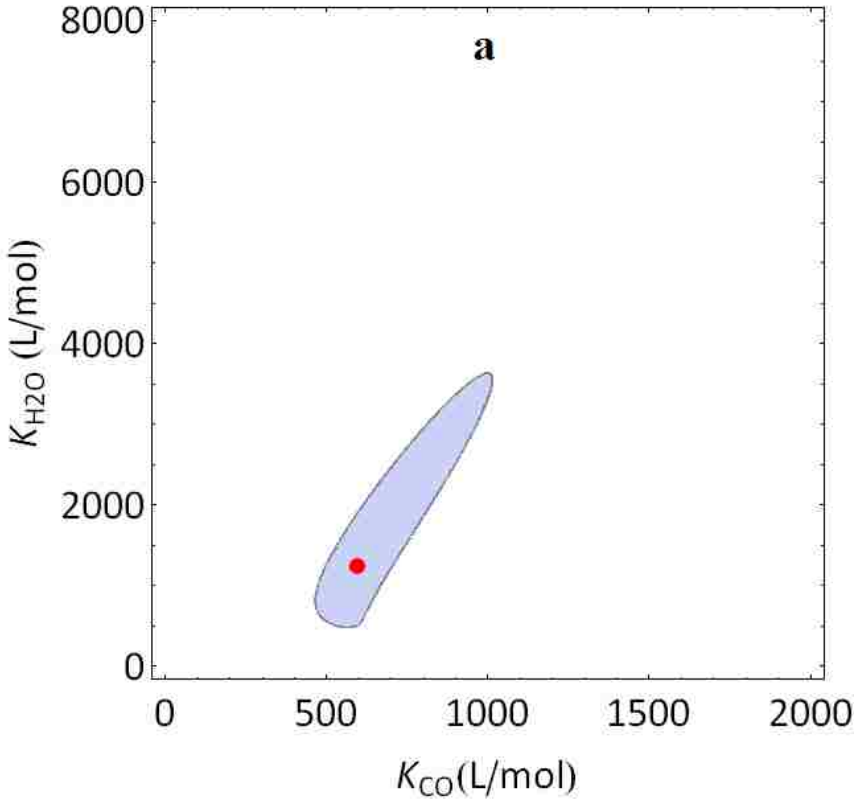

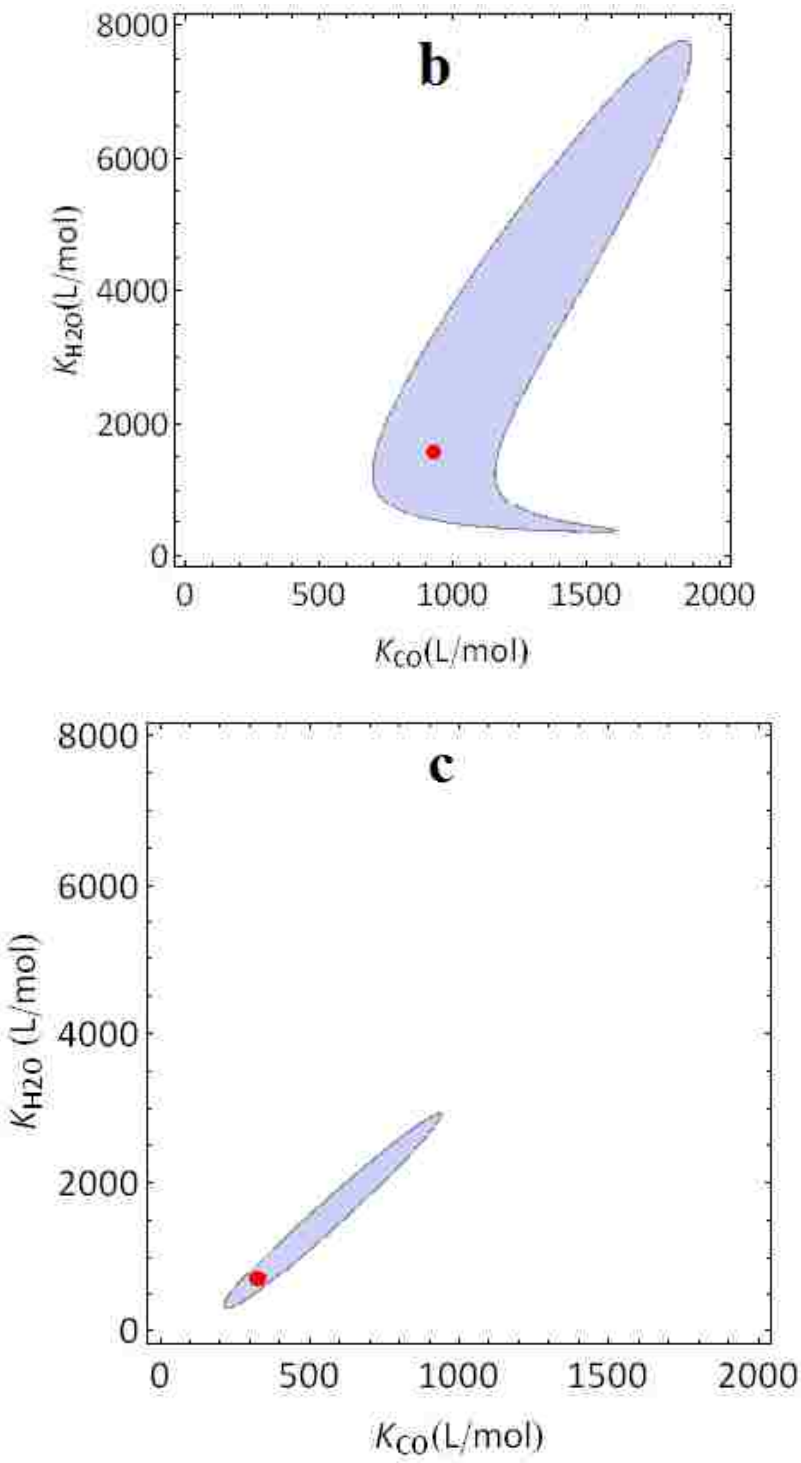

Figure 3.10: 95% joint confidence regions for the adsorption equilibrium constants of CO and H_2O for (a) 0La, (b) 0.5La, and (c) 5La catalysts. The dot indicates the optimum set of parameters while the shaded region indicates the feasible space of the parameters.

The power-law model provided the best fit of the data, but without providing significant mechanistic insight. Table 3.10 contains the power law kinetic parameters, which show that the reaction is positive order (~1) with respect to CO and zero order with respect to water. This independence of the rate on water (and the negative order for the 5La catalyst) can be well explained from the previous observations from the Langmuir-Hinshelwood model, where the adsorption equilibrium constant for water is larger than that for CO, indicating that water binds more strongly to the surface, thereby covering many of the surface sites and inhibiting the reaction. The 5La catalyst appears to have fewer sites available for binding and therefore the effect of water is worse. The highest positive order in CO is observed for the 0.5La catalyst because it favors CO adsorption more than the other two catalysts, as proposed by the LH model. The negative order of the products is justified by the reverse reaction competing for active sites and inhibiting CO adsorption and thus the overall rate of reaction, with the 0.5La catalyst having the largest negative orders due to its highest activity and CO conversion. The values of β_{eq}, which is the fractional approach to reaction equilibrium, are on the order of 10^{-3}, showing that the WGS reaction under the tested conditions was far from equilibrium, as expected for the approach to differential reaction conditions.

Table 3.11: Kinetic fitting parameters for the power-law model shown in Equation 2.18 at 400°C. 95% confidence intervals are given in brackets next to the corresponding predicted values.

Catalyst ID	k ($mol^{1-m-n-p-q}/(L^{m+n+p+q} \cdot min)$)	m	n	p	q
0La	0.0020 (± 0.0003)	1.02 (± 0.03)	0.11 (± 0.04)	-0.30 (± 0.02)	-0.30 (± 0.02)
0.5La	0.0088 (±0.0010)	1.50 (± 0.03)	0.09 (± 0.03)	-0.42 (± 0.02)	-0.42 (± 0.02)
5La	0.0014 (±0.0002)	0.85 (± 0.04)	-0.17 (± 0.04)	-0.13 (± 0.02)	-0.13 (± 0.02)

Further understanding of the WGS mechanism is provided by analyzing the results of the Eley-Rideal model, despite the worse fit compared to the LH model. Figure 3.11 shows the

parity plot for the 0La catalyst in which either H_2O or CO is chosen as the adsorbing species. The poor Eley-Rideal model fits suggest that the adsorption steps of both species are important in the WGS mechanism on these catalysts, which provides additional support for the LH model. This study has applied the general LH, redox, and Eley-Rideal models to examine the effect of lanthana on kinetic parameters of the generalized rate law models, but detailed and more accurate mechanistic studies based on isotopic tracer testing is outside the scope of this project. Further, the LH model could be empirically modified to include power dependencies of rate on the concentrations, depending on the elementary steps proposed and the intermediate species considered to outline the mechanism, as shown elsewhere [1, 50-55], but again was not justified within the purposes of the work.

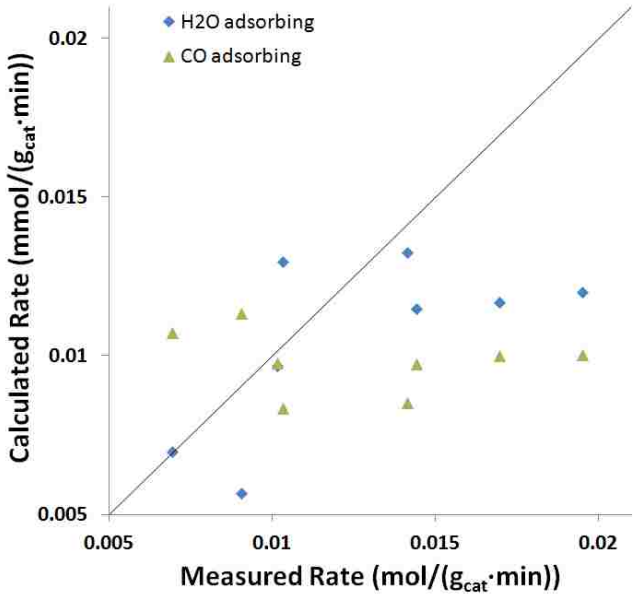

Figure 3.11: Eley-Rideal model fit for 0La catalyst with either H_2O adsorbing and CO non-adsorbing or CO adsorbing and H_2O non-adsorbing.

3.2.7 Summary of the High-Temperature Water-Gas Shift Work

The effect of small amounts (<5 wt%) of lanthana addition to standard $Fe_2O_3/Cr_2O_3/CuO$ high-temperature water-gas shift catalysts was investigated. The results showed that 0.5 wt% addition of lanthana produced a more stable and active catalyst with larger surface area after reaction. Lanthana addition beyond 0.5 wt%, however, had the opposite effects. Characterization techniques performed on the used catalysts suggest that these results are primarily due to structural changes as lanthana first integrates with and then disrupts the iron-chromium spinel structure. TPR results show that the most active catalyst with 0.5 wt% lanthana is also more easily reduced at lower temperatures; however, increased lanthana content causes the catalyst to be more reducible on a hydrogen consumption basis at higher temperatures. Fitting the kinetic data to Langmuir-Hinshelwood, Eley-Rideal, redox, and power-law rate models suggests that the reaction follows an adsorptive, Langmuir-Hinshelwood mechanism. The adsorption equilibrium constant of CO was largest for the catalyst with 0.5 wt% lanthana, indicating that lanthana possibly facilitates the adsorption of CO on the catalyst surface. Water inhibits the reaction, apparently due to strong adsorption on the catalyst surface.

CHAPTER 4. Extent of Reduction Study on Unsupported High-Temperature Water-Gas Shift Catalysts Using UV-Visible Spectroscopy

This chapter presents the experimental work, results, and discussion of the effects of lanthana on the extent of reduction (EOR) of unsupported iron-based WGS catalysts using UV-vis light absorbance along with mass spectrometry and X-ray absorption near edge spectroscopy (XANES) analysis. This study presents temperature-programmed reduction (TPR) profiles of iron WGS catalysts with varying amounts of lanthana and correlates them to *in-situ* UV-vis absorbance measurements. The Kubelka-Munk function is used to calibrate the UV-vis response to extent of reduction (EOR), or oxidation state of iron, determined by the TPR profiles. The resultant calibration curves are applied to scans performed on operating WGS catalysts to determine the effect of lanthana on the extent of reduction of these catalysts. The final results are compared with data acquired from XANES.

4.1 Experimental Methods and Apparatus

The experimental procedure for this study involved a set of temperature-programmed oxidations (TPO) with air and temperature-programmed reductions (TPR) with H_2 monitored using a UV-visible spectrophotometer and a mass spectrometer (MS). The used catalysts were analyzed with XRD for bulk iron phase. The flow diagram in Figure 4.1 shows these steps in order.

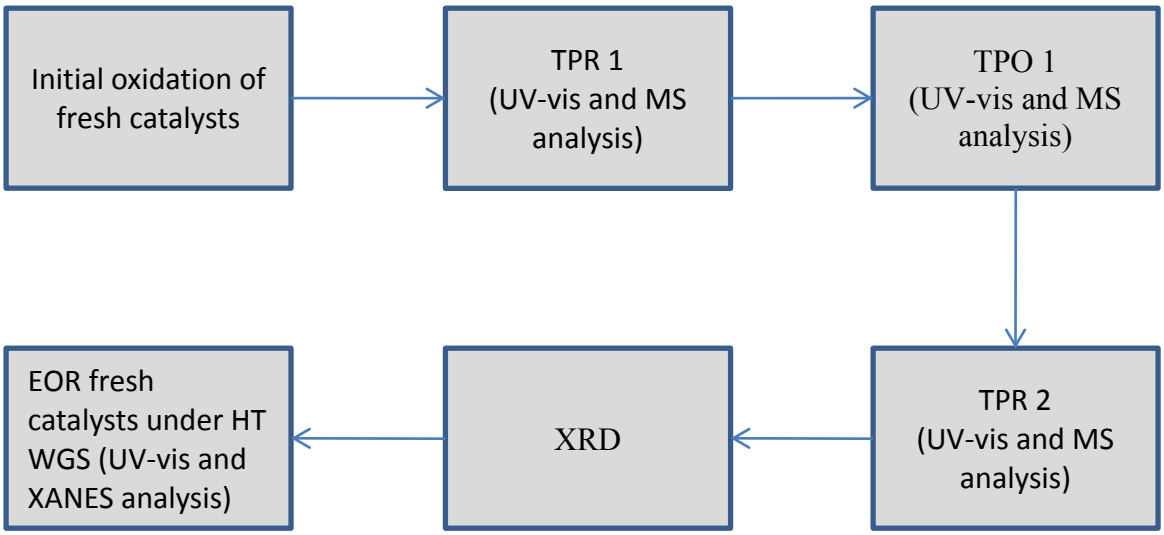

Figure 4.1: Flow diagram of the experimental procedure for the extent of reduction study of HT WGS iron-based catalysts.

4.1.1 Temperature-Programmed Reduction and Oxidation

A brief description of TPR experiments was given in Section 3.1.2.4 of the previous chapter. This section describes the oxidation as well as the reduction processes more thoroughly.

The catalysts, prepared by co-precipitation, as described in Section 3.1.1, contain varying amounts of lanthana added at the expense of iron(III) oxide. The five catalysts have (88 - x) wt% Fe_2O_3, 8 wt% Cr_2O_3, 4 wt% CuO, and x wt% lanthana, where x = 0, 0.5, 1, 2, and 5, and are designated as 0La, 0.5La, 1La, 2La, and 5La, respectively. Initially, 40 mg of catalyst were fully oxidized in flowing air (Zero Air, Airgas) at 30 sccm for 60 to 90 minutes at 450°C and then cooled to room temperature. The temperature ramp for the heating and cooling was 10°C/min. The flow rate of air was controlled by a calibrated 100 sccm rotameter (Omega). TPR's were performed in 10 mol% H_2/Ar (5 sccm of H_2 (99.95%, Airgas) and 45 sccm of Ar (99.997%, Airgas)) for 3 h and a temperature ramp of 10°C/min from room temperature to 450°C. The flow rates of H_2 and Ar were controlled using calibrated mass flow controllers (Porter

Instruments 201). The temperature was not increased beyond 450°C for all experiments due to limitations on the heater used. Hydrogen consumption was quantified *via* concomitant mass spectrometry (MKS Cirrus 100). Following the first TPR (TPR 1), the samples were reoxidized (TPO 1) in flowing air at 30 sccm for 3 h at a temperature ramp of 10°C/min from room temperature to 450°C. A similar procedure was followed by a second TPR (TPR 2) to check the cyclic reducibility of the catalysts. All experiments were performed at atmospheric pressure. Hydrogen consumption was quantified by integrating the areas under the peaks from the mass spectrometer data relative to a calibrated baseline. The following reactions were used to quantify the reduction due to hydrogen consumption:

$$3Fe_2O_3 + H_2 \rightleftharpoons 2Fe_3O_4 + H_2O_{(g)} \quad \text{(First reduction phase)} \quad (4.1)$$

$$Fe_2O_3 + 3H_2 \leftrightarrow 2Fe + 3H_2O_{(g)} \quad \text{(Overall reduction)} \quad (4.2)$$

4.1.2 *In-Situ* UV-Visible Experiments

A diffuse reflectance UV-visible spectrophotometer (Varian Cary 4000) with a high-temperature reaction chamber (Praying Mantis™ model HVC-VUV-4, Harrick Scientific) was used for this study. Diffuse reflectance detection is an important property of the spectrophotomer because it collects the light scattered from the rough surfaces of the powdery catalysts and minimizes any directly reflected light that could result in noisy data, and thus enhances the signal-to-noise ratio [115]. The technique involves a source of light (tungsten lamp for visible light and deuterium lamp for UV light), a monochromator that allows light of specific wavelengths to pass, a sample holder where the sample sits, a set of mirrors that either focus the light on the sample or collect the light scattered from the sample, a photomultiplier detector that receives the scattered light from the mirrors and converts the light signal to a digital signal, and

computer software that displays the reading. The software provided by Varian included a Scan® program that displays absorbance as a function of wavenumber and a Kinetics® program that displays absorbance as a function of time at a specific wavenumber. The Harrick Praying Mantis Cell attached to the UV-vis spectrophotometer focuses the incident light on the catalyst, which absorbs part of the light and scatters the rest and the mirrors collect the scattered light and direct it to the detector. Illustrations of the instrumentation used are shown in Figures 4.2 and 4.3.

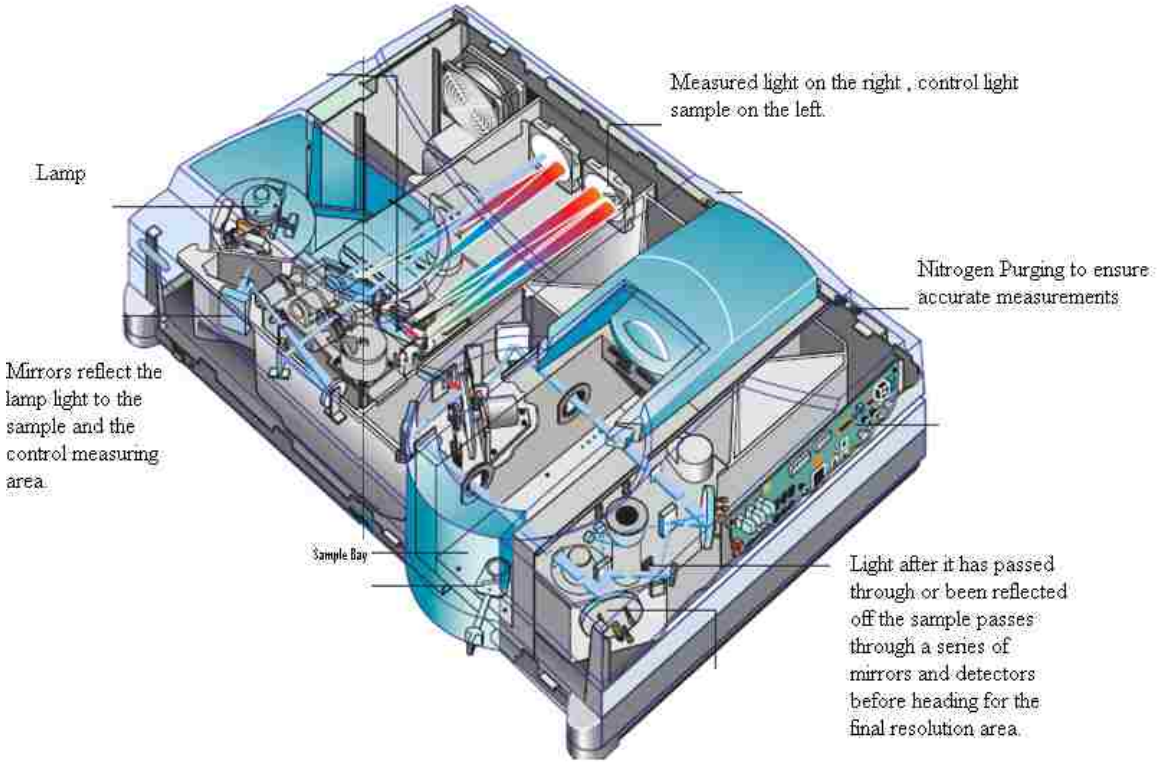

Figure 4.2: An illustration of Varian Cary 4000 UV-vis spectrophotometer given by Varian Corporation [116].

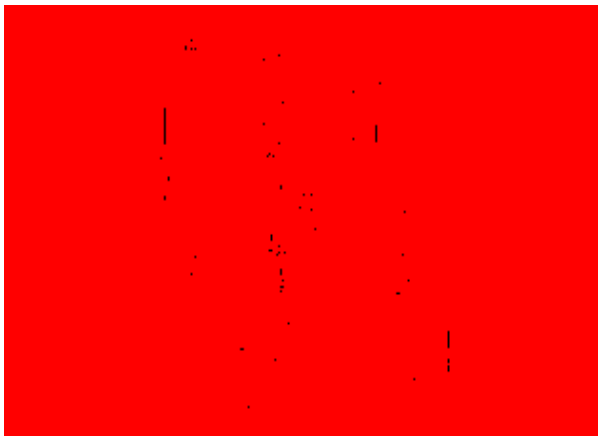

Figure 4.3: Harrick Praying Mantis Cell [117].

40 mg sample of catalyst, sieved to 100-250 μm agglomerate particle size, was placed in a cup holder and supported on a quartz frit with ~100 μm pores to provide flow uniformity. The surface of the sample was smoothened to give the best possible optical data. Instead of using the standard magnesia or Teflon reference for the Kubelka-Munk (K-M) function, the intensity of light collected from the sample surface was normalized relative to that of the fully oxidized sample at room temperature. During TPR and TPO experiments, absorbance data were collected using Varian Kinetics® software and hydrogen/oxygen consumption data were collected using the MKS mass spectrometer. The data obtained from the Kinetics® program were absorbance *vs.* time at 12,500 cm^{-1} (800 nm), which provided the most sensitivity during prior scans across the light spectrum from 12,500 cm^{-1} to 50,000 cm^{-1} (200 nm), for each temperature-programmed reduction and oxidation process. Subsequent scans collected K-M absorbance *vs.* light energy over the 12,500 to 50,000 cm^{-1} (800 nm to 200 nm with 2 nm per second steps) spectrum after the temperature of the catalyst sample cooled to room temperature. K-M values were calibrated against quantified extent of reduction obtained during simultaneous TPR measurements, as described in the previous section. Statistical analysis was performed on the parameters of the calibration using non-linear fitting tools available in R™ programming language (R Development

Core Team, v. 2.13.0) with 1000 points to acquire and plot the 95% confidence regions. The used catalyst samples were retained for further analysis.

4.1.3 High-Temperature Water-Gas Shift Reaction

UV-vis scans were collected for reduced samples under HT WGS conditions at 400°C and atmospheric pressure after different reaction times. The temperature ramp was 10°C/min. The fresh calcined catalyst was first pretreated for 2 h with a mixture of 12.5 sccm H_2, 2.1. sccm CO (99.995%, Airgas), and 25 sccm Ar that was saturated with distilled water bubbler prior to entering the UV-vis reactant chamber. H_2 flow was shut off after WGS reduction to proceed with the HT WGS reaction. The partial pressure of water was assumed to be 3.2 kPa, which is the water saturation pressure at room temperature.

4.1.4 XRD, EDS, and SEM Characterization

Powder XRD, EDS, and SEM analyses were performed on used samples after TPR and TPO experiments to determine the major bulk phase of iron in the catalysts. Details about XRD technique are presented in Section 3.1.2.3 while a detailed description about EDS and SEM is given in Section 3.1.2.2.

4.1.5 XANES (X-Ray Near-Edge Spectroscopy) Characterization

XANES experiments were performed on the X18A beamline at the NSLS at Brookhaven National Laboratory (NY, USA). Beamline X18A is a bending magnet line, which uses a Si {1 1 1} channel-cut monochromator and a rhodium-coated toroidal focusing mirror to provide a ~1.0 mm (horizontal) and ~0.5 mm (vertical) spot size with a flux of ~2.5×10^{11} photons/s at 10 keV.

After alignment using the spectra obtained from an Fe foil in the reference ion chamber, three consecutive scans were averaged and recorded simultaneously with those of the sample. Samples and reference compounds were diluted with boron nitride to achieve an edge jump of ~1 and encapsulated between two Kapton foil sheets.

4.2 Results and Discussion

This section reports the results of the characterization and UV-vis experiments, showing how the UV-vis absorbance data can be calibrated against surface EOR of iron, discussing EOR of 0La and 1La catalysts after WGS treatment, and comparing EOR results with those acquired from XANES.

4.2.1 Temperature-Programmed Reduction and Oxidation (TPR and TPO)

The full TPR profiles as functions of time and temperature for the five catalysts with varying quantities of La are shown in Figure 4.4. Two peaks were observed during the reduction of the catalysts with H_2, in which the first peak corresponds to the reduction of Fe_2O_3 to Fe_3O_4, CuO to Cu, and possibly Cr^{6+} to Cr^{3+}, while the second peak is attributed to the reduction of Fe_3O_4 to FeO and metallic Fe [34,36,112,113]. The second peak is much larger than the first peak because it requires 8 times the amount of H_2 to reduce Fe_3O_4 to Fe compared to Fe_2O_3 to Fe_3O_4. As presented in Section 3.2.4 and as shown in Figure 4.4, the 0.5La catalyst was the easiest to reduce of the catalysts containing La, as determined by the maximum of the first reduction peak occurring at the lowest temperature (~219°C).

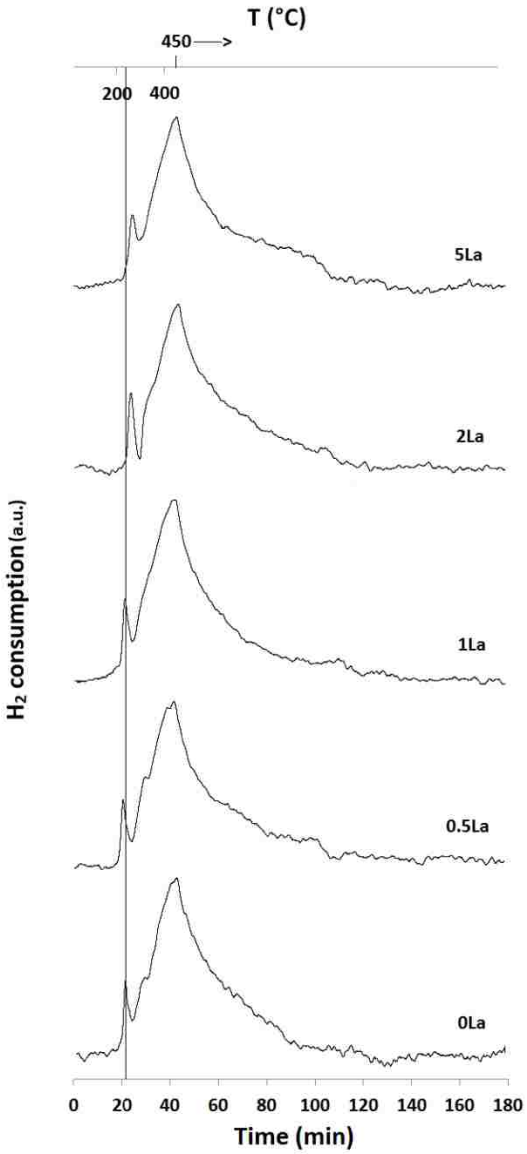

Figure 4.4: First temperature-programmed reduction profiles of all the catalysts (TPR 1, 10 mol% H2/Ar, total flow = 50 sccm, ramp rate = 10 °C/min). 0.5La catalyst starts reducing at the lowest temperature.

The maxima of the second peaks occur at almost the same times (temperature) for all the catalysts due to the temperature limitation. Table 4.1 shows the extent of reduction (EOR) for each of the catalysts. Hydrogen consumption increases with La content for the first reduction phase and is approximately the same for the second reduction phase (within the ±5% error for this experiment).

Table 4.1: Extent of reduction of all catalysts for TPR 1 and TPR 2 (10 mol% H2/Ar, total flow = 50 sccm).

Catalyst ID	TPR 1 (first peak) % EOR to Fe_3O_4	TPR 1 (both peaks) % EOR to Fe	TPR 2 % EOR to Fe
0La	42	82	42
0.5La	53	78	72
1La	67	85	53
2La	79	89	N/A
5La	82	89	57

However, even the uncertainty is considered, 2La and 5La appear to consume more hydrogen than 0.5La. This is explained in terms of the stabilized iron-chromium spinel that is formed in the 0.5La catalyst after it is reduced to the active magnetite form. Therefore, the 0.5La catalyst has a higher extent of reduction to magnetite than the 0La catalyst, but a lower extent of reduction to Fe than the 1 La, 2La, and 5La catalysts. Furthermore, the 2La and 5La catalysts start consuming hydrogen with the second peak later (i.e., at higher temperatures) possibly due to lanthana covering iron domains making them less accessible. The 2La and 5La catalysts consume more hydrogen than the 0.5La catalyst, possibly due to a disrupted spinel structure and loss of strong interaction between Fe and other elements (such as Cr), which make the catalysts more reducible in terms of hydrogen consumption, as discussed in the previous chapter.

Following an intervening full oxidation, the overall extent of reduction data during TPR 2 show a different trend. The maximum hydrogen consumption is now observed for the 0.5La catalyst, while 0La consumes the least and 1La and 5La consume less than 0.5La. The TPR 2 profiles, plotted in Figure 4.5, show that the peaks appear at higher temperatures (~300°C for the first peak and ~400°C for the second peak), with the second peak being much smaller than the first, as the heating does not go beyond 450°C, suggesting that the catalysts have been stabilized after the first TPR/TPO cycle. The 0.5La and 1La catalysts start consuming H_2 at 30-40°C lower

temperatures (3-4 minutes earlier) than the other catalysts. However, the 0.5La catalyst ends up consuming more hydrogen than the other samples by the time the temperature reaches 450°C (at approximately 43 minutes). This ease and extent of reducibility is correlated to the overall WGS reaction rates and catalytic stability previously reported for these catalysts in Section 3.2.5.

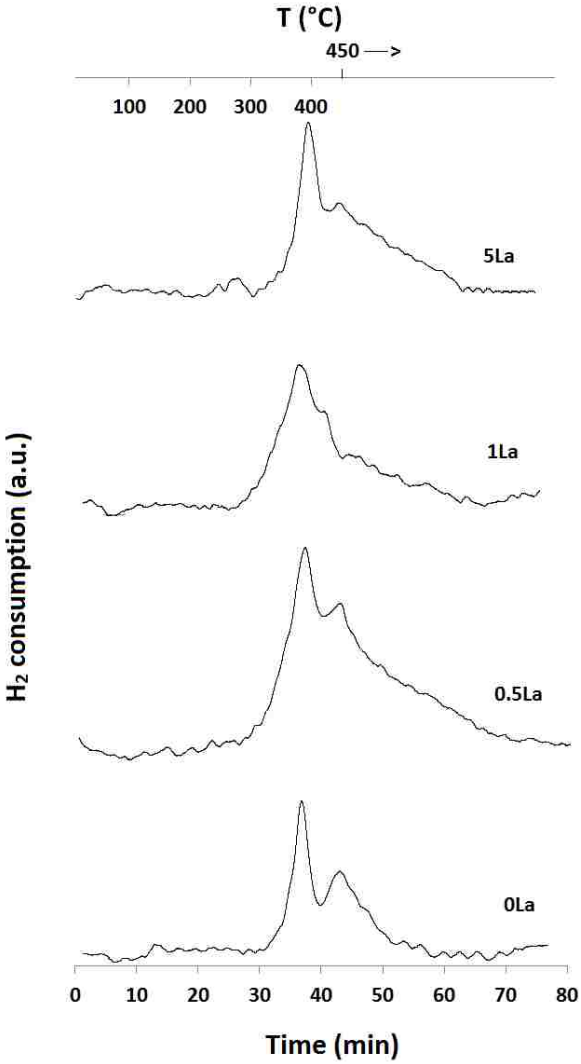

Figure 4.5: Second temperature-programmed reduction profiles of most of the catalysts (TPR 2, 10 mol% H2/Ar, total flow = 50 sccm, ramp rate = 10 °C/min). 0.5La catalyst has the highest hydrogen consumption.

The results of TPR 2 are significant because the 0.5La catalyst is a better catalyst candidate for re-use, as it has been deactivated the least. In fact, the extent of reduction for the

0.5La catalyst calculated from TPR 2 is 8% lower than that calculated from TPR 1, while those of the other catalysts are approximately 35% - 50% lower. The decreased reducibility of the catalyst comes as result of possible sintering and deactivation of the catalyst after TPR 1 treatment at 450°C for 3 h, consistent with the surface area data before and after reaction presented in Table 3.4. Qualitatively, these results also agree very well with what has been reported previously on the stability of the catalysts, where the WGS reaction rate decreased by 11% for the 0.5La catalyst after 120 h under reaction conditions compared to 20 – 25 % for the other catalysts. The promoting effect of lanthana in lowering the reduction temperature observed with the first and second peaks in TPR 1 is attributed to a stabilized spinel that starts forming at lower temperatures in the 0.5La catalyst and continues to consume H_2 until the hematite is reduced to magnetite. Further addition of lanthana appears to disrupt the spinel once formed, and possibly cover the surface, making the Fe domains less accessible to H_2, thus requiring higher temperatures for the catalysts to be reduced.

Previous XRD analysis has shown that the iron phase in the fresh calcined catalysts is ferrihydrite (see Section 3.2.2 and Figure 3.5). Similar plots were obtained for the other catalysts. Therefore, water is produced during the initial oxidation as the ferrihydrite transforms to hematite. Oxygen is consumed during TPO 1 to form hematite after the catalysts have been reduced during TPR 1. The amount of oxygen consumed for TPO 1 for the 0La catalyst is 80% of the hypothetical value required for full oxidation of metallic Fe to Fe_2O_3, which is in good agreement with the extent of reduction calculated from TPR 1 (82%).

4.2.2 Powder X-Ray Diffraction (XRD) Analysis

XRD spectra were collected for a specific set of samples post reduction/oxidation treatments, as shown in Figures 4.6 and 4.7. The spectra in Figure 4.6 qualitatively show that the

major iron phases in the catalysts post TPR 1 and TPR 2 are a mixture of metallic Fe and magnetite, based on comparison with the International Centre for Diffraction Data (ICDD) database. However, the peak at 44.7°, which is representative of metallic Fe, is much less intense and essentially negligible for the samples post TPR 2, when compared to the other samples post TPR 1. These results are in good agreement with the TPR trends discussed in the previous section, where the extent of reduction for TPR 2 is 50% lower than that for TPR 1 for the 0La and 5La samples. No peaks for FeO were detected in the XRD patterns because Fe_3O_4 and Fe are more thermodynamically stable than FeO for these shift catalysts at 400 – 450 °C [118]. The peaks of metallic Fe for the samples post TPR 2 are not intense compared to the peaks observed with samples post TPR 1, indicating a lower content of Fe and hence a lower extent of reduction. There are slight shifts to the left in the diffraction peaks at 57° and 62.5° for the 1La and 2La catalysts post TPR 1, and a clear left shift in the peaks at 35.5°, 57°, and 62.5° for the 5La catalyst post TPR 2, indicating larger lattice parameters and therefore larger unit cells for Fe_3O_4, suggesting incorporation of the larger La^{3+} ions. This trend is similar to that observed with the samples post WGS reaction [see Section 3.2.2]. The crystallite sizes, reported in Table 4.2, were calculated using the Scherrer equation from the representative peaks of Fe_3O_4 at 35.5°, 57°, and 62.5°.

Table 4.2: Crystallite sizes of some samples post TPR 1/TPR 2.

Catalyst ID	Crystallite Size (nm)
0La post TPR 1	26
0.5La post TPR 1	26
1La post TPR 1	24
2La post TPR 1	22
0La post TPR 2	18
5La post TPR 2	19

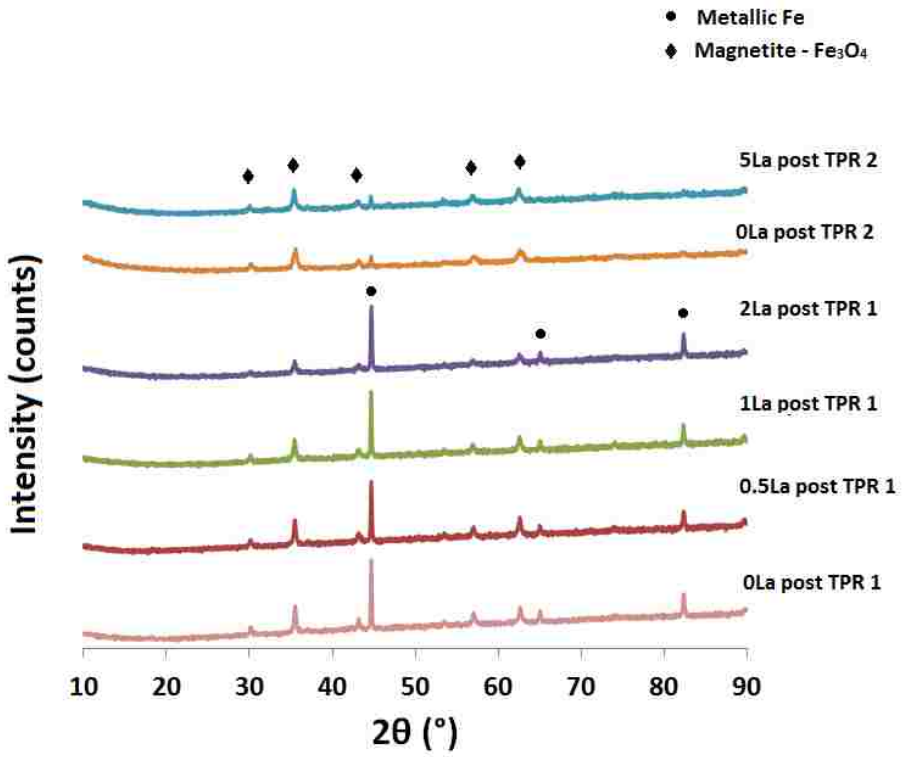

Figure 4.6: XRD patterns of catalysts after temperature-programmed reduction treatments (TPR 1and TPR 2). Metallic Fe is the major form of iron in samples after TPR 1. The peaks for metallic Fe are less intense for samples after TPR 2.

The 2La catalyst has the smallest crystal size among all the samples post TPR 1, corresponding to the less crystalline, intense, and broader Fe_3O_4 peaks. The crystallite sizes for the samples post TPR 2 are even smaller than those post TPR 1, indicating that the samples are not as crystalline after TPR 2, after they have experienced one reduction and oxidation cycle at the experimental conditions. This provides insight into the reusability of the catalysts and how well they maintain their structures after they have been activated and treated at high temperatures. The peaks for Fe at 44.7° are too narrow for accurate crystallite size calculations, but indicate crystallite sizes in excess of 50 nm.

Figure 4.7 compares the XRD spectrum for the 0La catalyst post TPO 2 with the reference hematite spectrum from the ICDD database. Clearly, the major iron oxide phase in the

bulk of the catalyst is hematite, thus iron is in the +3 oxidation state after full oxidation of the catalyst. However, a small peak at 30.2° indicates that Fe_3O_4 is still present in the bulk, but its intensity is negligible compared to the peaks of hematite.

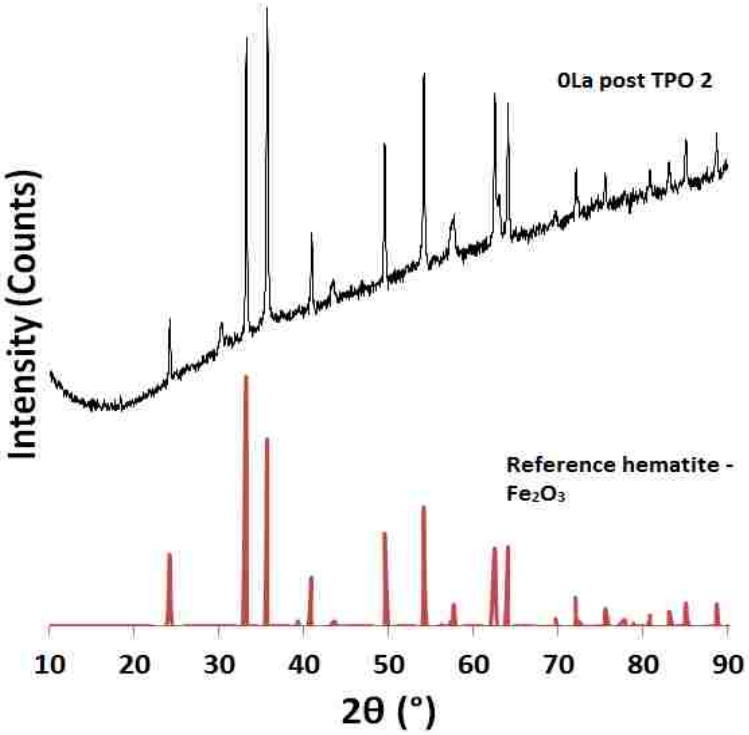

Figure 4.7: XRD pattern of 0La catalyst after the final temperature-programmed oxidation. The catalyst is oxidized with Fe2O3 as the major bulk phase of iron.

4.2.3 *Operando* UV-visible Spectroscopy

4.2.3.1 Absorption vs. Time Spectra

Diffuse reflectance light absorption data collected simultaneously with the data from the mass spectrometer show comparable results. Figure 4.8 shows the absorption signal response at 12,500 cm^{-1} as a function of time for the 0La, 0.5La, and 1La catalysts from the beginning of the reduction processes (TPR 1 and TPR 2) at room temperature to the maximum temperature of 450°C.

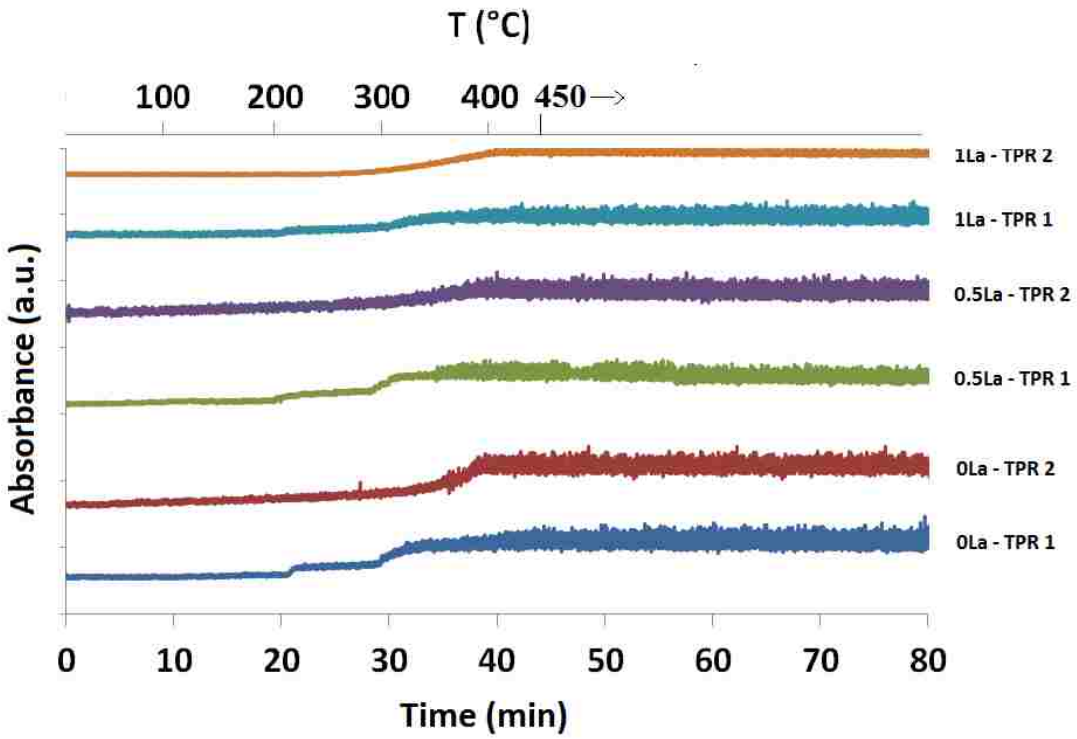

Figure 4.8: Kinetic spectra (absorbance vs. time) for the 0La, 0.5La, and 1La catalysts during TPR 1 and TPR 2. The absorbance signal increases simultaneously with the increase of the hydrogen consumption signal from the mass spectrometer.

The signals from the UV-vis spectrophotometer and mass spectrometer change simultaneously at the same temperature during the reduction processes. During TPR 1, there is a clear continuous increase in the UV-vis absorption signal as time proceeds. The jump occurs in 2 steps, for which the first step starts at around the 21-minute mark (about 230°C), while step 2 starts at around the 28-minute mark (about 300°C). The timings of steps 1 and 2 match with the times at which the H_2 signal from the mass spectrometer starts to show hydrogen consumption for the first and second reduction phases, respectively. On the other hand, only a long 1-step jump is observed at around the 32-minute mark (about 340°C) for the 0La catalyst and around the 28-minute mark (about 300°C) for the 0.5La and 1La catalysts during TPR 2, which corresponds to the hydrogen consumption peaks shown by the mass spectrometer where the second peak is small and

negligible compared to the first one. However, the absorbance signal for TPR 2 increases over a broader range of time, unlike that for TPR 1, which is sharper. The increase in the absorbance signal at 12,500 cm^{-1} is apparently due to the combined effect of reduction of Fe_2O_3 to Fe_3O_4 and metallic Fe, both of which have smaller band gaps than hematite, and the formation of oxygen vacancies.

Figure 4.9 shows the UV-vis absorbance as a function of time for the 0La catalyst post TPR 1, TPO, and TPR 2 on the same scale. The absorbance signal increases during the TPR experiments, while it decreases as the catalyst oxidizes during TPO. The asymptotic absorbance signal attained during TPR 2 is lower than that reached during TPR 1, indicating a lower extent of reduction. However, the absorbance signal starts with a lower value for TPR 2 compared to that for TPR 1. A possible explanation for this behavior is sintering of the particles due to thermal effects of the initial TPR and TPO. Furthermore, the absorbance at which TPO 1 ends is not the same as the signal at which TPR 2 starts (see Figure 4.9) due to temperature effects which are depicted in Figure 4.10. The same effect is observed for the signals at the end of TPR 1 and beginning of TPO 1. One process ends at 450°C while the other starts at 25°C. The effect of temperature can be explained as follows: higher temperatures increase the surface vibrational and rotational modes and therefore increase the absorbance [119].

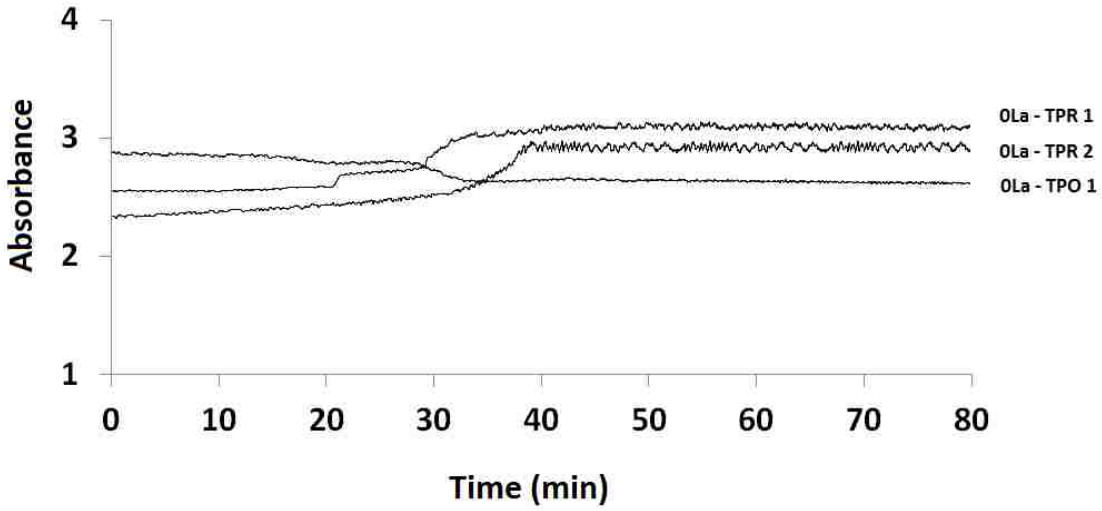

Figure 4.9: Kinetic spectra (absorbance vs. time) for the 0La catalyst during TPR 1, TPO 1, and TPR 2 combined on the same coordinates.

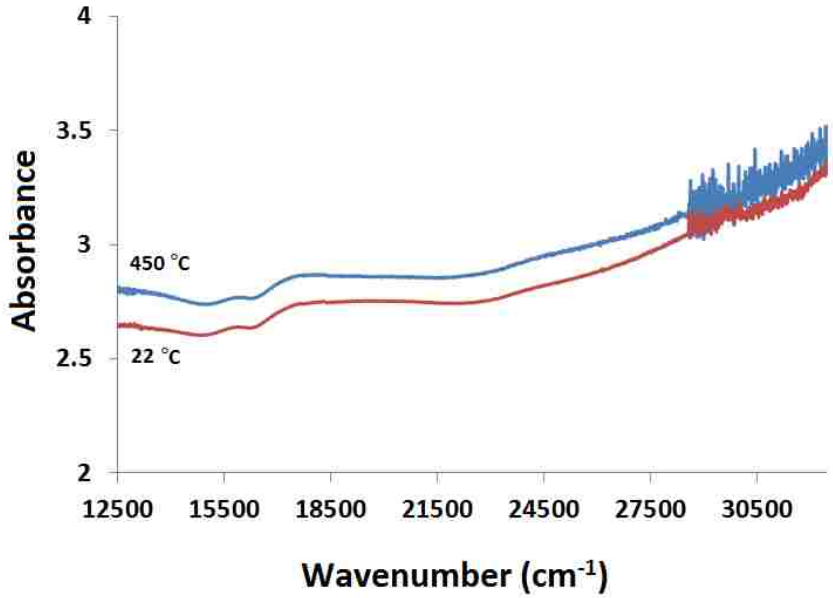

Figure 4.10: Absorbance scans of a fully oxidized 1La sample obtained at 22°C and 450°C. Higher temperatures cause the absorbance signal to increase.

The UV-vis spectroscopic analysis discussed in subsequent sections has been performed primarily on the 0La, 0.5La, and 1La catalysts because they produced the highest WGS rates reported in Chapter 3. Besides the activity trend, unexpected absorbance responses were observed for the 2La and 5La catalysts during TPR experiments. The spectra for the 2La and 5La

catalysts are plotted in Figure 4.11 to accentuate the different behaviors they show. Under normal TPR conditions (10 mol% H_2/Ar, total flow = 50 sccm), both catalysts do not show 2-step jumps corresponding to the two H_2 consumption peaks observed by the mass spectrometer signal. Furthermore, the absorbance signal decreases for both catalysts after an expected increase once they start reducing. Therefore, a third experiment was performed on the 2La catalyst under severe reducing conditions (50 mol% H_2/Ar) to ensure that this unusual behavior is not due to re-oxidation of the catalyst. The response is slightly different as the 2-step jump is now apparent, yet there is still a clear decrease in the absorbance signal after the second step. Moreover, the XRD pattern for the 2La catalyst post TPR 1 (shown in Figure 4.6) is expected based on the reduction conditions, with the presence of intense peaks for metallic Fe, suggesting that the catalyst has not been unintentionally re-oxidized at the end of TPR 1.

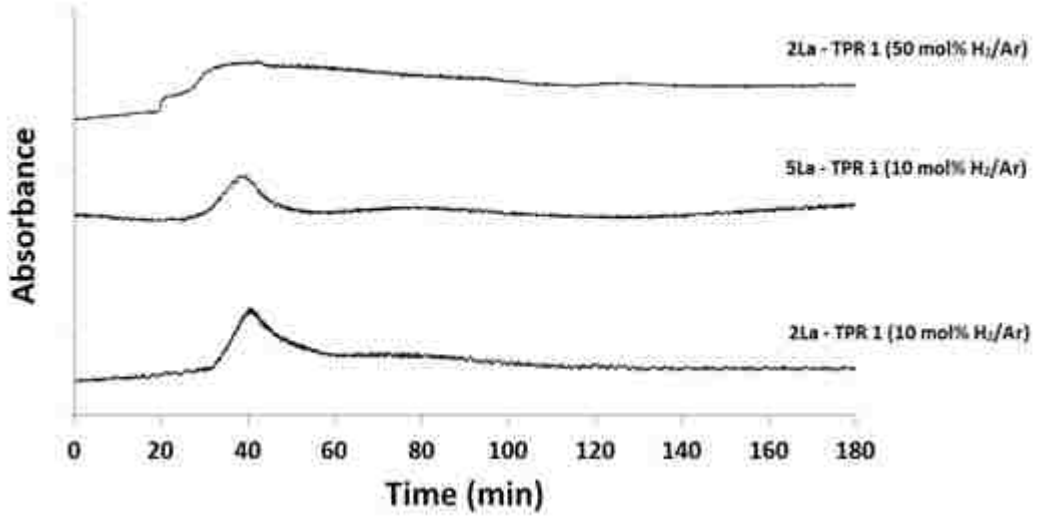

Figure 4.11: Kinetic spectra (absorbance vs. time) for the 2La and 5La catalysts during TPR 1. Absorbance signals drop down after the catalysts start reducing.

EDS analysis was performed on some samples post TPR 1 in order to further analyze and understand the causes of this behavior. EDS spectra are available in Appendix D. A notable

difference between the high-content lanthana catalysts (2La and 5La) post TPR 1 and the other samples (0La, 0.5La, 1La) post TPR 1 is the presence of sodium in these two catalysts, which remains from the catalyst synthesis using sodium hydroxide, despite repeated washing after synthesis. Sodium exists in larger amounts in the 2La and 5La catalysts, but the EDS peak was much less intense in the calcined 2La sample than it is in the reduced sample. Therefore, once these two catalysts start reducing, the sodium ions in the bulk appear to become more mobile and move to the surface of the catalyst, affecting the absorbance signal. Considering the reduction potentials of Na^{+} to Na (-2.71 V) and Fe^{3+} to Fe (0.33 V) [103], sodium is most probably present in its oxide or peroxide forms, which are white or light yellow compounds at the conditions of the TPR experiments. The appearance of oxides of sodium on the surface of the 2La and 5La catalysts during reduction is the probable explanation for the decreasing absorbance signal. Despite all of the catalysts being identically prepared and washed, the 2La and 5La catalysts retained more sodium. As a result, all further UV-visible spectra analyses are reported for the 0La, 0.5La, and 1La catalysts only.

4.2.3.2 Kubelka-Munk Scans and Calibration

The previous results presented in Section 4.2.3.1 show that light absorbance at 12,500 cm^{-1} is affected by the extent of reduction of the WGS catalysts. Scans across the UV-vis spectrum (K-M function values *vs.* wavenumber) are plotted in Figure 4.12 for the 0La catalyst. The reference for the modified K-M scan is a fully oxidized sample of each catalyst. The values of the normalized absorbance are the same as the K-M values when the catalysts are scanned under normalized absorbance scans, suggesting that the scattering term has minimal effect on the K-M function during the TPR and TPO experiments.

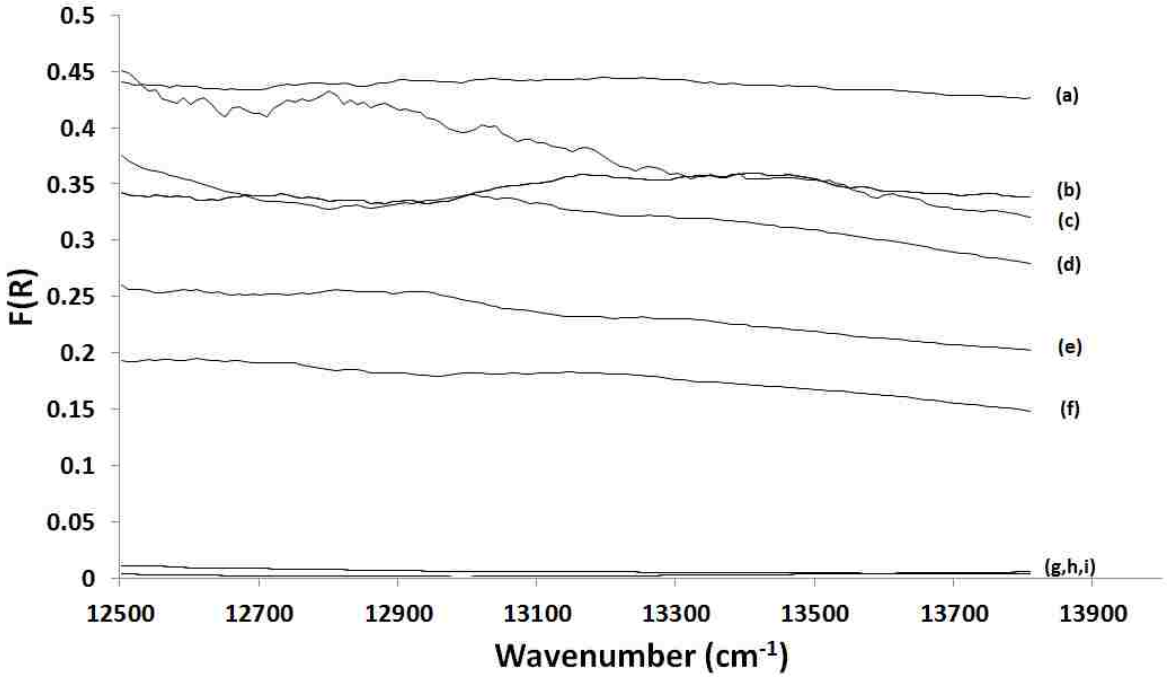

Figure 4.12: Kubelka-Munk scans for the: (a) 0.5La catalyst post TPR 1, (b) 0La catalyst post TPR 1, (c) 1La catalyst post TPR 1, (d) 0.5La catalyst post TPR 2, (e) 1La catalyst post TPR 2, (f) 0La catalyst post TPR 2, (g) 0La catalyst post TPO 1, (h) 0.5 La catalyst post TPO 1, and (i) 1La catalyst post TPO 1. The K-M values are higher for the more reduced samples and nearly zero for the fully oxidized samples.

These spectra are interpreted as follows. Figure 4.11 shows the temperature dependence of the spectra, with a lower absorbance signal at room temperature than that at 450°C. In order to avoid temperature effects on the absorbance signal, all K-M and baseline scans were acquired at room temperature for analysis. Furthermore, according to Figure 4.11, there is an absorption band centered around 17,500 cm^{-1}, or 2.2 eV, for the oxidized catalyst, which apparently is due to the band gap in Fe_2O_3 [63,120-122].

Since the K-M function is proportional to absorbance, the K-M value for each catalyst post TPR 1 is higher than those post TPR 2, which correlates to the differences in the extent of reduction from Fe_2O_3 to metallic Fe, as shown in Figure 4.12, and which is in agreement with the TPR results presented in Section 4.2.1. Furthermore, the 0La catalyst post TPR 2 has the lowest K-M value, which corresponds to the least extent of reduction. The K-M value post TPO 1 for the 0La catalyst is essentially zero near 12,500 cm^{-1}, confirming that the catalyst returned to the

fully oxidized state that was used as the reference in the K-M function. Absorbance is highest, which produces the largest K-M value for each specific spectrum, at 12,500 cm^{-1}, or 1.5 eV, because the reduced catalysts (primarily Fe or Fe_3O_4, which have no band gaps) absorb more light at this energy relative to the reference of the fully oxidized catalyst (primarily hematite). Figure 4.13 shows the K-M scans for the 0La catalyst over a wider range of wavenumbers to display other absorption bands at specific wavelengths. According to the spectra in Figure 4.13, the absorption bands are centered around 17,500 cm^{-1} and 21,000 cm^{-1} for the oxidized 0La sample. The first absorption band at 17,500 cm^{-1}, or 2.2 eV, is due to the band gap in Fe_2O_3 [63,120-122], while the second absorption band at 21,000 cm^{-1}, or 2.6 eV, is due to the Fe(3d) → Fe(3d) transition in hematite: $^6A_{1g} + {}^6A_{1g} \rightarrow {}^4T_{1g} + {}^4T_{1g}$ pair excitation [11,63,122]. For the 0La reduced samples, no absorption bands are identified for FeO, which is consistent with the absence of FeO in the XRD spectra (see Figure 4.6). The absorption bands near 22,500 cm^{-1}, or 2.8 eV, most probably correspond to the $^4A_{2g} \rightarrow {}^4T_{1g}$ transition of (pseudo-) octahedral Cr^{3+} [9].

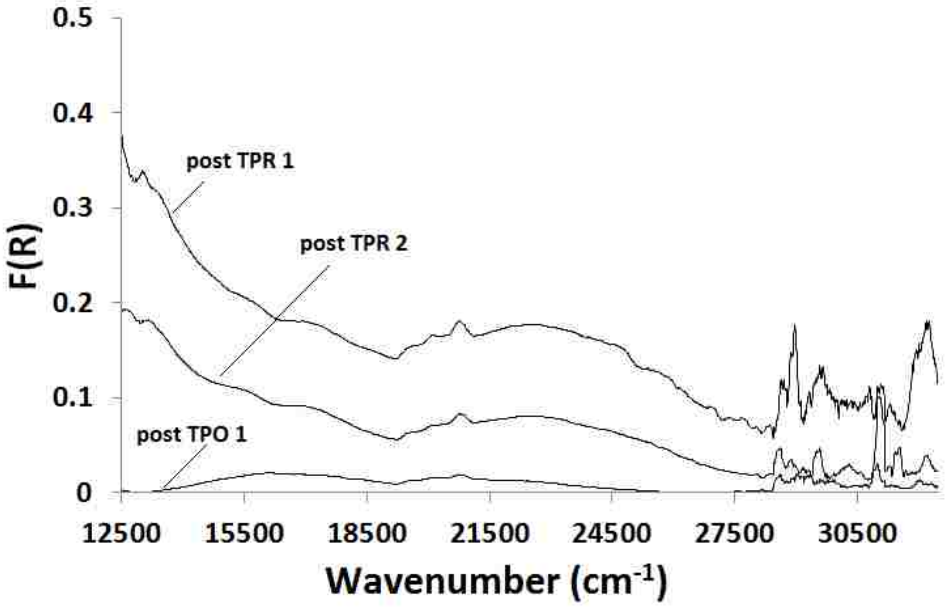

Figure 4.13: K-M scans for the 0La catalyst post TPR 1, TPO 1, and TPR 2. The values of the Kubelka-Munk function (F(R)) are higher for the more reduced samples and zero for the fully oxidized sample at 12,500 cm^{-1}.

In order to interpret these K-M values in terms of catalysis, a linearly regressed calibration line was generated (see Figure 4.14) to correlate K-M function (independent variable) and Fe oxidation state (dependent variable) on the surfaces of each of the three catalysts.

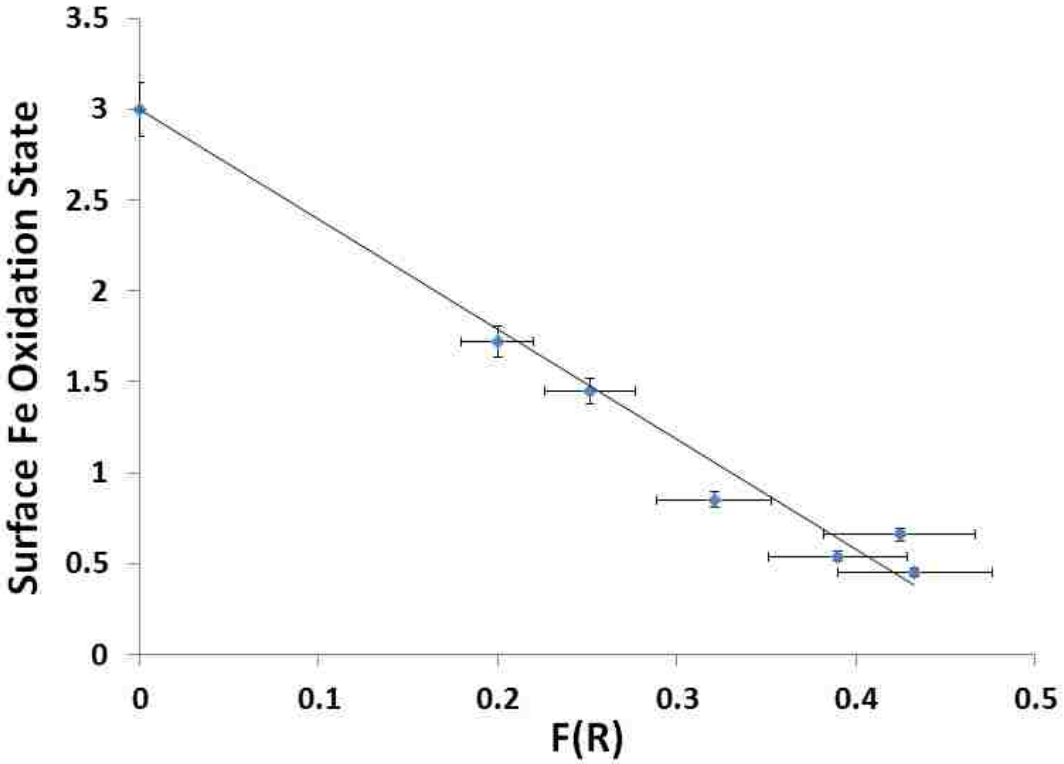

Figure 4.14: Calibration curve of surface Fe oxidation state as a function of Kubelka-Munk values with 10% error bars at 12,500 cm-1 and using TPR 1 and TPR 2 K-M values for the 0La, 0.5La, and 1La catalysts.

The slope and intercept of the calibration line with 95% confidence intervals are given in Table 4.3, along with the coefficient of determination (r^2) value to evaluate the quality of the data fit. The intercept is 3.0, which corresponds to the oxidation state of hematite (the fully oxidized phase of the samples, with a corresponding K-M value of zero due to the fully oxidized catalyst reference). The results show that the UV-vis technique is sensitive to and can be directly calibrated with extent of catalyst reduction with respect to iron.

Table 4.3: Slope, intercept, and coefficient of determination for the oxidation states vs. K-M calibration curve.

Slope	Intercept	r^2
-6.05 ± 0.39	3.00 ± 0.13	0.977

4.2.3.3 Water-Gas Shift Reaction: In-Situ and Ex-Situ Analyses

In-situ analysis on the 1La catalyst under varying times of HT WGS shift reaction is shown in Figure 4.15, with the scans performed at the reaction temperature of 400°C instead of room temperature.

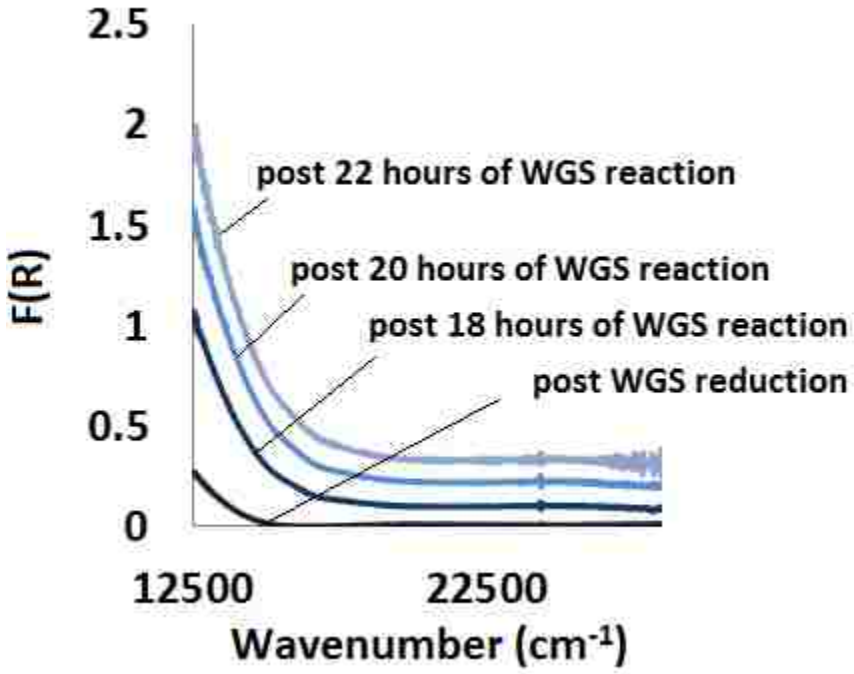

Figure 4.15: *In-situ* Kubelka-Munk spectra for the 1La catalyst under WGS reaction. The Kubelka-Munk values are higher than the values obtained during TPR experiments [123].

The K-M values are much higher (80% more) than those post TPR 1, even after accounting for the temperature effect on the absorbance signal. The K-M values significantly increase with time as the WGS reaction proceeds. Prior kinetic results of this work and others with these and similar catalysts indicate that they do not approach a steady state activity for about 100 h [124].

Thus, this evolution during the initial 24 h is likely associated with sintering processes that are observed as decreasing rate during this initial time.

Ex-situ analysis, presented in Figure 4.16, was performed at room temperature on the 0La and 1La catalysts after 10 days under high-temperature WGS reaction and show similar results: the normalized absorbance values are higher than those for TPR 1 and TPR 2 of either catalyst.

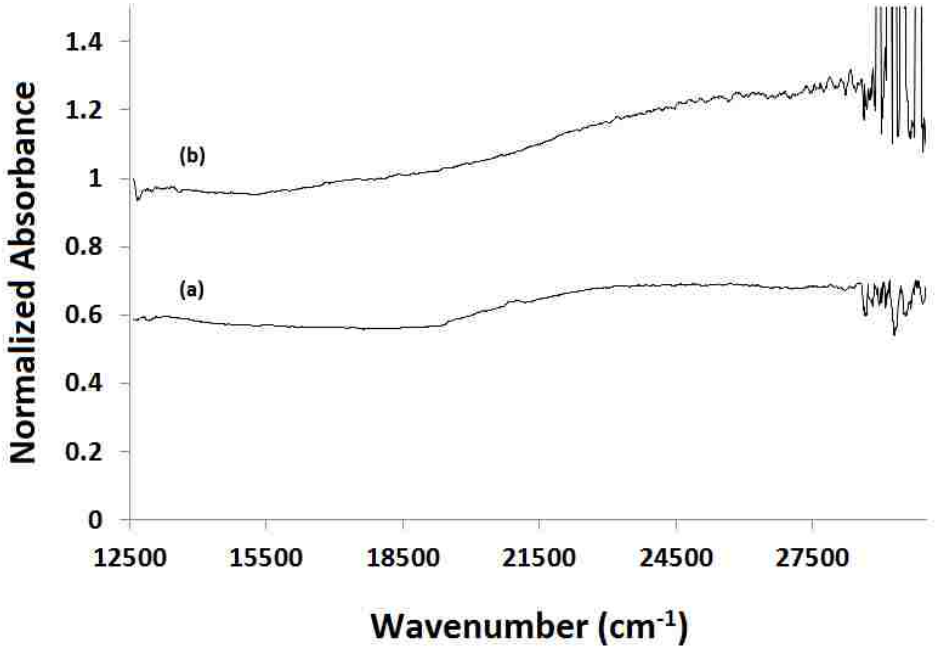

Figure 4.16: *Ex-situ* analysis after 240 h of WGS reaction. The spectra shown are normalized absorbance for (a) used 0La catalyst and (b) used 1La catalyst.

Although carbon deposition on the catalyst surface is a potential explanation for the increasing absorbance signal as a function of the WGS reaction time, this possibility has been discounted. No CO or CO_2 signals were detected during a TPO of the used catalysts in flowing air and no iron carbide phase was observed in the XRD and EDS results. Therefore, catalyst carbiding or formation of surface carbon species (e.g., graphite or coke) does not appear to occur. The apparent explanation is that there are morphological changes to the catalysts once steam is introduced in the feed. This was manifested by a physical change to the catalysts, which appear

to expand and fracture when exposed to water during WGS conditions. Since the K-M function is an absorbance to scattering ratio, morphological changes likely change the ratio of the absorbed and scattered (or diffusely reflected) light off the surface of the catalyst, which accounts for the increase in the K-M values. SEM analysis, shown in Figure 4.17, demonstrates the change in the particle size distribution after WGS treatment, suggesting that introduction of water physically alters the shapes of the particles of the catalysts. In contrast, the particle size distribution after TPR treatments remains almost the same.

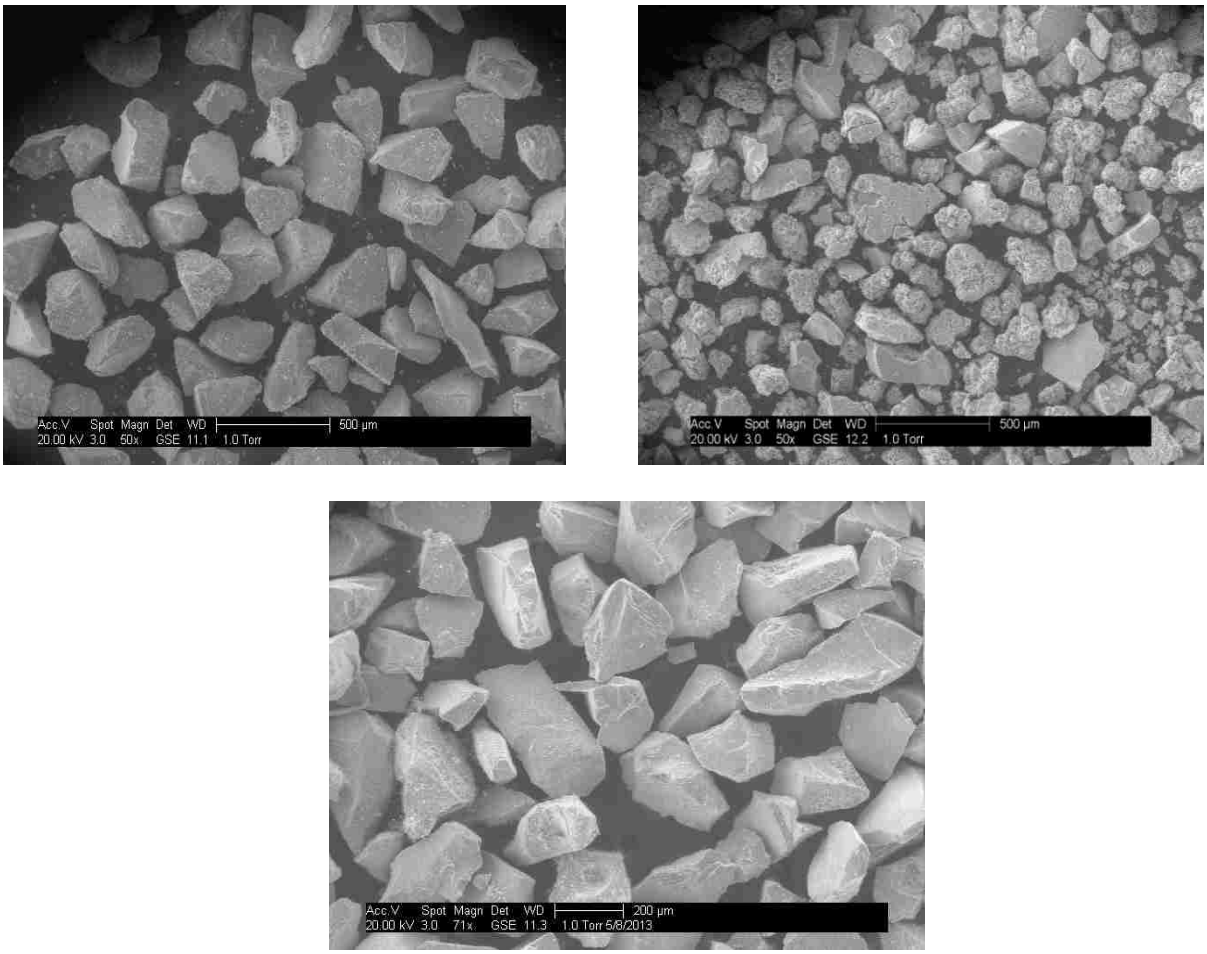

Figure 4.17: SEM images of calcined fresh 0La catalyst (top left), used 0La catalyst after WGS treatment (top right), and used 0La catalyst after TPR 1 treatment (bottom). The images show a change in particle size distribution after the catalyst was treated under HT WGS reaction conditions but not a significant change with TPR treatment.

Although the direct correlation between reduced centers and absorbance was not possible due to the morphological changes to the catalyst, the use of UV-vis spectroscopy to quantify extent of reduction should be broadly applicable to other, more physically stable catalysts. These studies will be presented in a future work.

However, in order to use of the calibration curve in Figure 4.14 and to apply it to quantify the reduced centers of the catalysts post WGS treatment, the ratio of normalized absorbance (which is the ratio of the K-M values excluding the scattering term) for both catalysts after WGS reaction has been compared with the slope of the calibration curve. This ratio of absorbance between two catalysts is an attempt to cancel out the surface disturbance to the signal cause by the smaller particle size distribution. This analysis presumes that the same morphological changes are occurring for all of the catalysts during the WGS reaction, which appears to be the case based on analysis of the SEM images. Taking the ratio of the normalized absorbances yields,

$$(3 - y_1)/(3 - y_0) = x_1/x_0 \quad (4.3)$$

where $y_0$and y_1 are the oxidation states of Fe in the 0La and 1La catalysts, respectively, and x_0 and x_1 are the K-M values for the 0La and 1La catalysts (which are equal to normalized absorbance values for which these calibration lines were derived), respectively. The ratio of the normalized absorbance at 12,500 cm^{-1}, x_1/x_0, post WGS treatment gives a value of 1.6 ± 0.16. Figure 4.18 correlates the ratio on the left-hand side of Equation 4.3 to different ratios of normalized absorbance within the 95% confidence of the fitted slopes for both catalysts.

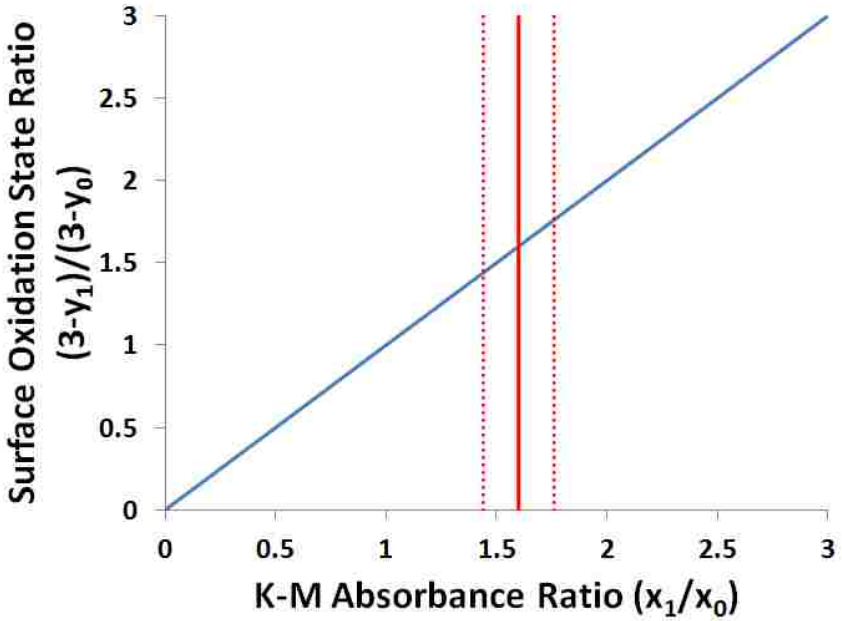

Figure 4.18: The ratio of surface Fe oxidation states in 1La to the oxidation state in 0La as a function of the ratio of the normalized absorbance. The figure shows the 95% upper and lower bounds of the regression.

Although these results do not give full quantification for the oxidation state of Fe on the surface during the WGS reaction, they correlate the oxidation state of Fe on the surface of the 1La catalyst to that on the surface of the 0La catalyst. If the value for the oxidation state of Fe in 0La is +2.57 (obtained from XANES spectra, shown in the next section), then the predicted value for the oxidation state of Fe in 1La is +2.31 ± 0.07.

These findings are consistent with the activity pattern reported in Section 3.2.5. The 0.5La catalyst had the highest WGS activity, which in this study also displayed higher extent of reduction from Fe_2O_3 to Fe_3O_4 than the 0La catalyst and a lower extent of reduction from Fe_2O_3 to Fe than the 1La, 2La, and 5La catalysts, presumably because its spinel structure was better maintained and stabilized. This suggests that addition of 0.5 wt% of lanthana maximizes the content of the active magnetite phase under reaction conditions.

4.2.3.4 X-Ray Absorption Near-Edge Structure (XANES) Spectra Compared to UV-Visible Spectra

The XANES spectra of the 0La and 1La samples after WGS reaction, along with those of reference compounds, iron (II, III) oxides and metallic iron, are shown in the Figure 4.19. Inspection of the spectral features, in particular, the position of the pre-edge feature and the position of the main edge suggest that oxidation state of iron in the samples is close to that of magnetite (+2.66), which is consistent with previous reports on iron oxide catalysts during the WSG reaction [125].

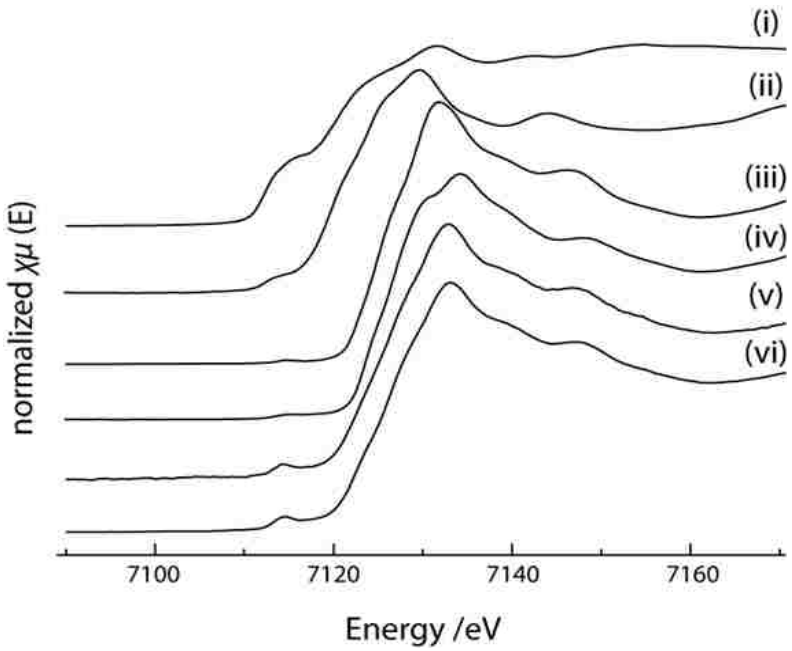

Figure 4.19: XANES region of the XAS spectra for (i) metal Fe foil; (ii) ferrous oxide, FeO; (iii) magnetite, Fe3O4; (iv) hematite, Fe2O3; (v) 0La sample after WGS reaction; (vi) 1La sample after WGS reaction. The pre-edge energies for both samples are close to the energy of magnetite.

An attempt to fit the XANES spectra of the samples as linear combination of reference spectra was unsuccessful, which is not uncommon for non-stoichiometric iron oxides. Hence, to establish the oxidation state of iron in the samples, the approach of Wilke [126] has been applied. In this method, the position of the pre-edge features are determined for the reference compounds

and plotted as a function of a formal oxidation state (or oxidation state measured independently, e.g., by Mössbauer spectroscopy, as proposed by Wilke *et al.*[126]) and fitting is used to obtain the oxidation state for the unknown material. Figure 4.20 shows the position of the pre-edge peaks for all materials plotted as a function of Fe^{3+}/Fe total. This ratio is zero when the all iron is Fe^{2+} and 1 when the all iron is Fe^{3+}. Any number between zero and 1 is a combination of the +2 and +3 oxidation states. From the interpolation of this data, the Fe oxidation in the used 0La sample is +2.57, while that in 1La is +2.54.

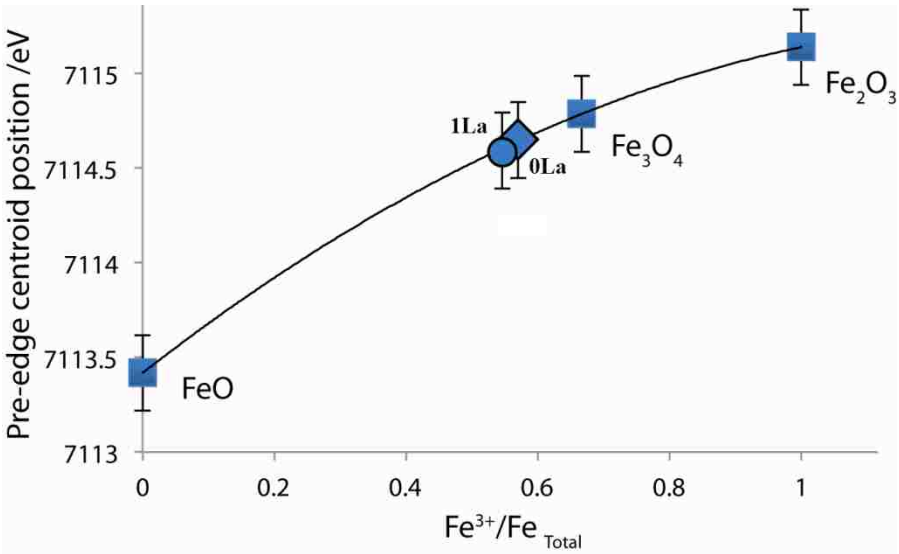

Figure 4.20: Interpolation of Fe oxidation state in 0La and 1La samples as a combination of Fe^{3+} and Fe^{2+}, which is predicted to be around +2.57.

Results obtained from the XANES spectra show that the used 1La sample is slightly more reduced than the used 0La sample, which is consistent with the UV-vis analysis. However, the UV-vis results suggest a greater difference between the oxidation states of Fe near the surface, which is not unexpected, considering that XANES detects bulk properties, while UV-vis spectroscopy is sensitive to properties near the surface. Cations near the surface tend to be more reduced (lower oxidation state) than those in the bulk of partially reduced metal oxide catalysts

[127], especially during the WGS surface reaction. Therefore, although the XANES analysis indicated that the bulk oxidation state of Fe is nearly the same in both samples, they are likely slightly different near the surface, as suggested by the UV-visible results. As shown in the previous section, if the oxidation state of Fe near the surface is +2.57 for the 0La sample, then the results from the UV-vis spectra calibration suggest an oxidation state between +2.24 and +2.38 for the 1La sample, with a most probable value of +2.31. From these results, UV-vis spectroscopy is proposed as a more precise technique for characterizing extent of reduction of catalytically active phases near the surface, which are relevant to surface kinetics.

4.3 Summary of Extent of Reduction Study Using UV-Visible Spectroscopy

A thorough study on the extent of reduction of iron-based high-temperature water-gas shift catalysts using different characterization techniques has been presented in this chapter. Temperature-programmed reduction studies using mass spectrometry have shown that 0.5 wt% addition of lanthana as a promoter to iron-chromium-copper oxide water-gas shift catalysts enhances the reducibility of the catalysts in terms of both total hydrogen consumption and reduction temperature. However, further additions of lanthana cause the catalysts to reduce at higher temperatures and to consume more hydrogen (i.e. over-reduce), possibly due to the disruption of the catalytically active Fe_3O_4 spinel structures by incorporation of the larger La^{3+} ions. A second temperature-programmed reduction was performed on each catalyst after they were fully reoxidized to examine the re-reducibility of the catalysts. The catalyst with the 0.5 wt% lanthana appeared to be the most reducible with only an 8% decrease in extent of reduction, as opposed to a 35-45% decrease in total hydrogen consumption from the first reduction experiment for the other catalysts. Analysis *via* UV-vis spectrometry showed that the

absorbance of light at 800 nm is very sensitive during the reduction processes of these catalysts due to alterations in the band gaps of the different iron oxide phases and could be calibrated to extent of reduction as determined during concomitant TPR. *Ex-situ* UV-visible analysis of the used catalysts also showed similar trends with the Kubelka-Munk values. The ratio of normalized absorbance correlated to the ratio of Fe oxidation states acquired from the calibration curve for the used catalysts with 0 wt% and 1 wt% lanthana showed that the extent of reduction for the latter catalyst was 1.1 times lower than for the former catalyst, suggesting that the catalyst with more lanthana reduced to a larger extent during water-gas shift treatment than the one with no lanthana, resulting in lower content of the active Fe_3O_4 phase due to over-reduction. XANES spectra showed only a slightly higher extent of reduction for 1La than for 0La (+2.54 average oxidation state for 1La compared to +2.57 for 0La), suggesting that UV-vis spectroscopy is a more sensitive tool appropriate for analyzing the extent of reduction of near-surface species relevant to catalysis.

CHAPTER 5. An Optimized Simulation Model for Iron-Based Fischer-Tropsch Catalyst Design: Mass and Heat Transfer Limitations as Functions of Operating and Design Conditions

From the previous two chapters, it is established that lanthana affects the activity and stability of iron-based WGS catalysts. These findings motivated a study on the lanthana effect on the activity, selectivity, and stability of similar iron-based FT catalysts. Before starting these studies for which the results are presented in the next chapter, it was crucial to understand and design optimal operating and design conditions for such a reaction that runs at high reaction pressures and moderate reaction temperatures and involves a wide array of gaseous, liquid, and solid products.

This chapter describes a simulation model that evaluates the performance of iron-based FTS catalysts in terms of effectiveness factor under different lab-scale operating and design conditions in a fixed-bed reactor. Although the catalyst design principles which the results of this work confirm are well established, the results are significant because the design principles are typically applied at a specific design condition, which represents a single point in the possible parameter space, instead of optimizing over a range of possible designs. Further, the model shows excellent agreement with experimental results and presents comprehensive contour maps of pressure drop and mass and heat transfer limitations as functions of critical design and operating variables that make the interdependencies easier to visualize for the entire parameter space. Therefore, the predictions of the model presented in this chapter 1) give guidance to the experimental design and operating conditions for the work presented in the next chapter and 2)

explore the limitations of the catalytic activity due to pore-diffusion and heat transfer resistances without running multiple experiments to test the effect of each design variable. Minimizing pore diffusion and heat transfer limitations by changing a set of design variables and conditions is crucial in driving a kinetically-limited reaction rate. The pressure drop down a catalyst bed is also considered because it is crucial for chemical reactions that require operation under high pressure, as the FTS reaction does. The particle size and therefore void fraction affect the pressure drop. Therefore, pressure drop must be evaluated and constrained while the model solves for the optimal particle size.

The equations and parameters in this model have been used to most accurately represent the catalysts and conditions reported in Brunner's dissertation [86]. The model can be modified for the desired reaction conditions. The results of the work presented in this chapter have been published in a peer-reviewed journal [128].

5.1 Theory: Model Equations and Derivations

This section discusses the model equations and parameters that describe the pore diffusion limitation, heat transfer limitations, the pressure drop, and the algorithm that solves the optimization problem.

5.1.1 Pore Diffusion Limitation

The approach to determining mass transfer limitations in the catalyst bed starts with solving the following mass balance on a differential shell within a spherical catalyst particle for a first order reaction as shown in Equation 5.1.

$$4\pi r^2 D_e \frac{dC_A}{dr}\Big]_{r+\Delta r} - 4\pi r^2 D_e \frac{dC_A}{dr}\Big]_{r} = -k_v C_A (\, 4\pi r^2 \Delta r) \qquad (5.1)$$

Equation 5.1 reduces to Equation 4 as the radius increment shrinks to zero $\left(\lim_{\Delta r \to 0}\right)$.

$$\frac{D_e}{r^2}\frac{d}{dr}\left(r^2\frac{dC_A}{dr}\right) = -k_v C_A \tag{5.2}$$

The boundary conditions for the solution of Equation 5.2 are $C_A = C_{As}$ at $r = R_p$ and $\frac{dC_A}{dr} = 0$ at $r = 0$ (neglecting film mass transfer). In these equations, C_A denotes the concentration of species *A*, C_{As} is the surface concentration of species *A,* k_v is the rate constant per unit volume, r is the radial distance from the center of the pellet, R_p is the radius of the pellet, and D_e is the effective diffusivity given by:

$$D_e = D \cdot \varepsilon_p/\tau \tag{5.3a}$$

$$\varepsilon_p = \frac{V_{pore} \cdot \rho_b}{1-\varepsilon_b} \tag{5.3b}$$

where ε_p is the particle porosity. The void fraction, ε_b, is either measured experimentally or estimated using a correlation developed by Benyahia and O'Neill [129]. In addition, τ is the tortuosity, and D is the combined diffusivity of the bulk (D_{AB}) and Knudsen (D_K) diffusivities from the Bosanquet approximation [130, 131]:

$$\frac{1}{D} = \frac{1}{D_{AB}} + \frac{1}{D_K} \tag{5.4}$$

For this work, D_{AB} was calculated using correlations developed by Erkey *et al.* [132, 133] for wide temperature and pressure ranges:

$$D_{AB}\left(\frac{cm^2}{s}\right) = \frac{0.945\sqrt{T/_K}}{\left(M_A/_{g\cdot mol^{-1}}\right)^{0.239}\left(M_B/_{g\cdot mol^{-1}}\right)^{0.781}\left(\sigma_A\sigma_B/_{Ang}\right)^{1.134}}\left(\bar{V}/_{L\cdot mol^{-1}} - \bar{V}_0/_{L\cdot mol^{-1}}\right) \tag{5.5}$$

where M_A is the molecular weight of the solute in g/mol (either CO or H_2), M_B is the molecular weight of the solvent ($C_{20}H_{42}$) in g/mol, σ_A is the hard-sphere diameter for the solute (either CO or H_2) in Angstroms, σ_B is the hard-sphere diameter for the solvent ($C_{20}H_{42}$) in Angstroms, and $\bar{V}$ is the specific volume of the different species in L/mol. The diffusivity of CO in wax is typically

slower than that of H_2 and is therefore the limiting diffusional resistance. However, when the feed stream has low concentrations of H_2, then it is appropriate to use the diffusivity of H_2 in wax as the limiting diffusivity. Therefore, species *A* is typically CO (which is the limiting reactant involved in diffusion) unless the mole fraction of H_2 is low (e.g., less than 25 mol% H_2 in a 35 mol% CO/40 mol% He stream). Erkey's work [133] showed that the average molecular weight of FT wax can be approximated as n-alkane hydrocarbons. Therefore, the hydrocarbon species *B* is a surrogate for diffusion calculations, assumed to be icosane ($C_{20}H_{42}$), as a representative average species for Fe-based FTS catalysis [86].

D_K is calculated using the following correlation obtained from the kinetic theory for gases [134]:

$$D_K\left(\frac{cm^2}{s}\right) = 4850 \cdot \frac{d_{pore}}{cm} \cdot \sqrt{\frac{T/K}{M_A/g \cdot mol^{-1}}} \tag{5.6}$$

where d_{pore} is the pore diameter in cm and T is the absolute temperature of the particle in Kelvin. D_K for the conditions of this study is two orders of magnitude larger than D_{AB} and is therefore a negligible diffusion resistance.

The solution of Equation 5.2 for spherical particles is:

$$\frac{C_A}{C_{As}} = \frac{R_p}{r}\frac{\sinh 3\phi r/R_p}{\sinh(3\phi)} \tag{5.7}$$

where sinh is the hyperbolic sine function and ϕ is the Thiele modulus [135], defined as:

$$\phi = L_p\sqrt{k_v/D_e} \tag{5.8}$$

The shape factor, L_p, is introduced to modify the solution as appropriate for geometries different than slabs, with $L_p = R_p/2$ for cylindrical and $L_p = R_p/3$ for spherical pellets.

The Thiele modulus is modified for n^{th} order reaction kinetics as shown in Equation 5.9 [136-139]:

$$\phi = L_p \sqrt{(n+1)\, k_v\, {C_{As}}^{n-1} \Big/ 2D_e} \tag{5.9}$$

The order of reaction used in the model is 0.55, based on previous work by Eliason for the FTS reaction on Fe-based catalyst [97].

The effectiveness factor, η, of the catalyst is defined as the ratio of the rate of reaction with diffusion effects (i.e. the observed rate) to that without diffusion (i.e. the intrinsic rate) and is a function of ϕ according to Equations 5.10 and 5.11 for the spherical ($d_p < 200\ \mu m$) and cylindrical ($d_p > 200\ \mu m$) geometries, respectively [136, 140]:

$$\eta_{sph} = \frac{3}{\phi}\left[\frac{1}{\tanh\phi} - \frac{1}{\phi}\right] \tag{5.10}$$

$$\eta_{cyl} = \frac{2I_1(\phi)}{\phi \cdot I_0(\phi)} \tag{5.11}$$

where I_0 and I_1 are Bessel functions of the first and second kind, respectively. Equations 5.10 and 5.11 are derived for first-order kinetics, but give close approximations to the actual effectiveness factor based on the Thiele modulus that is adjusted for nth-order kinetics as shown in Equation 5.9. The diameter breakpoint is arbitrary, but is based on literature references to account for the typically observed decreasing sphericity of the catalyst particles as their size increases [141].

The intrinsic rate constant, k_v, is generally unknown *a priori* and is therefore not useful for developing a model. Consequently, the Wagner-Weisz-Wheeler modulus, M_w, is used instead of ϕ to solve for the effectiveness factor because M_w is a function of the observed experimental rate, as shown in Equation 5.12 [140]:

$$M_w = \frac{{L_p}^2}{D_e}\frac{r_A \rho_p}{C_{As}}\frac{n+1}{2} = \phi^2 \cdot \eta \tag{5.12}$$

where ρ_p is the particle density (ε_p / V_{pore}), and r_A is the observed rate of reaction of species *A,* which is the rate of depletion of CO for the FTS reaction per unit mass of catalyst. The CO conversion, X_{CO}, and rate of CO depletion are calculated using the rate equation for a differential reactor modified for average partial pressures and a kinetic model developed by Eliason for FTS reaction on Fe-based catalysts [97], as shown in Equations 5.13 and 5.14:

$$X_{CO} = \frac{W_{cat}(-r_{CO})}{{F^0}_{CO}} \tag{5.13}$$

$$-r_{CO} = A \cdot \exp\left(\frac{-E_a}{R_g \cdot T}\right) \cdot {P_{CO}}^{-0.05} \cdot {P_{H_2}}^{0.6} \tag{5.14}$$

where W_{cat} is the mass of the catalyst bed, ${F^0}_{CO}$ is the inlet molar flow rate of CO, A is the Arrhenius pre-exponential factor, E_a is the activation energy over Fe-based catalyst, R_g is the universal gas constant, and P_{CO} and P_{H_2} are the average partial pressures for CO and H_2 in atm, respectively. The differential rate model depends on average partial pressures of reactant and is therefore appropriate to use with CO conversions reaching 25%. Further details and comparison with plug-flow reactor model are available in Appendix B. The concentration of surface CO (C_{CO_s}) and density of the bulk gas stream (ρ_g) were found using the Peng-Robinson equation of state at the reactor pressure and at the surface temperature of the catalyst (T_s) and the temperature of the bulk gas stream (T_g), respectively.

5.1.2 Heat Transfer Limitation

The energy balance in spherical coordinates around a catalyst particle is written as:

$$\frac{\lambda_e}{r^2}\frac{d}{dr}\left(r^2 \frac{dT}{dr}\right) = -r_{CO} \cdot \rho_p \cdot \Delta H_r \tag{5.15}$$

for which the boundary conditions are:

$$\left(\lambda_e \frac{dT}{dr}\right) = h \cdot \Delta T_{film} \quad \text{at} \quad r = R_p \quad \text{and} \quad \frac{dT}{dr} = 0 \quad \text{at} \quad r = 0 \tag{5.16}$$

Here, ΔH_r is the enthalpy of reaction generated by the FTS reaction, h is the convective heat transfer constant, ΔT_{film} is $(T_s - T_g)$, and λ_e is the effective thermal conductivity of the packed-bed of catalyst filled with gas and liquid found using a correlation developed by Matsuura *et al.* [142] as shown in Equation 5.17:

$$\lambda_e = 1.5\lambda_l \tag{5.17}$$

where λ_l is the liquid thermal conductivity (of $C_{20}H_{42}$ for this case). The thermal conductivity of the gas mixture within the void space is assumed to be negligible.

Solving for the first boundary condition in Equation 5.16 by using Equation 5.15 yields:

$$\Delta T_{film} = (-\Delta H_r) \cdot -r_{CO} \cdot \rho_p \cdot L_p / h \tag{5.18}$$

where again, $L_p = R_p/3$ for the spherical pellet.

The convective heat transfer coefficient, (h), was calculated using the following empirical formulae for packed-bed flows [143]:

$$h = j_H \cdot c_p \cdot \rho_g \cdot \left(\frac{\dot{V}_g}{A_{reac}}\right) \cdot (Pr)^{-2/3} \tag{5.19}$$

$$j_H = 2.19\, Re^{-2/3} + 0.78\, Re^{-0.381} \tag{5.20}$$

where j_H is the Chilton-Colburn factor, Re is the dimensionless Reynolds number for the gas, Pr is the dimensionless Prandtl number, ρ_g is the density of the bulk gas stream, c_p is the constant-pressure heat capacity of the bulk gas stream, $\dot{V}_g$ is the outlet volumetric flow rate of the bulk gas stream at the reaction T and P, and A_{reac} is the cross-sectional area of the reactor. The gas-phase viscosities were calculated using the DIPPR 801 database.

A simplified equation to find the temperature gradient (β_{th}) within the particle was used to determine the internal heat transfer limitation, as follows [136]:

$$\beta_{th} = \frac{(-\Delta H_r)\cdot C_{As}\cdot D_e}{T_s\cdot \lambda_e} = \frac{\Delta T_p}{T_s} \tag{5.21}$$

$$T_s = \Delta T_{film} + T_g \tag{5.22}$$

where ΔT_p is the temperature difference between the center and the surface of the particle.

5.1.3 Pressure Drop Model

The Ergun model for packed-beds (Equations 5.23 – 5.27) was used to predict the pressure drop down the catalyst bed $\left(\frac{\Delta P}{L_{bed}}\right)$ as reported by Froment and Bischoff and others [86,144-146], assuming constant pressure drop and using a friction factor correlation that is adjusted for turbulent flow that is valid over a wide range of Reynolds number ($0.1 < Re < 100{,}000$):

$$\frac{\Delta P}{L_{bed}} = \frac{\delta_{GW}}{\left(1-\frac{\varepsilon_{l,dyn}}{\varepsilon_b}\right)^3} - \rho_g g \tag{5.23}$$

$$\delta_{GW} = \frac{1-\varepsilon_w}{{\varepsilon_w}^3}\frac{\rho_g {u_g}^2}{d_{pe}} f \tag{5.24}$$

$$f = 4.2\left(\frac{1-\varepsilon_b}{Re}\right)^{1/6} + \frac{150(1-\varepsilon_b)}{Re} \tag{5.25}$$

$$\varepsilon_w = \varepsilon_b - \varepsilon_{l,stat} \tag{5.26}$$

$$\varepsilon_{l,dyn} = \left(\frac{\mu_l u_l}{{d_p}^2 g \rho_l}\right)^{1/3} \tag{5.27}$$

where δ_{GW} is the pressure drop per unit length for the gas flowing through a packed bed; $u_g$is the superficial velocity for the feed gas; f is the friction factor; g is the gravitational acceleration; $\varepsilon_{l,stat}$ is the static liquid holdup; $\varepsilon_{l,dyn}$is the dynamic liquid holdup; ε_w is the void fraction

adjusted for the static liquid hold up; μ_l is the liquid viscosity for icosane, calculated from the DIPPR 801 database; ρ_l is the liquid density for icosane, also calculated from the DIPPR 801 database; and d_{pe} is the effective pellet diameter which is the diameter of a spherical particle having the same volume as the actual particle. Details on d_{pe} and different geometries can be found elsewhere [86,140] and is calculated according to the following equation where Asp is the aspect ratio used for cylindrical particles:

$$d_{pe} = d_p(1.5\ Asp)^{1/3} \tag{5.28}$$

The length of the catalyst bed (L_{bed}) was found using the masses and the densities of the catalyst and silicon carbide (which was used as a diluent) according to Equation 5.29:

$$L_{bed} = (W_{cat}/\rho_b + W_{SiC}/\rho_{SiC})/A_{reac} \tag{5.29}$$

5.1.4 Deactivation

A model for deactivation developed by Eliason and Bartholomew [147] for unsupported Fe-based FTS catalysts promoted with potassium was used to predict catalytic deactivation at 250°C – 280°C and 10 atm – 20 atm, as shown in Equations 5.30-5.31:

$$a = (1 - a_\infty)e^{-k_d t} + a_\infty \tag{5.30}$$

$$k_d = A_d \cdot e^{-E_d/(R_g\,T)} \tag{5.31}$$

where a is the activity, a_∞ is the activity at infinite reaction time determined from the asymptotic approach of experimental data, k_d is the deactivation rate constant, E_d is the activation energy for deactivation, A_d is the pre-exponential factor for deactivation, and t is the reaction time. The deactivation model reported in Eliason's study uses a generalized power-law rate model for determining the deactivation rate (r_d), as shown in Equation 5.32, with no partial

pressure dependence on CO and H_2 because the effect of partial pressures on deactivation was observed to be insignificant when compared to the effects of temperature and time.

$$r_d = k_d\,(a - a_\infty) \tag{5.32}$$

5.1.5 Modeling: Optimization and Simulation

The nonlinear simulation model is optimized to achieve the best combination of decision variables (d_p, T, P, y_{CO}) that maximize the productivity of the catalyst ($\eta \cdot -r_{CO}$), as shown in the following standard form for nonlinear optimization problem.

$$\underset{d_p,\,T,\,P,\,y_{CO}}{\text{Maximize}} \quad \eta \cdot -r_{CO} \tag{5.33}$$

Subject to

Equality Constraints

Equations 5.3 – 5.6

Equations 5.9 – 5.33

Inequality Constraints

$$\beta \leq 10\% \tag{5.34}$$
$$\Delta T_{film} \leq 5°C \tag{5.35}$$
$$R \geq 0.66 \tag{5.36}$$
$$X_{CO} \geq 0.01 \tag{5.37}$$
$$\Delta P/P \leq 20\% \tag{5.38}$$
$$a \geq 0.5 \tag{5.39}$$

The objective function, the productivity (which is calculated by multiplying the effectiveness factor (η) by the intrinsic rate ($-r_{CO}$)), is maximized subject to the equality constraints that comprise the model in Equations 5.3 – 5.6 and 5.9 – 5.33 and certain inequality constraints (Equations 5.34 – 5.39). By maximizing the productivity, η is maximized and therefore ϕ and M_w are minimized. Here, R is the H_2:CO ratio in inlet feed stream and $\Delta P/P$ is the pressure drop down the catalyst bed as a fraction of the reaction pressure. Table 5.1 summarizes the design and analysis variables and functions. The lower limit for the particle diameter is 80 μm,

which is a reasonable limit for practical purposes (to avoid plugging of the reactor). The ranges on T and P are typical for the FTS reaction. The range of y_{CO} is chosen to keep H_2:CO ratio between 0.5 and 2 considering 40 mol% He diluent in the feed gas that was used in the experimental validation. The range of H_2:CO ratio is reasonable for industrial purposes that do not use ratios higher than 2 [73]. All empirical correlations for the stream's properties (viscosities, densities, and concentrations) are valid only over these ranges and were calculated using Mathcad (version 15, Mathsoft, PTC) and Excel (2010, Microsoft) software. The limits for the optimizer constraints are chosen to:

1- satisfy the conditions for insignificant internal and film heat transfer limitations;
2- keep the composition of CO in the inlet gas stream low enough to avoid rapid deactivation of the catalyst by carbon deposition, with $R \geq 0.66$ being typical for Fe-based FTS catalysts;
3- maintain non-zero CO conversion;
4- avoid pressure drops larger than 20% of the inlet reactor pressure; and
5- keep the activity of the catalyst above 50% of its initial activity.

Table 5.1: Design table of the optimization problem for the lab-scale reactor.

Design Variables:	**Variable Constraints**:
Particle diameter, d_p	$d_p > 80\ \mu m$
Reaction temperature, T	$220°C \leq T \leq 280°C$
Reaction pressure, P	$15\ bar \leq P \leq 30\ bar$
Mole fraction of CO in the feed, y_{CO}	$0.2 \leq y_{CO} \leq 0.4$
Analysis Functions:	**Additional Constraints**:
Productivity, $\eta \cdot -r_{CO}$	Maximize $\eta \cdot -r_{CO}$
Internal heat transfer, β	$\beta \leq 0.1$
Film heat transfer, ΔT_{film}	$\Delta T_{film} \leq 5°C$
H_2:CO feed ratio, R	$R \geq 0.66$
CO conversion, X_{CO}	$X_{CO} \geq 0.05$
Pressure drop, ΔP	$\Delta P/P \leq 20$
Activity, a	$a \geq 0.5$

Table 5.2 shows a list of key input parameters. While the design variables are the quantities that can be adjusted by the optimizer, the parameters are values that are set by the user to best reflect the experimental conditions. The analysis functions are equality and inequality constraints that should be met when the design variables are changed. Fixed empirical selectivities were used as input parameters for calculating the product distribution. A selectivity model that is sensitive to reaction conditions will be added in future studies to predict product distributions, but it is outside the scope of this study.

The optimization problem was solved with APMonitor (version 0.6.3, APMonitor) - Matlab (version R2013a, Mathworks) interface [148] using the Interior-Point Optimizer (IPOPT). Details on the approach and algorithm of this method are discussed elsewhere [149-150], but briefly, IPOPT uses an interior point method to solve a series of barrier problems. With each barrier problem, the solver computes a search direction with exact first (Jacobian) and second (Hessian) derivatives. IPOPT also performs a line-search along the search direction with a filter method to determine a suitable step towards the solution. At the final solution, the Karush-Kuhn-Tucker (KKT) conditions are satisfied and the line-search (or step size) is accepted if the new iteration leads to enough progress to minimize the objective function and to satisfy the constraints according to the logical conditions of the filter method. This line-search filter method was originally proposed by Fletcher and Leyffer [151] and has been customized in this algorithm. The code is attached in Appendix E.

Table 5.2: List of key parameters used in the model for the lab-scale reactor.

Parameter	Value
A	$3.32 \cdot 10^7$ mol/(g·min·atm$^{0.55}$) [86]
E_a	93.8 kJ/mol [86]
A_d	23183 h^{-1} [147]
E_d	60 kJ/mol [147]
W_{cat}	0.25 g
W_{SiC}	1 g
t	1000 h
d_{pore}	15 nm [measured]
V_{pore}	0.06 mL/g [measured]
ρ_b	0.80 g/mL [measured]
ρ_{SiC}	1.57 g/mL [measured]
$\varepsilon_{l,stat}$	0.035 [86]
τ	3.5
n	0.55 [97]
Asp	3
A_{reac}	0.72 cm^2
$\dot{V}_{in}$	150 sccm
ΔH_r	-165 kJ/(mol·K) [calculated, constant]
Selectivity of CH_4	0.04
Selectivity of C_2-C_4	0.1
Selectivity of CO_2	0.4
Selectivity of C_{5+}	0.46

5.1.6 Limitations of the Model

The limitations of this model are: (1) The use of nth-order Thiele modulus for calculating the effectiveness factor from an expression for first-order reaction kinetics. A more generalized expression for effectiveness factor with non-fixed reaction order needs to be used for more accurate predictions. (2) The use of correlations in the model that are valid over the temperature and pressure range specified in the model albeit the specified ranges are reasonable for FTS over iron-based catalysts. (3) The use of the Wheeler single pore model which uses fixed tortuosity

and pore volume values to determine effective diffusivity. (4) The use of constant selectivity values for FTS products. A selectivity model that predicts water-gas shift and hydrocarbon selectivities with varying reaction temperature, pressure, and feed CO composition for the tested catalysts needs to be included for more reasonable optimal solutions that maximize the productivity of the catalysts and the yield of desired products. (5) The assumption that partial pressures of CO and H_2 do not affect the deactivation rate significantly. A deactivation study on the tested catalysts needs to be performed for more accurate predictions of catalytic deactivation. (6) The assumption of constant pressure drop down the catalyst bed. The momentum differential equation for pressure drop should be solved numerically down the catalyst bed for the commercial-size reactor.

5.2 Experimental Procedure

The model uses correlations and catalytic properties that apply to unsupported iron-based FTS catalysts and was therefore used to predict the activity of those catalysts tested under the same design and operation conditions to validate the model. The experimental work was conducted by Professor William C. Hecker's catalysis research group at BYU and not by the author.

5.2.1 Catalyst Preparation

Precipitation of copper and iron was performed via the solvent deficient precipitation (SDP) method [86 – 90]. $Fe(NO_3)_3 \cdot 9H_2O$, $Cu(NO_3)_2 \cdot 2.5H_2O$, and SiO_2 (Cab-O-Sil) were added together and mixed well. Potassium bicarbonate ($KHCO_3$) and ammonium bicarbonate (NH_4HCO_3) were then added to the metal nitrate and silica mixture and vigorously stirred,

releasing not only the waters of hydration, but also CO_2. Stirring continued until precipitation of Fe and Cu hydroxides was complete, as indicated by cessation of the CO_2 bubbles. Reaction and mixing were complete within about 20 minutes. Then, the catalyst was dried for 16 - 48 h at 100°C, calcined at 300°C in flowing air for six h, and sieved to retain 250 - 600 μm and 125 - 200 μm particles. The catalyst was originally prepared by Dr. Hecker's group and further details of this preparation are described elsewhere [86]. Similar catalysts were prepared for this work, and the details will follow in Section 6.1.1.

5.2.2 Activity Measurements

FTS experiments were conducted in a fixed-bed reactor (stainless steel, 3/8 inch OD) described elsewhere [86]. Each sample (0.25 g) was diluted with 1 g silicon carbide to approach isothermal conditions in the catalytic zone.

Prior to FTS reaction, the samples were reduced *in situ* at 250°C in 10% H_2/He for 10 h followed by 100% H_2 for 6 h. After cooling to 180°C, the system was then pressurized to 20 bar in syngas (H2:CO = 1) to activate the catalysts at 250°C for 48 - 90 h using 40 mol% He as a diluent, bringing the total inlet flow rate to 75-100 mL/min.

After leaving the reactor, the exit gas and liquid effluent passed through a hot trap (90°C) and a cold trap (0°C) to respectively collect heavy hydrocarbons and liquid products. The effluent gaseous product was analyzed using an HP 6890 gas chromatograph equipped with a thermal conductivity detector and a 60/80 carboxene-1000 column. CO conversion and selectivities were determined with aid of an Ar internal standard. CO conversions were intended to be lower than 20% for the differential reactor approximation to be more accurate.

These experiments are described more thoroughly in Section 6.1.3.

5.3 Results and Discussion

This section reports the predictions of the model and compares them to experimental data acquired from the fixed-bed reactor.

5.3.1 Modeling

Table 5.3 reports the optimal values of the objective function, design variables, constraints, and intermediate functions obtained from the model. To maximize productivity, defined as the mass of product produced per mass of catalyst per time, the optimizer solved the problem with 99% effectiveness factor to prevent mass or heat transfer limitations. The solution was achieved with a reaction temperature of 255.8°C, maximum allowed reaction pressure (30 bar), and minimum y_{CO} (0.2). These operating conditions result in high reaction rates that maximize the productivity of the catalyst by: (1) increasing the rate constant with higher temperatures, (2) increasing the partial pressure of hydrogen with higher pressure, and (3) decreasing the partial pressure of CO with lower CO composition. The reaction temperature, however, is constrained by catalytic deactivation. The optimal reaction temperature (255.8°C) maximizes the reaction rate and keeps the activity of the catalyst above 50% of its initial activity after 1000 h, which is long enough for a to approach a_∞. The optimizer drove the value of d_p to the lower bound of its range (80 μm) suggesting that the pressure drop in Equation 5.35 is not a constraint. Smaller particle sizes are always preferred for decreased transport limitations but they also increase pressure drops down the catalyst bed; however, pressure drop is not a constraint under these operating conditions. ΔT_{film} is significantly higher than ΔT_p suggesting that external heat transfer is a more limiting resistance at these conditions.

Table 5.3: The optimal solution of the Fe-based FTS catalyst design for the lab-scale reactor.

Variable	Value for maximizing $\eta \cdot r_{CO}$
d_p (μm)	80
T (°C)	255.8
P (bar)	30
y_{CO}	0.20
M_w	0.06
ϕ	0.25
η	0.99
β	$1.0 \cdot 10^{-4}$
ΔT_{film} (°C)	0.017
R	2.0
ΔT_p (°C)	0.06
$\Delta P/P$	0.03%
a	0.5
X_{CO}	14%
$-r_{CO}$ (mol/kg·hr)	72.3
$\Delta P/L_{bed}$ (atm/m)	0.58
L_{bed} (cm)	1.33
h (W/m²·K)	3225
λ_e (W/m·K)	0.16
ε_b	0.35
D_K (cm²/s)	$3.1 \cdot 10^{-2}$
D_{AB} (cm²/s)	$2.3 \cdot 10^{-4}$
D_e (cm²/s)	$4.9 \cdot 10^{-6}$

Typical iron-based FTS operating conditions, however, favor lower reaction pressures (~20-25 atm) to reduce operating costs and higher CO compositions (1:1 H_2:CO) to produce desirable product distributions without producing excessive CO_2 from the water-gas shift reaction and because coal and biomass, which produce lower H_2:CO ratios during gasification, are often economic feedstocks. Furthermore, higher reaction temperatures and pressures expedite catalyst deactivation by forming hot spots within the bed with high reaction rates. Large H_2:CO ratios deactivate the catalysts by oxidation from higher production of water at high H_2

compositions and decrease the selectivity of C_{5+} in favor of methane resulting in lower productivity [3,152]. Future studies should add cost and selectivity models that are dependent on partial pressure of CO and H_2. The effect of this additional constraint would likely be to lower the reaction pressure to a level that will balance the economics of maximized productivity with the additional capital costs of larger vessels and decreased selectivity to the desired products.

Figure 5.1 shows contour plots for the effectiveness factor and the constraints as they vary with temperature and pressure at fixed d_p and y_{CO} (d_p increases from 250 μm to 600 μm to 1500 μm at a constant y_{CO} = 0.30 in plots A, B, and C, respectively, while d_p = 250 μm and y_{CO} increases to 0.36 in plot D). The black lines are the effectiveness factor contours. The green and red dashed lines are non-binding values of the external film heat transfer constraint and the internal particle heat transfer constraint, respectively. The effectiveness factor decreases with increasing temperature and decreasing pressure. The rate of CO depletion is faster at higher temperatures, causing M_w to increase. Lower pressures decrease the surface concentrations of CO, C_{CO_s}, which cause M_w to increase. Furthermore, film heat transfer is a much stronger limiting resistance than internal heat transfer resistance, as ΔT_{film} is a stronger function of temperature and pressure than ΔT_p. At particle sizes of 250 μm and 600 μm (contour plots A and B in Figure 5.1), however, both resistances are negligible and the rate of reaction is limited by pore diffusion resistance. The film heat transfer becomes a binding constraint ($\Delta T_{film} > 5°C$) at a particle size of 1.5 mm and $T > 260°C$. This is apparent in contour plot C in Figure 1 with the solid green line. Bigger particle sizes decrease the effectiveness factor and increase ΔT_{film} according to Equations 5.12 and 5.18. Therefore, smaller particle sizes are favored for a kinetically-limited reaction. In fact, the reaction rate is not significantly pore-diffusion limited

for particle sizes below 250 μm, where the effectiveness factor is greater than 90%. ΔT_p is affected by the particle size through the surface temperature of the catalyst, but is more strongly affected by y_{CO}, as can be observed in contour plot of Figure 1D, where ΔT_p is higher with the larger value of y_{CO}. This result is due to increased C_{CO_s}, which causes the particle temperature gradient, β_{th}, to increase (see Equation 5.21). Regarding catalytic deactivation, high reaction temperatures increase deactivation, as shown in contour plot E of Figure 5.1, where the solid purple line identifies an activity of 0.5. Increasing the temperature beyond 255.8°C reduces the catalytic activity below 50% of its initial activity. In fact, the activity is less than 0.2 at temperatures above 275°C.

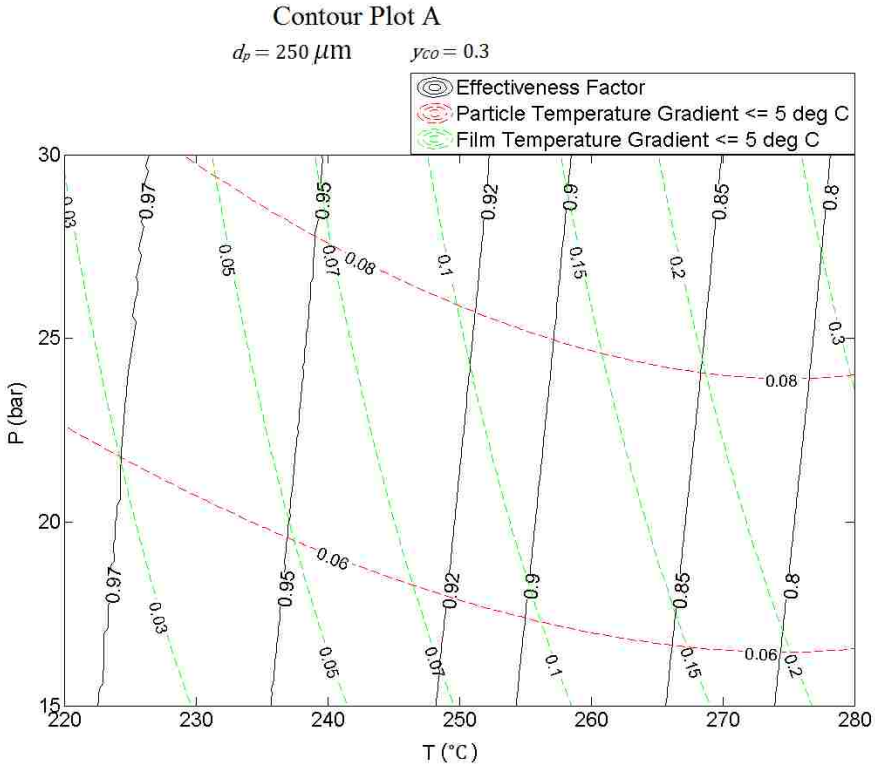

Contour Plot B

$d_p = 600\ \mu m$ $y_{CO} = 0.3$

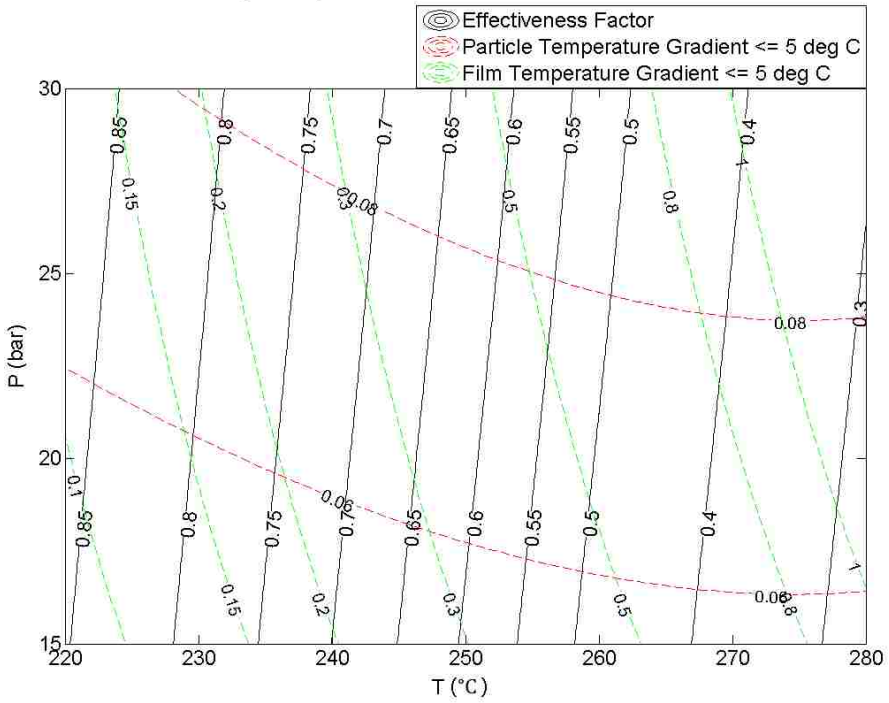

Contour Plot C

$d_p = 1.5$ mm $y_{CO} = 0.3$

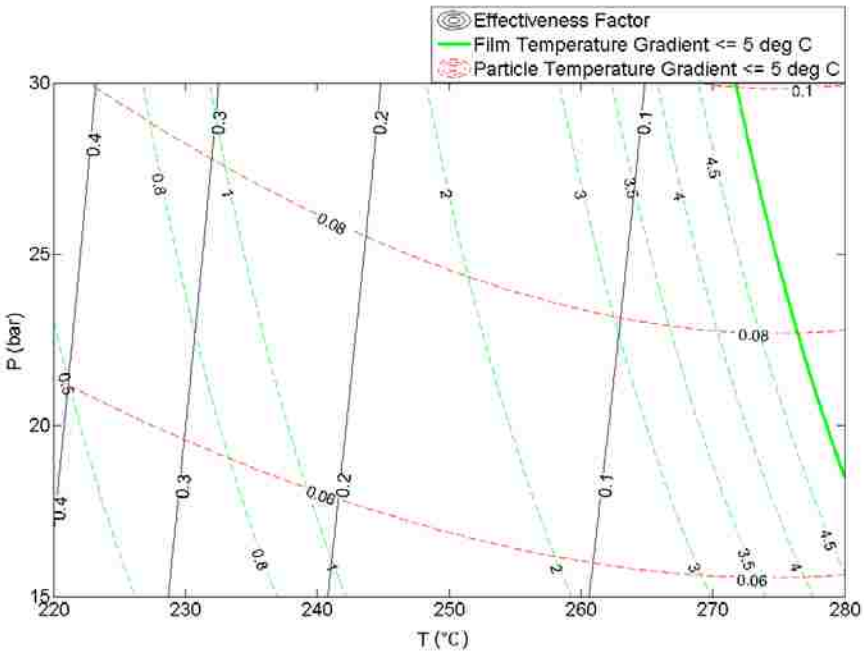

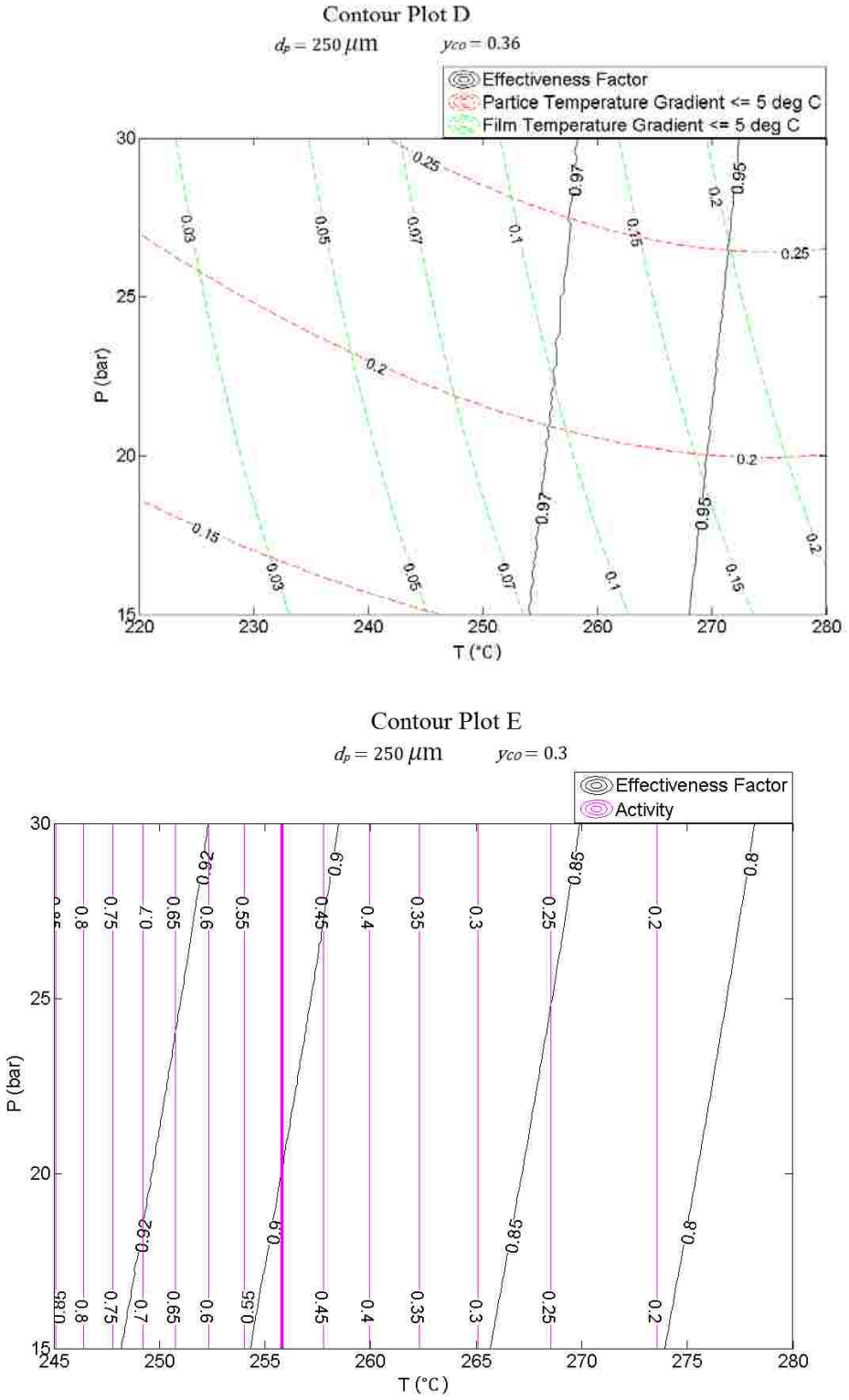

Figure 5.1: 2-D contour plots of effectiveness factor, ΔT_{film} and ΔT_p as functions of pressure and temperature at: A- d_p = 250 μm and y_{CO} = 0.3, B- d_p= 600 μm and y_{CO} = 0.3, C- d_p = 1500 μm and y_{CO} = 0.3, D- d_p = 250 μm and y_{CO} = 0.36, E- d_p = 250 μm and y_{CO} = 0.3 with activity contour plots.

The effects of d_p and y_{CO} on the effectiveness factor and the constraints are clarified in contour plots A – C in Figure 5.2. The solid cyan/blue line shows that $R > 0.66$ in Figures 5.2A and 5.2B becomes a binding constraint at or above $y_{CO} \geq 0.36$ (see Table 5.2). Furthermore, at high CO concentrations in the feed where $y_{CO} > 1/3$, the effectiveness factor increases over a broader range of particle diameters because H_2 has a higher diffusivity coefficient than CO in icosane ($54 \cdot 10^{-9}$ compared to $22 \cdot 10^{-9}$ m^2/s) and becomes the limiting diffusing reactant rather than CO at those H_2-deficient conditions. The red asterisks in contour plots A and B of Figure 5.2 represent the experimental results, which are discussed in the next section. The three-dimensional contour plot (Figure 5.2C) shows more clearly how the effectiveness factor varies with different y_{CO} and d_p at 250°C and 20 bar. η is nearly 1 for all values of y_{CO} and $d_p < 200\ \mu m$. η decreases with increasing particle size at different slopes, depending on the particle size as well as CO and H_2 compositions.

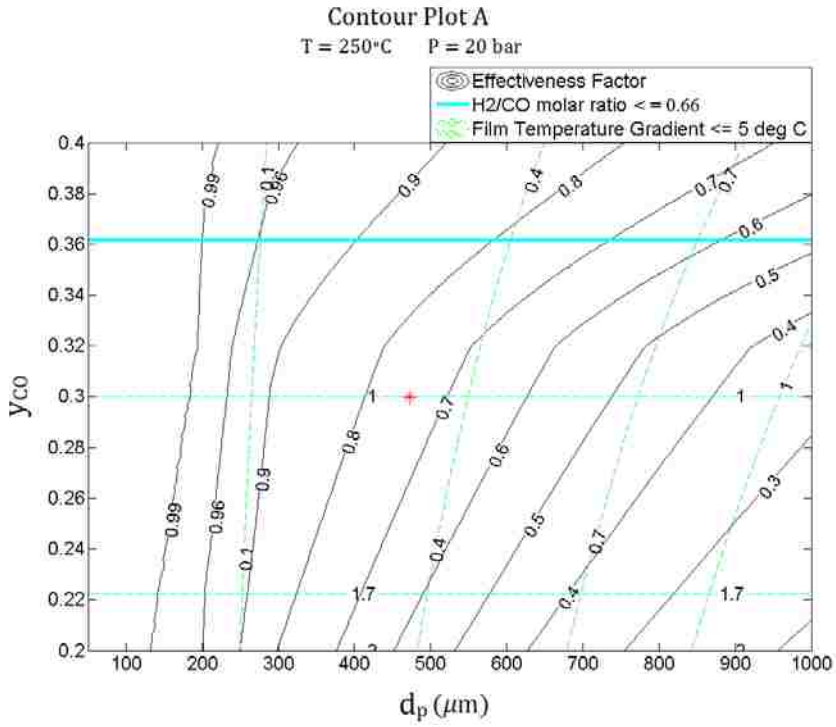

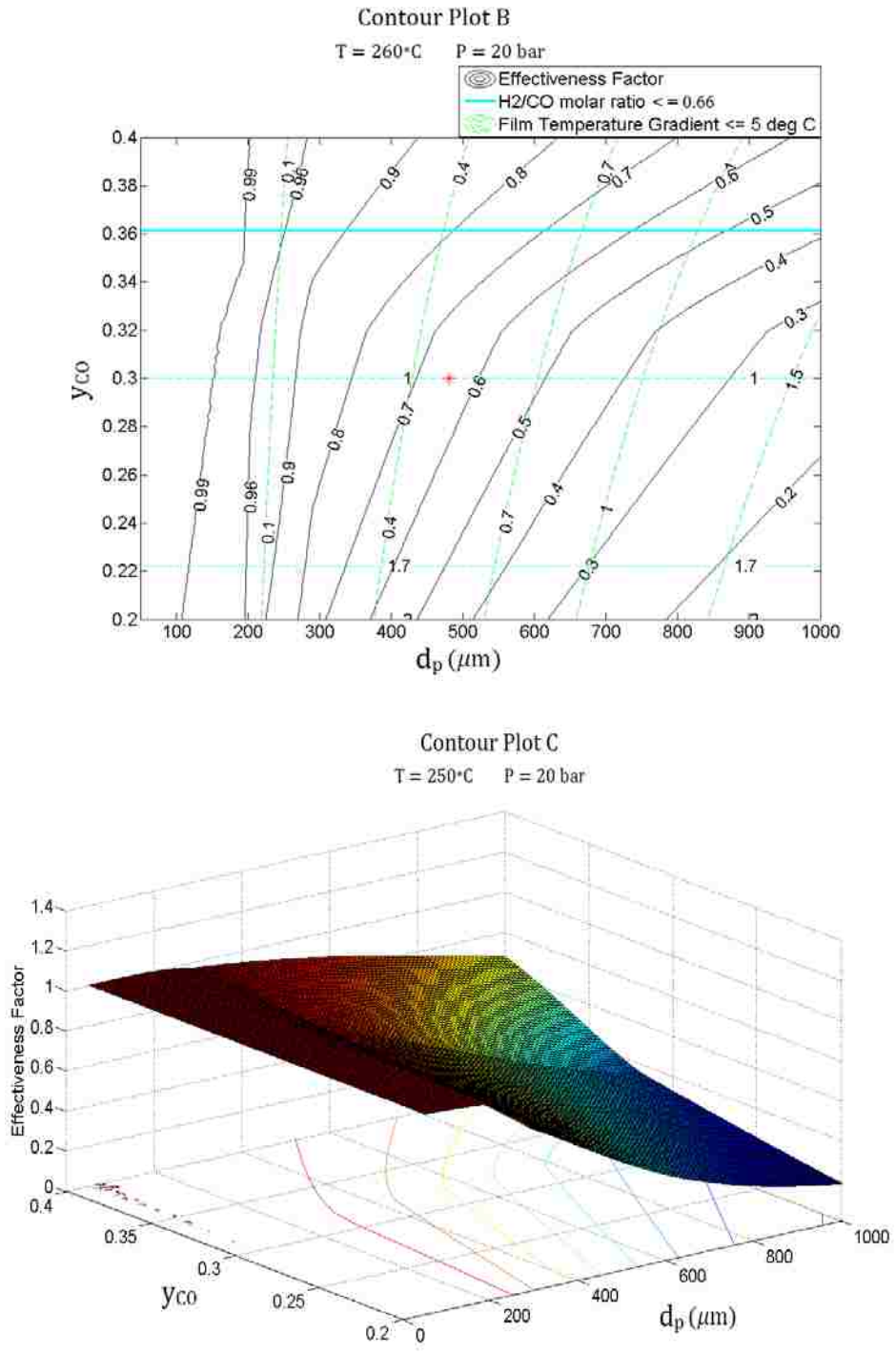

Figure 5.2: A- 2-D contour plot of effectiveness factor, ΔT_{film},, and R as functions of particle size and feed CO composition at T=250°C and P=20 bar. B- 2-D contour plot of effectiveness factor, ΔT_{film}, and R as functions of particle size and feed CO composition at $T = 260°C$ and $P = 20\ bar$. C- 3-D contour plot of effectiveness factor *vs.* particle size and feed CO composition at $T = 250°C$ and $P = 20\ bar$. The red asterisks in contours A and B represent the experimental datum acquired from the fixed-bed reactor at the indicated reaction conditions and on an average particle size of 425μm.

Figure 5.3 shows a plot of the effectiveness factor as it changes with the average carbon number of n-alkane. The effectiveness factor clearly decreases with increasing carbon number due to slower diffusion in heavier hydrocarbons and therefore smaller D_{AB} values. The effectiveness factor flattens at C_{28} which suggests that increasing the average carbon number beyond C_{28} will have minimal effect on the predicted effectiveness factor. C_{20} appears to be a reasonable average of FT wax and liquid hydrocarbons to consider in effective diffusivity calculations.

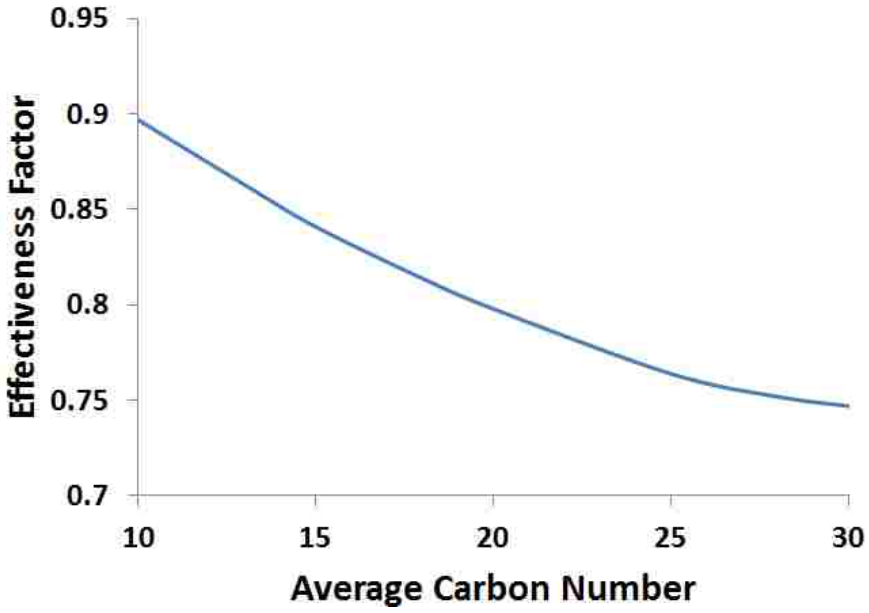

Figure 5.3: Effect of average carbon number of FT products on the predicted effectiveness factor at 250°C, 20 bar, and equimolar H_2:CO.

This summarizes the results obtained from the model that simulates mesoscale design of FTS iron-based catalysts. Details on reactor modeling can be found in other studies reported in the literature [6-8, 153-157].

5.3.2 Fixed-Bed Experiments and Comparison to Model Results

Table 5.4 shows the results of the rates of CO depletion obtained from the fixed-bed reactor at 250°C and 260°C. The effectiveness factors for both temperatures shown in Table 5.4 were calculated assuming that the reaction is not pore-diffusion limited in the particle size range of 125 – 200 μm. This is a reasonable assumption, considering the results obtained from the model predict that pore diffusion and heat transfer rates are not limiting for particle sizes smaller than 200 μm. The experimental effectiveness factors are approximately 74% and 64% at 250°C and 260°C, respectively.

Table 5.4: Rates of CO depletion obtained from the fixed-bed reactor runs and the model on unsupported FTS Fe-based catalyst at two reaction temperatures with different catalyst particle sizes (40 mol% He, 20 bar, 1:1 H2:CO).

d_p range (μm)	T (°C)	250 - 600	250-600	125 – 200	125-200
		Experimental	Predicted	Experimental	Predicted
Measured rate (mmol/gcat/h)[a]	250	38.5	38.0	52.3	48.1
Experimental effectiveness factor at (%)[b]	250	74	79	100	100
Measured rate (mmol/gcat/h)[a]	260	58.2	56.4	88.9	79.5
Experimental effectiveness factor (%)[b]	260	64	71	100	100

[a] The experimental results are within 10% error.

[b] The predicted effectiveness factors are reported for particle sizes of 425 μm.

Figure 5.4 shows a contour plot of the rate of CO depletion and CO conversion as they vary with temperature and pressure at equimolar feed compositions of CO and H_2, with red asterisks representing the experimental rates shown in Table 5.4. The rates from the model are in good agreement with the experimental rates and therefore the comparison of the modeled and experimental effectiveness factors are appropriate. Furthermore, the CO conversions are below

25% for the modeled temperature and pressure ranges (~ 10% at 250°C, and < 15% at 260°C) validating the assumption for differential conditions.

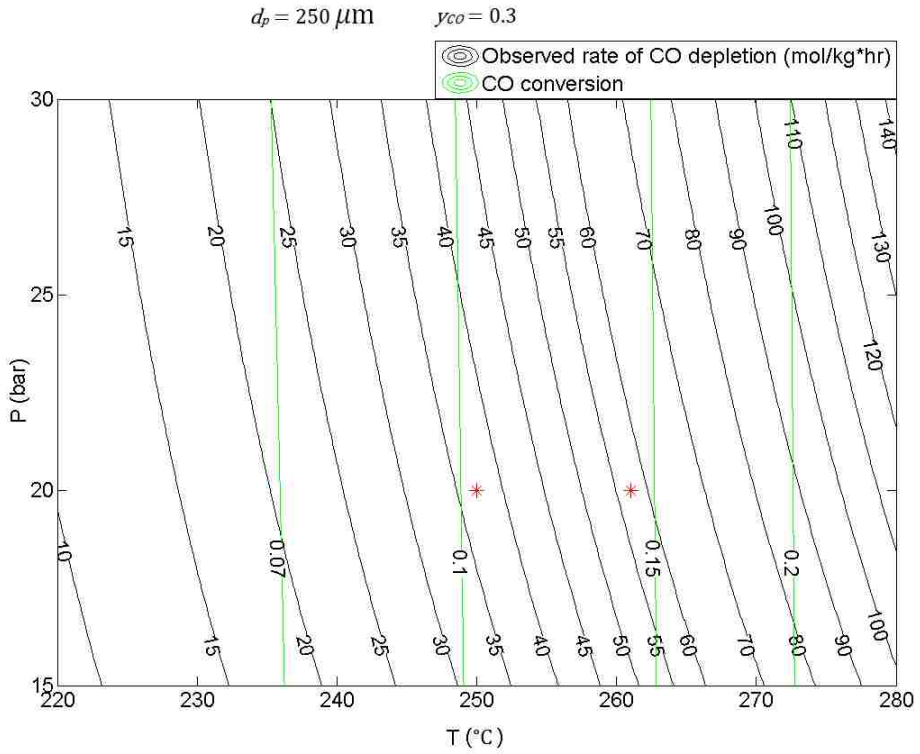

Figure 5.4: 2-D contour plot of observed rate and CO conversion as functions of reaction pressure and temperature and equimolar H2:CO molar ratio and 250 microns. The red asterisks in contours represent the experimental (measured) rates acquired from the fixed-bed reactor at 250°C and 260°C.

The red asterisks in contour plots A and B in Figure 5.2 show that the experimental effectiveness factors fall in the particle size range of 250 – 600 μm. The modeled effectiveness factor at 250°C, 20 bar, and H_2:CO = 1 is within ~5% of the experimental value (79% compared to 74%) at an average particle diameter of the 250 – 600 μm range (425 μm). Additionally, the predicted value at 260°C, 20 bar, and H_2:CO ratio = 1 is within ~10% of the experimental value (71% compared to 64%) at 425 μm. The experimental values at both temperatures fall in the range of 250 – 600 μm on Figures 5.2A and 5.2B. Therefore, the experimental measurements validate and support the predicted results from the developed model.

5.3.3 Scale-Up

Pressure drop problems do not rise at laboratory-scale conditions, even if the particle size is lowered to below 200 μm. However, ΔP is a strong function of the length of the catalyst bed (L_{bed}) and feed volumetric flow rate, ($\dot{V}_{in}$), which strongly affects the liquid dynamic hold-up value ($\varepsilon_{l,dyn}$) as well as the friction factor. Therefore, the model must be applied to a commercial-scale reactor to optimize the design variables for practical conditions. Tables 5.5 and 5.6 present the model input parameters changed from the lab-scale reactor to consider reactor scale-up and the corresponding optimized solution, respectively. Several design parameters, including CO conversion (60%), reactor inlet $T = 250°C$, reactor inlet $P = 20\ bar$, and inlet CO mole fraction $y_{CO} = 0.5$, were set at fixed values to highlight the effects of optimized particle diameter on pressure drop. An increase of 7°C between the inlet and the outlet temperature with an average catalyst bed temperature of 253.5°C were used to account for non-isothermality in the industrial reactor, as estimated elsewhere [86,140]. The rate constant per unit mass, k, was calculated using integral reactor design to account for non-differential conditions, as shown in Equation 5.36:

$$k = \frac{y_{CO}F^{0}_{CO}}{W_{cat}} \cdot \int_{0}^{0.6} \frac{1}{P_{CO}(X_{CO})^{-0.05}P_{H_2}(X_{CO})^{0.6}} dx_{CO} \qquad (5.36)$$

Table 5.5: Parameters for a commercial-size reactor at T=253.5°C, P=20 bar, and y_{CO}=0.5 (H_2:CO = 1).

Parameter	Value
Particle shape	Cylindrical
W_{cat} **(kg)**	3
W_{SiC} **(kg)**	0
A_{reac} **(cm^2)**	5.07
$\dot{V}_{in}$ **(m^3/h)**	24
y_{He}	0
X_{CO}	60%
k **(mol kg^{-1} h^{-1} atm$^{-0.55}$)**	29.3

Table 5.6: Optimized solution for the commercial-size reactor.

Variable	Value for maximizing $\eta \cdot -r_{CO}$
d_p (mm)	1.1
M_w	4.9
ϕ	3.0
η	0.54
Intrinsic $-r_{CO}$ (mol/kg·hr)	112
Observed $-r_{CO}$ (mol/kg·hr)	60.5
β	$1.5 \cdot 10^{-4}$
ΔT_{film} (°C)	0.3
R	1
ΔT_p (°C)	0.08
$\Delta P/P$	20%
ΔP (bar)	4
L_{bed} (m)	7.4
h (W/m²·K)	5374
λ_e (W/m·K)	0.16
ε_b	0.41
D_K (cm²/s)	$3.1 \cdot 10^{-2}$
D_{AB} (cm²/s)	$2.3 \cdot 10^{-4}$
D_e (cm²/s)	$5.3 \cdot 10^{-6}$

The pressure drop is significantly influenced by the longer catalyst bed, higher CO conversion, and higher flow rates of feed; hence, the optimum d_p is constrained. Furthermore, ΔT_{film} is significantly higher than the value reported for the laboratory-scale reactor due to increased rate of reaction and increased Reynolds number. Smaller reactor diameters provide better heat transfer because the convection is better with higher flow rates and the distance for conduction is decreased; however, decreasing the size of the reactor increases the length of the catalyst bed and therefore increases the pressure drop. The optimal particle size (1.1 mm) is constrained by $\Delta P/P \leq 20\%$ which decreases the effectiveness factor to 54%. This is made

clear in Figure 5.5 which shows a 2-D contour plot of η, ΔP, and ΔT_{film} as functions of d_p and $\dot{V}_{in}$ (Plot 5.5A) and a 3-D contour plot of ΔP *vs.* d_p and $\dot{V}_{in}$ (Plot 5.5B).

According to Figures 5.5A and 5.5B, pressure drop increases with increasing feed volumetric flow rate and decreasing particle size. Larger $\dot{V}_{in}$ increases the gas and liquid velocities, which increase $\varepsilon_{l,dyn}$ and δ_{GW} (Equations 5.24 and 5.27), and therefore increase $\frac{\Delta P}{L_{bed}}$ according to Equation 5.23. Smaller d_p decreases the bed void fraction (ε_b) and increases δ_{GW}, thus increasing pressure drop. Pressure drop appears to increase beyond 20% for particle sizes smaller than 1.5 mm and feed volumetric flow rate greater than 20 m^3/h.

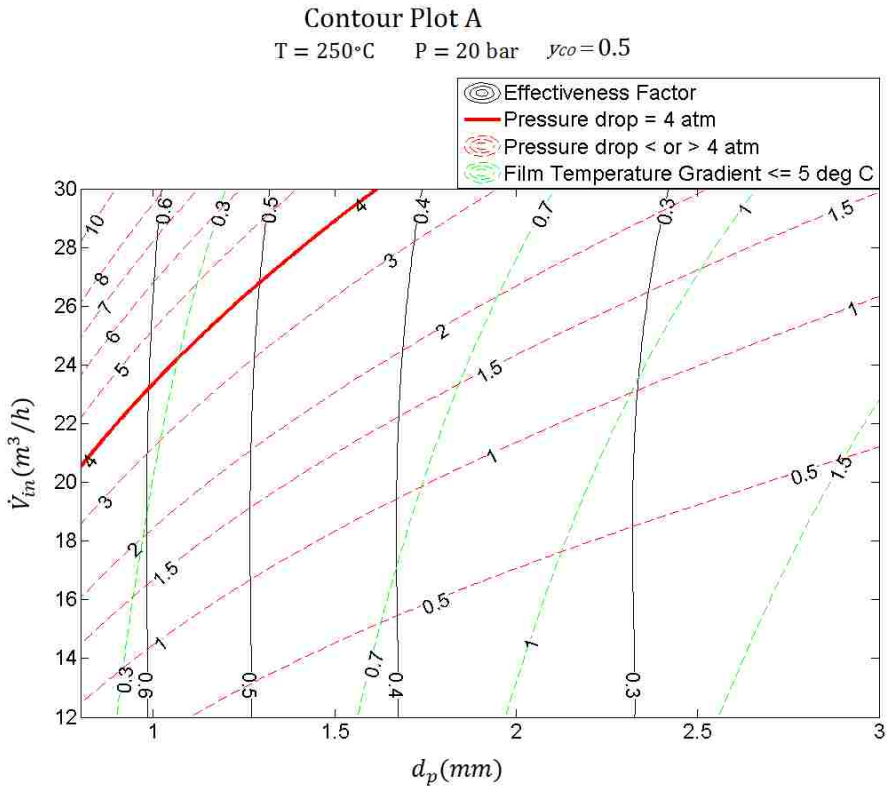

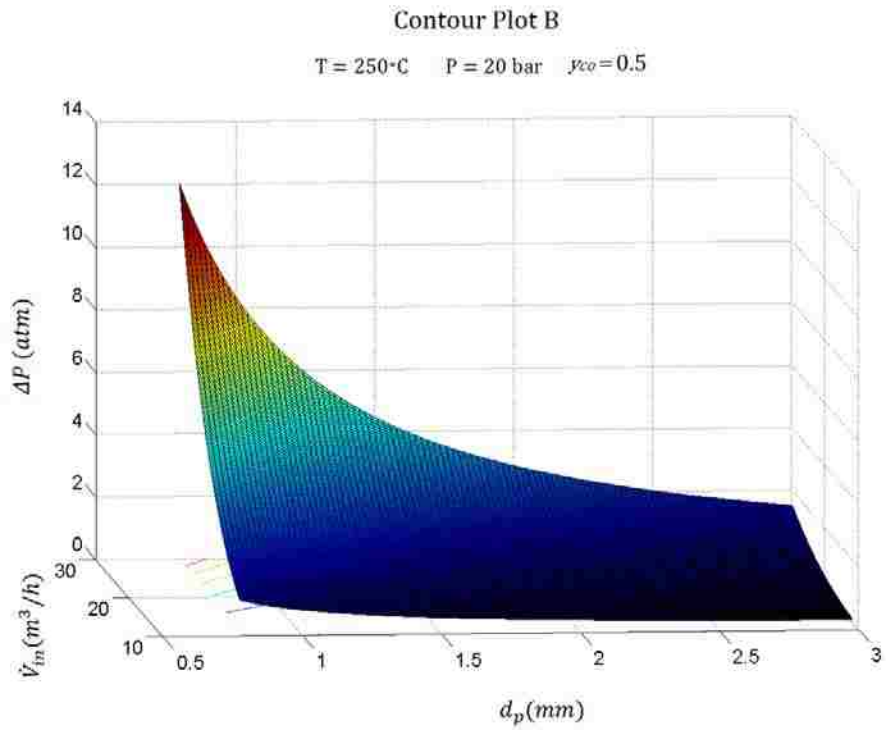

Figure 5.5: A- 2-D contour plot of effectiveness factor, ΔP, and ΔT_{film} as functions of particle size and feed volumetric flow rate at $P = 20\ bar, T = 250°C, y_{CO} = 0.5$. B- 3-D contour plot of ΔP as a function of particle size and feel volumetric flow rate at $P = 20\ bar, T = 250°C, y_{CO} = 0.5$.

5.4 Summary of Optimization and Simulation Models

An optimized model that simulates pressure drop and heat and mass transfer conditions for unsupported iron-based Fischer-Tropsch catalysts under different operating (temperature, pressure, and feed CO composition) and design (agglomerate particle size) conditions has been successfully developed and validated against experimental results. Higher reaction temperatures, higher reaction pressures, smaller particle size, and lower feed CO composition are favored for a maximized intrinsic reaction rate by driving a kinetically-controlled reaction that is not limited by heat and mass transfer limitations. These conditions suggest increased catalytic activity as well as better transfer rates, thereby increasing the productivity of the catalyst. However, reaction temperatures above 255.8°C result in the catalytic activity decreasing below 50% of initial

activity after 1000 h; therefore, the choice of reaction temperature is constrained by the rate of deactivation. Internal and film heat transfer resistances are not predicted to be limiting in the particle size range of 200 – 600 μm. However, film temperature gradients are expected to be more limiting than internal particle temperature gradients at typical operating Fischer-Tropsch synthesis conditions (250°C, 20 bar, and equimolar H_2:CO ratio). The reaction is not pore-diffusion limited at particle sizes below 250 μm where the effectiveness factor is greater than 95%. Finally, small particle sizes (< 250 μm) do not impose any pressure drop issues under laboratory-scale operating conditions. However, the model was used to optimize the particle size under commercial-scale reactor operating conditions and predicted that 1.1 mm cylindrical particles are optimum for a maximized effectiveness factor (54%) and minimized pressure drop (4 atm).

CHAPTER 6. WGS and FTS Kinetic Study of Unsupported Iron-Based Fischer-Tropsch Catalysts Promoted with Lanthana

This chapter presents the experimental work, results, and discussion of the kinetic and characterization studies performed on unsupported iron-based FTS catalysts promoted with lanthana. The effects of lanthana on the activity, selectivity, and stability of these catalysts during both water gas shift and Fischer-Tropsch synthesis conditions are explained.

6.1 Experimental Methods and Apparatus

The same experimental procedure was followed to prepare and test the unsupported iron-based FTS catalysts. The chart in Figure 6.1 summarizes the experimental work.

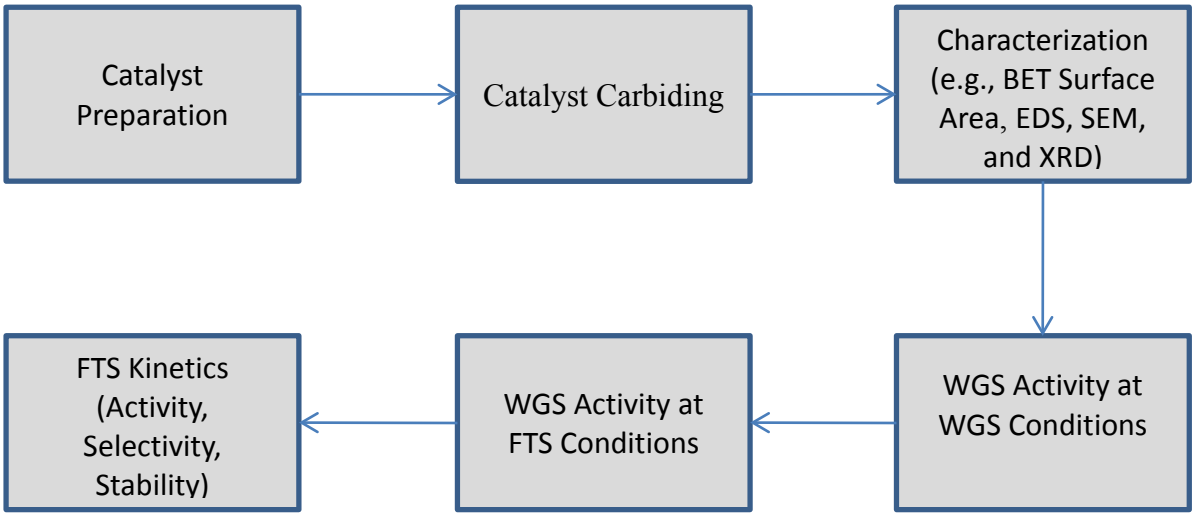

Figure 6.1: Flow of experimental work procedures for FTS catalysts.

6.1.1 Catalyst Preparation, Calcination, Screening, Reduction, and Carbiding

The methodology described in this section for catalyst preparation was based on Brunner's work [86]. Different batches of catalysts were prepared *via* the solvent deficient precipitation (SDP) method with nominal compositions of 5 parts Cu, 4 parts K, and 16 parts SiO_2 for 100 parts Fe. Table 6.1 shows the nominal compositions of the four catalysts prepared for this work.

Table 6.1: Compositions of metals in FTS catalysts.

Catlyst ID	Fe (wt%)	Cu (wt%)	K (wt%)	La(wt%)	SiO_2 (wt%)
0La FT	80.0	4.00	3.20	0.00	12.80
0.5La FT	79.6	3.98	3.18	0.50	12.74
2La FT	78.43	3.92	3.13	1.98	12.55
2La/2K FT	79.37	3.97	1.98	1.98	12.70

The synthesis of these catalysts occurs according to the following chemical reactions:

$$M(NO_3)_{x\,(hyd)} + x\,NH_4HCO_{3\,(hyd)} \rightarrow M(OH)_{x\,(s)} + xNH_4NO_{3\,(aq)} + xCO_{2\,(g)} \quad (6.1)$$

$$M(OH)_{x_{(s)}} + heat + \frac{x}{4}O_2 \rightarrow MO_{x\,(s)} + \frac{x}{2}H_2O_{(l)} \quad \text{(calcination)} \quad (6.2)$$

Appropriate amounts (shown in Table 6.2) of hydrated metal salts: $Fe(NO_3)_3{\cdot}9H_2O$ (99.99%, Sigma-Aldrich), $Cu(NO_3)_2{\cdot}2.5H_2O$ (98%, Sigma-Aldrich), and $La(NO_3)_3{\cdot}6H_2O$ (99.999%, Sigma-Aldrich), were mixed with SiO_2 (Cab-O-Sil, Sigma-Aldrich) in a large mortar without the addition of any solvent. $KHCO_3$ (99.7%, Sigma-Aldrich) and NH_4HCO_3 (99.5%, Sigma-Aldrich) were mixed together in a separate bowl. The bicarbonate mixture was then added to the nitrate mixture and the resultant was mixed forcefully for about 20-30 minutes with a pestle. During the process of vigorous mixing, bubbles of CO_2 and waters of hydration were released and metal hydroxides formed through the chemical reactions in Equation 6.1. After the process completed when CO_2 release ceased, the mixture was dried in an oven overnight at 100°C for 15-24 h.

Table 6.2: Weights of metal nitrates, silica, and bicarbonates for the preparation of 20-gram batches of unsupported FTS catalysts with different wt% of lanthana.

Catlyst ID	$Fe(NO_3)_3$ (g)	$Cu(NO_3)_2$ (g)	$La(NO_3)_3$ (g)	SiO_2 (g)	$KHCO_3$ (g)	NH_4HCO_3 (g)
0La FT	115.738	2.929	0.000	2.560	1.639	70.435
0.5La FT	115.162	2.914	0.310	2.547	1.631	70.257
2La FT	113.469	2.871	1.222	2.510	1.607	70.733
2La/2K FT	114.82	2.905	1.237	2.540	1.016	70.557

20 grams of the dried batches were calcined at 300°C for 6 h. The temperature was ramped from room temperature to 90°C at 1°C/min, soaked for 1 hour to get rid of moisture, then ramped to 210°C at 1°C/min, soaked for 4 h to decompose ammonium nitrate, and finally ramped to 300°C at 0.5°C/min and soaked for 6 h to convert metal hydroxides to oxides. The air flow (breathing air, Airgas) was set to achieve a gas hourly space velocity (GHSV) > 2000 mL air/(mL of cat · h). The calcined catalysts were ground with a pestle and sieved to retain 106-250 μm particle sizes to avoid pore diffusion and heat transfer limitations, as recommended by the results of the model presented in the previous chapter.

0.1 g of the calcined catalysts were reduced and carbided at 1 atm. For the reduction process, the temperature was ramped from room temperature to 250°C at 0.5°C/min, soaked for 1 hour, ramped to 300°C at 0.5°C/min, and soaked for 10 h in 10 mol% H_2/Ar with a GHSV > 2000. The reduction conditions were then switched to 100 mol% H_2 for another 6 h. The temperature was then lowered to 230°C at 1°C/min in Ar before syngas with equimolar compositions of CO and H_2 diluted with Ar (30 mol% CO (99.995%, Airgas), 30 mol% H_2/ (99.95%, Airgas) 40 mol% Ar (99.997%, Airgas)) was introduced. The temperature was then ramped to 250°C at 0.5°C/min until steady state was achieved. The carbided catalysts were passivated at room temperature. The composition of air in Ar was controlled to keep the temperature rise below ~ 10°C during the exothermic process of passivation. The flow rates of

gases were controlled using calibrated flow controllers (Porter Instruments 201). Table 6.3 shows the flow rates of gases for the reduction and carbiding processes.

Table 6.3: Flow rates of gases during the reduction and carbiding processes.

Gas	Flow rates during the reduction with 10 mol% H_2/Ar (sccm)	Flow rates during the reduction with 100 mol% H_2 (sccm)	Flow rates during carbiding (sccm)
H_2	5	25	15
CO	0	0	15
Ar	45	0	20

6.1.2 Characterization Procedures

Different techniques were used to characterize the physical and chemical properties of the calcined and carbided catalysts. Details about each analytical technique are described in the following subsections.

6.1.2.1 Nitrogen Physisorption, EDS, SEM, and XRD

Similar procedures for BET surface area measurements, EDS and SEM, and XRD analyses were followed as described in Sections 3.1.2.1, 3.1.2.2, and 3.1.2.3, respectively.

6.1.2.2 X-Ray Mapping

A scanning electron microscope (FEI, Helios NanoLab 600i) equipped with EDAX spectrometer (Ametek) was used to image the elemental distributions of promoters (Fe, Cu, K, La, Si) in 106-250 μm agglomerates of carbided catalysts. The maps were generated in Team® software with 256*200 resolution and with 20 keV voltage and 1.4 nA beam. The scans were made at 500x and 3500x magnifications to acquire maps for single and multiple particles.

6.1.2.3 CO Chemisorption

CO chemisorption was performed on carbided/reduced catalysts in a thermal gravimetric analysis (TGA DSC 1, Mettler Toledo) instrument equipped with an automated GC 200 gas controller. The analysis on 10 mg passivated carbided catalysts was not successful apparently because the reduction conditions of 10 mol% H_2/He at 100°C for 1 h were not sufficient to reduce the passivated oxide layer on the surface and therefore no CO uptake was observed. These reduction conditions were chosen for the passivated catalysts in an attempt to reduce the oxide layer but not iron carbide. CO uptake measurements were therefore performed at 100°C in 10 mol% CO/He on 10 – 20 mg of reduced samples. The reduction process was followed as discussed above and was stopped after the reduction with 100% H_2 at 300°C. The reduced catalysts were passivated at room temperature with a controlled air/Ar gas mixture that allowed a <~10°C temperature rise. Prior to CO uptake measurements, the passivated reduced catalysts were re-reduced *in situ* at 300°C for 6 h in 10 mol% H_2/He with 3°C/min ramp rate from room temperature. The flow rates of gases were set using calibrated rotameters.

6.1.3 Kinetic Analysis: Reaction Apparatus, Conditions, and Calculations

The catalyst performance metrics (activity, selectivity, and stability) were tested in a fixed-bed reactor at three different temperatures (240°C, 250°C, and 260°C). This section describes the system and conditions used to perform these measurements.

6.1.3.1 Catalyst Loading

Kinetic experiments were performed in a stainless steel microreactor (0.6 cm inside diameter, 30.5 cm long) fitted with an internal ring slightly smaller than the inner diameter of the

reactor to support the sample. The catalysts were embedded between two layers of quartz wool and were supported on 80 μm stainless steel mesh to retain the catalyst particles. 0.14 g of calcined catalyst was diluted with 0.56 g of silicon carbide to prevent hot spots and to approach isothermal conditions in the catalytic zone. At the end of each experiment, the used catalyst was recovered, while the reactor was cleaned with hot water and acetone to remove any residual wax.

6.1.3.2 Fixed-Bed Reactor Setup

Figure 6.2 shows the flow diagram of the fixed-bed reactor system used to perform the experiments on the FTS catalysts. The flow rates of CO, H_2, and Ar were set using calibrated mass flow controllers (Porter Instruments 201). CO with an Ar internal standard (88.2% CO and 11.8% Ar, Airgas) was used for conversion calculations. Water was metered (ISCO pump model 260d) at a 1:2 H_2O:CO molar ratio through a boiler operating at 250°C during the WGS study of the FT catalysts. The reactor was heated inside an electric furnace (National Element FA 120). A thermocouple in contact with the center of the catalyst bed itself measured the reaction temperature. Wax was collected in a hot trap heated at 100-120°C. Water and liquid hydrocarbons were collected in a cold trap at 0°C. After the cold trap, a back-pressure regulator (Swagelok) controlled the pressure inside the reactor. A desiccator column (Drierite, 97% anhydrous calcium sulfate) was used to de-humidify the exit gas stream prior to analysis in a gas chromatograph (GC, Agilent Technologies 7890A with a Supelco Carboxen 1004 packed column (2 m x 1.5 mm) and thermal conductivity detector). The reactor tubing prior to the water removal system was heat traced at 150°C and insulated to prevent water condensation during the WGS study.

6.1.3.3 Activation of Catalysts

Prior to activation, the catalysts were reduced *in situ* at 300°C and atmospheric pressure as described in Section 6.1.1. The catalyst was then cooled to 210°C in flowing Ar. Ar flow was shut off and syngas with 1:1 H_2:CO molar ratio was allowed to flow until the reaction pressure reached 320 psi. The flow rates of CO and H_2 were each set at 5.7 sccm to achieve about 40% CO conversion for fast activation and carbiding of the catalyst. The temperature was ramped from 210°C to 250°C at 0.5°C/min. The temperature was soaked for 3 h every 10°C interval to control the rate of the reaction and to avoid hot spots that could result from the high exothermicity of the FTS reaction. Once the rate of the reaction approached steady-state conditions, which took between 40 and 60 h, the flow rates of CO and H_2 were increased to 11.4 sccm and then to 22 sccm for each gas over the span of 24-36 h to control the heat of reaction and avoid hot spots in the catalyst as the differential reactor conditions were approached. The flow rates of CO and H_2 were finally increased to 40 sccm for each gas to bring CO conversion down to about 10%.

6.1.3.4 Fischer-Tropsch Activity and Selectivity Measurements

Data for the activity and selectivity of the four catalysts were acquired at 240°C, 250°C, and 260°C and at 320 psi. Reaction rates were calculated from the following differential reactor equation:

$$-r_{CO} = \frac{X_{CO} \cdot F^0{}_{CO}}{W_{cat}} \tag{6.3}$$

where $-r_{CO}$ is the rate of CO consumption, X_{CO} is the CO conversion, $F^0{}_{CO}$ is the inlet molar flow rate of CO at atmospheric P and T, and W_{cat} is the mass of the catalyst.

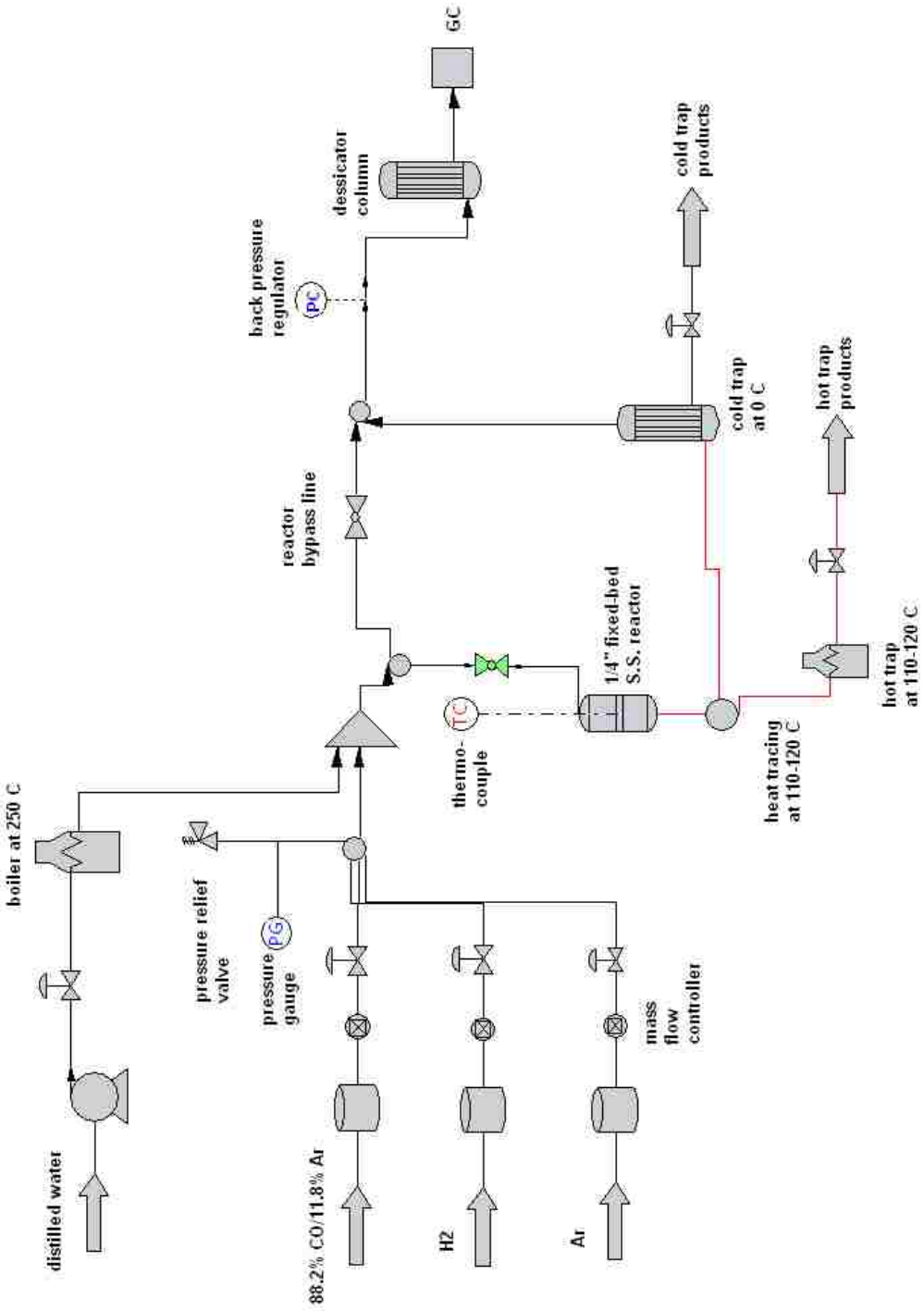

Figure 6.2: Fixed-bed reactor system for FTS experiments

CO conversion, X_{CO}, was calculated from equation (6.4):

$$X_{CO} = 1 - \frac{PA_{CO}}{PA^0{}_{CO}} \frac{PA^0{}_{Ar}}{PA_{Ar}} \tag{6.4}$$

where PA_i is the integrated GC peak area for gas i during FTS reaction and $PA^0{}_i$ is the integrated GC peak area for gas i when no reaction is taking place. The overall rate of reaction of the catalyst, r_{CO+H_2}, was calculated using equation (6.5):

$$r_{CO+H_2} = \frac{X_{CO} \cdot F^0{}_{CO} + X_{H_2} \cdot F^0{}_{H_2}}{W_{cat}} \tag{6.5}$$

The selectivity of any gaseous product (S_i) was calculated using equation (6.6):

$$S_i = \frac{n_i}{X_{CO}} \frac{PA_i}{PA_{Ar}} \frac{PA^0{}_{Ar}}{PA^0{}_{CO}} \frac{RF_{CO}}{RF_i} \tag{6.6}$$

where n_i is the number of carbon atoms in species i, and RF_i is the response factor of gas i acquired from GC calibrations (see Appendix A). The derivations of equations (6.4) and (6.6) can be found elsewhere [86]. The reaction rate constant, k, as a function of reaction temperature was regressed using the Arrhenius equation to determine the activation energies for the different catalysts. k was found using the reaction rate model and partial pressure dependencies proposed by Eliason [97], as given in equation (6.7):

$$k = \frac{-r_{CO}}{P_{CO}{}^{-0.05} P_{H_2}{}^{0.6}} \tag{6.7}$$

6.1.3.5 Water-Gas Shift Activity Measurements

The WGS activity of iron-based FT catalysts operating under either FTS or WGS conditions was also studied. The WGS study under FTS conditions was performed only on 0La FT, while all of the catalysts were operated under WGS conditions. Table 6.4 reports the conditions of both studies. The WGS conditions included four flow rates in order to extrapolate

to zero CO conversion (as described in Chapter 3). The FTS conditions were typical for FTS reaction, with the H_2O:CO ratio chosen to avoid deactivation by carbon deposition (at low H_2O:CO) or oxidation of catalyst by water (at high H_2O:CO). The CO and H_2O were diluted in Ar. After each run under FTS conditions, the reaction conditions were changed to 1:1 H_2:CO to evaluate the FTS reaction rate for deactivation at 250°C and 320 psi. The calculations for WGS activity are as reported in Section 3.1.3. The purpose of this study was to understand the behavior of the WGS activity on operating Fe FT catalysts with the WGS reaction de-coupled from the FT reaction.

Table 6.4: The operating conditions for the WGS study of FT catalysts.

WGS study conditions	Temperature (°C)	Pressure (atm)	H_2O/CO/Ar	Total inlet gas flow (sccm)	Active phase of iron
WGS run 1	400	1	3/1/0	3.65	Fe_3O_4
WGS run 2	400	1	3/1/0	7.30	Fe_3O_4
WGS run 3	400	1	3/1/0	11.0	Fe_3O_4
WGS run 4	400	1	3/1/0	14.3	Fe_3O_4
FTS run 1	250	21	1/2/2	20	χ-Fe_5C_2
FTS run 2	250	21	2/5/5	24	χ-Fe_5C_2
FTS run 3	250	2	2/3/3	16	χ-Fe_5C_2
FTS run 4	240	21	1/2/2	20	χ-Fe_5C_2
FTS run 5	240	21	2/5/5	24	χ-Fe_5C_2
FTS run 6	240	21	2/3/3	16	χ-Fe_5C_2
FTS run 7	260	21	1/2/2	20	χ-Fe_5C_2
FTS run 8	260	21	2/5/5	24	χ-Fe_5C_2
FTS run 9	260	21	2/3/3	16	χ-Fe_5C_2

6.2 Results and Discussion

This section discusses in detail the results of the characterization and kinetic experiments. The effect of lanthana on FTS catalysts is compared in terms of activity, selectivity, and stability.

6.2.1 Surface Area

Table 6.5 shows the BET surface areas (SA) and the average pore volume (V_{pore}) of the fresh calcined and carbided catalysts, along with the crystallite sizes (d_c) for the carbided samples. Addition of lanthana has no significant effect on the fresh BET surface area and average pore volume. However, lanthana has significant influence on the catalysts after carbiding. The carbided 2La/2K FT catalyst has the highest surface area and largest pore volume, which suggests that it is the most stable catalyst with the least reduction in surface area. The carbided 2La FT catalyst has the lowest surface with the smallest pore volume indicating less stability than the other catalysts. In fact, 2La/2K FT has triple the surface area of 2La FT and double the pore volume, which can significantly affect the selectivity of these catalysts under FT reaction conditions.

Table 6.5: BET surface area and average pore diameter measurements for the calcined and carbided catalysts along with crystallite sizes for the carbided catalysts.

Catalyst ID	Calcined (Fresh)		Carbided			
	SA (m^2/g_{cat})	V_{pore} (cm^3/g)	SA (m^2/g_{cat})	V_{pore} (cm^3/g)	d_c for Fe (nm)[a]	d_c for χ-Fe_5C_2 (nm)[b]
0La FT	125	0.14	21	0.08	8.1	19.1
0.5La FT	135	0.13	23	0.06	9.6	21.4
2La FT	110	0.14	10	0.05	9.9	22.6
2La/2K FT	125	0.14	29	0.1	9.2	20.4

[a] Fe crystallite sizes were calculated using the Debye-Scherrer equation and XRD peak broadening at 44.7°.
[b] χ-Fe_5C_2 crystallite sizes were calculated using the Debye-Scherrer equation and XRD peak broadening at 43.7°.

6.2.2 Powder X-ray Diffraction (XRD)

Figure 6.3, which shows the XRD patterns of the carbided FT catalysts, indicates that the major iron phase in all the samples is a mixture of χ-Fe_5C_2 and metallic Fe. Peaks for Fe_3O_4 at 35.5° and 63° were also observed, possibly due to oxidation of Fe during passivation, but their intensity is negligible compared to the carbide phase. These major phases were determined by comparing the diffraction angles with those from the International Centre for Diffraction Data (ICDD) database. Furthermore, addition of lanthana clearly left-shift the χ-Fe_5C_2 peaks at 43.7°, the metallic Fe peaks at 44.8°, and the Fe_3O_4 peaks at 35.5°, indicating larger unit cells and therefore larger lattice parameters with the addition of the larger La^{3+} cations. The crystallite sizes of iron reported in Table 6.5 suggest that lanthana increases the crystallite size of both iron and iron carbide and therefore worsens the dispersion of the active phase. However, the crystallite size of the 2La/2K FT catalyst is smaller than the other La-promoted FT catalysts, suggesting that adding lanthana at the expense of potassium provides better dispersion of the active phase than adding it at the expense of iron and other promoters. A better dispersion of iron can aid the stability of the catalyst by reducing the sintering of iron crystallites (as observed with the smaller crystallite sizes) and can provide more surface area and active phase for the FTS reaction.

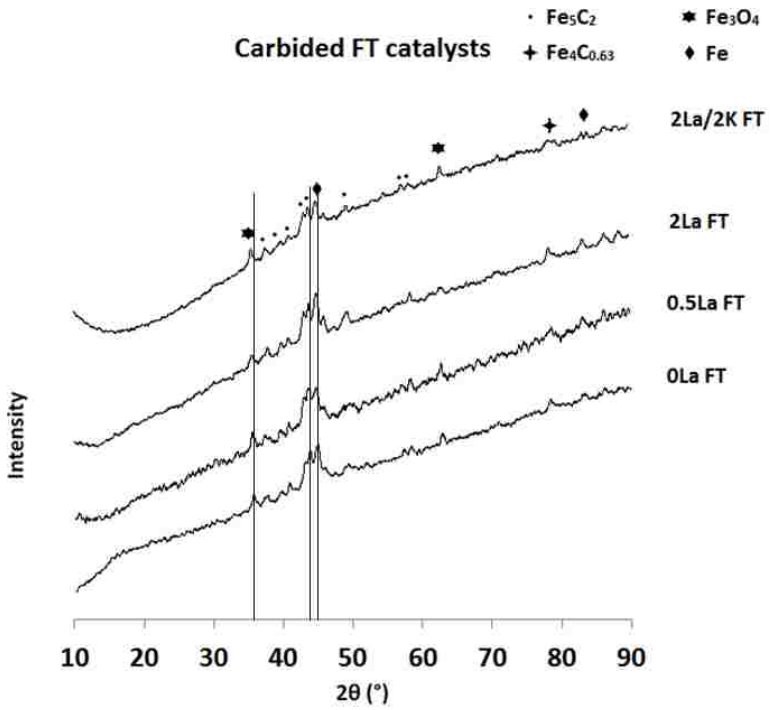

Figure 6.3: The XRD patterns of the carbided FT catalysts. The peaks of each corresponding iron phase are identified using the International Centre for Diffraction Data (ICDD) database.

6.2.3 Scanning Electron Microscopy and Energy-Dispersive Spectroscopy (EDS)

Figure 6.4 shows the scanning electron micrograph (SEM) images for the fresh calcined 0La FT, 0.5La FT, and 2La FT and 2La/2K FT catalysts. Agglomerate particle sizes of the fresh samples appear to be the same. The elemental compositions of the metals analyzed by EDS are approximately the same for the scans taken at different spots on each catalyst, except for the 2La FT catalyst, indicating that the bulk components are not well mixed in the 2La FT catalyst, as shown in Table 6.6. Quantitative analysis by the software is not accurate enough for calculating the low compositions of lanthana. However, it shows similar contents for the different scans with the desired 4/100 and 5/100 ratios of K/Fe and Cu/Fe, respectively.

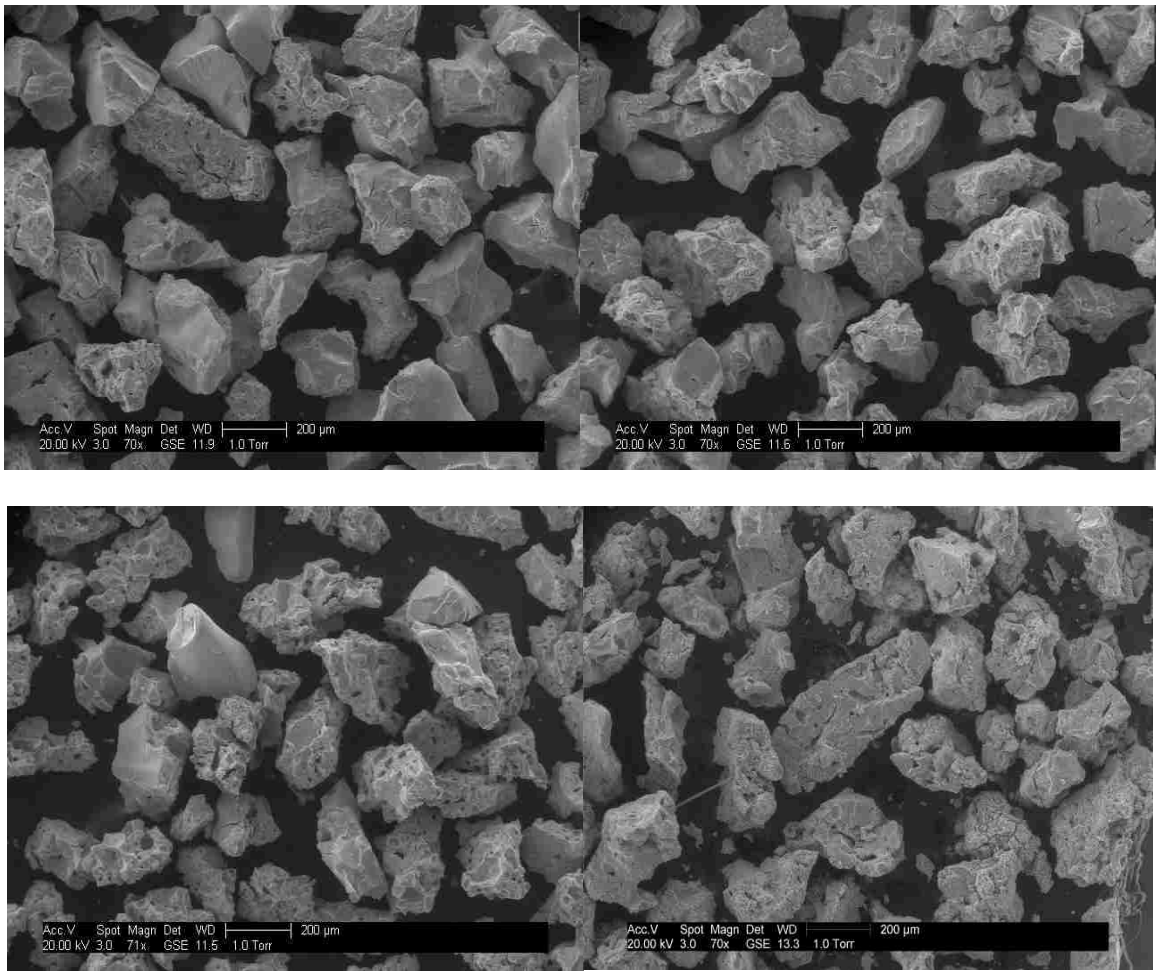

Figure 6.4: Scanning electron micrographs of fresh calcined 0La FT (top left), fresh calcined 0.5La FT (top right), fresh calcined 2La FT (bottom left), and fresh calcined 2La/2K FT (bottom right).

Table 6.6: Quantitative EDS analysis on the fresh calcined FT catalysts. The numbers show ppm of promoters normalized to 100 ppm of Fe for a scan across the surface of the sample holder and a one-point scan at a randomly chosen particle.

Catalyst ID	Scan Across Surface				One-point scan			
	La ppm	Cu ppm	K ppm	Fe ppm	La ppm	Cu ppm	K ppm	Fe ppm
0La FT	0.00	5.99	4.01	100	0.00	6.09	4.29	100
0.5La FT	0.85	4.62	4.30	100	0.94	4.62	4.32	100
2La FT	1.98	5.58	3.75	100	2.40	6.54	5.51	100
2La/2K FT	1.81	5.76	1.39	100	2.08	5.34	1.47	100

The SEM images of the carbided catalysts, shown in Figure 6.5, are quite different. The 2La FT catalyst appears have experienced the most physical damage. This observation is

consistent with the surface area results that show the 2La FT catalyst is the least physically stable catalyst after carbiding.

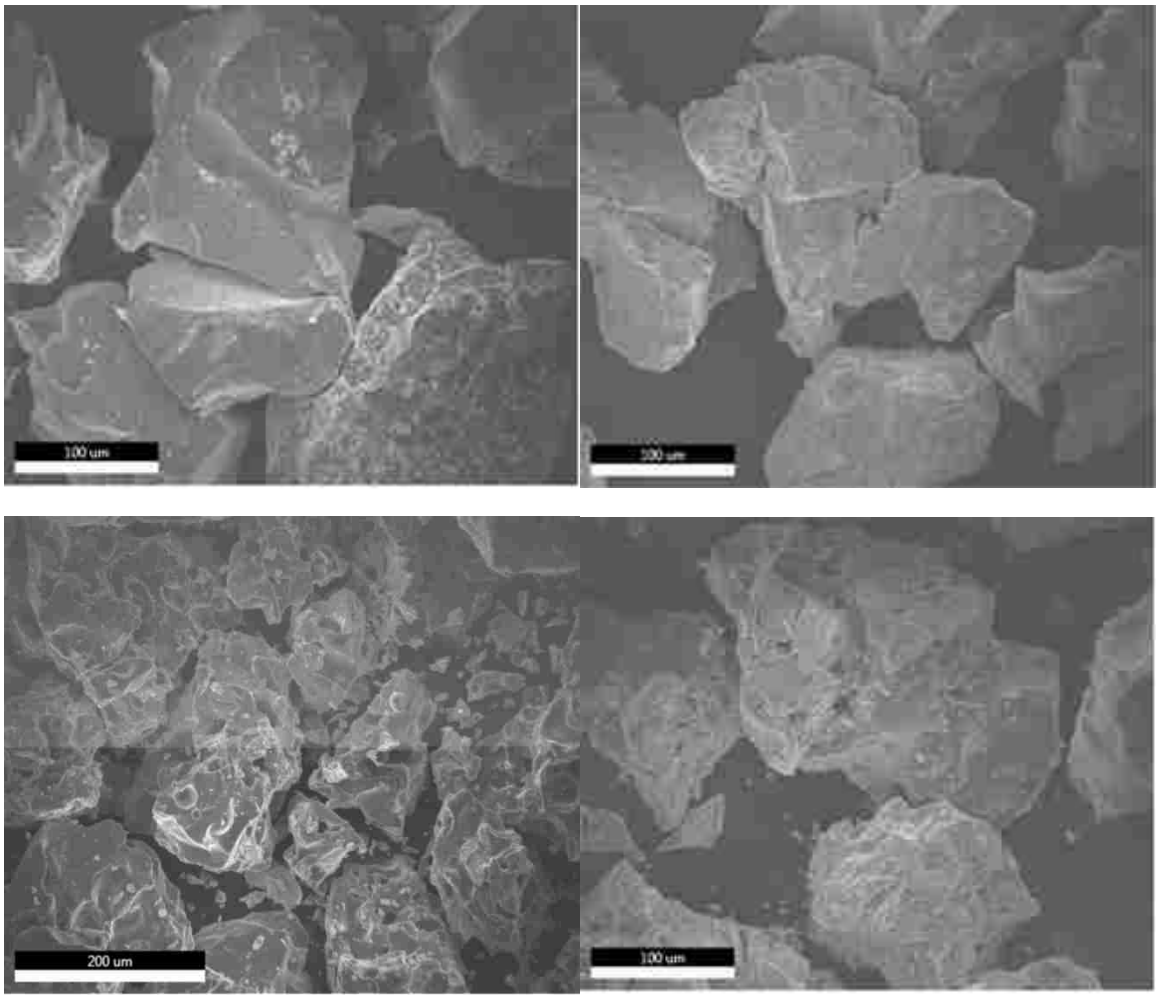

Figure 6.5: Scanning electron micrographs of carbided 0La FT (top left), carbided 0.5La FT (top right), carbided 2La FT (bottom left), and carbided 2La/2K FT (bottom right).

6.2.4 X-Ray Mapping

Differences in the elemental distribution among the different catalysts are depicted in X-ray maps of 100 μm agglomerates shown in Figures 6.6 - 6.9.

The X-ray maps of the 0La FT catalyst suggest that the K and Cu promoters are well distributed when compared to Fe. The dark spots observed in Figures 6.6a, b, and c are due to the uneven surfaces of the catalyst and not to uneven distribution of the components. Si distribution, however, is less satisfactory, as shown by the increased number of bright and dark spots observed in Figure 6.6d. Oxygen distribution shown in Figure 6.6e is quite similar to that of Si, suggesting that the detected oxygen is attributed to silica, rather than to Fe, Cu, or K oxides.

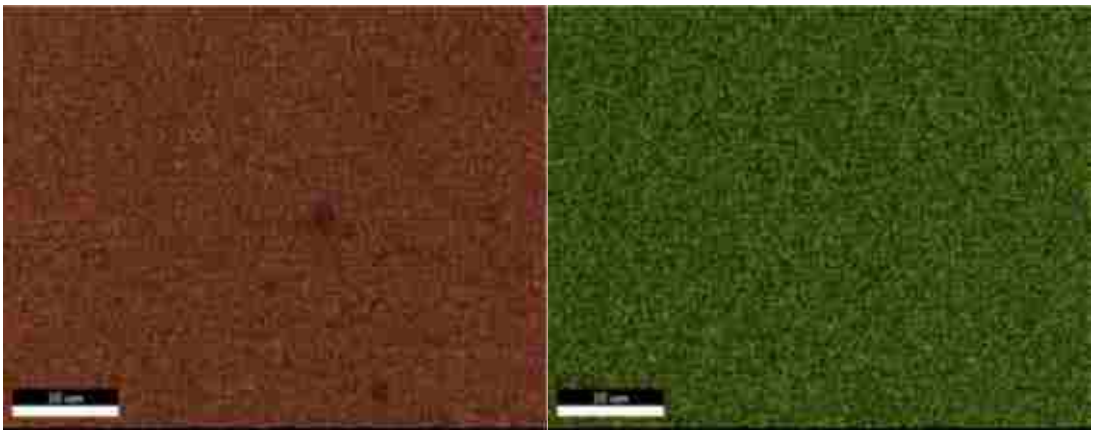

(a) Fe (b) Cu

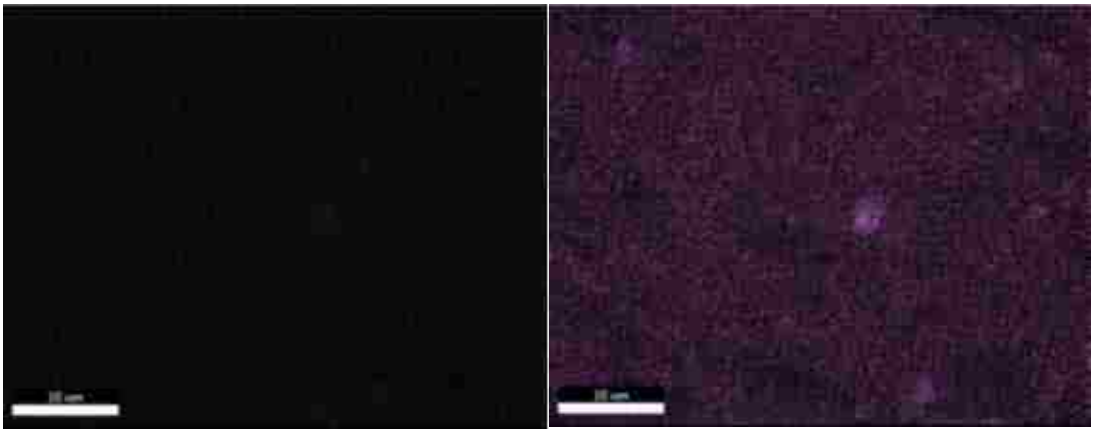

(c) K (d) Si

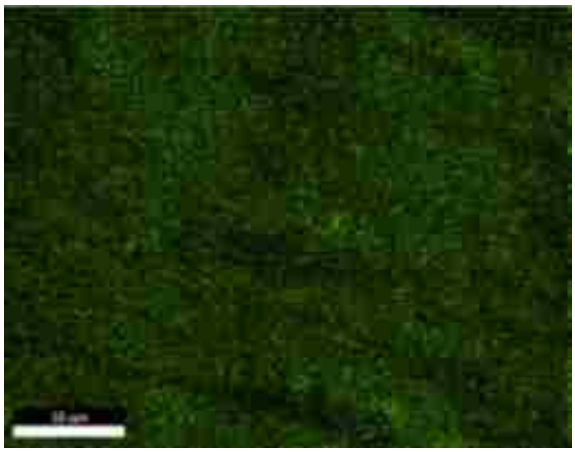

(e) O

Figure 6.6: X-ray maps for carbided 0La FT that show elemental distribution of (a) Fe, (b) Cu, (c) K, (d) Si, and (e) O.

The X-ray maps of the 0.5La FT catalyst suggest that the distribution of K, Cu, and La promoters is different from that of Fe. The contents of K, Cu, and La are less in areas where Fe is more concentrated. Si and O distributions are again similar, but worse than the promoters, as can be observed when the bright and dark spots in Figures 6.7e and 6.7f are compared to those of Fe in Figure 6.7a.

(a) Fe (b) Cu

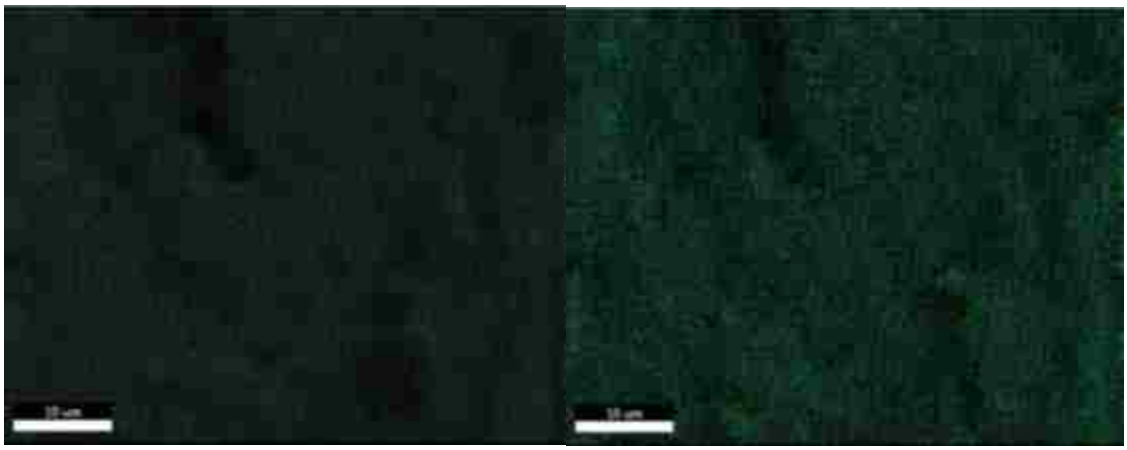

(c) K (d) La

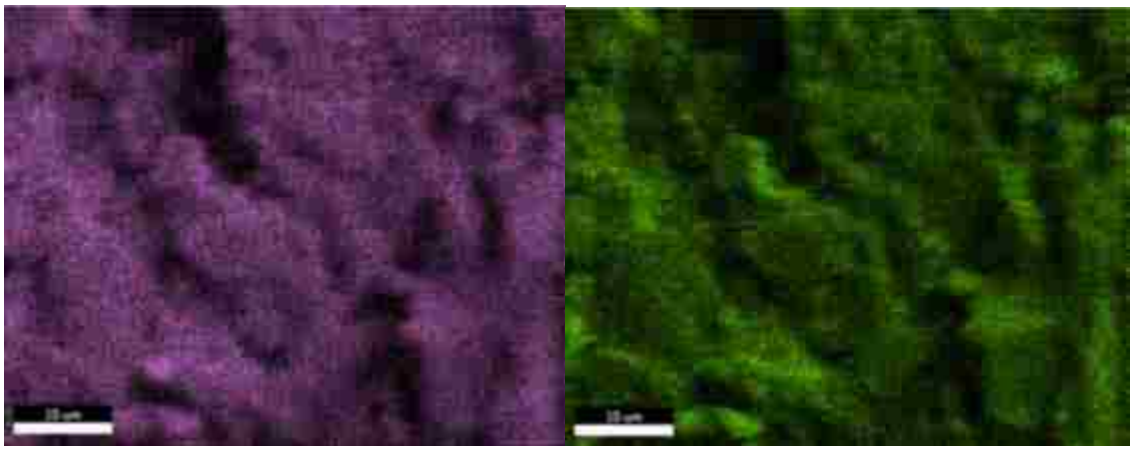

(e) Si (f) O

Figure 6.7: X-ray maps for carbided 0.5La FT that show elemental distribution of (a) Fe, (b) Cu, (c) K, (d) La, (e) Si, and (f) O.

Similar to 0.5La FT, the X-ray maps of the 2La FT catalyst suggest that the distributions of K, Cu, and La promoters are different from that of Fe, indicating real distribution changes rather than surface morphological effects. Fe is more concentrated in areas where Cu, K, and La are not. Si and O distributions are alike and again worse than the promoters.

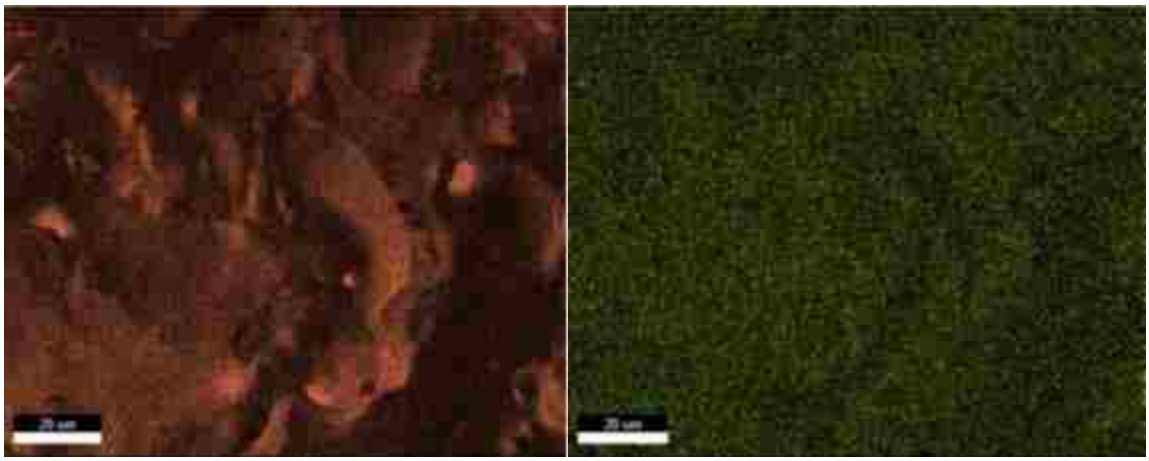

(a) Fe (b) Cu

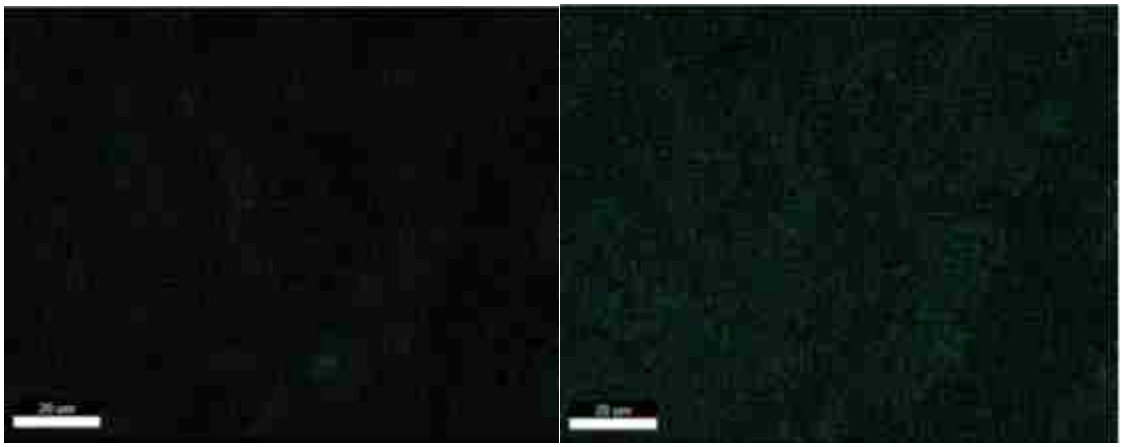

(c) K (d) La

(e) Si (f) O

Figure 6.8: X-ray maps for carbided 2La FT that show elemental distribution of (a) Fe, (b) Cu, (c) K, (d) La, (e) Si, and (f) O.

The X-ray maps of the 2La/2K FT catalyst suggest that the distributions of K, Cu, and La promoters are clearly better than those in the 0.5La FT and 2La FT catalysts. However, like the other samples, Si and O distributions are even less uniform, with clear similarity in the distribution of both elements.

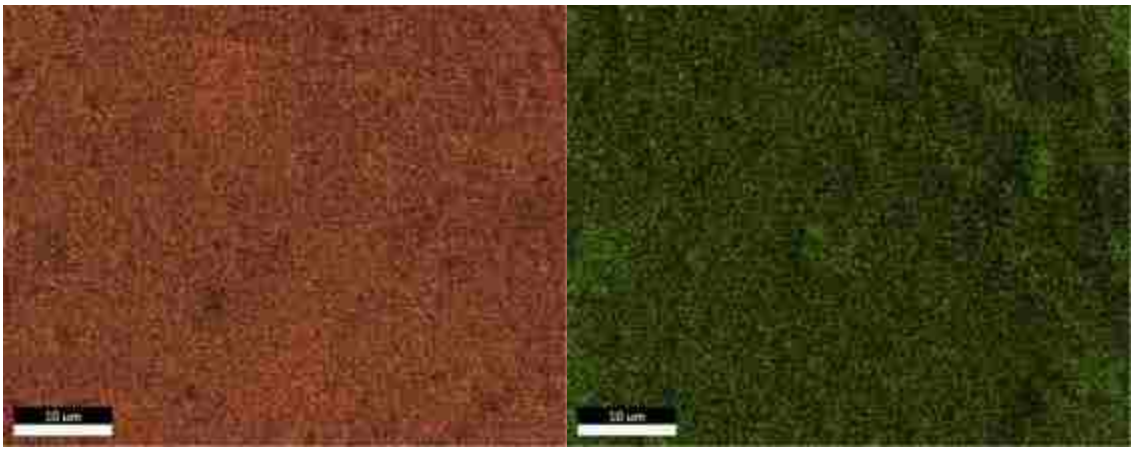

(a) Fe (b) Cu

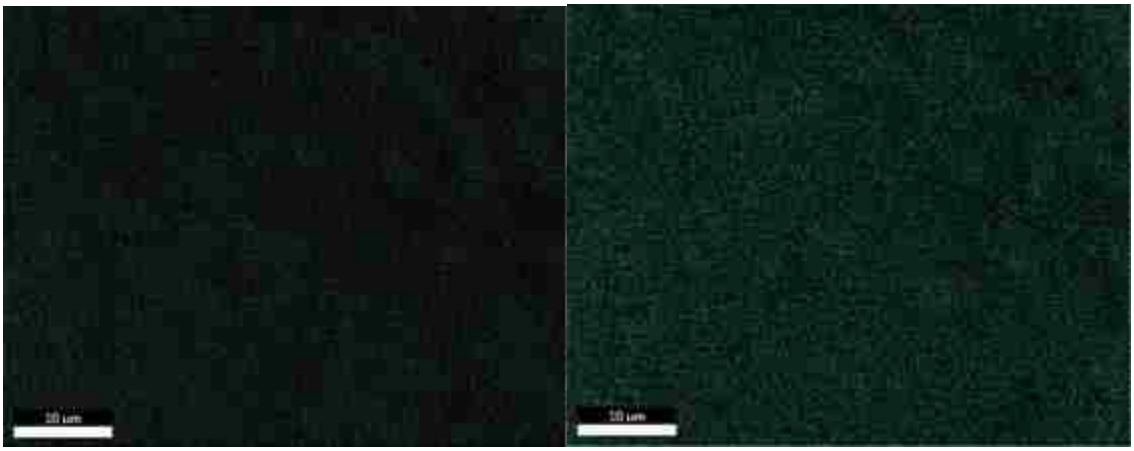

(c) K (d) La

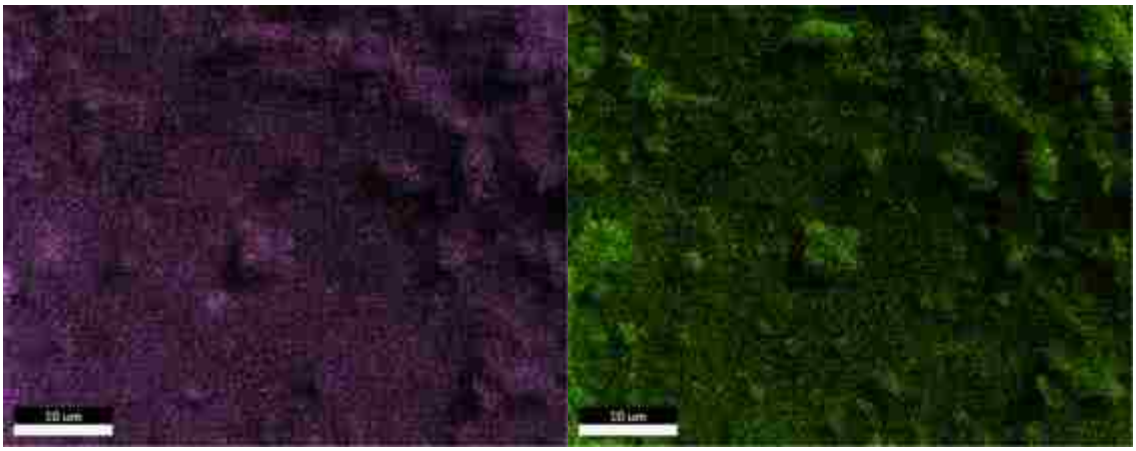

(e) Si (f) O

Figure 6.9: X-ray maps for carbided 2La/2K FT that show elemental distribution of (a) Fe, (b) Cu, (c) K, (d) La, (e) Si, and (f) O.

In summary, elemental distributions in the La-promoted catalysts are less uniform than that in the unpromoted catalyst. However, adding lanthana at the expense of potassium does not seem to impose any negative changes to the distribution of promoters. The uniformity of promoter distribution with Fe in the 0La FT and 2La/2K FT catalysts compared to the 0.5La FT and 2La FT can be explained in terms of the apparent incorporation of lanthana into the lattice structure, which affects the interaction of Fe and the other promoters and therefore segregates K and Cu from Fe. Si distribution is significantly different and less uniform than the other promoters for all of the catalysts, which is not unexpected because the SiO_2 is not a metal and is added to act as a textural promoter to increase surface area and dispersion of the other components. O distribution is very similar to that of Si, suggesting that the oxide phase is indeed largely SiO_2. Silicon's presence as an oxide after carbiding explains the significant segregation of this oxide phase from Fe and the other promoters.

6.2.5 CO Chemisorption

With the physical properties of fresh and carbided catalysts examined, the chemical properties of the FT catalysts are addressed in this section. The reduced 0.5La FT and 2La FT catalysts have the largest CO uptake, indicating that they chemisorbed the most CO. Further explanation of this observed behavior is presented in Figure 6.10 in the following section.

Table 6.7: CO chemisorption of reduced FT catalysts.

Catalyst ID	% mass increase	CO uptake (μmol CO/g_{cat})
0La FT	0.62	221
0.5La FT	1.26	450
2La FT	1.48	529
2La/2K FT	0.30	107

6.2.6 Catalyst Performance: Activity, Selectivity, and Stability

The overall reaction rates of the FT catalysts are compared in Table 6.8. The FTS reaction rate is lowest for the 2La FT catalyst and highest for the 0La FT catalyst. However, 2La/2K FT performed nearly as well as the 0La FT at 240°C and 250°C and even better at the higher reaction temperature of 260°C. This is in in good agreement with the surface area pattern noted in Table 6.5, consistent with higher stability for the 2La/2K FT and therefore enhanced performance at higher temperatures. According to the XRD and X-ray mapping characterization results, the carbided 0.5La FT and 2La FT catalysts exhibited iron dispersion and promoter distributions that are worse than those shown by the carbided 0La FT and 2La/2K FT catalysts. These factors are believed to affect the FTS activity of these FT catalysts. The rate of CO depletion ($-r_{CO}$) for the 0La FT catalyst was compared with Brunner's best catalyst 1UHa [86], after first adjusting the reaction conditions to those used in Brunner's work. The value of $-r_{CO}$ for the 1UHa catalyst is 38.5 mol kg^{-1} h^{-1} as reported in [86] and is 46.6 mol kg^{-1} h^{-1} after the

adjustments, which is about 75% of the measured value of the 0La FT catalyst reported in Table 6.8, indicating that the catalyst prepared for this work is superior as far as rate is concerned. This value also shows excellent agreement with the modeling results presented in Chapter 5.

Table 6.8: Activity and activation energies of FT catalysts at 320 psi with P^0_{CO} = 9.91 atm, $P^0_{H_2}$ = 10.59 atm, P^0_{Ar} = 1.26 atm. Rates are lower for the lanthana-promoted catalysts.

Catalyst ID	E_a (kJ/mol)	TOS (h)	T (°C)	X_{CO} (%)	X_{CO+H_2} (%)	$-r_{CO}$ (mol kg^{-1} h^{-1})	r_{CO+H_2} (mol kg^{-1} h^{-1})
0La FT	86.9 ± 13.5	166	240	7.15	7.58	48.9	104.3
			250	9.08	11.5	62.1	146.3
			260[a]	13.9	14.0	95.0	197.6
0.5La FT	104.9 ± 1.26	170	240	4.88	5.18	33.4	71.2
			250	7.73	7.36	52.9	106.7
			260	12.2	10.6	83.1	160.3
2La FT	97.3 ± 0.28	153	240	4.87	5.56	33.3	73.4
			250	7.53	7.40	51.5	105.6
			260	11.4	9.58	77.8	147.8
2La/2K FT	95.8 ± 23	168	240	6.58	6.51	45.0	92.5
			250	8.45	9.52	57.8	127.3
			260	14.1	13.7	96.3	196.1

[a] The reaction rate at 260°C was adjusted from 261.8°C using E_a for 0La FT.

The stability of the catalysts is compared in Figure 6.10, which plots the catalytic activity as a function of time during activation at 250°C. 0La FT and 2La/2K FT are more stable, with no deactivation observed for the first 65 h. In contrast, although 2La FT activates the fastest, it is clearly the least stable, as it starts deactivating after 28 h onstream. The faster activation of 2La FT and 0.5La FT catalysts is consistent with the chemisorption results reported in Section 6.2.5 where the 2La FT catalyst adsorbed CO the most. Furthermore, high CO uptakes can possibly mean carbon deposition, and therefore deactivation of the catalyst.

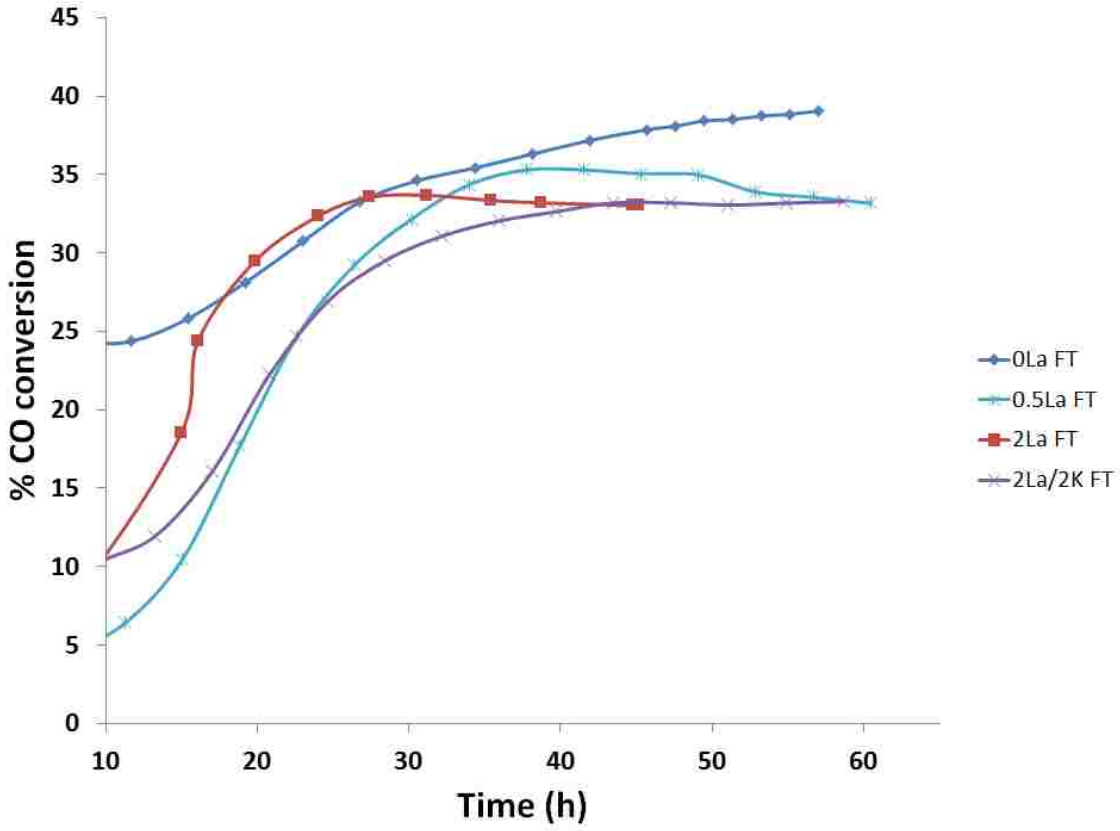

Figure 6.10: Activation of FT catalysts at 250°C.

Selectivity is the final performance metric that is discussed in this section. Table 6.9 reports the olefin (ethylene) to paraffin (ethane) ratios (O/P) as well as the selectivities of CO_2 (S_{CO_2}), methane (S_{CH_4}), ethane and ethylene (S_{C_2}), and hydrocarbons heavier than C_2 (S_{3+}) for all of the catalysts.

S_{CH_4} and S_{C_2} increase with increasing lanthana content, which makes 0La FT the most selective catalyst to liquid hydrocarbons. Increasing basicity is a well-established method to decrease cracking catalytic sites and therefore decrease methane selectivity [85, 158]. Despite the increasing basicity, the pore volumes of carbided 0.5La FT and 2La FT catalysts are significantly lower than that of 0La FT, which possibly decrease the selectivity to liquid hydrocarbons. This correlation between pore volume and hydrocarbon selectivity has also been observed by others

[159, 160]. The scenario is quite different for the 2La/2K FT catalyst because it has lower potassium content and therefore higher methane selectivity than 0La FT. A more thorough future study that includes ammonia TPD should be performed to further understand the effect of basic sites on S_{CH_4} as a function of pore volume. With regards to O/P ratio, lanthana clearly enhances the yield of olefins (based on the yield of ethylene). The presence of the basic oxide phase of lanthana can possibly suppress the adsorption of hydrogen or enhance the desorption of olefins on the catalyst surface and therefore inhibit olefin hydrogenation.

Table 6.9: Selectivities of FT catalysts at 320 psi with $P^0{}_{CO}$ = 9.91 atm, $P^0{}_{H_2}$ = 10.59 atm, $P^0{}_{Ar}$ = 1.26 atm. Methane and water-gas shift activities are higher with the lanthana-promoted catalysts.

		Selectivities				CO_2-free selectivities			
Catalyst ID	T (°C)	S_{CO_2} (%)	S_{CH_4} (%)	S_{C_2} (%)	S_{3+} (%)	S_{CH_4} (%)	S_{C_2} (%)	S_{3+} (%)	O/P[a]
0La FT	240	15.8	2.52	3.19	78.5	3.00	3.79	93.2	0.443
	250	21.6	3.13	3.34	71.9	4.00	4.26	91.8	0.397
	260	25.1	3.37	3.11	68.4	4.51	4.15	91.4	0.398
0.5La FT	240	29.0	4.77	4.45	61.7	6.73	6.27	87.0	0.584
	250	31.3	5.02	3.91	59.8	7.31	5.68	87.0	0.527
	260	33.2	5.37	3.70	57.7	8.05	5.54	86.4	0.541
2La FT	240	25.1	3.90	4.35	66.6	5.21	5.80	89.0	0.492
	250	28.8	4.07	3.89	63.3	5.72	5.45	88.8	0.442
	260	31.7	4.61	4.10	59.6	6.74	6.00	87.2	0.472
2La/2K FT	240	16.0	4.06	3.57	76.3	4.83	4.26	90.9	0.689
	250	23.5	5.04	4.61	66.8	6.59	6.02	87.4	0.659
	260	28.3	5.58	4.06	62.0	7.79	5.67	86.5	0.674

[a] O/P is calculated using the ratio of the yields of ethylene to ethane.

6.2.7 Water-Gas Shift Activity

The WGS activity of the catalysts increases with increasing temperature and lanthana content and decreasing potassium content, as shown in the third column of Table 6.9. Previous researchers reported that the WGS activity of FTS iron-based catalysts increases with increasing potassium content, increasing reaction temperature, decreasing reaction pressure, and decreasing space velocity [85, 161]. Therefore, adding lanthana, that is a basic oxide like K_2O, might facilitate the adsorption and dissociation of H_2O molecules produced during the FTS reaction

and the dehyrdrogenation of the formate species produced during the WGS reaction and hence increase the WGS rate [162]. S_{CO_2} is lower for the 2La/2K FT catalyst because of the lower potassium content. Compared to Brunner's 1 UHa [86], the WGS selectivity of the 0La FT catalyst is 1.5 times lower than that of 1UHa, despite the fact that they have been prepared in the same way with the same chemical constituents. The explanation to this observation can be approached in three ways: (1) The inlet partial pressures of CO and H_2 used in this study are higher than those used by Brunner [86]. The WGS activity depends heavily on and is inversely proportional to the partial pressure of H_2 in the reactor, meaning that increasing the partial pressure of H_2 in the reactor decreases the WGS activity [96,98,100,101]. (2) The activation processes in both studies are different in that the conversion was controlled very carefully in this study to abstain from temperature rises above 3°C and therefore avoid the formation of hot spots in the catalyst. Hot spots might increase the WGS activity of the catalyst. (3) The CO conversions in this study were about 10% which might have been lower than the CO conversions achieved in Brunner's work [86]. High CO conversions increase the partial pressure of H_2O and decrease the partial pressure of H_2, which therefore increase the WGS rate.

Furthermore, based on the data presented in the activation plot in Figure 6.10, the carbide content is expected to increase for the 0La FT and the 2La/2K FT catalysts as their rates keep increasing, which would result in fewer active sites (Fe_3O_4) for the WGS reaction. However, the opposite behavior was observed for these catalysts under WGS conditions (400°C, 1 atm, and Fe_3O_4 active phase), as shown in Figure 6.11. This performance follows the $-r_{CO}$ trend in Table 6.8 and the opposite trend of S_{CO_2} presented in Table 6.9. The explanation to this resides in the previously described physical and chemical characteristics of the catalysts, including surface area, promoter dispersion, crystallite sizes, and extent of reduction. The 2La FT catalyst has the

lowest surface area, least uniform promoter distribution, largest crystallite size, and the least stability, which suggests that it performs the worst under WGS reaction conditions. Extent of reduction is also a crucial characterization for the WGS reaction, since Fe_3O_4 is the active phase and therefore the catalysts can experience under/over-reduction from the active phase. Further, the water-gas shift activity under water-gas shift conditions is ~12 times higher than that under FT conditions, which might suggest that temperature plays a bigger role that pressure does in the activity of these catalysts that have ~100 kJ/mol activation energies. The significance of this work and Figure 6.11 is that evaluating the WGS activity of FT catalysts under WGS conditions is not reliable to explain and to clarify the selectivity performance of these catalysts under FT conditions.

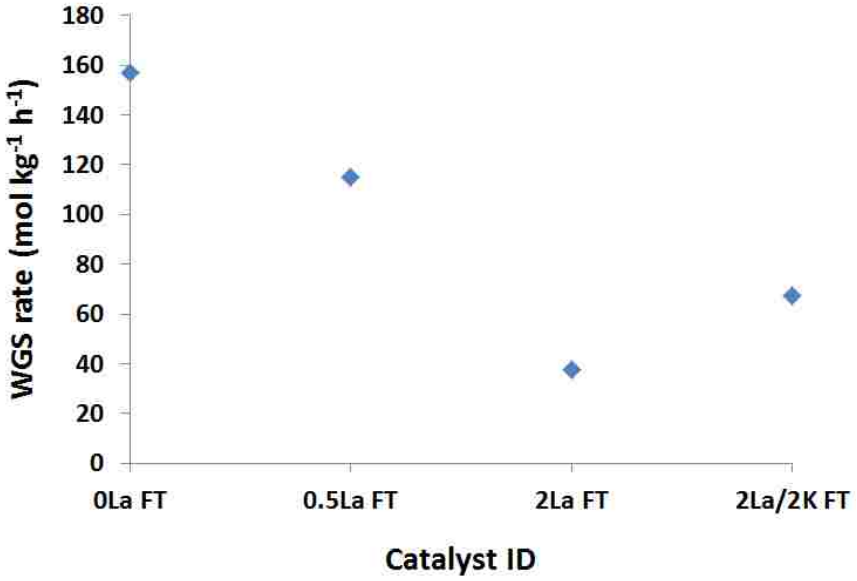

Figure 6.11: WGS activity of FT catalysts at 400°C and 1 atm on the Fe_3O_4 active phase.

The WGS study of the 0La FT catalyst under FT conditions was unsuccessful due to deactivation, as can be concluded from Table 6.10, which shows the catalyst becomes less FTS active after the WGS runs. The runs along with the operating conditions were given in Table 6.4. The deactivation does not seem to be due to oxidation of catalyst because the CO conversion to

CO_2 decreases from FTS run 1 to FTS run 2 (as observed by the GC peak areas), suggesting that Fe_3O_4 content is not increasing with reaction time and CO partial pressure. Furthermore, an increase in methane selectivity and a decrease in CO_2 selectivity were observed during FTS activity after FTS run 2 when the GC peak areas are compared to those of the first run (initial FTS activity) with larger peak area for CO (meaning lower CO conversion) and larger peak area for CH_4 (meaning higher selectivity to CH_4). This suggests that indeed the catalyst did not oxidize when water was introduced. This observation was also seen by another research group that shows introduction of water at high reaction temperatures (>230°C) does not oxidize the catalyst [163]. The probable explanation to the observed deactivation is that carbon deposition competes with catalytic oxidation at high reaction temperatures and pressures and low H_2O:CO ratios. The observed increase in methane selectivity and decrease in CO_2 selectivity are attributed to the introduction of higher partial pressures of water that might cause an increase in the concentration of OH groups making the catalyst surface more acidic. Increasing acidic sites increase methane selectivity and lower CO_2 selectivity [158]. Therefore, no rate model can be derived due to limited data and the concurrent deactivation.

Table 6.10: WGS study on 0La FT at 250°C and 320 psi on the χ-Fe_5C_2 active phase.

Experiment [a]	T (°C)	PA_{CO}	PA_{CO_2}	PA_{CH_4}
Initial FTS activity	250	61791	5048	489
FTS run 1	250	93894	10873	0
FTS run 2	250	96001	8092	0
FTS activity after FTS run 2	250	79422	4215	610

[a] The run ID's were given in Table 6.4.

6.2.8 Conclusions

The effect of small amounts (≤2 wt%) of lanthana addition to standard Fe/Cu/K/Si Fischer-Tropsch catalysts was investigated. The results showed that lanthana addition produced catalysts that are less active for FTS and less selective to liquid hydrocarbons. However, lanthana addition at the expense of potassium produced a catalyst that has higher surface area and pore volume that performs very similar to the catalyst with no lanthana in terms of activity and selectivity to CO_2, but higher selectivity to CH_4. The catalyst with no lanthana has the highest selectivity to liquid hydrocarbons. Characterization techniques performed on the carbided catalysts suggest that these results are primarily due to larger crystallites and less uniform promoter and Fe distributions with the lanthana-promoted catalysts. The primary positive effect of lanthana addition lies in increasing the olefin to paraffin ratio. Finally, the water-gas shift study of these Fischer-Tropsch catalysts suggests that they behave differently under water-gas shift conditions with water-gas shift activity that is significantly lower than the actual water-gas shift catalysts.

CHAPTER 7. SUMMARY AND RECOMMENDATIONS FOR FUTURE WORK

This chapter summarizes the work presented in this dissertation and recommends future work that can be continued based on this work.

7.1 Summary

Crude oil serves as one of the primary energy resources to the world. Considering that these resources are not just dwindling in abundance, but also are becoming harder and more expensive to extract from deep offshore areas, it is essential that alternative energy resources and more feasible chemical processes are developed. The work presented in this dissertation focused on the production of: (1) hydrogen *via* the water-gas shift reaction and (2) liquid hydrocarbons *via* the Fischer-Tropsch synthesis reaction, as alternative energy sources. Both of these reactions are related in a manner that the former reaction is a side-reaction of the latter on iron-based catalysts; therefore, a significant effort is invested in the water-gas shift activity of iron-based catalysts. Water-gas shift catalysis has been thoroughly studied over the past few decades; however, industrial plants look for more active catalysts that can provide higher yields of hydrogen, as well as more stable catalysts that can withstand and operate at high reaction temperatures. Fischer-Tropsch technology gained much attention from researchers in the past few years due to the abundant supply of natural gas that became more accessible with hydraulic fracturing technology and the potential for renewable energy sources, such as biomass. The

Fischer-Tropsch process has been commercialized worldwide by large energy companies like Shell and Sasol. Enhancement of the activity, selectivity, and stability of Fischer-Tropsch catalysts, however, is required for higher yields and more economic production of the desired products.

The work presented in this dissertation focused on studying the effect of lanthana addition to unsupported iron-based catalysts for the water-gas shift reaction and Fischer-Tropsch synthesis, taking into consideration that the water-gas shift reaction is a side reaction of the Fischer-Tropsch synthesis on iron-based catalysts. In addition to that, a new technique that uses UV-visible spectroscopy was applied to quantify the extent of reduction of iron during water-gas shift catalysts. Finally, a particle model was developed and optimized to map heat and mass transfer limitations as well as pressure drop for Fischer-Tropsch catalysts under different operational (reaction temperature, reaction pressure, and feed syngas composition) and design (pellet size) conditions. The model was validated with experimental data and was scaled-up to model commercial-size reactors.

The main findings of the projects discussed in this dissertation are presented in the following sections along with recommendations for relevant future research work.

7.2 Study on Water-Gas Shift Catalysts

Unsupported iron-based $Fe_2O_3/Cr_2O_3/CuO$ high-temperature water-gas shift catalysts were prepared with varying amounts of lanthana (0, 0.5, 1, 2, and 5 wt%) added at the expense of Fe_2O_3 *via* co-precipitation. This study examined the structural and functional roles that lanthana played in modifying these catalysts. These effects are highlighted below:

- Minor addition of lanthana (0.5 wt%) promotes water-gas shift activity (30% increase) and enhances the stability (50% increase) of the catalysts, apparently through the stabilization of the iron-chromium cubic spinel, while further addition of lanthana disrupts the spinel structure.
- XRD results suggest that adding 0.5 wt% of lanthana to the water-gas shift catalysts increases their crystallinity and crystallite sizes. The crystallinity of these catalysts was attributed to the iron-chromium spinel structure that forms once the catalysts are activated and Fe_2O_3 converts to Fe_3O_4.
- Stabilization of the spinel results in larger surface area of the reduced catalyst with 0.5 wt% lanthana, which implies a more physically stable catalyst that performs much better at higher reaction temperatures. SEM images also show that this catalyst appears more physical stable than the other tested catalysts.
- Addition of 0.5 wt% of lanthana enhances the reducibility of the catalysts by decreasing the reduction temperature. Furthermore, it increases the extent of reduction of Fe_2O_3 to Fe_3O_4, but not to metallic Fe.
- Modeling kinetic data show that the water-gas shift reaction over these catalysts tends to follow an adsorptive, Langmuir-Hinshelwood type mechanism, rather than a reduction-oxidation mechanism
- Kinetic parameters that were used to fit data to four rate models suggest that the catalyst with 0.5 wt% lanthana promotes CO adsorption on the catalyst surface.
- Statistical analysis and 95% confidence regions for the adsorption equilibrium constants of CO and H_2O suggest that H_2O adsorbs more strongly than CO, which covers much of the catalyst surface and therefore inhibits the reaction activity. These observations are

reflected in the kinetic parameters for the power-law model, which show zero to slightly negative dependency on H_2O concentrations and positive dependency (~ 1) on CO concentrations.

7.3 *Operando* UV-Visible Study

Operando UV-visible spectroscopy was used to quantify the extent of reduction of iron in high-temperature water-gas shift catalysts. The goal of this technique is to study the surface chemistry and oxidation states of iron in these catalysts and to ultimately replace XANES for determining oxidation states. Extent of reduction is a key characterization for the water-gas shift catalysts because it quantifies the amount of active Fe_3O_4 phase. The following bullet points are the key findings of this study:

- Temperature-programmed reduction experiments show that addition of 0.5 wt% of lanthana decreases the reduction temperature of the catalysts, increases the extent of reduction to Fe_3O_4, and decreases the extent of reduction to metallic Fe. These observations are attributed to the stabilization of the iron-chromium spinel that forms once the catalysts are activated and Fe_2O_3 converts to Fe_3O_4.
- Second temperature-programmed reduction experiments performed on the same catalysts after re-oxidation prove that the catalyst with 0.5 wt% lanthana is the most stable catalyst, with only 8% decrease in its reducibility, compared to 50% decrease in reducibility for the unpromoted (i.e., without La) catalyst.
- XRD results suggest the presence of a mixture of metallic Fe and Fe_3O_4 after TPR experiments. FeO appears to decompose into Fe and Fe_3O_4.

- Simultaneous measurements of light absorption as a function of reduction temperature show increases in the absorption when the catalysts first reduce from Fe_2O_3 to Fe_3O_4 (first reduction phase) and Fe_3O_4 to Fe (second reduction phase).
- Increase in absorption was normalized relative to a fully-oxidized catalyst surface using the Kubelka-Munk function. The Kubelka-Munk values acquired from the surfaces of the reduced catalysts were calibrated against surface oxidation state of Fe. The extents of reduction that were used in generating the calibration curve were acquired from peak integrations of the TPR profiles.
- Applying the calibration curve to water-gas shift catalysts under operation shows that addition of 1 wt% of lanthana causes higher extents of reduction than those for the unpromoted catalysts. Over-reduction to oxidation state lower than $Fe^{+2.7}$ for the catalyst with 1 wt% lanthana is a reasonable conclusion when the TPR profiles and is a possible explanation for the lowered water-gas shift activity.
- XANES analysis showed that the oxidation state of Fe in the unpromoted catalyst was higher than the catalyst with 1 wt% lanthana, suggesting that lanthana increases the extent of reduction. This work suggests that UV-visible spectroscopy is a potential and more sensitive tool for studying surface chemistry and oxidation states.

7.4 Meso-Scale Optimization and Modeling of Fischer-Tropsch Catalysts

A simulation model that evaluates the performance of iron-based Fischer-Tropsch catalysts under different laboratory-scale operating and design conditions in a fixed-bed reactor was developed and optimized. The results of this work are significant because the model shows excellent agreement with experimental data and presents comprehensive contour maps of mass

and heat transfer limitations and pressure drop as functions of critical design (pellet size) and operating (reaction temperature, reaction pressure, and feed syngas composition) variables that make the interdependencies and the effects of variables easier to visualize. Therefore, this model can save experimentalists time as it gives them guidance to the experimental design and operating conditions before preparing and testing samples in a fixed-bed reactor. The goal of this work was to determine the optimal design and operational conditions that minimize pore diffusion, heat transfer limitations, pressure drop, and catalytic deactivation in order to achieve a kinetically-limited reaction rate with reasonable catalytic performance. Significant conclusions are:

- The catalyst pellet size and the resulting void fraction affect the pressure drop, which is important for the model to simulate while solving for the optimal pellet size.
- Higher reaction temperatures, higher reaction pressures, smaller pellet sizes, and lower feed CO compositions are favored for a maximized observed reaction rate that is not limited by heat or mass transfer resistances.
- Optimal reaction temperatures should not exceed 256°C to keep catalytic deactivation below 50% after 1000 h onstream.
- Decreasing the pellet size is only limited by the lower bound specified by the user to avoid small particles causing excessive pressure drop or plugging the reactor. Pressure drop is not a concern under laboratory conditions.
- Pore diffusion limitations are negligible (effectiveness factor above 97%) for pellet sizes below 250 μm. The effectiveness factor decreases to 78% at 425 μm pellet sizes, 250°C, 20 bar, and equimolar H_2/CO ratio.

- Intraparticle heat transfer resistance is negligible compared to film heat transfer resistance. They both are not limiting resistances in the pellet size range of 200 – 600 μm. However, film heat transfer resistance becomes limiting at pellet sizes above 1000 μm.
- The optimal cylindrical pellet size was 1.1 mm, with a 57% effectiveness factor and 4 bar pressure drop for a commercial-size reactor operating at 20 bar, 250°C, and equimolar H_2/CO ratio with 3 kg catalyst in 1 inch inside diameter fixed-bed reactor.

7.5 Study on Fischer-Tropsch Catalysts

Unsupported iron-based Fe/Cu/K Fischer-Tropsch catalysts were prepared with varying amounts of lanthana (0, 0.5, and 2 wt%) *via* the solvent-deficient precipitation method. A separate sample was prepared with 2 wt% lanthana added at the expense of K. This study examined the performance of these four catalysts in terms of activity, selectivity, and stability. Furthermore, their water-gas shift activities were also studied. The findings from this project are highlighted below:

- Addition of lanthana lowers the Fischer-Tropsch activity of the catalysts, decreases their stability, and increases their water-gas shift and methane selectivities. Adding lanthana at the expense of potassium increases the activity and stability of the catalysts and also lowers their water-gas shift selectivity when compared to a lanthana-promoted catalyst with a similar lanthana content.
- Addition of lanthana enhances the olefin-to-paraffin ratio. The ratio is highest for the catalyst with 2 wt% lanthana added at the expense of potassium.

- The surface area and pore volume of the carbided catalysts are notably smaller for the catalyst with 2 wt% lanthana. These measurements are largest for the catalyst with 2 wt% lanthana added at the expense of K.
- Methane selectivity is proportional to the catalyst pore volume.
- Catalysts that are the least active, stable, and selective to liquid hydrocarbons, which are the catalysts with 0.5 wt% and 2 wt% lanthana, contain the least uniform dispersion of iron and promoters.
- XRD results show that addition of lanthana increases the crystallite sizes of the catalysts and therefore might decrease dispersion of iron and the iron carbide active phase.
- The water-gas shift activities of the Fischer-Tropsch catalysts under water-gas shift conditions (400°C, 1 atm, and Fe_3O_4 active phase) follow the opposite trend of the water-gas shift selectivities observed under Fischer-Tropsch conditions.
- Modeling the water-gas shift kinetic data under Fischer-Tropsch conditions was unsuccessful due to catalytic deactivation.

7.6 Original Contribution

The most significant contributions that this dissertation adds to the scientific community are as follows:

- The development of a new iron-based high-temperature water-gas shift catalyst that is more active and stable than current industrial-like catalysts and that can operate at higher reaction temperatures, yet maintains its stability.

- The development of 95% confidence regions for the adsorption equilibrium constants of carbon monoxide and water. These contour plots allow visualization of the dependency of one reactant on the other in the feasible 95% confidence space as well as the relative interaction of each reactant with the surface of the catalyst.
- The development of a calibration curve that correlates surface iron oxidation states to Kubelka-Munk measurements obtained from diffuse reflectance UV-visible spectrometry. The calibration curve was applied to operating iron-based water-gas shift catalysts, with the results compared to those obtained from X-ray absorption near-edge structure analysis.
- The development of a model that optimizes design and operational conditions for the Fischer-Tropsch reaction in a fixed-bed reactor. The model also generates comprehensive contour plots that map pore diffusion, internal heat transfer, film heat transfer, pressure drop, and catalytic deactivation as function of particle sizes, reaction temperatures, reaction pressures, and feed syngas compositions.
- The development of a new unsupported iron-based Fischer-Tropsch catalyst that includes the addition of lanthana at the expense of potassium, which increases the olefin-to-parrafin ratio. This finding spotlights new ideas and protocols for the synthesis and preparation of unsupported iron-based Fischer-Tropsch catalysts.

7.7 Future Work and Recommendations

The following studies and investigations are recommended for further scientific advancement based on the projects completed in this dissertation:

- A study on the effect of 0.2 wt% lanthana added to unsupported high-temperature water-gas shift catalysts is recommended for further enhancement of the activity and stability of these catalysts.
- High-temperature water-gas shift catalysts prepared for this study used lanthana as the only promoter for industrial-like catalysts. Future studies should consider the addition of minor amounts other rare-earth oxides (such as ceria) and other transition metal oxides (such as silver or lead oxides) and other noble metals (such as platinum) to further enhance the performance of these catalysts.
- The development of a new microkinetic model that is derived from elementary mechanistic steps and that describes the water-gas shift kinetics more accurately over the unsupported iron-based water-gas shift catalysts is recommended. The model needs to be fit to more kinetic data to obtain more statistically reliable reaction rate and equilibrium constants.
- A study that investigates the effect of pellet size of iron-based water-gas shift catalysts on Kubelka-Munk measurements is needed. This study can be incorporated into the work presented in this dissertation to develop a calibration curve that considers pellet size as one of the variables.
- XANES analysis used in this study was an *ex-situ* analysis. *Operando* XANES measurements on iron-based water-gas shift catalysts are required for more accurate bulk oxidation state measurements.
- The development of a new technique that investigates the extent of carbiding of iron-based Fischer-Tropsch catalysts using UV-visible spectroscopy would extend the results presented here. These catalysts become darker in color (more black) as they carbide.

Therefore, the amount of light absorbed relative to a catalyst that is fully reduced with hydrogen (meaning that the surface contains metallic iron only) can be calibrated against the extent of carbiding. The acquired spectra can be compared to spectra for reference χ-Fe_5C_2 and graphite samples to determine if the increase in absorption spectra is due to carbon deposition or carbiding of iron. This work could be very useful for deactivation studies.

- The meso-scale model assumes fixed selectivities for modeling the product distribution of the iron-based Fischer-Tropsch catalysts. Incorporating a selectivity model is warranted for accurate optimization of the yield of the desired products that excludes any light gases.
- Incorporating a rate model for the water-gas shift reaction in FTS is crucial for determining selectivity to carbon dioxide.
- Non-homogeneous temperature gradients are required to describe heat transfer limitations in the model for a commercial-size FTS reactor.
- The Thiele modulus used in this study considers a power-law rate model that depends on carbon monoxide concentration. Deriving a more rigorous expression for the Thiele modulus using more accurate rate expressions would be an improvement.
- Preparation of unsupported iron-based Fischer-Tropsch catalysts with lanthana content < 0.5 wt% is needed to observe any possible enhancements of activity, selectivity, and stability of these catalysts.
- The catalyst with optimal lanthana content should be prepared again with lanthana added at the expense of potassium. The experimental design should consider changing both variables.

- Other preparation details, such as drying temperature, calcination temperature, and activation temperature, should be considered for promoting the performance of the iron-based Fischer-Tropsch catalysts.
- Ammonia temperature-programmed desorption studies need to be performed to further understand the effect of changing basicity with variable lanthana and potassium contents on the performance of the Fischer-Tropsch catalysts.

REFERENCES

[1] M. V. Twigg, Catalyst Handbook, 2nd ed. Wolfe, London, 1989.

[2] R. Ramachandran, K. M. Raghu, An overview of industrial uses of hydrogen, Int. J. Hydrog. Energy. 23 (1998) 593-598.

[3] C. H. Bartholomew, R. J. Farrauto, Fundamentals of Industrial Catalytic Processes, 2nd ed. Wiley-InterScience, New York, 2005.

[4] T. Sato, S. Kurosawa, R. L. Smith, T. Adschiri, K. Arai, Water gas shift reaction kinetics under noncatalytic conditions in supercritical water, J. Supercrit. Fluids. 29 (2004) 113-119.

[5] R. B. Anderson, The Fischer Tropsch Synthesis, Academic Press, Orlando, Florida, 1984.

[6] N. O. Elbashir, B. Bao, M. El-Halwagi, An approach to the design of advanced Fischer-Tropsch reactor for operation in near-critical and supercritical phase media, Advances in Gas Processing: Proceedings of the 1st Annual Symposium on Gas Processing Symposium (2009) 423–433.

[7] D. B. Bukur, X. Lang, A. Akgerman, Z. Feng, Effects of process conditions on olefin selectivity during conventional and supercritical Fischer-Tropsch synthesis, Ind. Eng. Chem. Res. 36 (1997) 2580–2587.

[8] C. H. Bartholomew, Recent technological developments in Ficher-Tropsch catalysis, Catal. Lett. 7 (1990) 303–315.

[9] B. M. Weckhuysen, A. A. Verberckmoes, J. Debaere, K. Ooms, I. Langhans, R. A. Schoonheydt, In situ UV-vis diffuse reflectance spectroscopy – *on line* activity measurements of supported chromium oxide catalysts: relating isobutane dehydrogenation activity with Cr-speciation via experimental design, J. Mol. Catal. A: Chem. 151 (2000) 115-131.

[10] I. E. Wachs, Recent conceptual advances in the catalysis science of mixed metal oxide catalytic materials, Catal. Today. 100 (2005) 79-94.

[11] P. Atkins, D. Shriver, Inorganic Chemistry, Oxford University Press, New York, U.S., 2006.

[12] C. N. R. Rao, Ultra-violet and visible spectroscopy: chemical applications, Butterworth-Heinemann, London, U.K., 1974.

[13] J. A. Tossell, D. Vaughan, K. H. Johnson, The electronic structure of rutile, wüstite and hematite from molecular orbital calculations, J. Am. Mineral. 59 (1974) 319-334.

[14] D. C. Koningsberger, R. Prins, X-ray absorption: principles applications techniques of EXAFS SEXAFS and XANES, chemical analysis, John Wiley & Sons, New York, U.S., 1988.

[15] K. K. Gunter, L. M. Miller, M. Aschner, R. Eliseey, D. Depuis, C. E. Gavin, T. E. Gunter, XANES spectroscopy: A promising tool for toxicology: A tutorial, Neurotoxicology. 23 (2002) 127-146.

[16] C. Bosch, W. Wild, Canadian Patent. 153.

[17] K. Kochloefl, in: G. Etrl, H. Knozinger, J. Weitkamp (Eds.), Handbook of heterogeneous catalysis, vol. 4, Wilet-VCH, Weinheim, 1997, pp. 1831-1843.

[18] C. N. Satterfield, Heterogeneous catalysis in industrial practice, 2nd ed., McGraw-Hill, New York, 1991.

[19] W. Ruettinger, O. Ilinich, in: S. Lee (Ed.), in: Encyclopedia of chemical processing, Taylor & Francis, 2006.

[20] D. S. Newsome, The water-gas shift reaction, Catalysis Reviews: Science and Engineering 21 (1980) 275-318.

[21] M. I. Markina, G. K. Boreskov, F. P. Ivanowski, L. Yudovskaya, Investigation of catalytic activity of iron-based catalysts in the process of water-gas shift reaction, Kinet Katal 2 (1961) 867-871.

[22] F. Domka, A. Basinka, R. Fieldcrow, Porous structure of Fe_2O_3 – Cr_2O_3 catalysts prepared from iron-oxide hydroxide systems, Surf. Coat. Tech. 18 (1983) 275-282.

[23] H. J. Yearian, J. M. Kortright, R. H. Langenheim, Lattice parameters of the $FeFe_{(2-X)}Cr_XO_4$ spinel system, J. Chem. Phys. 22 (1954) 1196-1198.

[24] D. M. Sherman, Oxide and hydroxide minerals, In AccessScience, McGraw-Hill, New York, 2008.

[25] G. K. Reddy, P. Boolchand, P. G. Smirniotis, Sulfur tolerant metal doped Fe/Ce catalysts for high temperature WGS reaction at low steam to CO ratios – XPS and Mössbauer spectroscopic study, J. Catal. 282 (2011) 258-269.

[26] G. Doppler, A. X. Trautwein, H. M. Ziethen, E. Akmbach, R. Lehnert, M. J. Sprague, U. Gonser, Physical and catalytic properties of high-temperature water-gas shift catalysts based upon iron-chromium oxides, Appl Catal. 40 (1988) 119-130.

[27] G. C. Chinchen, R. H. Logan, M. S. Spencer, Water-gas shift reaction over an iron oxide/chromium oxide catalyst III: Kinetics of reaction, Applied Catalysis 12 (1984) 97-103.

[28] Y. Tanaka, T. Utaka, R. Kikuchi, K. Sasaki, K. Eguchi, CO removal from reformed fuel over $Cu/ZnO/Al_2O_3$ catalysts prepared by impregnation and coprecipitation methods, Applied Catal. A: General 238 (2003) 11-18.

[29] C. Rhodes, P. B. Williams, F. King, G. J. Hutchings, Promotion of Fe_3O_4/Cr_2O_3 high temperature water gas shift catalyst, Catal. Commun. 3 (2002) 381-384.

[30] J. Y. Lee, D.-W. Lee, K.-Y. Lee, Y. Wang, Cr-free Fe-based metal oxide catalysts for high temperature water-gas shift reaction of fuel processor using LPG, Catal. Today 146 (2009) 260-264.

[31] E. Xue, M. O. O'Keeffe, J. R. H. Ross, Water-gas shift conversion using a feed with a low steam to carbon monoxide ratio and containing sulfur, Catal. Today. 30 (1996) 107-118.

[32] J. Xu, G. F. Froment, Methane steam reforming, methanation and water-gas shift: Intrinsic kinetics, AIChE J. 35 (1989) 88-96.

[33] W.-H. Chen, T.-H. Hsieh, T. L. Jiang. An experimental study on carbon monoxide conversion and hydrogen generation from water gas shift reaction, Energ. Convers. Manage. 49 (2008) 2801-2808.

[34] C. Rhodes, G. J. Hutchings, Studies of the role of the copper promoter in the iron-oxide/chromia high temperature water gas shift catalyst, Phys. Chem. Chem. Phys. 5 (2003) 2719-2723.

[35] M. A. Edwards, D. M. Whittle, C. Rhodes, A. M. Ward, D. Rohan, M. D. Shannon, G. J. Hutchings, C. J. Kiely, Microstructural studies of the copper promoted iron oxide/chromia water-gas shift catalyst, Phys. Chem. Chem. Phys. 4 (2002) 3902-3908.

[36] A. Puig-Molina, F. M. Cano, T. V. W. Janssens, The Cu promoter in an iron-chromium-oxide based water-gas shift catalyst under industrial conditions studied by in-situ XAFS, J. Phys. Chem. C. 114 (2010) 15410-15416.

[37] A. Andreev, V. Idakiev, D. Mihajlova, D. Shopov, Iron-based catalysts for the water-gas shift reaction promoted by first-row transition metal oxides, Appl. Catal. 22 (1986) 385-387.

[38] Y. Lei, N. W. Cant, D. L. Trimm, Activity patterns for the water gas shift reaction over supported precious metal catalysts, Catal. Lett. 103 (2005) 133-136.

[39] Y. Lei, N. W. Cant, D. L. Trimm, Kinetics of the water-gas shift reaction over a rhodium-promoted iron-chromium oxide catalyst, Chem. Eng. J. 114 (2005) 81-85.

[40] P. Patnaik, Handbook of Inorganic Chemical Compounds, McGraw-Hill, New York, 2002.

[41] E. Aneggi, M. Boaro, C. de Leitenburg, G. Dolcetti, A. Trovarelli, Insights into the dynamics of oxygen storage/release phenomena in model ceria-zirconia catalysts as inferred from transient studies using H_2, CO and soot as reductants, Catal. Today. 112 (2006) 94-98.

[42] Y. Hu, H. Jin, J. Liu, D. Hao, Reactive behaviors of iron-based shift catalyst promoted by ceria, Chem. Eng. J. 78 (2000) 147-152.

[43] C. Pellerin, S. M. Booker, Reflections on hexavalent chromium: health hazards of an industrial heavyweight, Environ. Health Persp. 108 (2000) A402-407.

[44] M. S. Lee, J. Y. Lee, D.-W. Lee, D. J. Moon, K.-W. Lee, The effect of Zn addition into $NiFe_2O_4$ catalyst for high-temperature shift reaction of natural gas reformate assuming no external steam addition, Int. J. Hydrog. Energ. 37 (2012) 11218-11226.

[45] C. Martos, J. Dufour, A. Ruiz, Synthesis of Fe_3O_4-based catalysts for high temperature water gas shift reaction. Int. J. Hydrog. Energ. 34 (2009) 4475-4481.

[46] I. Júnior, M. Lima, M. Jean-Marc, M. Aouine, M. R. do Carmo, The role of vanadium on the properties of iron based catalysts for the water gas shift reaction, Appl. Catal. A: General 283 (2005) 91-98.

[47] S. S. Hla, Y. Sun, G. J. Duffy, L. D. Morpeth, A. Ilyushechkin, A. J. Cousins, J. H. Edwards, Kinetics of the water-gas shift reaction over a $La_{0.7}Ce_{0.2}FeO_3$ perovskite-like catalyst using simulated coal-derived syngas at high temperature, Int. J. Hydrog. Energ. 36 (2011) 518-527.

[48] Y. Sun, S. S. Hla, G. J. Duffy, A. J. Cousins, D. French, L. D. Morpeth, J. H. Edwards, D. G. Roberts, Effect of Ce on the structural features and catalytic properties of $La_{(0.9-x)}Ce_xFeO_3$ perovskite-like catalysts for the high temperature water-gas shift reaction, Int. J. Hydrog. Energ. 36 (2011) 79-86.

[49] D.-W. Lee, M. S. Lee, J. Y. Lee, S. Kim, J.-J. Eom, D. J. Moon, K.-W. Lee, The review of Cr-free Fe-based catalysts for high-temperature water-gas shift reactions, Catal Today. 210 (2013) 2-9.

[50] W. F. Podolski, Y. G. Kim, Modeling the water-gas shift reaction, Ind. Eng. Chem. Process Des. Dev. 13 (1974) 415-422.

[51] T. Salmi, L. E. Lindfors, S. Boström, Modeling of the high temperature water gas shift reaction with stationary and transient experiments, Chem. Eng. Sci. 41 (1986) 929-936.

[52] Y. Choi, H. G. Stenger, Water gas shift reaction kinetics and reactor modeling for fuel cell grade hydrogen, J. Power Sources 124 (2003) 432-439.

[53] C. A. Callaghan, Kinetics and catalysis of the water-gas-shift reaction: A microkinetic and graph theoretic approach, Ph.D. thesis, Worcester Polytechnic Institute, Worcester, MA, 2006. 41, 116.

[54] C. Callaghan, I. Fishtik, R. Datta, M. Carpenter, M. Chmielewski, A. Lugo, An improved microkinetic model for the water gas shift reaction on copper, Surf, Sci, 541 (2003) 21-30.

[55] C. Callaghan, I. Fishtik, R. Datta, The water-gas shift reaction: A reaction network analysis of the microkinetic model, Abstr. Pap. Am. Chem. S. 48 (2003) 678.

[56] M. D. Argyle, K. Chen, C. Resini, C. Kebs, A. T. Bell, E. Iglesia, *In situ* UV-visible assessment of extent of reduction during oxidation reactions on oxide catalysts, Chem. Commun. (2003) 2082-2083.

[57] M. D. Argyle, K. Chen, E. Iglesia, A. T. Bell, *In situ* UV-visible spectroscopic measurements of kinetic parameters and active sites for catalytic oxidation of alkanes on vanadium oxides, J. Phys. Chem. B. 109 (2005) 2414-2420.

[58] X. Gao, J. M. Jehng, I. E. Wachs, *In situ* UV-vis-NIR diffuse reflectance and raman spectroscopic studies of propane oxidation over ZrO_2-supported vanadium oxide catalysts, J. Catal. 209 (2002) 43-50.

[59] O. Ovsister, C. Maymol, B. Angelika, K. V. Evgenii, Dynamics of redox behavior of nano-sized VOx species over Ti–Si-MCM-41 from time-resolved in situ UV/Vis analysis, J. Catal. 265 (2009) 8-18.

[60] B. J. Clark, T. Frost, M. A. Russell, UV spectroscopy: Techniques, instrumentation, data handling, Chapman & Hall, London, 1993.

[61] Z. Zhang, C. Boxall, G. H. Kelsall, Photoelectropheresis of colloidal iron oxides. Part 2 – magnetite (Fe_3O_4), J. Chem. Soc., Faraday Trans. 92 (1996) 791-802.

[62] R. M. Cornell, U. Schwertmann, The Iron Oxides: Structure, Properties, Reactions, Occurrences and Uses, Wiley-VCH, New York, 2003.

[63] D. M. Sherman, Electronic structures of iron(III) and manganese(IV) (hydr)oxide minerals: Thermodynamics of photochemical reductive dissolution in aquatic environments, Geochim. Cosmochim. Acta. 69 (2005) 3249-3255.

[64] D. M. Sherman, Electronic stuctures of Fe^{3+} coordination sites in iron oxides: Applications to spectra, bonding, and magnetism. Phys. Chem. Mineral.12 **(**1985) 161-175.

[65] A. A. Christy, O. M. Kvalheim, R. A. Velapoldi, Quantitative analysis in diffuse reflectance spectrometry: A modified Kubelka-Munk equation, Vib. Spectrosc. 9 (1995) 19-27.

[66] V. Džimbeg-Malčić, Ž. Barbarić-Mikočević, K. Itrić, Kubelka-Munk theory in describing optical properties of paper (I), Techn. Gazette 18 (2011) 117-124.

[67] P. Kubelka, F. Munk, Ein Beitrag zur Optik der Farbanstriche (A contribution to the optics of paint), Z. Tech Phys. 12 (1931) 593-601.

[68] A. Schuster, Radiation through a foggy atmosphere, Astrophys. J. 21 (1905) 1-22.

[69] G. Wyszecki, W. S. Stiles, Color Science. 2nd ed., John Wiley & Sons, New York, 2000.

[70] J. Doak, R. K. Gupta, K. Manivannan, K. Ghosh, P. K. Kahol, Effect of particle size distributions on absorbance spectra of gold nanoparticles, Physica E. 42 (2010) 1605 – 1609.

[71] H. C. Van de Hulst, Light Scattering by Small Particles, John Wiley & Sons, New York, 1957.

[72] T. Herranz, S. Rojas, F. Perez-Alonso, M. Ojeda, P. Terreros, J. L. G. Fierro, Carbon oxide hydrogenation over silica-supported iron-based catalysts: Influence of the preparation route, Appl. Catal. A: General 308 (2006) 19-30.

[73] A. Steynberg, M. Dry, Fischer-Tropsch Technology, volume 152 of *Studies in Surface Science and Catalysis*, 2004.

[74] Y. Yang, H.-W. Xiang, Y.-Y. Xu, L. Bai, Y.-W. Li, Effect of potassium promoter on precipitated iron-manganese catalyst for Fischer-Tropsch synthesis, Appl. Catal. A: General 266 (2004) 181-194.

[75] A. P. Raje, R. J. O'Brien, B. H. Davis, Effect of potassium promotion on iron-based catalysts for Fischer-Tropsch synthesis, J. Catal. 180 (1998) 36-43.

[76] D. B. Bukur, D. Mukesh, S. A. Patel, Promoter effects on precipitated iron catalysts for Fischer-Tropsch synthesis, Ind. Eng. Chem. Res. 29 (1990) 194-204.

[77] B. Graf, M. Muhler, The influence of the potassium promoter on the kinetics and thermodynamics of CO adsorption on a bulk iron catalyst applied in Fischer-Tropsch synthesis: a quantitative adsorption calorimetry. Temperature-programmed desorption, and surface hydrogenation study. Phys. Chem. 13 (2011) 3701-3710.

[78] M. E. Dry, T. Shingles, L. J. Boshoff, C. S. van H. Botha, Factors influencing the formation of carbon on iron Fischer-Tropsch catalysts: II. The effect of temperature and of gases and vapors present during Fischer-Tropsch synthesis, J. Catal. 17 (1970) 347-354.

[79] W. Ma, E. Kugler, D. Dadyburjor, Promotional effect of copper on activity and selectivity to hydrocarbons and oxygenates for Fischer-Tropsch synthesis over potassium-promoted iron catalysts supported on activated carbon, Energ. & Fuels 25 (2011) 1931-1938.

[80] C.-H. Zhang, Y. Yang, B.-T. Teng, T.-Z. Li, H.-Y. Zheng, H.-W. Xiang, Y.-W. Li, Study of an iron-manganese Fischer-Tropsch synthesis catalyst promoted with copper, J. Catal. 237 (2006) 405-415.

[81] N. Lohitharn, J. G. Goodwin, E. Lotero, Fe-based Fisher-Tropsch synthesis catalysts containing carbide-forming transition metal promoters, J. Catal. 255 (2008): 104-113.

[82] T. Wang, Y. Ding, Y. Lü, H. Zhu, L. Lin, Influence of lanthanum on the performance of Zr-Co/activated carbon catalysts in Fischer-Tropsch synthesis." J. Nat. Gas Chem. 17 (2008) 153-158.

[83] D. B. Bukur, L. Nowicki, X. Lang, Fischer-Tropsch synthesis in a stirred tank slurry reactor, Chem. Eng. Sci. 49 (1994) 4615-4625.

[84] D. B. Bukur, X. Lang, Highly active and stable iron Fischer-Tropsch Catalysts for synthesis gas conversion to liquid fuels, Ind. Eng. Chem. Res. 38 (1999) 3270-3275.

[85] D. B. Bukur, K. Okabe, M. P. Rosynek, C. Li, D. Wang, K. R. P. M. Rao, G. P. Huffman, Activation studies with a precipitated iron catalyst for Fischer-Tropsch Synthesis, J. Catal. 155 (1995) 353-365.

[86] K. M. Brunner, Novel Iron Catalyst and Fixed-Bed Reactor Model for the Fischer-Tropsch Synthesis, Ph.D. thesis, Brigham Young University, Provo, UT, 2012.

[87] S. Liu, Q. Liu, J. Boerio-Goates, B. F. Woodfield, Preparation of a wide array of ultra-high purity metals, metal oxides, and mixed metal oxides with uniform particle sizes, J. Adv. Mater. 39 (2007) 18-23.

[88] S. J. Smith, Q. Liu, J. Boerio-Goates, B. F. Woodfield, The mechanism behind a novel two-step solid-state method for synthesizing metal oxide nanoparticles, in: Abstracts, Joint 63rd Northwest and 21st Rocky Mountain Regional Meeting of the American Chemical Society, Park City, Utah.

[89] S. J. Smith, The Synthesis and Structural Characterization of Metal Oxide Nanoparticles Having Catalytic Applications, Ph.D. thesis, Brigham Young University, Provo, UT, 2012.

[90] C. H. Bartholomew, B. F. Woodfield, H. Baiyu, R. E. Olsen, L. Astle, Method for making highly porous, stable metal oxides with a controlled pore structure, 2011. US 20110257008

[91] S. Li, W. Ding, G. D. Meitzner, E. Iglesia, Spectroscopic and transient kinetic studies of site requirements in iron-catalyzed Fischer-Tropsch synthesis, J. Phys. Chem. B. 106 (2002) 85-91.

[92] J. Xu, Rational Design of Silica-Supported Platinum Promoted Iron Fischer-Tropsch Synthesis Catalysts Based on Activity-Structure Relationships, Ph.D. thesis, Brigham Young University, Provo, UT, 2003.

[93] C. H. Bartholomew, M. W. Stoker, L. Mansker, A. K. Datye, (Eds.), Effects of pretreatment, reaction, and promoter on microphase structure and Fischer-Tropsch activity of precipitated iron catalysts. Catalyst Deactivation, ed. B. Delmon, G. F. Froment, Elsevier Science, 1999, 265.

[94] H. Itoh, H. Hosaka, T. Ono, E. Kikuchi, Properties and product selectivities of iron ultrafine particles as a catalyst for liquid phase hydrogenation of carbon monoxide, Appl Catal. 40 (1988) 53-66.

[95] E. S. Lox, G. F. Froment, Kinetics of the Fischer-Tropsch reaction on a precipitated promoted iron catalyst. 2. Kinetic modeling, Ind. Eng. Chem. Res. 32 (1993) 71-82.

[96] W. H. Zimmerman, D. B. Bukur, Reaction kinetics over iron catalysts used for the Fischer-Tropsch synthesis, Can. J. Chem. Eng. 68 (1990) 292-301.

[97] S. A. Eliason, Deactivation by Carbon of Unpromoted and Potassium-Promoted Iron Fischer-Tropsch Catalysts, Ph.D. thesis, Brigham Young University, Provo, UT, 1994.

[98] Y.-N. Wang, W.-P. Ma, Y.-J. Lu, J. Yang, Y.-Y. Xu, H.-W. Xiang, Y.-W. Li, Y.-L. Zhao, B.-J. Zhang, Kinetics modeling of FT synthesis over an industrial Fe-Cu-K catalysts, Fuel 82 (2003) 195-213.

[99] J. Yang, Y. Liu, J. Chang, Y.-N. Wang, L. Bai, Y.-Y. Xu, H.-W. Xiang, Y.-W. Li, B. Zhong, Detailed kinetics of Fischer-Tropsch synthesis on an industrial Fe-Mn catalyst, Ind. Eng. Chem. Res. 42 (2003) 5066-5090.

[100] B.-T. Teng, J. Chang, J. Yang, G. Wang, C.-H. Zhang, Y.-Y. Xu, H.-W. Xiang, Y.-W. Li, Water gas shift reaction kinetics in Fischer-Tropsch synthesis over an industrial Fe-Mn catalyst, Fuels 84 (2005) 917-926.

[101] G. P. van der Laan, A. A. C. M. Beenackers, Intrinsic kinetics of the gas-solid Fischer-Tropsch and water gas shift reactions over a precipitated iron catalyst, Appl. Catal. A: General 193 (2000) 39-53.

[102] B. B. Hallac, J. C. Brown, L. L. Baxter, M. D. Argyle, A kinetic study on the structural and functional roles of lanthana in iron-based high temperature water-gas shift catalysts, Int. J. Hyd. Ener. 39 (2014) 7306-7317.

[103] P. Patnaik, Handbook of Inorganic Chemicals, McGraw-Hill, New York, 2003.

[104] S. Brunauer, P. H. Emmett, E. Teller, Adsorption of gases in multimolecular layers, J. Am. Chem. Soc. 60 (1938) 309-319.

[105] E. P. Barrett, L. G. Joyner, P. P. Halenda, The determination of pore volume and area distributions in porous substances. I. Computations from nitrogen isotherms, J. Am. Chem. Soc. 73 (1951) 373-380.

[106] P. Scherrer, Determination of the size and internal structure of colloidal particles using X-rays, Nachr. Ges. Wiss. Göettingen, Math.-Phys. KI. 2 (1918) 98-100.

[107] O. Renaud, M. Victoria-Feser, A robust coefficient of determination for regression, J. Statist. Plann. Inference 140 (2010) 1852-1862.

[108] G. A. F. Seber, C. J. Wild, Nonlinear Regression, John Wiley & Sons, New York, 2003.

[109] J. Zhao, F. E. Huggins, Z. Feng, G. P. Huffman, Ferrihydrite: Surface structure and its effects on phase transformation, Clays Clay. Miner. 42 (1994) 737-746.

[110] R. Longbottom, L. Kolbeinsen, Iron ore reduction with CO and H_2 gas mixtures-thermodynamic and kinetic modelling, Proceedings of the 4th Ulcos Seminar, New Direct Reduction, October 2008.

[111] G. K. Reddy, K. Gunasekera, P. Boochland, J. Dong, P. G. Smirniotis, High temperature water gas shift reaction over nanocrystalline copper codoped-modified ferrites, J. Phys. Chem. C. 115 (2011) 7586-7595.

[112] J. C. González, M. G. González, M. A. Laborde, N. Moreno, Effect of temperature and reduction on the activity of high temperature water gas shift catalysts, Appl. Catal. 20 (1986) 3-13.

[113] L. Kundakovic, M. Flytzani-Stephanopoulos, Reduction characteristics of copper oxide in cerium and zirconium oxide systems, Appl. Catal. A. 171 (1998) 13-29.

[114] H. Lin, Y. Chen, C. Li, The mechanism of reduction of iron oxide by hydrogen, Thermochim. Acta. 400 (2003) 61-67.

[115] D. A. Skoog, F. J. Holler, S. R. Crouch, Principles of Instrumental Analysis, 6th ed., Brooks:COle Cengage Learning, California, 2006.

[116] Varian Corp. Varian Cary 4000 UV-visible spectrometer. Varian Corporation. http://www.varianinc.com.cn/products/spectr/uv/brochure/1942.pdf (accessed Sep 25, 2010).

[117] Harrick Scientific. Harrick praying mantis cell. Harrick Scientific. http://www.harricksci.com/ftir/accessories/group/Praying-Mantis%E2%84%A2-Diffuse-Reflection-Accessory (accessed Mar 30, 2012).

[118] N. N. Greenwood, A. Earnshaw, Chemistry of the Elements, Butterworth-Heinemann, London, 1997.

[119] X. Li, Y. Wang, P. Xu, Q. Zhang, K. Nie, X. Hu, B. Kong, L. Li, J. Chen, Effects of temperature and wavelength choice on in-situ dissolution test of cimetidine tablets, J. Pharm. Anal. 3 (2013) 71-74.

[120] Y. Zhu, D. Sun, Q. Huang, X. Jin, H. Liu, UV-vis spectra of perovskite iron-doped $Ba_{0.72}Sr_{0.28}TiO_3$, Mater. Lett. 62 (2008) 407-409.

[121] J. Y. Kim, G. Magesh, D. H. Youn, J. Jang, J. Kubota, K. Domen, J. S. Lee, Single-crystalline, wormlike hematite photoanodes for efficient solar water splitting, Sci. Rep. 3 (2013) 2681-2688.

[122] D. M. Sherman, T. D. Waite, Electronic spectra of Fe^{3+} oxides and oxide hydroxides in the near-IR to near-UV, Am. Mineral. 70 (1985) 1262-1269.

[123] J. Brown, UV-Visible Spectra Analysis of High Temperature Water Gas Shift Catalysts Made from Iron, Lanthanum, Copper, and Chromium Oxides, Master's thesis, Brigham Young University, Provo, UT, 2012.

[124] T. Popa, G. Xu, T. F. Barton, M. D. Argyle, High temperature water gas shift catalysts with alumina, Appl. Catal. A: General 379 (2010) 15-23.

[125] A. Patlolla, E. V. Carino, S. N. Ehrlich, E. Stavitski, A. I. Frenkel, Application of operando XAS, XRD, and Raman spectroscopy for phase speciation in water gas shift reaction catalysts, ACS Catal. 2 (2012) 2216-2223.

[126] M. Wilke, O. Hahn, A. B. Woodland, K. Rickers, The oxidation state of iron determined by Fe K-edge XANES – Applications to iron Gall Ink in Historical Manuscripts, J. Anal. Atom. Spectrom. 24 (2009) 1364-1372.

[127] J. A. Labinger, K. C. Ott, Is there a difference between surface and bulk oxidation levels in partially reduced metal oxide catalysts? Evidence from methane oxidative coupling kinetics. Catal. Lett. 4 (1990) 245-250.

[128] B. B. Hallac, K. Keyvanloo, J. D. Hedengren, W. C. Hecker, M. D. Argyle, An optimized simulation model for iron-based Fischer-Tropsch catalyst design: Transfer limitations as functions of operating and design conditions, Chem. Eng. J. accepted October 2014, DOI: 10.1016/j.cej.2014.10.108

[129] F. Benyahia, K. E. O'Neill, Enhanced voidage correlations for packed beds of various particle shapes and sizes, Part. Sci. Technol. 23 (2005) 169–177.

[130] C.H. Bosanquet, British TA Report BR-507, September 27, 1944.

[131] W. G. Pollard, R. D. Present, On gaseous self-diffusion in long capillary tubes, Phys. Rev. 73 (1948) 762-774.

[132] C. Erkey, J. B. Rodden, A. Akgerman, A correlation for predicting diffusion coefficients in alkanes, Can. J. Chem. Eng. 68 (1990) 661-665.

[133] C. Erkey, J. B. Rodden, A. Akgerman, Diffusivities of synthesis gas and n-alkanes in Fischer-Tropsch wax, Energy & Fuels 4 (1990) 275–276.

[134] J. R. Welty, C. E. Wicks, R. E. Robert, G. L. Rorrer, Fundamentals of Momentum, Heat and Mass Transfer, 5th ed., John Wiley & Sons, 2008.

[135] E. W. Thiele, Relation between catalytic activity and size of particle, Ind. Eng. Chem. 31 (1939) 916-920.

[136] M. E. Davis, R. J. Davis, Fundamentals of Chemical Reaction Engineering, 1st ed., McGraw-Hill, New York, 2003.

[137] R. Aris, Normalization for the Thiele Modulus, Ind. Eng. Chem. Fundam. 4 (1965) 227-229.

[138] E. E. Petersen, A general criterion for diffusion influenced chemical reactions in porous solids, Chem. Eng. Sci. 20 (1965) 587-591.

[139] K. B. Bischoff, Effectiveness factors for general reaction rate forms, AIChE J. 11 (1965) 351-355.

[140] O. Levenspiel, Chemical Reaction Engineering, third ed., John Wiley & Sons, New York, 1999.

[141] K. L. Dishman, P. K. Doolin, J. F. Hoffman, Comparison of particle size of cracking catalyst determined by laser light scattering and dry sieve methods, Ind. Eng. Chem. Res. 32 (1993) 1457-1463.

[142] A. Matsuura, Y. Hitaka, T. Akehata, T. Shirai, Effective radial thermal conductivity in packed beds with gas-liquid downflow, Heat. Transf. - Jpn. Res. 8 (1979) 44–52.

[143] R. B. Bird, W. E. Stewart, E. N. Lightfoot, Transport Phenomena, 3rd ed., John Wiley & Sons, New York, 2001.

[144] G. F. Froment and K. B. Bischoff, Chemical Reactor Analysis and Design, John Wiley & Sons, New York, 1990.

[145] K. M. Brunner, J. C. Duncan, L. D. Harrison, K. E. Pratt, R. P. S. Peguin, C. H. Bartholomew, W. C. Hecker, A trickle fixed-bed recycle reactor model for the Fischer-Tropsch synthesis, Int. J. Chem. Reac. Eng. 10 (2012) 1-36.

[146] J. A. Tallmadge, Packed bed pressure drop-an extension to higher Reynolds numbers, AIChE J. 16 (1970) 1092-1093.

[147] S. A. Eliason, C. H. Bartholomew, Reaction and deactivation kinetics for Fischer-Tropsch synthesis on unpromoted and potassium-promoted iron catalysts, App. Catal. A: General 186 (1999) 229-243.

[148] J. D. Hedengren, S. R. Asgharzadeh, K. M. Powell, T. F. Edgar, Nonlinear modeling, estimation and predictive control in APMonitor, Comput. Chem. Eng. 70 (2014) 133-148.

[149] A. Wächter, L. Biegler, On the implementation of a primal-dual interior point filter line search algorithm for large-scale nonlinear programming, Math. Progr. 106 (2006) 25–57.

[150] A. Forsgren, P. E. Gill, M. H. Wright, Interior methods for nonlinear optimization, Soc. Ind. Appl. Math. 44 (2002) 525-597.

[151] R. Fletcher, S. Leyffer, Nonlinear programming without a penalty function, Math. Progr. 91(2002) 239–269.

[152] G. P. van der Laan, A. A. C. M. Beeenackers, Hydrocarbon selectivity model for the gas-solid Fischer-Tropsch synthesis on precipitated iron catalysts, Ind. Eng. Chem. Res. 38 (1999) 1277-1290.

[153] R. J. Madon, E. Iglesia, Hydrogen and CO intraparticle diffusion effects in Ruthenium-catalyzed hydrocarbon synthesis, J. Catal. 149 (1994) 428–437.

[154] E. Iglesia, S.C. Reyes, S.L. Soled, Reaction-transport selectivity models and the design of Fischer-Tropsch catalysts, in: R. Becker, C.J. Pereira (Eds.), Compute-Aided Design of Catalysts, Marcel Dekker Inc., New York, 1993, pp. 199–258.

[155] A. K. Mogalicheria, E. E. Elmalik, N. O. Elbashir, Enhancement in the intraparticle diffusion in the supercritical phase Fischer-Tropsch synthesis, Chem. Eng. Process. 62 (2012): 59-68.

[156] M. R. Rahimpour, H. Elekaei, Optimization of a novel combination of fixed and fluidized-bed hydrogen- permselective membrane reactors for Fischer-Tropsch synthesis in GTL technology, Chem. Eng. J. 152 (2009) 543–555.

[157] Y. N. Wang, Y. Y. Xu, Y. W. Li, Y. L. Zhao, B. J. Zhang, Heterogeneous modeling for fixed-bed Fischer-Tropsch synthesis: Reactor model and its applications, Chem. Eng. Sci. 58 (2003) 867–875.

[158] A. N. Pour, S. M. K. Shahri, H. R. Bozorgzadeh, Y. Zamani, A. Tavasoli, M. A. Marvast, Effect of Mg, La and Ca promoters on the structure and catalytic behavior of iron-based catalysts in Fischer-Tropsch synthesis, App. Catal. A: General 348 (2008) 201-208.

[159] Ø. Borg, S. Eri, E. A. Blekkan, S. Storsæter, H. Wigum, E. Rytter, A. Holmen, Fischer-Tropsch synthesis over γ-alumina-supported cobalt catalysts: Effect of support variables, J. Catal. 248 (2007) 89-100.

[160] K. Keyvanloo, J. Horton, W. C. Hecker, M. D. Argyle, Effects of preparation variables on an alumina-supported FeCuK Fischer-Tropsch catalyst, Catal. Sci. Tech. DOI: 10.1039/c4cy00510d (2014).

[161] C. Zhang, G. Zhao, J. Chang, H. Xiang, Y. Li, Factors influencing the WGS reaction in Fischer-Tropsch synthesis over-iron based catalysts, State Key Laboratory of Coal Conversion, Institute of Coal Chemistry, Chinese Academy of Sciences, Taiyuan, People's Republic of China.

[162] A. Boudjemaa, C. Daniel, C. Mirodatos, Mohamed Trari, A. Auroux, R. Bouarab, In situ DRIFTS studies of high-temperature water-gas shift reaction on chromium-free iron oxide catalysts, Comp. Rend. Chimie 14 (2011) 534-538.

[163] V. R. R. Pendyala, G. Jacobs, J. C. Mohandas, M. Luo, H. H. Hamdeh, Y. Ji, M. C. Ribeiro, B. H. Davis, Fischer-Tropsch synthesis: Effect of water over iron-based catalysts, Catal. Lett. 140 (2010) 98-105.

APPENDIX A. Calibration of Gas Chromatograph

For FTS experiments, GC was calibrated using a standard calibration gas with the following known compositions: (20.2% CO, 35% H_2, 3.2% Ar, 0.6% CH_4, 1.6% CO_2, 39.4% He). The concentrations of gases were changed by flowing He gas with the calibration gas to dilute it. The GC response factor (RF) for each gas was calculated relative to Ar by taking the ratios of their calibration slopes shown below. The response factors for C_2H_6 and C_2H_4 were estimated from previous works by Brunner and Argyle.

$RF_{CO} = 0.911$

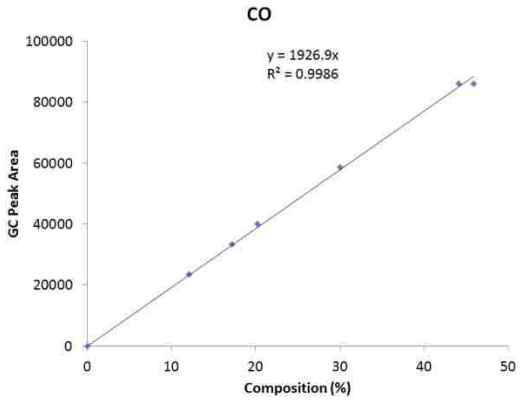

Figure A.1: GC calibration curve for CO.

$RF_{H_2} = 0.060$

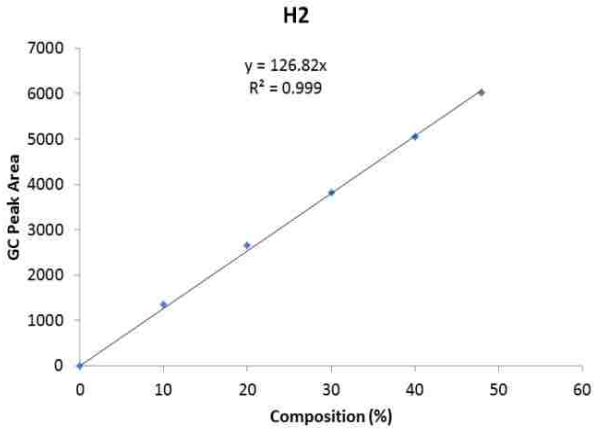

Figure A.2: GC calibration curve for H_2.

$RF_{CO_2} = 1.269$

$RF_{CH_4} = 0.625$

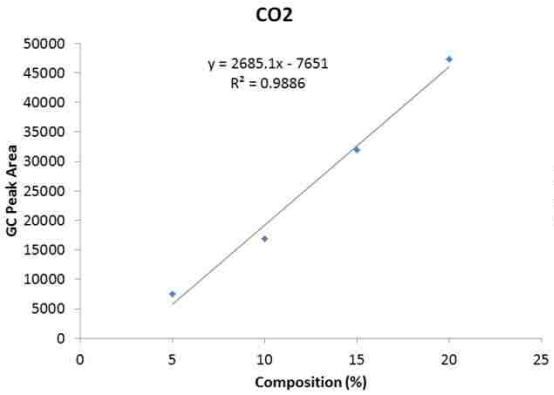

Figure A.3: GC calibration for CO_2.

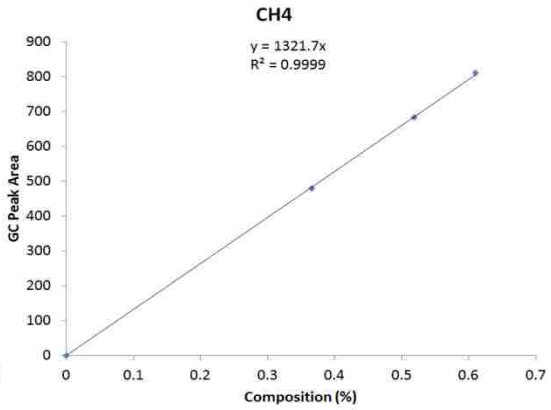

Figure A.4: GC calibration for CH_4.

$$RF_{Ar} = 1.000$$

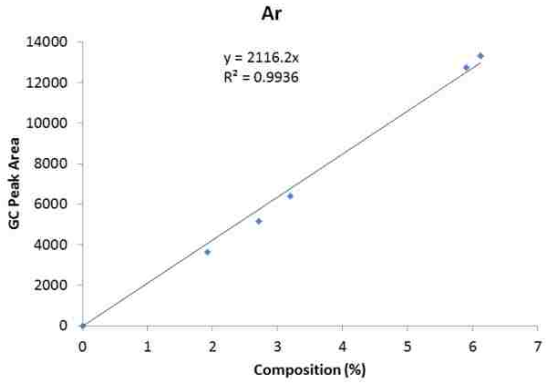

Figure A.5: GC calibration for Ar.

For the WGS experiments, the GC was calibrated for CO_2 relative to CO using CO and CO_2 gases only with high compositions of CO (>70%). The intercept of the calibration curve shown in Figure A.6, which is 1.707, is the factor that adjusts the CO GC peak area to represent actual compositions.

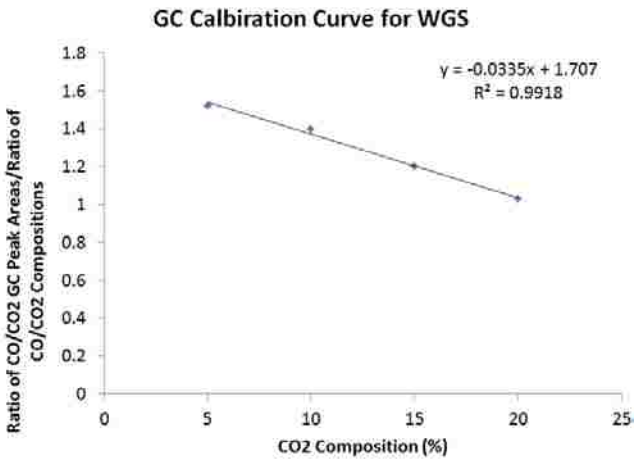

Figure A.6: GC calibration curve for WGS experiments.

APPENDIX B. Sample Calculations

B.1. Preparation of 0.5La High-Temperature Water-Gas Shift Catalyst

Below is a Mathcad sheet of calculations for the preparation of 0.5La HT WGS catalyst.

0.5La Catalyst Preparation

Ferric Nitrate nonahydrate	Ferric oxide 87.5 wt%
Chromium(III) nitrate nonahydrate	Chromium(III) oxide 8 wt%
Copper(II) nitrate 2.5 hydrate	Copper(II) oxide 4 wt%
Lanthanum (III) nitrate hexahydrate	Lanthanum Oxide 0.5 wt%

Fe(NO3)3 + 3NaOH ----> Fe(OH)3 + 3Na(NO3)
2Fe(OH)3 ----> Fe2O3 + 3H2O upon heating

Cr(NO3)3 + 3NaOH --> 3NaNO3 + Cr(OH)3
2Cr(OH)3 ----> Cr2O3 + 3H2O upon heating

Cu(NO3)2 + 2NaOH ----> Cu(OH)2 + 2Na(NO3)
Cu(OH)2 --> CuO +H2O upon heating

La(NO3)3 + 3NaOH ----> La(OH)3 + 3Na(NO3)
2La(OH)3 ---> La2O3 +3H2O upon heating

Assuming theoretic 100% yield and

The nitrates are the limiting reagents in all three reactions because sodium hydroxide is in excess.

$m_{cat} := 20gm$ Mass of batch of catalyst

Molecular weights of metal nitrates and oxides

$MW_{fo} := 159.69\frac{gm}{mol}$ $MW_{cho} := 151.99\frac{gm}{mol}$ $MW_{co} := 79.545\frac{gm}{mol}$ $MW_{lo} := 325.81\frac{gm}{mol}$

$MW_{fn} := 403.99\frac{gm}{mol}$ $MW_{chn} := 400.21\frac{gm}{mol}$ $MW_{cn} := (187.56 + 2.5 \cdot 18.015)\cdot\frac{gm}{mol}$

$MW_{ln} := 433.03\frac{gm}{mol}$

Mass fractions and masses of metal oxides

$y_{lo} := 0.005$ $y_{cho} := 0.08$ $y_{co} := 0.04$ $y_{fo} := 1 - y_{lo} - y_{cho} - y_{co} = 0.875$

$m_{fo} := y_{fo}\cdot m_{cat}$ $m_{cho} := y_{cho}\cdot m_{cat}$ $m_{co} := y_{co}\cdot m_{cat}$ $m_{lo} := y_{lo}\cdot m_{cat}$

Stoichiometric calculations

$n_{fo} := \frac{m_{fo}}{MW_{fo}} = 0.11\,mol$ $n_{cho} := \frac{m_{cho}}{MW_{cho}} = 0.011\,mol$ $n_{co} := \frac{m_{co}}{MW_{co}} = 0.01\,mol$ $n_{lo} := \frac{m_{lo}}{MW_{lo}}$

$n_{f\_hyd} := 2\cdot n_{fo}$ $n_{ch\_hyd} := 2\cdot n_{cho}$ $n_{c\_hyd} := n_{co}$ $n_{l\_hyd} := 2\cdot n_{lo}$

$n_{fn} := n_{f\_hyd} = 0.219\ mol$ $m_{fn} := n_{fn} \cdot MW_{fn}$ $n_{ln} := n_{l\_hyd}$

$n_{chn} := n_{ch\_hyd} = 0.021\ mol$ $m_{chn} := n_{chn} \cdot MW_{chn}$

$n_{cn} := n_{c\_hyd} = 0.01\ mol$ $m_{cn} := n_{cn} \cdot MW_{cn}$ $m_{ln} := n_{ln} \cdot MW_{ln}$

$m_{fn} = 88.544 \cdot gm$ $m_{chn} = 8.426 \cdot gm$ $m_{cn} = 2.339 \cdot gm$ $m_{ln} = 0.266 \cdot gm$

$n_{NaOH\_1} := 3 \cdot n_{fn}$ $n_{NaOH\_2} := 3 \cdot n_{chn}$ $n_{NaOH\_3} := 3 \cdot n_{cn}$

$n_{NaOH} := n_{NaOH\_1} + n_{NaOH\_2} + n_{NaOH\_3} = 0.751\ mol$ $MW_{NaOH} := 40.0 \frac{gm}{mol}$

$m_{NaOH} := n_{NaOH} \cdot MW_{NaOH}$ $m_{NaOH} = 30.034 \cdot gm$

pH calculations at 25 deg C and 1 atm

ORIGIN := 1 $i := 1 .. 4$

$$\begin{pmatrix} 1 \\ 2 \\ 3 \\ 4 \end{pmatrix} = \begin{pmatrix} \text{"Fe(OH)3"} \\ \text{"Cr(OH)3"} \\ \text{"Cu(OH)2"} \\ \text{"La(OH)3"} \end{pmatrix} \qquad K_{sp} := \begin{pmatrix} 1 \cdot 10^{-38} \\ 6.3 \cdot 10^{-31} \\ 2.2 \cdot 10^{-20} \\ 2 \cdot 10^{-21} \end{pmatrix}$$

Fe(OH)3--->Fe3+ + 3OH- $K_{sp} = x(3x)^3$

Cr(OH)3--->Cr3+ + 3OH- $K_{sp} = x(3x)^3$

Cu(OH)2--->Cu2+ + 2OH- $K_{sp} = x(2x)^2$

La(OH)3--->La3+ + 3OH- $K_{sp} = x(3x)^3$

$$sol_{FeOH3} := \left(\frac{K_{sp_1}}{27}\right)^{\frac{1}{4}} \cdot \frac{mol}{L} = 1.387 \times 10^{-10} \cdot \frac{mol}{L} \qquad C_{OH1} := sol_{FeOH3} \cdot 3 = 4.162 \times 10^{-10} \cdot \frac{mol}{L}$$

$$sol_{CrOH3} := \left(\frac{K_{sp_2}}{27}\right)^{\frac{1}{4}} \cdot \frac{mol}{L} = 1.236 \times 10^{-8} \cdot \frac{mol}{L} \qquad C_{OH2} := sol_{CrOH3} \cdot 3 = 3.708 \times 10^{-8} \cdot \frac{mol}{L}$$

$$sol_{CuOH2} := \left(\frac{K_{sp_3}}{4}\right)^{\frac{1}{3}} \cdot \frac{mol}{L} = 1.765 \times 10^{-7} \cdot \frac{mol}{L} \qquad C_{OH3} := sol_{CuOH2} \cdot 2 = 3.53 \times 10^{-7} \cdot \frac{mol}{L}$$

$$sol_{LaOH3} := \left(\frac{K_{sp_4}}{27}\right)^{\frac{1}{4}} \cdot \frac{mol}{L} = 2.934 \times 10^{-6} \cdot \frac{mol}{L} \qquad C_{OH4} := sol_{LaOH3} \cdot 3 = 8.801 \times 10^{-6} \cdot \frac{mol}{L}$$

$$C_{OH} := \begin{pmatrix} C_{OH1} \\ C_{OH2} \\ C_{OH3} \\ C_{OH4} \end{pmatrix} \qquad pOH_i := -\log\left(\frac{C_{OH_i}}{\frac{mol}{L}}\right) \qquad pH_i := 14 - pOH_i \qquad pH = \begin{pmatrix} 4.619 \\ 6.569 \\ 7.548 \\ 8.945 \end{pmatrix}$$

B.2. Preparation of 0La FT Catalyst

Below is a Mathcad sheet of example calculations for the preparation of 0La FT catalyst.

0La FT (100Fe/5Cu/4K/16Si) catalyst preparation

Ferric Nitrate nonahydrate	Silica 12.8 wt%
Silica	K 3.2 wt%
Copper(II) nitrate 2.5 hydrate	Cu 4 wt%
Lanthanum nitrate hexahydrate	Fe 80 wt%
Potassium nitrate	

The nitrates are the limiting reagents in all three reactions b/c ammonium bicarbonate is in excess.

Assuming theoretic 100% yield:

Fe(NO3)3 + 3NH4(HCO3) ----> Fe(HCO3)3 + 3NH4(NO3)
2Fe(HCO3)3 ----> Fe2O3 + 6CO2+3H2O upon heating
Fe2O3 -----> 2Fe + other gases upon reduction

2KHCO3 ----> K2O + 2CO2+ H2O upon heating
K2O -----> 2K + other gases upon reduction

Cu(NO3)2 + 2NH4HCO3 ----> Cu(HCO3)2 + 2NH4NO3
Cu(HCO3)2 ---> CuO +H2O + 2CO2 upon heating
CuO -----> Cu + other gases upon reduction

La(NO3)3 + 3NH4(HCO3) ----> La(HCO3)3 + 3NH4(NO3)
2La(HCO3)3 ----> La2O3 + 6CO2+3H2O upon heating
La2O3 -----> 2La + other gases upon reduction

$m_{cat} := 20gm$ mass of catalyst batch

Molecular weights of metal nitrates, bicarbonates, and pure metals

$MW_{fe} := 55.85\frac{gm}{mol}$ $MW_K := 39.10\frac{gm}{mol}$ $MW_{cu} := 63.54\frac{gm}{mol}$ $MW_{la} := 138.91\frac{gm}{mol}$

$MW_{fn} := 403.999\frac{gm}{mol}$ $MW_{Kbc} := 100.115\frac{gm}{mol}$ $MW_{cun} := (187.56 + 2.5 \cdot 18.015)\cdot\frac{gm}{mol}$

$MW_{ln} := 433.03\frac{gm}{mol}$

Mass fractions and masses of metals and promoters

$y_{la} := 0$ $y_K := 0.032$ $y_{cu} := 0.04$ $y_{sil} := 0.128$ $y_{fe} := 1 - y_{la} - y_K - y_{cu} - y_{sil}$

$m_{fe} := y_{fe}\cdot m_{cat}$ $m_K := y_K\cdot m_{cat}$ $m_{cu} := y_{cu}\cdot m_{cat}$ $m_{la} := y_{la}\cdot m_{cat}$ $m_{sil} := y_{sil}\cdot m_{cat}$

Stoichiometric caluclations

$n_{fe} := \frac{m_{fe}}{MW_{fe}} = 0.286\,mol$ $n_K := \frac{m_K}{MW_K} = 0.016\,mol$ $n_{cu} := \frac{m_{cu}}{MW_{cu}} = 0.013\,mol$ $n_{la} := \frac{m_{la}}{MW_{la}}$

$n_{fo} := 0.5 \cdot n_{fe}$ $n_{Ko} := 0.5 \cdot n_K$ $n_{cuo} := n_{cu}$ $n_{lo} := 0.5 \cdot n_{la}$

$n_{fe\_carb} := 2 \cdot n_{fo}$ $n_{K\_carb} := 2 \cdot n_{Ko}$ $n_{cu\_carb} := n_{cuo}$ $n_{la\_carb} := 2 \cdot n_{lo}$

$n_{fn} := n_{fe\_carb} = 0.286\,mol$ $m_{fn} := n_{fn} \cdot MW_{fn}$ $n_{ln} := n_{la\_carb}$

$n_{K\_carb} = 0.016\,mol$ $m_{Kbc} := n_{K\_carb} \cdot MW_{Kbc}$ $m_{ln} := n_{ln} \cdot MW_{ln}$

$n_{cun} := n_{cu\_carb} = 0.013\,mol$ $m_{cun} := n_{cun} \cdot MW_{cun}$

Masses of metal nitrates and bicarbonates required for the catalyst preparation

$m_{fn} = 115.738 \cdot gm$ $m_{Kbc} = 1.639 \cdot gm$ $m_{cun} = 2.929 \cdot gm$ $m_{ln} = 0 \cdot gm$ $m_{sil} = 2.56 \cdot gm$

Mass of stoichiometric ammonium bicarbonate

$n_{NH4\_1} := 3 \cdot n_{fn}$ $n_{NH4\_3} := 2 \cdot n_{cun}$ $n_{NH4\_4} := 3 \cdot n_{ln}$

$n_{NH4} := n_{NH4\_1} + n_{NH4\_3} + n_{NH4\_4} = 0.885\,mol$ $MW_{NH4} := 79.056 \frac{gm}{mol}$

$m_{NH4} := n_{NH4} \cdot MW_{NH4}$ $m_{NH4} = 69.935 \cdot gm$

B.3. Differential *vs.* Integral Reactor Calculations for Fischer-Tropsch Synthesis

Parameters and Reaction Conditions

$R_g := 8.31447 \frac{J}{mol \cdot K}$ Universal gas constant

$p := 20bar$ Reaction pressure

$v_{in} := 150 \frac{mL}{min}$ Feed volumetric flow rate

$t := 280\,°C$ Reaction temperature

$n_C := 20$ Average carbon number

$y_{co} := 0.3$ Feed CO composition

$y_{He} := 0.4$ Feed He composition

$w_{cat} := 0.25gm$ Mass of catalyst

$x_{cof} := 0.264$ Final CO conversion at reaction conditions

$s_{CH4} := 0.04$ Selectivity to methane

$s_{C2} := 0.03$ Selectivity to C2

$s_{C3} := 0.03$ Selectivity to C3

$s_{C4} := 0.04$ Selectivity to C4

$s_{CO2} := 0.4$ Selectivity to CO2

$mmol := 10^{-3} mol$

Calculations of Partial Pressures

$y_{H2} := 1 - y_{co} - y_{He} = 0.3$ Feed H2 composition

$s_{C5plus} := 1 - s_{CH4} - s_{C2} - s_{C3} - s_{C4} - s_{CO2} = 0.46$ Selectivity to C5+

$F_{in} := \frac{v_{in} \cdot 1\,atm}{R_g \cdot 298K} = 0.368 \frac{mol}{hr}$ Feed molar flow rate $F_{He} := y_{He} \cdot F_{in} = 0.147 \frac{mol}{hr}$ molar flow rate of He

Soichiometric ratioi of H2 to CO:

$$H2_{CO\_stoich} := \frac{2 \cdot n_C + 1}{n_C} \cdot s_{C5plus} + 3 \cdot s_{CH4} + \left(\frac{5}{2}\right) \cdot s_{C2} + \left(\frac{7}{3}\right) \cdot s_{C3} + \left(\frac{9}{4}\right) \cdot s_{C4} - s_{CO2} = 0.898$$

$F_{co}(x_{co}) := y_{co} \cdot F_{in} \cdot (1 - x_{co})$ Outlet molar flow rate of CO

$F_{H2}(x_{co}) := F_{in} \cdot y_{H2} - H2_{CO\_stoich} \cdot y_{co} \cdot F_{in} \cdot x_{co}$ Outlet molar flow rate of H2

$F_{CO2}(x_{co}) := F_{in} \cdot y_{co} \cdot x_{co} \cdot s_{CO2}$ Outlet molar flow rate of CO2

$F_{CH4}(x_{co}) := F_{in} \cdot y_{co} \cdot x_{co} \cdot s_{CH4}$ Outlet molar flow rate of CH4

$F_{C2}(x_{co}) := \frac{F_{in} \cdot y_{co} \cdot x_{co} \cdot s_{C2}}{2}$ Outlet molar flow rate of C2

$F_{C3}(x_{co}) := \frac{F_{in} \cdot y_{co} \cdot x_{co} \cdot s_{C3}}{3}$ Outlet molar flow rate of C3

$F_{C4}(x_{co}) := \frac{F_{in} \cdot y_{co} \cdot x_{co} \cdot s_{C4}}{4}$ Outlet molar flow rate of C4

$F_{H2O}(x_{co}) := (s_{C5plus} + s_{CH4} + s_{C2} + s_{C3} + s_{C4} - s_{CO2}) \cdot y_{co} \cdot F_{in} \cdot x_{co}$ Outlet molar flow rate of steam

$F_{tot}(x_{co}) := F_{He} + F_{co}(x_{co}) + F_{H2}(x_{co}) + F_{H2O}(x_{co}) + F_{CH4}(x_{co}) \cdots$ Total outlet molar flow rate
$+ (F_{CO2}(x_{co}) + F_{C2}(x_{co})) + F_{C3}(x_{co}) + F_{C4}(x_{co})$

$p_{co}(x_{co}) := \frac{F_{co}(x_{co})}{F_{tot}(x_{co})} \cdot p$ $p_{h2}(x_{co}) := \frac{F_{H2}(x_{co})}{F_{tot}(x_{co})} \cdot p$ Outlet partial pressures of CO and H2

Integral Reactor Calculations

$$k_{int}(x_{cof}) := \frac{y_{co} \cdot F_{in}}{w_{cat}} \cdot \int_0^{x_{cof}} \frac{1}{p_{co}(x_{co})^{-0.05} \cdot p_{h2}(x_{co})^{0.6}} \, dx_{co}$$

$$k_{int}(x_{cof}) = 45.767 \cdot \frac{mol}{atm^{0.55} \cdot kg \cdot hr}$$ Rate constant from integral reactor calculations

Differential Reactor Calculations

$r_{CO\_diff} := 117.4 \frac{mol}{kg \cdot hr}$ Rate predicted from differential reactor model

$$k_{diff} := \frac{r_{CO\_diff}}{\left[\left(\frac{p_{co}(x_{cof}) + y_{co} \cdot p}{2}\right)^{-0.05} \cdot \left(\frac{p_{h2}(x_{cof}) + p \cdot y_{H2}}{2}\right)^{0.6}\right]}$$

Rate constant from differential reactor calculations using average partial pressures

$$k_{diff} = 46.108 \cdot \frac{mol}{atm^{0.55} \cdot kg \cdot hr}$$

$$\frac{\left|k_{int}(x_{cof}) - k_{diff}\right|}{k_{int}(x_{cof})} = 0.745 \cdot \%$$

Error between differential and integral reactors <1%.

It is appropriate to use the differential reactor model with average partial pressures of CO and H2 at conversions up to 26%.

APPENDIX C. Macro-Kinetic Rate Modeling for the WGSR

C.1. Derivation of Rate Models for the WGS Reaction

C.1.1. Langmuir Hinshelwood Model

The proposed Langmuir-Hinshelwood mechanism can be written as:

$H_2O + s \rightleftharpoons H_2O - s$ (quasi-equilibrium) (C.1)
$CO + s \rightleftharpoons CO - s$ (quasi-equilibrium) (C.2)
$CO - s + H_2O - s \rightleftharpoons CO_2 - s + H_2 - s$ rds, reversible (C.3)
$CO_2 - s \rightleftharpoons CO_2 + s$ (quasi-equilibrium) (C.4)
$H_2 - s \rightleftharpoons H_2 + s$ (quasi-equilibrium) (C.5)

The assumptions made in this mechanism are that water adsorbs non-dissociatively at first, and that the rate-determining step (rds) describes the rate of CO depletion as an elementary step.

The rate of CO depletion becomes:

$$-r_{CO} = k_3 \frac{[CO-s][H_2O-s]}{[L]} - k_{-3} \frac{[CO_2-s][H_2-s]}{[L]} \quad \text{(C.6)}$$

where k_3 is the rate constant for the forward reaction in C.3, k_{-3} is the reversible reaction rate constant, and $[i-s]$is the concentration of adsorbed surfaced species i. From equations (C.1, C.2, C.4, and C.5), the concentrations of surface species can be found in terms of adsorption equilibrium constants K_i, measurable gas-phase species concentrations $[i]$, and concentration of catalyst surface sites $[s]$:

$$[i-s] = K_i[i][s] \quad \text{(C.7)}$$

Upon substitution for these surface species concentrations, equation C.6 becomes:

$$-r_{CO} = k_3 K_{CO} K_{H_2O} [CO][H_2O] \frac{[s]^2}{[L]} - k_{-3} K_{CO_2} K_{H_2} [CO_2][H_2] \frac{[s]^2}{[L]} \quad \text{(C.8)}$$

By doing a site balance on the surface of the catalyst and using equation C.7, an expression for $[s]$ is obtained in terms of the total surface concentration, $[L]$:

$$[L] = [s] + [CO - s] + [H_2O - s] + [CO_2 - s] + [H_2 - s] \quad \text{(C.9)}$$

$$[s] = \frac{[L]}{1 + K_{CO}[CO] + K_{H_2O}[H_2O] + K_{CO_2}[CO_2] + K_{H_2}[H_2]} \quad \text{(C.10)}$$

Equation C.8 then becomes:

$$-r_{CO} = \frac{k_3 K_{CO} K_{H_2O} [L]([CO][H_2O] - \frac{k_{-3} K_{CO_2} K_{H_2}}{k_3 K_{CO} K_{H_2O}} [CO_2][H_2])}{(1 + K_{CO}[CO] + K_{H_2O}[H_2O] + K_{CO_2}[CO_2] + K_{H_2}[H_2])^2} \quad \text{(C.11)}$$

The reaction equilibrium constant, K, is defined as the ratio $\frac{k_3}{k_{-3}} \frac{K_{CO} K_{H_2O}}{K_{CO_2} K_{H_2}}$, and the effective rate constant for the reaction, k, is defined as $k_3[L]$. Therefore, equation C.11 becomes:

$$-r_{CO} = \frac{k K_{CO} K_{H_2O} ([CO][H_2O] - [CO_2][H_2]/K)}{(1 + K_{CO}[CO] + K_{H_2O}[H_2O] + K_{CO_2}[CO_2] + K_{H_2}[H_2])^2} \quad \text{(C.12)}$$

C.1.2. Eley-Rideal Model

The proposed Eley-Rideal mechanism for CO –adsorbing can be written as:

$CO + s \rightleftharpoons CO - s$ (quasi-equilibrium) (C.13)
$CO - s + H_2O \rightleftharpoons CO_2 - s + H_2$ rate-determining step, reversible (C.14)
$CO_2 - s \rightleftharpoons CO_2 + s$ (quasi-equilibrium) (C.15)

The proposed Eley-Rideal mechanism for H_2O –adsorbing can be written as:

$H_2O + s \rightleftharpoons H_2O - s$ (quasi-equilibrium) (C.16)

$CO + H_2O - s \rightleftharpoons CO_2 + H_2$ rate-determining step, reversible (C.17)
$H_2 - s \rightleftharpoons H_2 + s$ (quasi-equilibrium) (C.18)

Per the Eley-Rideal model, only one reactant in the rate-determining step is assumed to be adsorbed on the surface, which is equivalent to assuming that it is the most abundant reactive intermediate (MARI), while the other gas phase reactant interacts directly with the surface species.

The rate of CO depletion becomes:

$-r_{CO} = k_2[CO - s][H_2O] - k_{-2}[CO_2 - s][H_2]$ CO-adsorbed (C.19)
$-r_{CO} = k_2[CO][H_2O - s] - k_{-2}[CO_2][H_2 - s]$ H_2O-adsorbed (C.20)

where k_2 is the rate constant for the forward reaction in C.14 or C.17, k_{-2} is the reverse reaction rate constant, and $[i - s]$ is the concentration of adsorbed surfaced species i. From equations C.13 or C.16, the concentrations of surface species can be found in terms of adsorption equilibrium constants K_i, species concentrations $[i]$, and concentration of catalyst surface sites $[s]$, as shown below:

$[i - s] = K_i[i][s]$ (C.21)

Equations C.17 and C.18 become:

$-r_{CO} = k_2K_{CO}[CO][H_2O][s] - k_{-2}K_{CO_2}[CO_2][H_2][s]$ CO-adsorbed (C.22)
$-r_{CO} = k_2K_{H_2O}[CO][H_2O][s] - k_{-2}K_{H_2}[CO_2][H_2][s]$ H_2O-adsorbed (C.23)

From a site balance with MARI assumption, an expression for $[s]$ is obtained in terms of the total surface site concentration, $[L]$:

$[L] = [s] + [CO - s]$ CO-adsorbed (C.24)

$[L] = [s] + [H_2O - s]$ H_2O-adsorbed (C.25)

$$[s] = \frac{[L]}{1+K_{CO}[CO]} \qquad \text{CO-adsorbed} \qquad \text{(C.26)}$$

$$[s] = \frac{[L]}{1+K_{H_2O}[H_2O]} \qquad H_2O\text{-adsorbed} \qquad \text{(C.27)}$$

Equations C.22 and C.23 then become:

$$-r_{CO} = \frac{k_2 K_{CO}[L]([CO][H_2O]-\frac{k_{-2}K_{CO_2}}{k_2\ K_{CO}}[CO_2][H_2])}{(1+K_{CO}[CO])} \qquad \text{CO-adsorbed} \qquad \text{(C.28)}$$

$$-r_{CO} = \frac{k_2 K_{H_2O}[L]([CO][H_2O]-\frac{k_{-2}\ K_{H_2}}{k_2\ K_{H_2O}}[CO_2][H_2])}{(1+K_{H_2O}[H_2O])} \qquad H_2O\text{-adsorbed} \qquad \text{(C.29)}$$

The reaction equilibrium constant, K, is the ratio $\frac{k_2}{k_{-2}}\frac{K_{CO}}{K_{CO_2}}$ for the CO-adsorbed case, and $\frac{k_2}{k_{-2}}\frac{K_{H_2O}}{K_{H_2}}$ for the H_2O-adsorbed case. The effective rate constant for the reaction, k, is defined as $k_2[L]$. Therefore, equations C.28 and C.29 become:

$$-r_{CO} = \frac{kK_{CO}([CO][H_2O]-[CO_2][H_2]/K)}{(1+K_{CO}[CO])} \qquad \text{CO-adsorbed} \qquad \text{(C.30)}$$

$$-r_{CO} = \frac{kK_{H_2O}([CO][H_2O]-[CO_2][H_2]/K)}{(1+K_{H_2O}[H_2O])} \qquad H_2O\text{-adsorbed} \qquad \text{(C.31)}$$

C.1.3. Redox Model

The proposed Redox mechanism can be written as:

$$H_2O + * \rightleftharpoons H_2 + O* \qquad \text{reversible} \qquad \text{(C.32)}$$
$$CO + O* \rightleftharpoons CO_2 + * \qquad \text{reversible, rate-determining step} \qquad \text{(C.33)}$$

where $*$ is the reduced center and $O*$ (which is an adsorbed atomic oxygen) is the oxidized center. The rates of formation and consumption of the oxidized center are assumed to be equal, or in other words, $O*$ is treated as a reactive intermediate, and equation C.33 is assumed to be the rds. The rate of CO depletion becomes:

$$-r_{CO} = k_1[CO][O*] - k_{-1}[CO_2][*] \quad \text{(C.34)}$$

where k_1 is the reaction rate constant for the forward reaction in C.33, k_{-1} is the reverse reaction rate constant. The concentration of the oxidized center can be found from the pseudo steady-state hypothesis by equating its rates of formation and consumption:

$$k_1[CO][O*] + k_{-2}[H_2][O*] = k_{-1}[CO_2][*] + k_2[H_2O][*] \quad \text{(C.35)}$$

Solving for $[O*]$:

$$[O*] = \left(k_2[H_2O][*] + k_{-1}[CO_2][*]\right) \Big/ \left(k_1[CO] + k_{-2}[H_2]\right) \quad \text{(C.36)}$$

By doing a site balance on the surface of the catalyst and using equation C.36, an expression for $[*]$ can obtained in terms of the total surface concentration, $[L]$:

$$[L] = [*] + [O*] = [*]\left(1 + \frac{(k_2[H_2O]+k_{-1}[CO_2])}{(k_1[CO]+k_{-2}[H_2])}\right) \quad \text{(C.37)}$$

$$[*] = \frac{[L](k_1[CO]+k_{-2}[H_2])}{k_1[CO]+k_2[H_2O]+k_{-1}[CO_2]+k_{-2}[H_2]} \quad \text{(C.38)}$$

Equation C.34 then becomes:

$$-r_{CO} = \frac{k_1k_2[CO][H_2O]L - k_{-1}k_{-2}[CO_2][H_2]L}{k_1[CO]+k_2[H_2O]+k_{-1}[CO_2]+k_{-2}[H_2]} \quad \text{(C.39)}$$

The reaction equilibrium constant, K, is defined as the ratio $\frac{k_1}{k_{-1}}\frac{k_2}{k_{-2}}$, and to match the form of the equation from the literature, $[L]$ is lumped into k_1k_2 . C.39 becomes:

$$-r_{CO} = \frac{k_1k_2([CO][H_2O] - [CO_2][H_2]/K)}{k_1[CO]+k_2[H_2O]+k_{-1}[CO_2]+k_{-2}[H_2]} \quad \text{(C.40)}$$

C.2. Equations Used for Fitting the Models to Experimental Data

In order to provide reasonable initial guesses for the parameters before using Solver® in Excel, the partial derivatives in the form of equation B2 were solved simultaneously for all parameters used in the fitting. The parameters for CO_2 and H_2 were assumed to be the same due to their equal low concentrations, thereby reducing the number of degrees of freedom. The partial derivative that was initially solved in Mathcad® software is:

$$\epsilon = \left(r_{pred} - r_{meas}\right)^2 \qquad \text{(C.41)} \qquad \frac{\partial \epsilon}{\partial p} = 0 \qquad \text{(C.42)}$$

where ϵ is the sum squared of errors, r_{pred} is the rate predicted using the corresponding model, r_{meas} is the measured experimental rate, and p is a fitting parameter.

The generalized reduced gradient (GRG) algorithm available in Excel was then used to further optimize the fitting.

C.3. Sample Calculations for Fitting of Kinetic Data

Below is a sample Mathcad sheet for calculating initial values for the adsorption equilibrium and rate constants of the LH model for 0.5La catalyst. These values were then used in Excel® for further optimization of fitting parameters that minimize the sum squared errors. The initial guesses that go in the solve block were acquired from Poloski *et al.*[50].

Sample Calculations for Fitting 0.5La Kinetic Data to Langmuir-Hinshelwood Model

ORIGIN:= 1 $i := 1..8$ $j := 1..4$ $K_{eq} := 12.115$

Measured data

$$r_{meas} := \begin{pmatrix} 0.011643201 \\ 0.010827026 \\ 0.007979587 \\ 0.015493484 \\ 0.011912514 \\ 0.018692096 \\ 0.02259573 \\ 0.025317564 \end{pmatrix} \frac{mol}{gm \cdot min}$$

$$C := \begin{array}{c} \begin{matrix} \text{"CO"} & \text{"H2O"} & \text{"CO2"} & \text{"H2"} \end{matrix} \\ \begin{pmatrix} 2.69E\text{-}03 & 1.12E\text{-}02 & 1.13E\text{-}03 & 1.13E\text{-}03 \\ 2.09E\text{-}03 & 1.31E\text{-}02 & 7.96E\text{-}04 & 7.96E\text{-}04 \\ 1.99E\text{-}03 & 1.29E\text{-}02 & 8.71E\text{-}04 & 8.71E\text{-}04 \\ 3.69E\text{-}03 & 9.43E\text{-}03 & 1.32E\text{-}03 & 1.32E\text{-}03 \\ 3.44E\text{-}03 & 8.97E\text{-}03 & 1.50E\text{-}03 & 1.50E\text{-}03 \\ 3.21E\text{-}03 & 1.12E\text{-}02 & 1.00E\text{-}03 & 1.00E\text{-}03 \\ 3.39E\text{-}03 & 1.18E\text{-}02 & 8.05E\text{-}04 & 8.05E\text{-}04 \\ 3.57E\text{-}03 & 1.20E\text{-}02 & 7.07E\text{-}04 & 7.07E\text{-}04 \end{pmatrix} \end{array} \frac{mol}{L}$$

LH model and error equations

$$r_{calc}(k, K_{CO}, K_{H2O}, K_{comb}, i) := k \cdot \frac{K_{CO} \cdot K_{H2O} \cdot \left(C_{i,1} \cdot C_{i,2} - \frac{C_{i,3} \cdot C_{i,4}}{K_{eq}} \right)}{\left(1 + K_{CO} \cdot C_{i,1} + K_{H2O} \cdot C_{i,2} + 2 \cdot K_{comb} \cdot C_{i,3} \right)^2}$$

$$\varepsilon_{err}(k, K_{CO}, K_{H2O}, K_{comb}) := \sum_{i=1}^{8} \left(\left(r_{calc}(k, K_{CO}, K_{H2O}, K_{comb}, i) - r_{meas_i} \right) \right)^2$$

$$d_{KCO}(k, K_{CO}, K_{H2O}, K_{comb}) := \frac{d}{dK_{CO}} \varepsilon_{err}(k, K_{CO}, K_{H2O}, K_{comb})$$

$$d_{KH2O}(k, K_{CO}, K_{H2O}, K_{comb}) := \frac{d}{dK_{H2O}} \varepsilon_{err}(k, K_{CO}, K_{H2O}, K_{comb})$$

$$d_{Kcomb}(k, K_{CO}, K_{H2O}, K_{comb}) := \frac{d}{dK_{comb}} \varepsilon_{err}(k, K_{CO}, K_{H2O}, K_{comb})$$

$$d_{k}(k, K_{CO}, K_{H2O}, K_{comb}) := \frac{d}{dk} \varepsilon_{err}(k, K_{CO}, K_{H2O}, K_{comb})$$

$K_{CO} := 1000$ $K_{H2O} := 1000$

$K_{comb} := 4000$ $k := 0.26$

Units of the adsorption equilibrium constants are L/mol as reported in Section 3.6 of the Dissertation. Rate constant is in mol/g*min

Adsoprtion equilibrium constants for CO2 and H2 are combined as one constant because they are equal

Given

$d_{KCO}(k, K_{CO}, K_{H2O}, K_{comb}) = 0$ $d_{Kcomb}(k, K_{CO}, K_{H2O}, K_{comb}) = 0$

$d_{KH2O}(k, K_{CO}, K_{H2O}, K_{comb}) = 0$ $0 = d_{k}(k, K_{CO}, K_{H2O}, K_{comb})$

$K_{comb} > 0$ $K_{CO} > 0$ $K_{H2O} > 0$

$$\begin{pmatrix} K_{CO} \\ k \\ K_{H2O} \\ K_{comb} \end{pmatrix} := \text{Find}(K_{CO}, k, K_{H2O}, K_{comb})$$

$k = 0.327$ $K_{comb} = 7.784 \times 10^{3}$ $K_{CO} = 1.409 \times 10^{3}$ $K_{H2O} = 2.387 \times 10^{3}$

$\varepsilon_{err}(k, K_{CO}, K_{H2O}, K_{comb}) = 4.386 \times 10^{-5}$ sum squared error

C.4. Statistical Analysis Using Mathematica®

Below is a sample code for 0.5La HT WGS catalyst from Mathematica® for generating 95% joint confidence regions for K_{CO} and K_{H_2O}. The standard error on the estimates were adjusted in Excel® to account for non-fixed values of K_{CO2}, K_{H_2}, and k.

In[18]:=
```
data = {{0.00269, 0.0112, 0.00113, 0.00113, 0.0116432},
  {0.00209, 0.0131, 0.000796, 0.000796, 0.010827026},
  {0.00199, 0.0129, 0.000871, 0.000871, 0.007979587},
  {0.00369, 0.00943, 0.00132, 0.00132, 0.015493484},
  {0.00344, 0.00897, 0.0015, 0.0015, 0.011912514},
  {0.00321, 0.0112, 0.001, 0.001, 0.018692096},
  {0.00339, 0.0118, 0.000805, 0.000805, 0.02259573},
  {0.00357, 0.012, 0.000707, 0.000707, 0.025317564}}
```

Out[18]=
```
{{0.00269, 0.0112, 0.00113, 0.00113, 0.0116432},
 {0.00209, 0.0131, 0.000796, 0.000796, 0.010827},
 {0.00199, 0.0129, 0.000871, 0.000871, 0.00797959},
 {0.00369, 0.00943, 0.00132, 0.00132, 0.0154935},
 {0.00344, 0.00897, 0.0015, 0.0015, 0.0119125},
 {0.00321, 0.0112, 0.001, 0.001, 0.0186921},
 {0.00339, 0.0118, 0.000805, 0.000805, 0.0225957},
 {0.00357, 0.012, 0.000707, 0.000707, 0.0253176}}
```

In[19]:=
```
nlm = NonlinearModelFit[data,
  k kco kh2o (co h2o - co2 h2 / ke) / (1 + kco co + kh2o h2o + kco2 co2 + kh2 h2)^2 /.
   {ke → 12.115, kco2 → 5900, kh2 → 5900, k → 0.363517794},
  {kco, kh2o}, {co, h2o, co2, h2}, MaxIterations → 10000];
nlm[{"ParameterConfidenceIntervalTable", "ANOVATable"}]
```

Out[19]=

	Estimate	Standard Error	Confidence Interval
kco	931.329	76.7754	{743.466, 1119.19}
kh2o	1577.76	626.009	{45.9722, 3109.55}

	DF	SS	MS
Model	2	0.00215824	0.00107912
Error	6	0.0000411183	6.85305×10^{-6}
Uncorrected Total	8	0.00219936	
Corrected Total	7	0.000263035	

In[20]:=
```
residual = k kco kh2o (#1 #2 - 0.08254230293025175` #3 #4) / (1 + kco #1 + kh2o #2 + kco2 #3 + kh2 #4)^2 & @@@ data[[All, 1 ;; 4]] -
  data[[All, 5]]
```

Out[20]=

$$\left\{-0.0116432 + \frac{0.0000300226\ k\ kco\ kh2o}{(1 + 0.00269\ kco + 0.00113\ kco2 + 0.00113\ kh2 + 0.0112\ kh2o)^2},\right.$$

$$-0.010827 + \frac{0.0000273267\ k\ kco\ kh2o}{(1 + 0.00209\ kco + 0.000796\ kco2 + 0.000796\ kh2 + 0.0131\ kh2o)^2},$$

$$-0.00797959 + \frac{0.0000256084\ k\ kco\ kh2o}{(1 + 0.00199\ kco + 0.000871\ kco2 + 0.000871\ kh2 + 0.0129\ kh2o)^2},$$

$$-0.0154935 + \frac{0.0000346529\ k\ kco\ kh2o}{(1 + 0.00369\ kco + 0.00132\ kco2 + 0.00132\ kh2 + 0.00943\ kh2o)^2},$$

$$-0.0119125 + \frac{0.0000306711\ k\ kco\ kh2o}{(1 + 0.00344\ kco + 0.0015\ kco2 + 0.0015\ kh2 + 0.00897\ kh2o)^2},$$

$$-0.0186921 + \frac{0.0000358695\ k\ kco\ kh2o}{(1 + 0.00321\ kco + 0.001\ kco2 + 0.001\ kh2 + 0.0112\ kh2o)^2},$$

$$-0.0225957 + \frac{0.0000399485\ k\ kco\ kh2o}{(1 + 0.00339\ kco + 0.000805\ kco2 + 0.000805\ kh2 + 0.0118\ kh2o)^2},$$

$$\left.-0.0253176 + \frac{0.0000427987\ k\ kco\ kh2o}{(1 + 0.00357\ kco + 0.000707\ kco2 + 0.000707\ kh2 + 0.012\ kh2o)^2}\right\}$$

In[21]:= **func = residual.residual**

Out[21]=
$$\left(-0.0119125+\frac{0.0000306711\ k\ kco\ kh2o}{(1+0.00344\ kco+0.0015\ kco2+0.0015\ kh2+0.00897\ kh2o)^2}\right)^2+$$
$$\left(-0.0154935+\frac{0.0000346529\ k\ kco\ kh2o}{(1+0.00369\ kco+0.00132\ kco2+0.00132\ kh2+0.00943\ kh2o)^2}\right)^2+$$
$$\left(-0.0186921+\frac{0.0000358695\ k\ kco\ kh2o}{(1+0.00321\ kco+0.001\ kco2+0.001\ kh2+0.0112\ kh2o)^2}\right)^2+$$
$$\left(-0.0116432+\frac{0.0000300226\ k\ kco\ kh2o}{(1+0.00269\ kco+0.00113\ kco2+0.00113\ kh2+0.0112\ kh2o)^2}\right)^2+$$
$$\left(-0.0225957+\frac{0.0000399485\ k\ kco\ kh2o}{(1+0.00339\ kco+0.000805\ kco2+0.000805\ kh2+0.0118\ kh2o)^2}\right)^2+$$
$$\left(-0.0253176+\frac{0.0000427987\ k\ kco\ kh2o}{(1+0.00357\ kco+0.000707\ kco2+0.000707\ kh2+0.012\ kh2o)^2}\right)^2+$$
$$\left(-0.00797959+\frac{0.0000256084\ k\ kco\ kh2o}{(1+0.00199\ kco+0.000871\ kco2+0.000871\ kh2+0.0129\ kh2o)^2}\right)^2+$$
$$\left(-0.010827+\frac{0.0000273267\ k\ kco\ kh2o}{(1+0.00209\ kco+0.000796\ kco2+0.000796\ kh2+0.0131\ kh2o)^2}\right)^2$$

In[22]:= **func = func /. kh2 → kco2**

Out[22]=
$$\left(-0.0119125+\frac{0.0000306711\ k\ kco\ kh2o}{(1+0.00344\ kco+0.003\ kco2+0.00897\ kh2o)^2}\right)^2+$$
$$\left(-0.0154935+\frac{0.0000346529\ k\ kco\ kh2o}{(1+0.00369\ kco+0.00264\ kco2+0.00943\ kh2o)^2}\right)^2+$$
$$\left(-0.0186921+\frac{0.0000358695\ k\ kco\ kh2o}{(1+0.00321\ kco+0.002\ kco2+0.0112\ kh2o)^2}\right)^2+$$
$$\left(-0.0116432+\frac{0.0000300226\ k\ kco\ kh2o}{(1+0.00269\ kco+0.00226\ kco2+0.0112\ kh2o)^2}\right)^2+$$
$$\left(-0.0225957+\frac{0.0000399485\ k\ kco\ kh2o}{(1+0.00339\ kco+0.00161\ kco2+0.0118\ kh2o)^2}\right)^2+$$
$$\left(-0.0253176+\frac{0.0000427987\ k\ kco\ kh2o}{(1+0.00357\ kco+0.001414\ kco2+0.012\ kh2o)^2}\right)^2+$$
$$\left(-0.00797959+\frac{0.0000256084\ k\ kco\ kh2o}{(1+0.00199\ kco+0.001742\ kco2+0.0129\ kh2o)^2}\right)^2+$$
$$\left(-0.010827+\frac{0.0000273267\ k\ kco\ kh2o}{(1+0.00209\ kco+0.001592\ kco2+0.0131\ kh2o)^2}\right)^2$$

In[23]:=
```
func = func /. k → 0.363517794
```

Out[23]=

$$\left(-0.0119125 + \frac{0.0000111495\ \text{kco kh2o}}{(1 + 0.00344\ \text{kco} + 0.003\ \text{kco2} + 0.00897\ \text{kh2o})^2}\right)^2 +$$
$$\left(-0.0154935 + \frac{0.0000125969\ \text{kco kh2o}}{(1 + 0.00369\ \text{kco} + 0.00264\ \text{kco2} + 0.00943\ \text{kh2o})^2}\right)^2 +$$
$$\left(-0.0186921 + \frac{0.0000130392\ \text{kco kh2o}}{(1 + 0.00321\ \text{kco} + 0.002\ \text{kco2} + 0.0112\ \text{kh2o})^2}\right)^2 +$$
$$\left(-0.0116432 + \frac{0.0000109137\ \text{kco kh2o}}{(1 + 0.00269\ \text{kco} + 0.00226\ \text{kco2} + 0.0112\ \text{kh2o})^2}\right)^2 +$$
$$\left(-0.0225957 + \frac{0.000014522\ \text{kco kh2o}}{(1 + 0.00339\ \text{kco} + 0.00161\ \text{kco2} + 0.0118\ \text{kh2o})^2}\right)^2 +$$
$$\left(-0.0253176 + \frac{0.0000155581\ \text{kco kh2o}}{(1 + 0.00357\ \text{kco} + 0.001414\ \text{kco2} + 0.012\ \text{kh2o})^2}\right)^2 +$$
$$\left(-0.00797959 + \frac{9.3091 \times 10^{-6}\ \text{kco kh2o}}{(1 + 0.00199\ \text{kco} + 0.001742\ \text{kco2} + 0.0129\ \text{kh2o})^2}\right)^2 +$$
$$\left(-0.010827 + \frac{9.93374 \times 10^{-6}\ \text{kco kh2o}}{(1 + 0.00209\ \text{kco} + 0.001592\ \text{kco2} + 0.0131\ \text{kh2o})^2}\right)^2$$

In[24]:=
```
const = nlm["ANOVATableSumsOfSquares"][[2]]
  (1 + 2 / (Length[data] - 3) Quantile[FRatioDistribution[3, Length[data] - 3], 0.95])
```

Out[24]= 0.000130089

In[25]:=
```
Show[ContourPlot[Evaluate[func == const /. kco2 → 5900], {kco, 0, 2000},
  {kh2o, 0 , 8000}, FrameLabel → {"kco (L/mol)", "kH2o (L/mol)"},
  MaxRecursion → 10, LabelStyle → {FontFamily → "Calibri", FontSize → 18}],
 Graphics[{Red, PointSize[Large], Point[{nlm["ParameterTableEntries"][[1, 1]],
    nlm["ParameterTableEntries"][[2, 1]]}]}]]
```

Out[25]=

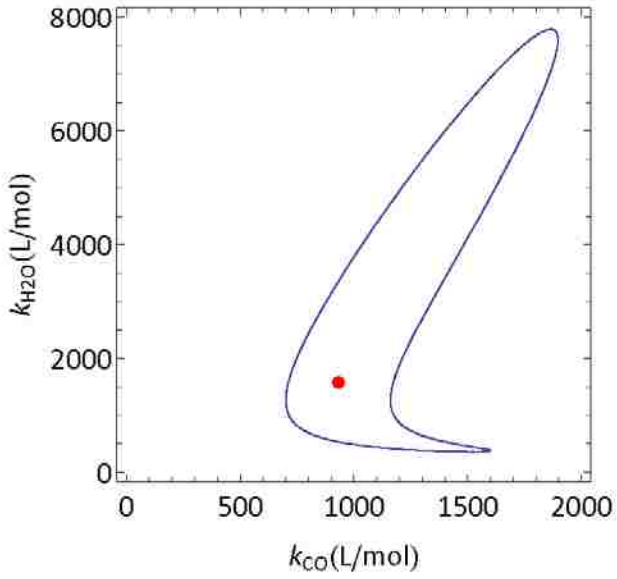

In[26]:=
```
Show[RegionPlot[Evaluate[func < const /. kco2 → 5900], {kco, 0, 2000},
  {kh2o, 0, 8000}, FrameLabel → {"k_CO (L/mol)", "k_H2O (L/mol)"},
  MaxRecursion → 10, LabelStyle → {FontFamily → "Calibri", FontSize → 18}],
 Graphics[{Red, PointSize[Large], Point[{nlm["ParameterTableEntries"][[1, 1]],
    nlm["ParameterTableEntries"][[2, 1]]}]}]]
```

Out[26]=

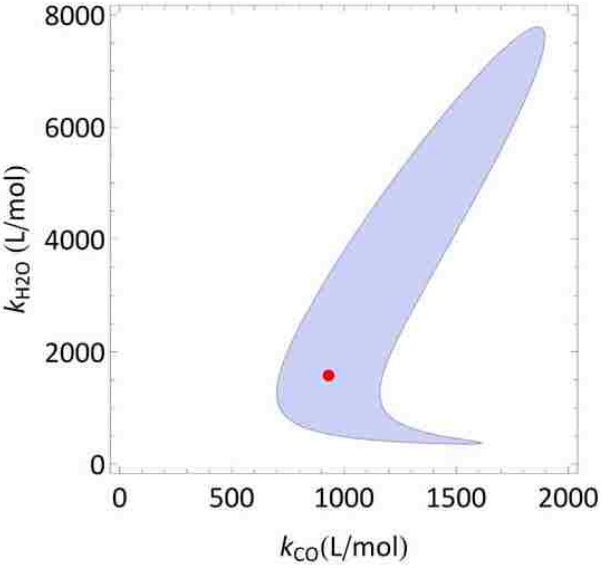

C.5. Statistical Analysis Using R®

TXT FILE

E_a data half.txt

Temp	rate
623.15	0.0083409
648.15	0.0162442
673.15	0.0306417
698.15	0.0483152

R Script

```
local({pkg <- select.list(sort(.packages(all.available = TRUE)),graphics=TRUE)
if(nchar(pkg)) library(pkg, character.only=TRUE)})
data3<-read.table("E_a data one.txt", header=TRUE)
data3<-read.table("E_a data one.txt", header=TRUE)
data3
nls3<-nls(rate~A*exp(-Ea/(8.31447*Temp)), data3, start=list(A=10^6, Ea=10^5))
nls3<-nls(rate~A*exp(-Ea/(8.31447*Temp)), data3, start=list(A=10^5, Ea=10^5))
summary(nls3)
nls3<-nls(rate~A*exp(-Ea/(8.31447*Temp)), data3, start=list(A=10^6, Ea=10^6))
nls3<-nls(rate~A*exp(-Ea/(8.31447*Temp)), data3, start=list(A=10^5, Ea=10^5))
summary(nls3)
cr3<-ConfRegions(nls3,exp=5,length=1000)
cr3<-ConfRegion(nls3,exp=5,length=1000)
cr3<-nlsConfRegions(nls3,exp=5,length=1000)
plot(cr3$cr[,1],cr3$cr[,2],"*", xlab="A/c (mol/(g*min))",ylab="E (J/mol)")
plot(cr3$cr[,1],cr3$cr[,2],pch = "*", xlab="A/c (mol/(g*min))",ylab="E (J/mol)")
points(1380,63074,col="red",pch=4,lwd=4)
data4<-read.table("E_a data two.txt", header=TRUE)
data4
nls4<-nls(rate~A*exp(-Ea/(8.31447*Temp)), data4, start=list(A=10^5, Ea=10^5))
summary(nls4)
cr4<-ConfRegions(nls4,exp=5,length=1000)
cr4<-nlsConfRegions(nls4,exp=5,length=1000)
plot(cr4$cr[,1],cr4$cr[,2],pch = "*", xlab="A/c (mol/(g*min))",ylab="E (J/mol)")
points(1342,64358,col="red",pch=4,lwd=4)
data5<-read.table("E_a data five.txt", header=TRUE)
data5
nls5<-nls(rate~A*exp(-Ea/(8.31447*Temp)), data5, start=list(A=10^5, Ea=10^5))
summary(nls5)
cr5<-nlsConfRegions(nls5,exp=5,length=1000)
plot(cr5$cr[,1],cr5$cr[,2],pch = "*", xlab="A/c (mol/(g*min))",ylab="E (J/mol)")
points(1657,66178,col="red",pch=4,lwd=4)
data<-read.table("E_a data.txt", header=TRUE)
data
nls<-nls(rate~A*exp(-Ea/(8.31447*Temp)), data, start=list(A=10^6, Ea=10^5))
summary(nls)
cr1<-nlsConfRegions(nls,exp=5,length=1000)
plot(cr1$cr[,1],cr1$cr[,2],pch = "*", xlab="A/c (mol/(g*min))",ylab="E (J/mol)")
points(674758,96241,col="red",pch=4,lwd=4)
data2<-read.table("E_a data half.txt", header=TRUE)
data2
nls2<-nls(rate~A*exp(-Ea/(8.31447*Temp)), data2, start=list(A=10^6, Ea=10^5))
summary(nls2)
cr2<-nlsConfRegions(nls2,exp=5,length=1000)
plot(cr2$cr[,1],cr2$cr[,2],pch = "*", xlab="A/c (mol/(g*min))",ylab="E (J/mol)")
points(52181,80578,col="red",pch=4,lwd=4)
##############################################################################
###This R script estimates the activation energies and Arrhenius constants###
###(divided by the partial pressure dependence which is assumed to be a constant###
### function of temperature. The input data are "txt" files with two columns ###
### of temperature and measured rate ###
```

Appendix D. Electron-Dispersive X-ray Spectra for HT WGS Catalysts

A notable difference between the 2La and 5La samples and the other samples after TPR 1 is the presence of sodium in these two catalysts. The peak at around 1.1 keV corresponds to Na-Kα and shows that sodium exists in larger amounts in the 2La and 5La catalysts when it is compared to Fe-Lα peak at around 0.7 keV. However, this same sodium peak at 1.1 keV appears to be much less intense in the calcined 2La sample than it is in the reduced sample. Therefore, once these two catalysts start reducing, the sodium ions in the bulk become more mobile and move to the surface of the catalyst, affecting the absorbance signal. Considering the reduction potentials of Na^{+} to Na (-2.71 V) and Fe^{3+} to Fe (0.33 V), sodium is most probably present in its oxide form, which is a white powder, at the conditions of the TPR experiments. The diffusion of the sodium oxide white powder to the surface of the 2La and 5La catalysts during reduction cause the absorbance signal to go down.

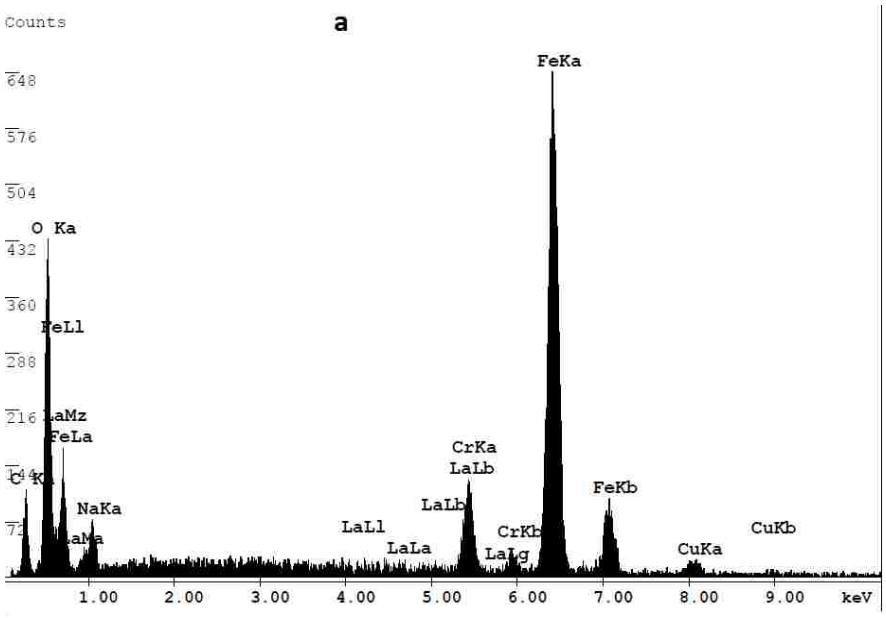

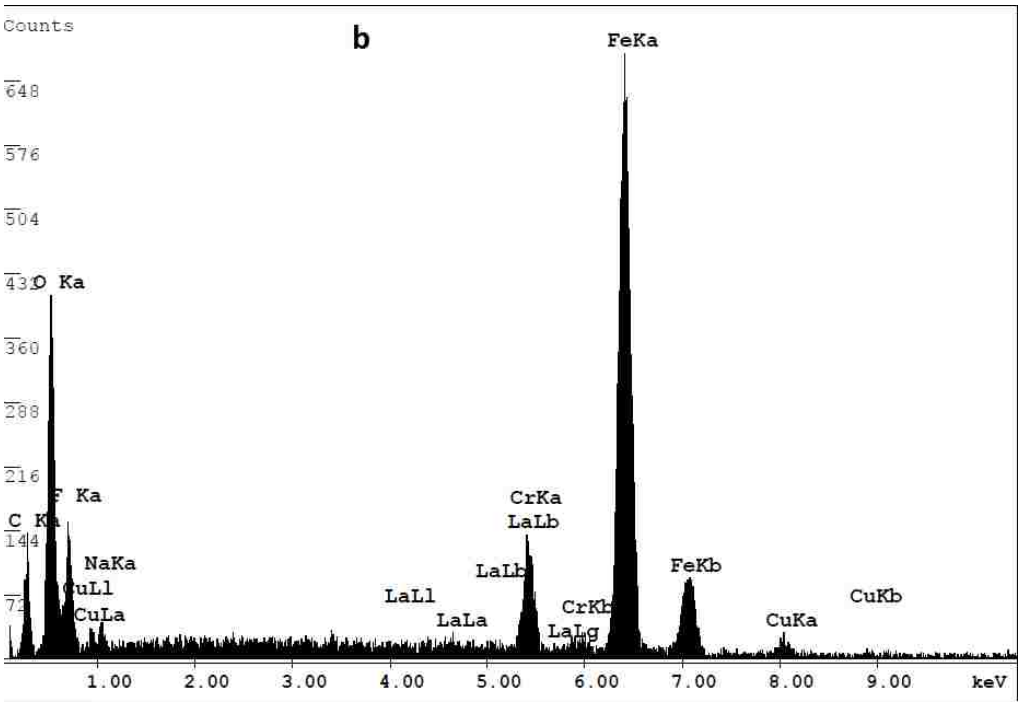
b
Counts
648
576
504
O Ka
360
288
216
F Ka
C Ka
144
NaKa
MgKa
AlKa
SiKa
CuLl
CuLa
LaLl
LaLa
CrKa
LaLb
LaLb
FeKa
CrKb
LaLg
FeKb
CuKa
CuKb
1.00
2.00
3.00
4.00
5.00
6.00
7.00
8.00
9.00
keV

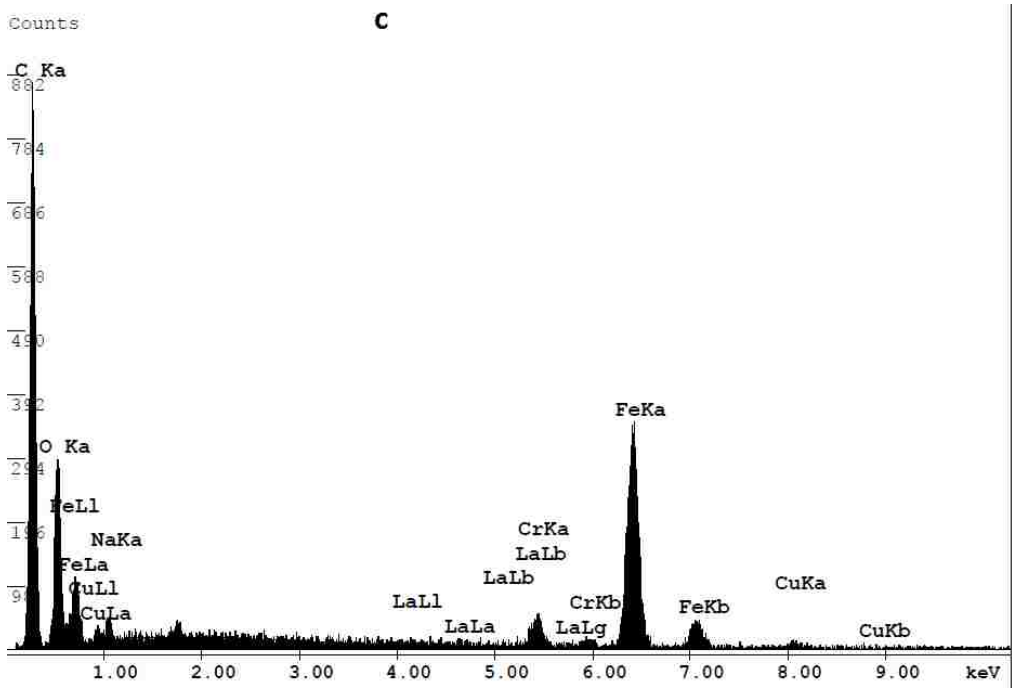
c
Counts
C Ka
784
588
490
O Ka
FeLl
NaKa
FeLa
CuLl
CuLa
LaLl
LaLa
CrKa
LaLb
LaLb
FeKa
CrKb
LaLg
FeKb
CuKa
CuKb
1.00
2.00
3.00
4.00
5.00
6.00
7.00
8.00
9.00
keV

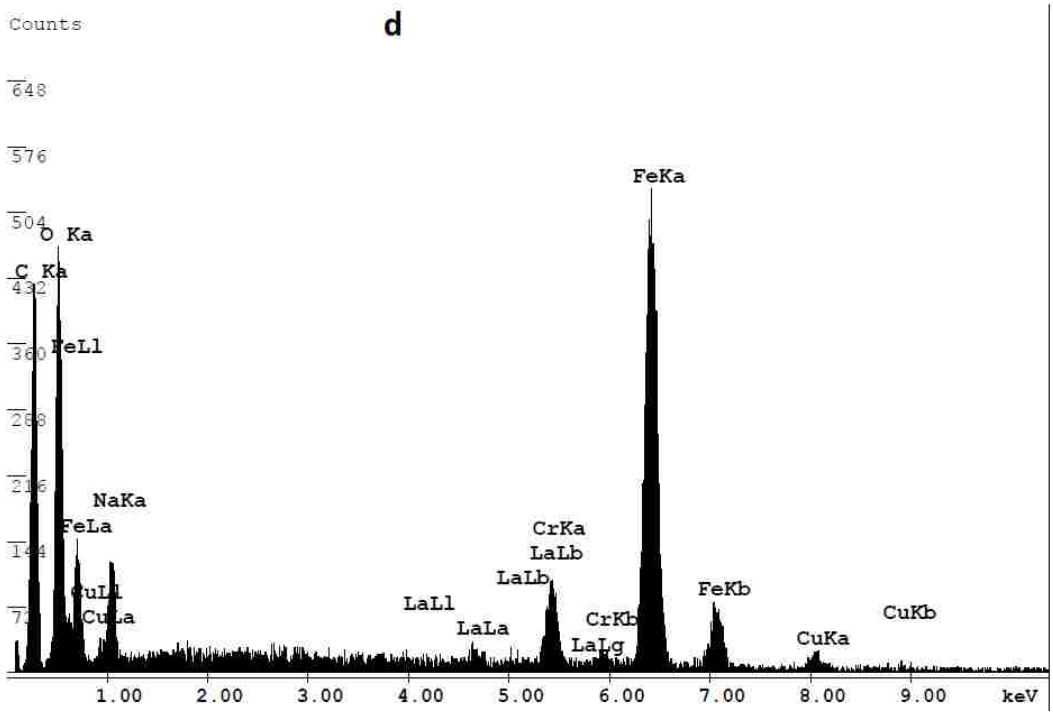
d
Counts
648
576
504
432
360
288
216
144
72
O Ka
C Ka
FeLl
NaKa
FeLa
CuLl
CuLa
LaLl
LaLa
CrKa
LaLb
LaLb
CrKb
LaLg
FeKa
FeKb
CuKa
CuKb
1.00
2.00
3.00
4.00
5.00
6.00
7.00
8.00
9.00
keV

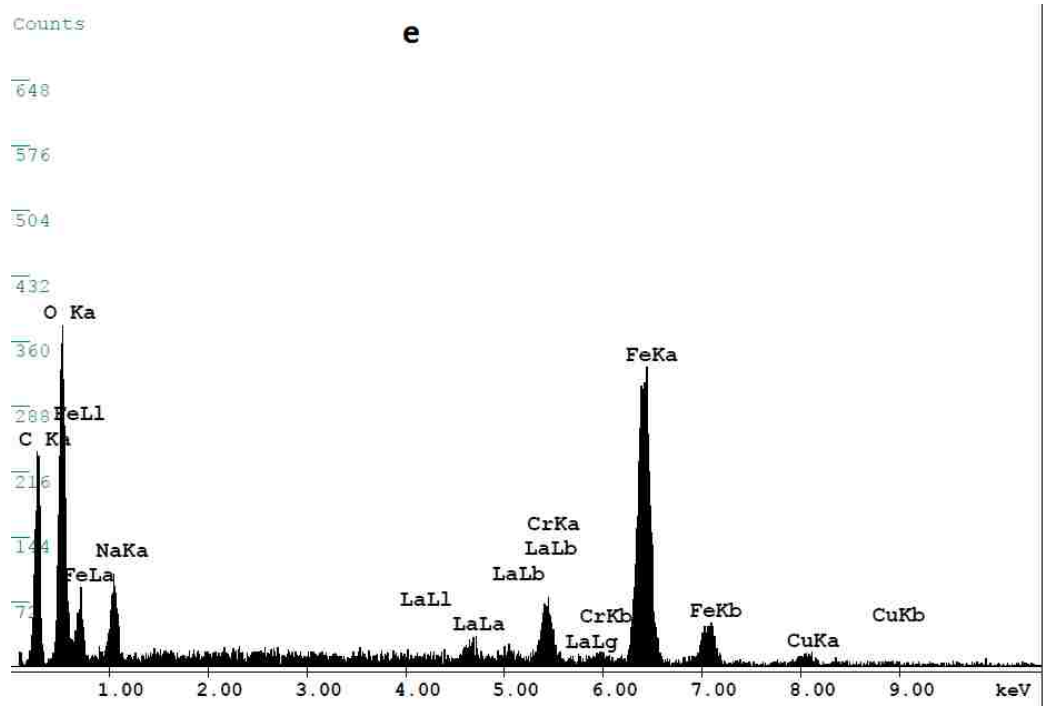
e
Counts
648
576
504
432
360
288
216
144
72
O Ka
FeLl
C Ka
NaKa
FeLa
LaLl
LaLa
CrKa
LaLb
LaLb
CrKb
LaLg
FeKa
FeKb
CuKa
CuKb
1.00
2.00
3.00
4.00
5.00
6.00
7.00
8.00
9.00
keV

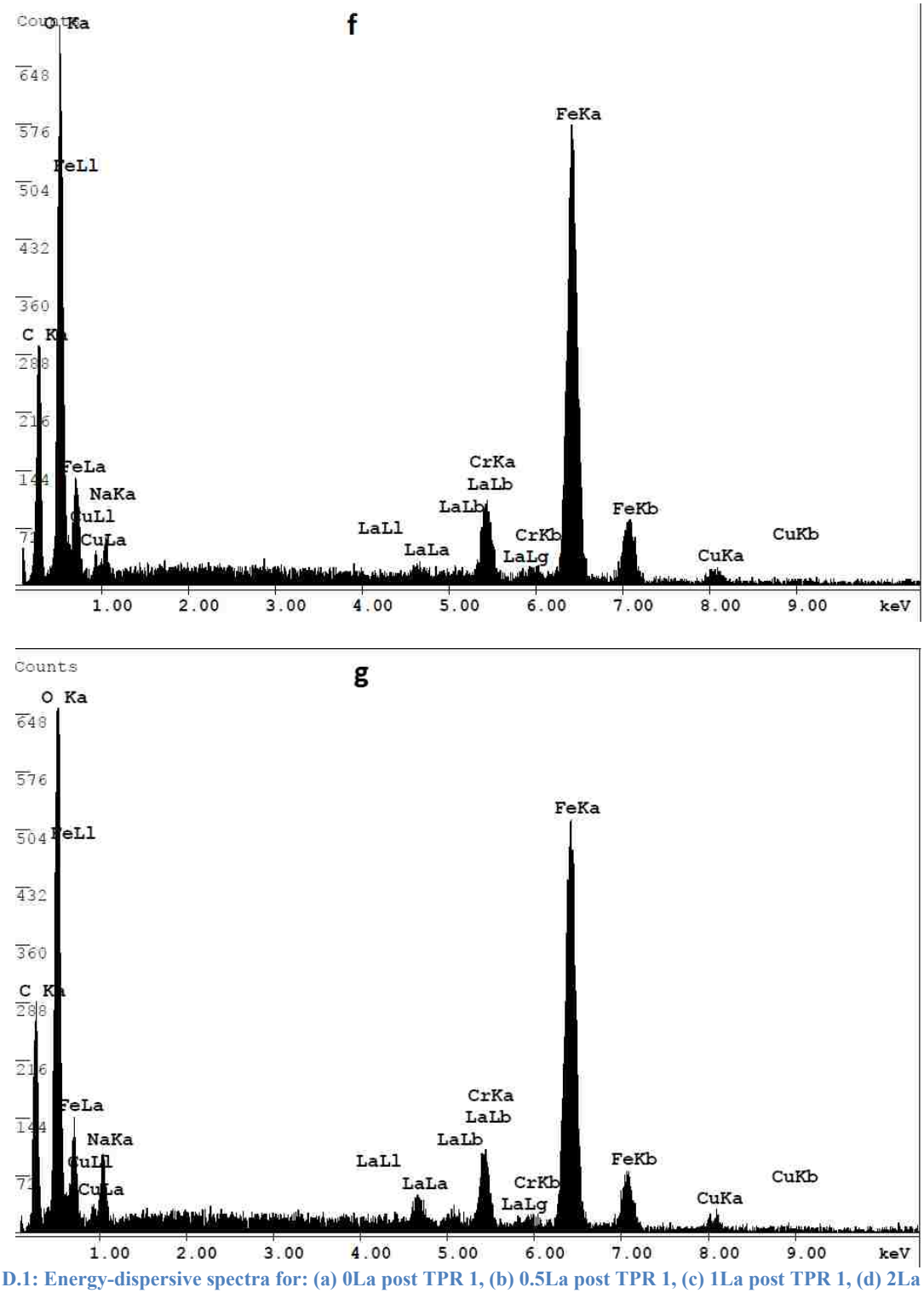

Figure D.1: Energy-dispersive spectra for: (a) 0La post TPR 1, (b) 0.5La post TPR 1, (c) 1La post TPR 1, (d) 2La post TPR 1, (e) 5La post TPR 1, (f) 2La calcined, and (g) 5La calcined.

Appendix E. Particle Model for Fischer-Tropsch Reaction

Below is the APM file code developed for the optimization of catalyst design for the lab-scale reactor and for which the results were presented in Chapter 5 of this dissertation.

APM FILE (LAB-SCALE)

```
Model
    Constants
      pi= 3.14159
    End Constants

    Parameters
     sigma_CO = 3.59                    ! Hard-sphere diameter for
CO in Angstroms
     sigma_H2 = 2.92                    ! Hard-sphere diamaeter in
Angstroms
     sigma_ico = 8.753                  ! Hard-sphere diameter for
icosane in Angstroms
     mw_co = 28.011                     ! Molecular weight of CO in
g/mol
     mw_H2 = 2.016                      ! Molecular weight of H2 in
g/mol
     mw_He = 4.002                      ! Molecular weight of He in
g/mol
     mw_ico = 282.556                   ! Molecular weight of C20H42
in g/mol
     mw_H2O = 18.015                    ! Molecular weight of H2O in
g/mol
     mw_CO2 = 44.01                     ! Molecular weight of CO2 in
g/mol
     mw_CH4 = 16.04                     ! Molecular weight of CH4 in
g/mol
     mw_C2 = 29                         ! Molecular weight of C2 in
g/mol
     mw_C3 = 43                         ! Molecular weight of C3 in
g/mol
     mw_C4 = 57                         ! Molecular weight of C4 in
g/mol
     tau = 3.5                          ! Turtuosity
     den_bulk = 0.8                     ! Bulk density of catalyst
in g/cm^3
     d_pore = 14.9*10^(-9)              ! Pore diameter in m
     v_pore = 0.06                      ! Pore volume of catalyst in
cm^3/g
     sa_cat = 20                        ! Surface area of catalyst
in m^2/g
     ea = 93800                         ! Activation energy in J/mol
     arr = 3.32*10^7/(60)               ! Arrhenius pre-exponential
faction in mol/(atm^0.55*min*g)
     t0 = 298.15                        ! Ambient temperature in
Kelvin
     p0 = 102942                        ! Ambient pressure in Provo
in Pa
     rg = 8.31446                       ! Gas constant L*kPA/mol*K
     del_Hr = -165*10^3                 ! heat of reaction in J/mol
     d_reac= 9.525*10^(-3)              ! Diameter of the reactor in
meters
     si = 0.92                          ! Shape factor
     cp_stream = 26.331                 ! Heat capacity of inlet gas
stream in J/(mol.K)
     k_g = 0.19                         ! Thermal conductivity of
inlet gas stream in W/(m*K)
     y_He = 0.4                         ! Molar fraction of He in
inlet feed stream
     n = 0.55                           ! Order of reaction
     v_in  = 150                        ! Inlet volumetric flow rate
of feed stream in sccm
     g = 9.81                           ! Gravitational constant in m/s^2
```

```
     w_cat = 0.25                                          ! Mass of catalyst in g
     w_silcarb = 1                                         ! Mass of silicon carbide in g

     den_silcarb = 1.57                                    ! Density of silicon carbide
in g/cm^3
     selC5plus = 0.46                                      ! Selectivity of liquid
hydrocarbons
     selC2C4 = 0.1                                         ! Selectivity of C2 - C4
hydrocarbons
     selCO2 = 0.4                                          ! Selectivity of WGS
reaction
     selCH4 = 0.04                                         ! Selectivity of methane
     ed = 60000                                            ! Activation energy for
deactivation in J/mol
     ad = 23183                                            ! Arrehnius pre-exponential
factor for deactivation in 1/hr
     time = 1000                                           ! Time of reaction in hours
    End Parameters

    Variables
     d_p = 425*10^(-6), >= 80*10^(-6) , <= 0.01            ! Particle diameter in
meters
     t = 543.15, >= 493.15 , <= 553.15                     ! Reaction temperature in
Kelvin
     p = 2.0*10^6, >= 1.5*10^6, <= 3*10^6                  ! Reaction pressure in Pa
     y_co = 0.3, >= 0.2, <=0.4                             ! Molar fraction of CO in
inlet feed stream
     !M_W                                                  ! Weisz Modulus
     prod                                                  ! Productivity
   End Variables

    Intermediates
         ! Rate of CO consumption calculations
         l_p = d_p/6                                       ! Characteristic length for
a shpere
         coef_CO = -(20*selC5plus+1*selCH4+3*selC2C4+1*selCO2)          !
stoichiometric coefficient of CO
         coef_H2 = -(41*selC5plus+3*selCH4+7*selC2C4-1*selCO2)          !
stoichiometric coefficient of H2
         coef_ico = 1*selC5plus                                         !
stoichiometric coefficient of icosane
         coef_H2O = 20*selC5plus+1*selCH4+3*selC2C4+1-selCO2            !
stoichiometric coefficient of H2O
         coef_CH4 = 1*selCH4                                            !
stoichiometric coefficient of CH4
         coef_C2C4 = 1*selC2C4                                          !
stoichiometric coefficient of C2-C4
         coef_CO2 = 1*selCO2                                            !
stoichiometric coefficient of CO2
         H2CO_stoich = 41*selC5plus/20+3*selCH4+(7/3)*selC2C4-selCO2    !
stoichiometric H2 to CO
         kreac = arr*exp(-ea/(rg*t))                       ! Reaction rate constant in
mol/atm^0.55*g*min
         n_in = v_in*p0/(rg*t0)*10^(-6)                    ! Inlet molar flow rate of
feed stream in mol/min
         x_co = 0.845*(4.05556*10^(-7)*t^3 - 0.00057669*t^2 + 0.274055*t -
43.51460)+0.267*(1.8429*y_co^2 - 1.6779*y_co + 0.4296) ! CO conversion
         del = (coef_CO + coef_H2 + coef_ico + coef_H2O)/(-coef_CO)             !
volumertic expansion factor
         vout = (v_in/1000)*(1+del*y_co*x_co)*(t/t0)*(p0/p)                     !
Volumetric flow rate of the gas stream in the outlet in L/min
         c_co = y_co*n_in*(1-x_co)/vout                                         !
Concentration of CO in the outlet in mol/L
```

```
        y_H2 = 1-y_co-y_He                                                    !
Inlet molar fraction of H2
        c_H2 = (y_H2*n_in-H2CO_stoich*y_co*n_in*x_co)/vout                    !
Concentration of H2 in the outlet in mol/L
        n_co_o = y_co*n_in*(1-x_co)                                           !
Molar flow rate of CO in the outlet in mol/min
        n_H2_o = y_H2*n_in-H2CO_stoich*y_co*n_in*x_co                         !
Molar flow rate of H2 in the outlet in mol/min
        n_H2O_o = (selC5plus+selC2C4+selCH4-selCO2)*y_co*n_in*x_co            !
Molar flow of H2O in the outlet in mol/min
        n_CO2_o = selCO2*y_co*n_in*x_co                                       !
Molar flow of CO2 in the outlet in mol/min
        n_CH4_o = selCH4*y_co*n_in*x_co                                       !
Molar flow of CH4 in the outlet in mol/min
        n_C2_o = 0.03*y_co*n_in*x_co/2                                        !
Molar flow of C2 in the outlet in mol/min
        n_C3_o = 0.03**y_co*n_in*x_co/3                                       !
Molar flow of C3 in the outlet in mol/min
        n_C4_o = 0.04*y_co*n_in*x_co/4                                        !
Molar flow of C4 in the outlet in mol/min
        n_He = y_He*n_in                                                      !
Molar flow rate of He in mol/min
        ng_tot = n_co_o+n_H2_o+n_H2O_o+n_CO2_o+n_CH4_o+n_C2_o+n_C3_o+n_C4_o+n_He
! Total molar flow rate outlet
        y_co_o = n_co_o/ng_tot                                  ! Molar fraction of
CO in the outlet
        y_H2_o = n_H2_o/ng_tot                                  ! Molar fraction of
H2 in the outlet
        y_co_r = (y_co_o+y_co)/2                                ! Average molar
fraction of CO in the reactor
        y_H2_r = (y_H2+y_H2_o)/2                                ! Average molar
fraction of H2 in the reactor
        p_co_r = y_co_r*p/101325                                ! Average partial
pressure of CO in the reactor in atm
        p_H2_r = y_H2_r*p/101325                                ! Average partial
pressure of H2 in the reactor in atm
        r_co = kreac*(p_co_r)^(-0.05)*(p_H2_r)^(0.6)            ! Rate of CO
consumption in mol/(g*min)

        ! Diffusion calculations
        v0 =
(1.206+0.0632*(sigma_co/sigma_ico))*(6.022*10^23*(sigma_ico*10^(-10))^3)*10^3/sqrt(2
)                       ! specific volume in L/mol
        v = 1*10^(-6)*(t-273.15)^2 + 2*10^(-5)*(t-273.15) + 0.3786
                                ! specific volume in L/mol
        d_ab = 94.5*10^(-5)*(t^0.5)*(1/(mw_CO^0.239)) *
(1/(mw_ico^0.781))*(1/(sigma_co*sigma_ico)^1.134)*(v-v0)*1000      ! Bulk
diffusivity of CO in C20H42 in cm^2/s
        y_H2O_o = n_H2O_o/ng_tot
        y_CO2_o = n_CO2_o/ng_tot
        y_CH4_o = n_CH4_o/ng_tot
        y_C2_o = n_C2_o/ng_tot
        y_C3_o = n_C3_o/ng_tot
        y_C4_o = n_C4_o/ng_tot
        mw_mix = y_H2_o*mw_H2+y_co_o*mw_CO +
y_He*mw_He+y_H2O_o*mw_H2O+y_CO2_o*mw_CO2+y_CH4_o*mw_CH4+y_C2_o*mw_C2+y_C3_o*mw_C3+y_
C4_o*mw_C4    ! Molecular weight of mixture of feed gas stream in g/mol
        d_k = 4850*(d_pore*100)* (t/mw_co)^0.5          ! Knudsen diffusivity in
cm^2/s
        diff = (1/d_ab + 1/d_k)^(-1)                    ! Combined diffusivity in
cm^2/s

        ! Selectivity calculations from ASF model
```

```
        to = 6.1686*(y_H2_o*P/1000000)^(-0.5)          ! Olefin productivity

        pp = 13.8*(y_co_o*P/1000000)^(0.43)*(y_H2_o*P/1000000)^(-0.47) ! Paraffin
productivity
        alpha = pp/(1+pp+to)                           ! propagation growth
probability
        selCH4new = (1-alpha)^2*alpha^(1-1)*1          ! New CH4 selectivity
        selC2new = (1-alpha)^2*alpha^(2-1)*2           ! New C2 selectivity
        selC3new = (1-alpha)^2*alpha^(3-1)*3           ! New C3 selectivity
        selC4new = (1-alpha)^2*alpha^(4-1)*4           ! New C4 selectivity
        selC5plusnew = 1-selCO2-selC2new-selC3new-selC4new-selCH4 ! New C5plus
selectivity

        ! Heat Transfer coefficients calculations
        phi_p = 1.0                                    ! Sphericity
        e_b = 0.1504 + 0.2024/phi_p + 1.0814/((d_reac/d_p)+0.1226)^2    ! void
fraction
        den_part = den_bulk /(1-e_b)                   ! Particle density in g/cm^3
        e_p = den_part * v_pore                        ! Particle porosity
        den_T = 0.21048*0.001*(0.0018*(t-273.15)^2-1.8808*(t-273.15)+851.77)   ! T
is in Celcius and den_T is in mol/L
        den_P = 0.76568*0.001*(1.5711*(P/6895)+1.968)                          !
den_T is in mol/L and P is in Psi
        den_gas = (den_T + den_P)                                              !
Density of gas stream in mol/L
        a_reac = pi * (d_reac)^2/4                                             !
Cross-sectional area of the reactor in m^2
        u_g = vout*1000 / ((a_reac)*10^(4)*60)                                 !
Velocity of gas stream in cm/s
        a_coef = 6 * (1-e_b)/d_p                                               !
Surface area per volume in 1/m
        mu_CO=1.1127*10^(-6)*t^0.5338/(1+94.7/t+0/t^2)                         !
Vapor viscosity of CO in Pa*s
        mu_H2=1.7970*10^(-7)*t^0.6850/(1-0.59/t+140/t^2)                       !
Vapor viscosity of H2 in Pa*s
        mu_He=3.2530*10^(-7)*t^0.7162/(1-9.60/t+107/t^2)                       !
Vapor viscosity of He in Pa*s
        mu_H2O=1.7096*10^(-8)*t^1.1146/(1+0/t+0/t^2)                           !
Vapor viscosity of H2O in Pa*s
        mu_CO2=2.148*10^(-6)*t^0.4600/(1+290/t+0/t^2)                          !
Vapor viscosity of CO2 in Pa*s
        mu_CH4=5.2546*10^(-7)*t^0.59006/(1+105.67/t+0/t^2)                     !
Vapor viscosity of CH4 in Pa*s
        mu_C2=2.5906*10^(-7)*t^0.67988/(1+98.902/t+0/t^2)                      !
Vapor viscosity of C2 in Pa*s
        mu_C3=4.9054*10^(-8)*t^0.90125/(1+0/t+0/t^2)                           !
Vapor viscosity of C3 in Pa*s
        mu_C4=3.4387*10^(-8)*t^0.94604/(1+0/t+0/t^2)                           !
Vapor viscosity of C4 in Pa*s
        mu_g =
y_co_o*mu_CO+y_H2_o*mu_H2+y_He*mu_He+y_H2O_o*mu_H2O+y_CO2_o*mu_CO2+y_CH4_o*mu_CH4+y_
C2_o*mu_C2+y_C3_o*mu_C3+y_C4_o*mu_C4            ! Viscosity of the feed gas stream
in Pa.s and T is in Kelvin
        re = den_gas*mw_mix*u_g/(a_coef*mu_g*100*si)                           !
Reynold's number
        j_H = 2.19 * re^(-2/3)+0.78*re^(-0.381)                                !
Chilton-Colburn factor
        pr = cp_stream * mu_g*1000/(k_g*mw_mix)                                !
Prandtl number
        h = j_H*cp_stream*den_gas*u_g*(pr)^(-2/3)*10                           !
Convective heat transfer coefficient in W/(m^2*K)
        deltatfilm = (-del_Hr)*r_co * l_p * den_part / h *10^6/60              !
Temperature difference between the bulk stream and the catalyst surface in Kelvin
```

```
        ts = t + deltatfilm                                                    !
Temperature of the catalyst surface in Kelvin
        den_Ts = 0.21048*0.001*(0.0018*(ts-273.15)^2-1.8808*(ts-273.15)+851.77)
        c_co_s = (den_Ts +den_P)*y_co_o                                        !
Surface concentration of CO in mol/m^3
        lambda = -0.0003*(t-273.15) + 0.2353                                   !
Thermal conductivity of the catalyst bed in W/(m*K)
        betta = 0.1 * (-del_Hr) * (diff*e_p /tau) * c_co_s/(ts*lambda)   ! Ratio of
particle temperature difference to surface temperature
        deltatpart = betta * ts                                                !
Particle temperature gradient
        ! sc = miog/(den_gas*d_ab1*mw_mix)*1000
        ! kc = j_H*u_g*(sc)^(-2/3)                                 ! cm/s
        ! mt_ext = r_co * den_part*l_p/(kc*c_co)*100000/60
        ratio=y_H2/y_co                    ! Feed ratio of H2 to CO
        M_W = l_p^2*(n+1)/2*(r_co/c_co_s)/(v_pore*diff/tau)*10^7/60            !
Weisz-Wheeler modulus
        ph =
(l_p)*sqrt((n+1)/2*((r_co/c_co_s^n)*c_co_s^(n-1))/(v_pore*diff/tau)*10^7/60)! Thiele
modulus from k
        eta = (3/ph)*(1/tanh(ph)-1/ph)                                         !
Effectiveness factor

       ! Pressure drop
        e_s = 0.035                                                  ! static
liquid holdup
        mu_liq = exp(-18.315+2283.5/t+0.95485*log(t))                ! liquid
viscosity for icosane in Pa*s
        den_liq = (0.18166/(0.23351^(1+(1-t/768)^0.28571)))*1000     ! liquid
density for icosane in mol/m^3
        sel_C5plus = 0.46                                            !
selectivity of C5plus of iron
        n_liq = y_co*n_in*sel_C5plus*x_co*(coef_ico/(-coef_co))      ! liquid
molar flow rate for icosane in mol/min
        u_liq = n_liq/(den_liq*a_reac*60)                            !
superficial liquid velocity for icosane in m/s
        e_dyn = (1000*mu_liq*u_liq/(g*den_liq*mw_ico*d_p^2))^(1/3)   ! dynamic
liquid holdup
        e_w = e_b - e_s                                              ! void
fraction adjusted for liquid buildup
        f = 4.2*((1-e_b)/re)^(1/6) + 150*(1-e_b)/re                  ! friction
factor
        d_pe = d_p                                                   ! effective
pellet size for sphere
        del_GW = 0.0001*((1-e_w)/(e_w^3))*den_gas*mw_mix*(u_g^2)*f/d_pe! pressure
drop for gas flowing through a packed bed in Pa/m
        delP_L = (del_GW/((1-e_dyn/e_b)^3))-den_gas*g*mw_mix         ! pressure
drop in Pa/m
        V_cat = (w_cat/den_bulk+w_silcarb/den_silcarb)/1000000       ! volume of
sample in reactor in m^3
        L_bed = v_cat/a_reac                                         ! Length of
catalyst bed in m
        delP = (delP_L*L_bed)                                        ! pressure
drop in Pa

       ! Deactivation
        ainf = 0.00055*t^2-0.608565*t+168.518                        ! Activity
at infinite time
        kd = ad*exp(-ed/(rg*t))                                      ! Rate
constant in 1/hr
        a = (1-ainf)*exp(-kd*time)+ainf                              ! Activity
     End Intermediates
```

```
      ! Optimization problem statement
      Equations
         Maximize prod
         !Minimize M_w
         !Equality constraints
         !prod = selC5plusnew*eta*r_co
         prod = eta*r_co
         !M_W = l_p^2*(n+1)/2*(r_co/c_co_s)/(v_pore*diff/tau)*10^7/60   !
Weisz-Wheeler modulus
         !Inequality constraints
         betta <= 0.1
         deltatfilm <= 5
         ! mt_ext <= 0.1
         x_co >= 0.01
         ratio >= 0.66
         delP/p <= 0.1
         a > 0.5
      End Equations

End Model
```